



The
University
Of
Sheffield.

**Investigation of the role of MAP1a light chain
(LC2) in Nav1.7 surface expression and in the
excitability of sensory neurons using a
Veratridine based calcium imaging assay**

By:

**Zainab Assim Mohammed
Abaalkhail Alogaily**

*A thesis submitted in partial fulfilment of the requirements for the degree
of Doctor of Philosophy*

**The University of Sheffield
Faculty of Science
Department of Biomedical Science**

September / 2017

Abstract

Nociceptors are a subpopulation of DRG neurons that detects noxious stimuli and signal pain. Voltage gated sodium channels (VGSC) are key factors in action potential initiation and propagation. VGSC family includes nine α -VGSC and four β -subunit subtypes. VGSC play an essential role in nociceptors hyperexcitability induced by nerve injury and inflammation, therefore, they have been extensively studied as potential targets for novel analgesics. Veratridine (VTD) is commonly used to screen for novel analgesics (VGSC blockers). Despite the wide use of VTD in functional assays, there is no information on its effect on DRG neurons. Therefore, the first part of this study aimed to investigate the effect of VTD on a primary culture of DRG neurons in calcium imaging to be able to use it to assess neuronal excitability. The data showed that VTD produces distinct calcium responses in mouse DRG neurons that vary in frequency of occurrence and cell size distribution. I classified VTD responses according to their calcium decay rate and number of peaks into Slow Decay (SD, 24%), Intermediate Decay (ID, 13%), Rapid Decay (RD, 13%) and Oscillatory (OS, 48%) response profiles. VTD-response profiles correlated with both cell size and various nociceptive markers. OS, ID and RD response profiles were produced mainly by nociceptors (small diameter neurons) in contrast to the SD response profile that showed a strong correlation with non-nociceptor (large diameter) neurons. The variation in VTD response profiles reflects the qualitative and quantitative differences in the protein constellation for each neuron subtype which ultimately results in a "VTD fingerprint" response. In support of this hypothesis, I tested different specific VGSC blockers (PF-04856264 as Nav1.7 blocker, and A-803467 as Nav1.8 blocker) on VTD elicited profiles. I found that Nav1.7 plays an essential role in eliciting all VTD response profiles while Nav1.8 is particularly required for only the OS-producing nociceptors. The result of this study showed a correlation between VTD response profiles, nociceptive markers and specific VGSC subtypes and therefore VTD is suitable to assess excitability in functional studies and drug screens.

The second part of this study focuses on the regulation of Nav1.7 surface expression. Nav1.7 is a peripherally expressed VGSC subtype that is crucial for pain signalling. In human, Nav1.7 gain of function mutations are linked to painful conditions (e.g. inherited erythromelalgia and paroxysmal extreme pain disorder), while loss of function mutation is linked to channelopathy-associated insensitivity to pain.

Therefore, Nav1.7 is proposed to be a potential target for pain relief in human. Nav1.7 protein partners play an important role in regulating the channel cellular and functional kinetics under (patho)-physiological conditions. In this study, I reported a novel interaction between Nav1.7 and the light chain (LC2) of microtubule-associated protein 1A (MAP1A) in DRG sensory neurons. I showed that Nav1.7 colocalizes with MAP1A heavy chain in the axons and neurites of the DRG neurons. I also showed that LC2 seems to negatively regulates Nav1.7 surface expression, most likely by acting as an adapter protein that links Nav1.7 to the actin cytoskeleton and other proteins. This study provides insight into the distribution of MAP1A in DRG sensory neurons and its role in regulating Nav1.7 surface expression level. This work opens new perspectives for investigating the role of the cytoskeleton networks in regulating VGSC in normal and pathological conditions.

Acknowledgement

I would like to express my sincere gratitude and appreciation to my supervisor Dr. Mohammed Nassar for being the best supervisor and mentor one could ever ask for. He believed in me when no one else did! His constant support and encouragement empowered me to always do my best and never give up. Thank you for your patience, guidance, trust, generosity and this invaluable opportunity. You have changed my life Dr. Nassar and I am forever grateful to you.

My thanks and appreciation extend to the amazing people in the department of biomedical science, particularly Dr. Liz Seward, Dr. Kai Erdmann and Prof. David Grundy for their constructive feedback and advice that have shaped my research. Thank you for your encouraging words and for helping me become a better scientist. Many thanks to Prof. Mimoun Azzouz who has generously opened his lab and provided all the help needed for the lentivirus production.

During the past four years, I was blessed to be surrounded by amazing friends and family: Aga, Maha, Ciara, Shruti, Noor and Jenan. You girls were my "Sheffield family". You have loved me, helped me and kindly welcomed me as part of your families. You showered me with many beautiful memories and lifelong friendship that I will always cherish. Aga, thank you for all your visits to the darkroom to check if I was still "alive" and bringing positive vibes when I was feeling down. Ciara, thank you for being the coolest post-doc and friend. You always knew how to encourage me, comfort me and fire-fight my worries. Maha, words are not enough to express my gratitude to you and your amazing family. You were my shelter, my food supplier and my entertainment centre. You made me feel home where it is not home. I would also like to thank my friends and colleagues; Rika, Nipa, Marta, Asma, Rania, Claudia and Donna for their help and support, the many laughs, the coffee breaks and the great memories that we have shared together. Many thanks to all my friends from back home for their phone-calls, texts, kind thoughts and prayers. Thank you for making me feel home whenever I talked to you.

Finally, my deepest and sincere gratitude to my loving family: Dad, Mom, Layan, Mohammed and Jaafar. Without your unconditional love and endless support, your comforting phone calls, your prayers, your unfailing faith in me and your sacrifice I would not have been able to reach this far. The journey was hard but became only bearable because of you. I am grateful to my sister and brothers for being my best friends and the shoulder to lean on. Thank you for loving me and making me smile every day. I am forever indebted to my parents for believing in me even when I did not, for trusting me to go through this journey and for the strength and courage that they have given me every single day of my life. I am who I am today only because of you. This work is fully dedicated for each and every one of you. I love you.

Declaration

I declare that the work presented in this thesis is my own original research and has been composed entirely by myself. All supporting literature, resources, and collaborative contributions have been acknowledged clearly.

Part of this work has been published prior to submission of this thesis under the title: "Veratridine produces distinct calcium response profiles in mouse dorsal root ganglia neurons, Scientific Reports, 2017".

Signature

Zainab Assim Mohammed,

September, 2017

REQUEST TO SUBMIT AN ALTERNATIVE FORMAT THESIS

Students should use this form to request permission to submit a doctoral thesis which contains sections which are in a format suitable for submission for publication in a peer-reviewed journal (or other appropriate outlet for academic research), alongside more traditional thesis chapters. This avoids the need for students to spend time rewriting publications into thesis chapters, as well as enhancing their writing for publication skills.

Requests to submit an alternative format thesis must be supported by the student's supervisory team and also require approval from the relevant Faculty and must therefore be made well in advance of the student submitting their thesis and no later than the end of the student's 3rd year of study.

Students wishing to submit in this format must read the guidance on structure of an alternative format thesis at: <https://www.sheffield.ac.uk/rs/code/altformat>

SECTION 1: STUDENT'S DETAILS	
NAME: Zainab A. Mohammed (old name) <u>New Name:</u> Zainab Assim M. Abaalkhail-Alogaily	REGISTRATION NUMBER: 130239769
DEPARTMENT: Biomedical Science	FACULTY: Science
PROPOSED THESIS TITLE: The role of MAP1A light chain (LC2) in Nav1.7 surface expression and in the excitability of sensory neurons	
REASON FOR THE REQUEST: Please use this space to provide details of the published papers that will be incorporated into your thesis and how your thesis will be structured (continue on a separate sheet, if required)	
<p>The data that was published in Scientific Reports (an open access journal) will comprise the first result chapter. It includes a detailed characterisation of the Veratridine calcium responses in mouse dorsal root ganglion under normal condition (baseline). All the experiments required for the basic characterisation were included in the paper. No additional experiments or further discussion is required or added for this part, therefore the paper can be included as a result chapter as it is with no further modifications. The rest of the work is included in the other two results' chapters.</p> <p>Thesis format:</p> <p>Chapter 1: General introduction. This chapter is a summary of the relevant literatures that provides the basis for all the results' chapters.</p> <p>Chapter 2: Materials and Methods. This chapter include a detailed lists and descriptions of all the materials and methods protocols used in the thesis.</p> <p>Chapter 3: Characterization of VTD distinct calcium responses in DRG neurons. This chapter demonstrates results that are the basis for the other two chapters. It demonstrates a detailed characterisation of the functional assay used in the thesis. I have published the results of this chapter in Scientific Reports, 2017 (<i>Veratridine produces distinct calcium response profiles in mouse Dorsal Root Ganglia neurons</i>)¹.</p> <p>Chapter 4: Differential effects of VGSC blockers on VTD calcium response profiles in mouse DRG neurons. This chapter contains further characterisation of the functional assay used in Chapter 3 (published). The results demonstrate the specific effect of the VGSC blockers on the Veratridine response profiles. This chapter consists of an introduction, method, results and discussion sections.</p> <p>Chapter 5: The role of MAP1A light chain (LC2) in the excitability of sensory neurons. This</p>	

chapter represent data that characterised a novel interaction between Nav1.7 channel and the light chain of MAPIA protein (LC2). It contains the biochemical characterisation as well as the functional characterisation based on the data obtained from the functional assay described in chapter 3 (published) and chapter 4. This chapter consists of an introduction, method, results and discussion sections.

Chapter 6: Discussion. This chapter discusses the results obtained in the three results' chapters and highlights the current limitations and the future perspective of the work represented in the thesis.

Reference:

- 1 Mohammed, Z. A., Doran, C., Grundy, D. & Nassar, M. A. Veratridine produces distinct calcium response profiles in mouse Dorsal Root Ganglia neurons. *Scientific Reports* **7**, 45221, doi:10.1038/srep45221 (2017).

SIGNATURE: Zainab A. Mohammed

DATE 20/11/2017

SECTION 2: SUPERVISOR'S COMMENTS

NAME:

DEPARTMENT:

COMMENTS IN SUPPORT OF THE REQUEST:

Zainab has one paper published in a quality peer reviewed journal. The publication process involved writing a manuscript and dealing with reviewers comments. Therefore, it is best of that chapter is presented as the published paper rather than rewrite it for her thesis.

SIGNATURE:

Mohammed Nassar

DATE: 20/11/17

Please return this completed form to one of the following email addresses, depending on your Faculty: Arts & Humanities - pgrarts@sheffield.ac.uk; Engineering - pgreng@sheffield.ac.uk; Medicine, Dentistry & Health - pgrmdh@sheffield.ac.uk; Science - pgrsci@sheffield.ac.uk; Social Sciences - pgrsocscl@sheffield.ac.uk

SECTION 3: FACULTY CONSIDERATION

NAME:

FACULTY:

COMMENTS ON DECISION:

Good idea to let us know before submission next time !!



I approve this request for submission of an alternative format thesis



I do not approve this request for submission of an alternative format thesis

SIGNATURE:

[Signature]

DATE:

28/11/17



List of abbreviations

AIS	Axonal initial segment
Adcyap1	Adenylate Cyclase Activating Polypeptide 1
AITC	Allyl isothiocyanate
AUC	Area under the curve
BDNF	Brain-derived neurotrophic factor
BKCa	calcium-activated potassium channel
Caco-2	Human colon colorectal adenocarcinoma epithelial cell line
CAP	Capsaicin
CGRP	calcitonin gene-related peptide
CIP	Channelopathy-associated insensitivity to pain
CNS	Central nervous system
co-IP	Co-immunoprecipitation
Cpne6	Copine 6
cRet	Rearranged during transfection
DIV	Days in vitro
DKO	Double knock-out
DRG	Dorsal root ganglia
ERK1/2 MAPK	Extracellular signal regulated kinase 1/2 mitogen-activated protein kinase
FGF-13	Fibroblast growth factor – 13
FLIPR	Fluorescence imaging plate reader
Gal	Galanin And GMAP Prepropeptide
GDNF	glial-cell-line-derived neurotrophic factor
GECI	genetically encoded calcium indicator
Gfra3	GDNF Family Receptor Alpha 3
HEK293	Human Embryonic Kidney cell line
I.D	Integrated density
IB4	isolectin B4
ID	Intermediate decay
IEM	Inherited erythromelalgia
KD	Knock-down

KO	Knock-out
LC1	Light chain of MAP1B protein
LC2	Light chain of MAP1A protein
LTMR	Low threshold mechanoreceptors
LV	Lentivirus
MAP	Microtubule-associated protein
MOI	Multiplicity of infections
Mrgpra3	Mas-related G-protein coupled receptor member A3
Mrgpra4	Mas-related G-protein coupled receptor member A4
N2a	Neuroblastoma-2a cell line
Nedd4	<u>N</u> euronal precursor cell <u>e</u> xpressed <u>d</u> evelopmentally <u>d</u> ownregulated type 4
Nedd4-2	<u>N</u> euronal precursor cell <u>e</u> xpressed <u>d</u> evelopmentally <u>d</u> ownregulated type 4-2
NF	Neurofilament heavy chain
NF200	Neurofilament 200
NGF	Nerve growth factor
NMDAR	N-methyle-d-aspartate receptor
NP	Non-peptidergic
NP _{os}	Non-persistent oscillations
Nppb	Natriuretic Peptide B
NT-3	neurotrophin
Ntrk1	Neurotrophic Receptor Tyrosine Kinase 1
Nxph1	Neurexophilin 1
OS	Oscillatory
PD	Pore-domain
PEP	Peptidergic
PEPD	Paroxysmal extreme pain disorder
PIC	Protease inhibitor cocktail
PNS	Peripheral nervous system
P _{os}	Persistent oscillations
PSD-93	Post-synaptic density – 93

PTM	Post-translational modification
Pvalb	Parvalbumin
RD	Rapid decay
Ret	
Rspo1	R-Spondin 1
S100b	S100 Calcium Binding Protein B
Scrm	Scrambled
SD	Slow decay
SNI	spared nerve injury model
SS1 and SS2	Self-similarity domain
STORM	Stochastic optical reconstruction microscopy
TH	Tyrosine hydroxylase
TNP-ATP	Triethylammonium salt
Trk	Tropomyosin receptor kinase or Tyrosine receptor kinase
TTX	Tetrodotoxin
TTX-R	Tetrodotoxin-resistant channel
TTX-S	Tetrodotoxin-sensitive channel
UBE2L3	E2 ubiquitin conjugase
VGCC	Voltage-gated calcium channel
VGKC	Voltage-gated potassium channel
VGS	Voltage-sensor domain
VGSC	Voltage-gated sodium channel
Y2H	Yeast-2-hybrid

Table of Content

	Page
Chapter 1: Introduction.....	2
1.1. Dorsal root ganglia (DRG) sensory neurons	2
1.1.1. Heterogeneity of sensory neurons	2
1.1.2. EXCITABILITY OF DORSAL ROOT GANGLIA (DRG) AND PAIN SIGNALING	5
1.2. Voltage-gated sodium channels (VGSC) in DRG neurons	8
1.2.1. VGSC structure.....	8
1.2.2. The voltage-dependence gating of VGSC	10
1.2.3. VGSC tissue expression and biophysical properties	11
1.3. Nav1.7 VGSC subtype	13
1.3.1. Nav1.7 expression pattern	13
1.3.2. Evidence for Nav1.7 implications in pain	14
1.3.2.1. Human mutations	14
1.3.2.2. Animal knock-out (KO) studies	18
1.3.3. Nav1.7 interacting protein partners	19
1.4. Neuronal Microtubule Cytoskeleton and Microtubule-Associated Proteins.	22
1.4.1. Microtubules : composition, structure and organisation.	22
1.4.2. Biological functions of the microtubules.	25
1.4.3. Microtubule-Associated Proteins (MAPs)	26
1.4.4. Structural Microtubule-Associated Proteins (Structural MAPs)	27
1.4.5. MAP1 family of proteins	31
1.4.5.1. Structural features of MAP1 proteins	31
1.4.5.2. Functional roles of MAP1 heavy and light chains.	34
1.5. Calcium imaging assay for assessing DRG excitability	41
1.5.1. Calcium imaging indicators	41

1.5.2. In vitro calcium imaging of DRG neurons	42
1.5.3. In vivo calcium imaging of DRG neurons.....	43
1.5.4. The use of Veratridine to activate neurons in calcium imaging assay.....	45
1.6. Aims	47
Chapter 2: Materials and Methods	49
2.1. Materials.....	49
2.1.1. Animals.....	49
2.1.2. Mammalian cell lines	49
2.1.3. Bacterial strains	49
2.1.4. Cell culture reagents.....	50
2.1.5. Bacterial Culture and molecular cloning reagents.....	51
2.1.6. Restriction enzymes	51
2.1.7. Pharmacological compounds.....	52
2.1.8. Reagents, Chemicals and Solvents	52
2.1.9. Commercial Kits.....	54
2.1.10. Primary Antibodies.....	55
2.1.11. Secondary Antibodies.....	56
2.1.12. DNA Plasmids.....	56
2.1.13. Primers	57
2.1.14. MAP1A miRNA sequences.....	58
2.1.15. Tools and labware	58
2.1.16. Buffer, solution and medium recipes.....	59
2.2. METHODS	63
CELL CULTURE RELATED METHODS.....	63
2.2.1. Mouse dorsal root ganglia primary culture.....	63
2.2.1.1. DRG isolation.....	63
2.2.1.2. DRG digestion.....	63

2.2.1.3. DRG dissociation and culture preparation.....	63
2.2.2. Mammalian cell lines	64
2.2.2.1. Cell line types and culture media	64
2.2.2.2. Cell line sub-culturing.....	64
2.2.3. Cell line DNA transfection.....	64
2.2.4. DRG neuron LV transduction.....	66
PROTEIN RELATED METHODS	66
2.2.5. Western blot.....	66
2.2.5.1. Sample lysis and protein extraction.....	66
2.2.5.2. Protein quantification.....	67
2.2.5.3. Sample preparation.....	67
2.2.5.4. SDS-PAGE sample loading and running.....	67
2.2.5.5. Transfer.....	68
2.2.5.6. Blocking and primary antibody incubation	68
2.2.5.7. Protein signal revelation	68
2.2.6. Co-immunoprecipitation (co-IP)	69
2.2.7. Cell surface biotinylation	70
2.2.8. Immunofluorescence (IF)	70
2.2.8.1. Immunocytochemistry (ICC).....	70
2.2.8.2. Immunohistochemistry (IHC).....	71
NUCLEIC ACID RELATED METHODS.....	72
2.2.9. Plasmid preparation.....	72
2.2.9.1. Bacterial transformation	72
2.2.9.2. Amplification, isolation and purification of plasmid DNA.....	72
2.2.9.3. Qualitative and quantitative DNA analysis.....	72
2.2.10. Molecular cloning.....	73
2.2.10.1. Restriction enzyme digestion and gel electrophoresis	73

2.2.10.2. DNA ligation	74
2.2.11. MAP1A miRNA preparation	74
2.2.11.1. Design and structure of MAP1A pre-miRNA sequences	74
2.2.11.2. Cloning MAP1A pre-miRNA sequence into BLOCK-iT™ Pol II miR RNAi expression vector.....	75
2.2.11.3. Chaining of miRNAs	75
2.2.12. Production of LC2-myc (full length and deletion constructs)	77
2.2.12.1. Primers.....	77
2.2.12.2. Polymerase Chain Reaction (PCR).....	78
LENTIVIRUS RELATED METHODS.....	79
2.2.13. Production of lentivirus particles	79
2.2.13.1. Preparation of LV DNA constructs	79
2.2.13.2. Sub-cloning of miRNA cassette into lentivirus vector	79
2.2.13.3. Seeding HEK-293 cells for transfection.....	79
2.2.13.4. DNA transfection of HEK-293 cells	80
2.2.13.5. Harvesting lentivirus particles.....	80
2.2.13.6. Lentivirus titre measurement	80
FUNCTIONAL ASSAY	81
2.2.14. Calcium Imaging	81
2.2.14.1. Seeding cells for calcium imaging experiment	81
2.2.14.2. Cell loading with Fura-2AM calcium dye	81
2.2.14.3. Experimental set-up and image acquisition.....	82
2.2.15. Data processing and statistical analysis	82
2.2.15.1. Calcium imaging data.....	82
2.2.15.2. Western Blot data analysis.....	83
2.2.15.3. Immunofluorescence data analysis	83
Chapter 3: Characterization of Veratridine distinct calcium response profiles in mouse DRG neurons.....	87

Chapter 4: Differential effects of VGSC blockers on VTD calcium response profiles in mouse DRG neurons.....	107
4.1.Introduction.....	107
4.2.Aim.....	109
4.3.Methods.....	109
4.4.Results.....	111
Nav1.7 BLOCKER (PF-04856264) RESULTS.....	111
4.4.1. PF-04856264 (5µM) reduces all VTD response profiles.....	111
4.4.2. PF-04856264 (5 µM) reduces the relative frequency of the OS response profile.....	113
4.4.3. PF-04856264 has no effect on the maximum peak amplitude and on the area under the curve (AUC) of VTD responses.....	114
4.4.4. PF-04856264 (5 µM) causes delayed RD responses.....	117
Nav1.8 BLOCKER (A-803467) RESULTS.....	118
4.4.5. A-803467 preferentially reduces the percentage of the OS response profile.....	118
4.4.6. A-803467 reduces the relative frequency of the OS response profile and its persistent subtype.....	120
4.4.7. The effect of A-803467 on the maximum peak amplitude and area under the curve (AUC).....	122
4.4.8. A-803467 has no effect on the latency of VTD responses.....	123
4.5.Discussion.....	124
Chapter 5: The role of MAP1A light chain (LC2) in the excitability of sensory neurons.....	130
5.1. Introduction.....	130
5.2. Aims.....	132
5.3. Methods.....	133
5.3.1. Calcium imaging.....	133

5.4. Results	134
5.4.1. MAP1A expression pattern in adult mouse DRG neurons.	134
5.4.2. LC2 interacts with Nav1.7 in Neuroblastoma-2a and mouse DRG neuron.....	144
5.4.3. Knock-down of MAP1A protein in N2a and DRG neurons.....	148
5.4.3.1. MAP1A miRNA cloning, testing and optimisation of MAP1A knock-down in N2a cells	149
5.4.3.2. MAP1A KD functional effect on the surface expression level of endogenous Nav1.7 in N2a cells.....	151
5.4.3.3. Optimization of lentivirus multiplicity of infection (MOI) for DRG neuron transduction.	153
5.4.3.4. Production of LV-MAP1A miRNA and in vitro determination of MAP1A KD efficiency in DRG sensory neurons.....	157
5.4.4. The effect of MAP1A KD on Nav1.7 surface expression in mouse DRG neurons:.....	162
5.4.5. The effect of MAP1A KD on neuronal excitability	165
5.4.5.1. LV transduction increases neuronal excitability.....	165
5.4.5.2. LV-MAP1A miRNA does not affect the distribution of VTD response profiles	165
5.4.5.3. Long-term DRG culture has a different distribution of VTD response profiles	169
5.4.5.4. Cell size distribution of LV-transduced DRG neurons	171
5.4.5.5. Analysis of the various VTD response parameters in LV-transduced and untransduced DRG neurons	172
5.4.6. Localisation of Nav1.7 binding site in LC2.	176
5.5. Discussion.....	179
5.5.1. MAP1A (HC and LC2) showed distinct distribution patterns in mouse DRG neurons.....	179

5.5.2. Nav1.7 interacts with the Light chain (LC2) of microtubule-associated protein 1 A (MAP1A) in N2a cells and DRG neurons.....	181
5.5.3. Nav1.7 surface expression level and activity increased upon LC2 KD.	182
Chapter 6: Discussion	188
6.1. The use of Veratridine in assessing neuronal excitability of DRG neurons - An old drug, a new tale.....	188
6.2. LC2 specifically interacts with Nav1.7 and negatively regulates Nav1.7 membrane expression in DRG neurons.	192
6.3. Limitations of MAP1A – Nav1.7 work	194
Bibliography.....	193

List of Figures

Figure Title	Page
CHAPTER 1	
Figure 1.1: Schematic representation of the various types of DRG sensory neurons and their projection sites within the spinal cord	4
Figure 1.2: Demonstration of the generation and conduction of action potential signals in afferent pain pathway	6
Figure 1.3: Structure of voltage-gated sodium channel (VGSC)	9
Figure 1.4: Schematic representation of inactivation coupled activation of VGSC	10
Figure 1.5: The sodium current biophysical properties and activation potential of peripheral VGSC (Nav1.7, Nav1.8 and Nav1.9)	13
Figure 1.6: Illustration of the gain-of-function mutations of Nav1.7 channel	17
Figure 1.7: Schematic representation of the microtubules structure and MT dynamic instability	23
Figure 1.8: Schematic representation of the microtubule orientations at different neuronal sites	25
Figure 1.9: Classification of different types of structural MAPs	28
Figure 1.10: Morphological differences of various types of MAPs	29
Figure 1.11: MAP1A and MAP1B structural features	32
Figure 1.12: Schematic representation of MAP1A structure	33
CHAPTER 2	
Figure 2.1: Representation of the sites where each of the four MAP1A miRNA sequences targets	75
Figure 2.2: The structure of the designed pre-miRNA	75
Figure 2.3: An illustration the steps required to produce pcDNA™ 6.2-GW/EmGFP-miR expression clone	76
Figure 2.4: An illustration of the steps required to chain two miRNAs into one expression vector	77

Figure 2.5: Schematic representation of the primer positions on MAP1A-light chain (LC2)	77
Figure 2.6: An example of unmodified raw images of Nav1.7 and MAP1A-HC immunostaining and their negative control in mouse DRG culture.....	84
Figure 2.7. Illustration of the Nav1.7 membrane quantification method by ImageJ software	85

CHAPTER 3

Figure 1: Veratridine elicits TTX-sensitive calcium responses in DRG neurons	89
Figure 2: Veratridine produces four calcium response profiles that differ in their frequency of occurrence and latency to peak	90
Figure 3: Veratridine OS, RD and ID response profiles occur in neurons smaller than 30 μm in diameter	91
Figure 4: Veratridine SD and RD response profiles are under-represented in capsaicin - sensitive neurons	92
Figure 5: Veratridine SD and RD response profiles are under – represented in α , β -methylene ATP – sensitive neurons	93
Figure 6: The Veratridine OS, ID and RD response profiles are enriched in nociceptors	94
Figure 7: VTD response profiles correlate with classical functional markers of nociceptors	95
Figure 8: Distribution of sensitivity to the three nociceptive markers within the four VTD response profiles	95
Figure 9 : Comparison of the sensitivity to the three nociceptive markers based on published RNASeq and our functional imaging data	97
Figure S1: Order of Veratridine and capsaicin application does not affect VTD response profiles	102
Figure S2: The order of Veratridine and α , β -methylene ATP application does not affect VTD response profiles	103
Figure S3: The order of Veratridine α , β -methylene ATP, capsaicin and AITC application does not affect VTD response profiles	104
Figure S4: Relationship between AITC sensitivity and the four Veratridine profiles	105

CHAPTER 4

Figure 4.1: Aryl sulfonamide binding site in α -subunit of VGSC	108
Figure 4.2: Illustration of the calcium imaging protocol used in the experiments presented in this chapter	110
Figure 4.3: The effect of PF-04856264 on the total number of VTD responding neurons	111
Figure 4.4: Analysis of the inhibitory effect of PF-04856264 on VTD response profiles	112
Figure 4.5: Comparison of the relative frequency of each VTD response profile in the presence of PF-04856264	113
Figure 4.6: Analysis of the effect of PF-04856264 on the oscillatory pattern of OS responding neurons	115
Figure 4.7: Analysis of the effect of PF-04856264 on the maximum VTD peak responses and their area under the curve	116
Figure 4.8: Analysis of the effect of PF-04856264 on latency of VTD response profiles	117
Figure 4.9: The effect of A-803467 on the total number of VTD responding neurons	118
Figure 4.10: Analysis of the inhibitory effect of A-803467 on VTD response profiles	119
Figure 4.11: Comparison of the relative frequency of each VTD response profile in the presence of A-803467	121
Figure 4.12: Analysis of the effect of A-803467 blocker on the oscillatory pattern of OS responding neurons	121
Figure 4.13: Analysis of the effect of A-803467 on the maximum VTD peak responses and their area under the curve	122
Figure 4.14: Analysis of the effect of A-803467 on latency of VTD response profiles	123

CHAPTER 5

Figure 5.1: Co-immunostaining of LC2 and β III-tubulin in mouse DRG section	135
---	-----

Figure 5.2: Co-immunostaining of LC2 and NF-200 in mouse DRG section ...	135
Figure 5.3: Co-immunostaining of LC2 and NF-200 in mouse DRG section	136
Figure 5.4: Co-immunostaining of LC2 and NF-200 in mouse DRG section	136
Figure 5.5: immunostaining pattern of MAP1A-HC and LC2 in mouse DRG culture	138
Figure 5.6: immunostaining pattern of MAP1A-HC and Actin in mouse DRG culture	139
Figure 5.7: immunostaining pattern of MAP1A-HC and Nav1.7 in the neurites of DRG neurons	140
Figure 5.8: Immunostaining pattern of MAP1A-HC DRG neurons	141
Figure 5.9: immunostaining pattern of MAP1A-HC in the soma of DRG neurons	142
Figure 5.10: immunostaining pattern of MAP1A-HC in the soma and neurites of DRG neurons	142
Figure 5.11: immunostaining pattern of LC2 in the soma of DRG neurons	143
Figure 5.12: Co-immunoprecipitation of Nav1.7 and LC2 in N2a cells	144
Figure 5.13: Co-immunoprecipitation of Nav1.7 and LC2 in mouse DRG	145
Figure 5.14: Co-immunoprecipitation of Nav1.7 in N2a cells	147
Figure 5.15: Flow chart demonstration of the work flow followed in this chapter to test the functional effect of MAP1A KD in adult mouse DRG neurons	149
Figure 5.16: Quantification of MAP1A KD in N2a cells by miRNA chaining approach	150
Figure 5.17: Specificity of MAP1A miRNA in N2a cells.....	151
Figure 5.18: The effect on MAP1A KD on surface Nav1.7 expression level in N2a cells	152
Figure 5.19: GFP expression in dissociated adult DRG culture transduced with GFP-lentivirus	154
Figure 5.20: GFP expression in dissociated adult DRG culture transduced with GFP-lentivirus	155
Figure 5.21: Lentivirus transduction efficiency in adult mouse DRG culture	156

Figure 5.22: Quantification of MAP1A KD in N2a cells using LV vector	157
Figure 5.23: Distribution of MAP1A-HC integrated density in DRG culture	159
Figure 5.24: Lentivirus mediated MAP1A knock-down in adult mouse DRG culture	160
Figure 5.25: β III-tubulin expression level in adult mouse DRG culture transduced with lentivirus expressing MAP1A miRNA	161
Figure 5.26: Correlation between Nav1.7 (membrane / cytoplasm) ratio and MAP1A in adult mouse DRG culture	163
Figure 5.27: Nav1.7 (membrane / cytoplasm) ratio in LV mediated MAP1A KD in adult mouse DRG culture	164
Figure 5.28: Comparison of Nav1.7 (membrane / cytoplasm) ratio in LV mediated MAP1A KD in adult mouse DRG culture within the various MAP1A expression levels	164
Figure 5.29: The percentage of VTD responding DRG neurons transduced with lentivirus	166
Figure 5.30: The distribution of VTD response profiles within GFP (+) DRG neurons	167
Figure 5.31: The distribution of VTD response profiles within GFP (-) DRG neurons	168
Figure 5.32: The distribution of VTD response profiles within GFP (+ & -) DRG neurons	170
Figure 5.33: Cell size distribution of adult mouse DRG culture transduced with lentivirus expressing MAP1A miRNA	171
Figure 5.34: Analysis of the effect of MAP1A KD on the maximum VTD peak responses	173
Figure 5.35: Analysis of the effect of MAP1A KD on the area under the peak (AUC) of VTD responses	174
Figure 5.36: Analysis of the effect of MAP1A KD on the VTD responses onset	175
Figure 5.37: Validation of the expression of LC2 deletion mutants by western blotting	177
Figure 5.38: Validation of the expression of LC2-myc by immunostaining	178

Figure 5.39: Schematic diagram that illustrates the role of LC2 in regulating Nav1.7 membrane expression in DRG sensory neurons 185

List of Tables

Table Title	Page
CHAPTER 1	
Table 1.1: Summary of MAP1A and MAP1B protein interactions	40
CHAPTER 2	
Table 2.1: Mammalian cell line seeding density	65
Table 2.2: The concentration of DNA ($\mu\text{g}/\text{mL}$) of different constructs used in transfection experiments	65
Table 2.3: Lysis buffer volumes used for sample lysis and protein extraction in different experiments	67
Table 2.4: SDS-PAGE recipe (Bio-Rad protocols)	68
Table 2.5: Description of the PCR mixture components	78
Table 2.6: Optimized annealing temperature used for different primer pairs	78

CHAPTER 1

INTRODUCTION

Chapter 1: Introduction

1.1. Dorsal root ganglia (DRG) sensory neurons

The function of the nervous system greatly relies on a highly elaborated network of neurons that mediates the communication between the brain and the different parts of the body. The nervous system consists of two main parts: The Central Nervous System (CNS) and the Peripheral Nervous System (PNS) that conveys information from the peripheral tissues to the CNS through afferent (sensory) neurons, and the outgoing signal is transmitted back to the periphery via efferent (motor) neurons. The pseudounipolar somata of the sensory neurons aggregate outside the spinal cords forming the Dorsal Root Ganglia (DRG). Sensory neurons send both peripheral axons to innervate the peripheral tissues and central axons to the spinal cord.

1.1.1. Heterogeneity of sensory neurons:

Sensory neurons are highly specialised cell population that detects noxious and innocuous peripheral stimuli. Sensory neurons are heterogeneous population that includes neurons that respond to changes in temperature (thermosensors), changes in pressure (mechanoreceptors), itch (pruriceptors), body movement and balance (proprioceptors), and noxious and painful stimuli (nociceptors). Yet within each type, a considerable level of heterogeneity is present which can be further sub-divided according to differences in the molecular expression pattern of signalling molecules, ion channels and receptors. Sensory neurons are widely known as “polymodal” in which multiple modalities can be integrated by one neuron, e.g. thermal and mechanical stimuli. Such high level of molecular and functional heterogeneity is essential for sensory neurons to be able to detect and integrate wide range of sensory information (innocuous and noxious) ^{16,17}.

Several efforts have been made to classify DRG neurons according to various properties. The earliest attempts to classify peripheral neurons were made by Erlanger and Gasser in the 1927. The classification of peripheral fibres was made based on the conduction velocity and was correlated to the diameter size in later studies. They divided the sensory fibres into three groups: A β , A δ and C-fibres. They found that the larger the diameter, the higher the velocity of conduction and magnitude of electrical response but the lower the threshold of excitation. These properties are characteristic

of myelinated group A fibres. The opposite applies for groups C fibres which are unmyelinated, small diameter with low conduction velocity and higher threshold ^{18,19}.

In addition, DRG neurons are also classically classified according to their soma size into large, medium and small diameter neurons. DRG morphology is correlated to neuronal function, where small and medium size neurons are mostly nociceptors that send their unmyelinated C-fibres and thinly myelinated A δ - fibres to the outer layer of the spinal cord (lamina I-II). While, large diameter neurons are mostly mechanoreceptors and proprioceptors that send their thickly myelinated A β - fibres to deeper regions in the spinal cord (lamina III-V) ^{20,21}, Fig.1.1.

DRG neurons are also classified according to the expression of certain molecular markers. Some are essential for the development and maturation of specific neuronal subtypes like Tyrosine receptor kinase (TrkA, TrkB, TrkC and cRet) which are receptors for nerve growth factor (NGF), brain-derived neurotrophic factor (BDNF), neurotrophin (NT3) and glial-derived neurotrophic factor (GDNF), respectively ^{13,22-24}. DRG neuron subpopulation can be identified by a combination of those markers along with others. Large diameter neurons are generally identified by neurofilament expression (NF-200), but can be further sub-classified. Proprioceptive large diameter neurons are known to be TrkC expressing cells (TrkC⁺). While the large diameter, low threshold, mechanoreceptive neurons (LTMR) are TrkC⁺ and / or TrkB⁺. On the other hand, small diameter neurons are sub-classified according to their isolectin B4 (IB4)-binding and to their neuropeptide content (substance P and calcitonin gene-related peptide CGRP) into IB4⁺ (non-peptidergic neurons, TrkA⁻, cRet⁺) and IB4⁻ (peptidergic neurons, TrkA⁺). Small diameter, LTMR C-fibres is a distinct (IB4⁻, non-peptidergic) subset within the small diameter neurons predominantly characterised by tyrosine hydroxylase expression (TH) ^{23,25-28}.

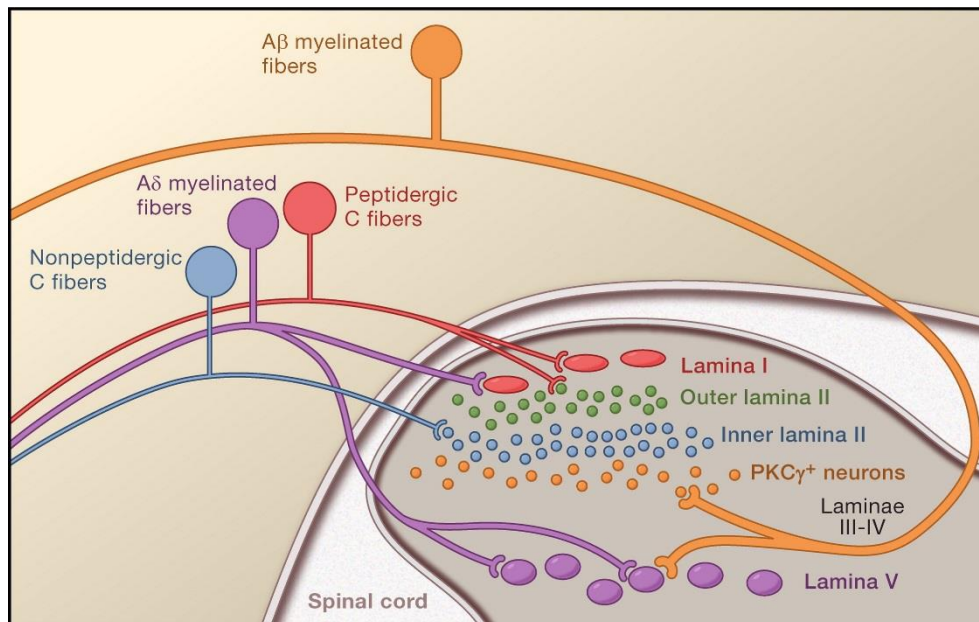


Figure 1.1: Schematic representation of the various types of DRG sensory neurons and their projection sites within the spinal cord. Sensory neuron somata reside outside the spinal cord. The neurons are pseudounipolar, where they have a short stalk that divides into two projections (a central and peripheral). The central projections terminate at distinct regions within the spinal cord. The unmyelinated, peptidergic C-fibers (red) and the myelinated Aδ-fibres terminate at superficial layer of the spinal cord making synapse with large projection neurons (red) in lamina I and interneurons in the outer layer of lamina II. The unmyelinated, non-peptidergic C-fibres neurons synapse with interneurons (blue) in the inner layer of lamina II. Large, myelinated Aβ-fibers (orange) synapse with PKCγ expressing interneurons in that reside deep in the ventral half of the inner lamina II. A distinct set of projection neurons in lamina V (purple) receive signals from Aδ- and Aβ- fibres. Source (Basbaum et al., 2009) ¹³.

Several “functional” classifications of DRG neurons are available today. Some are based on their calcium responses elicited by an array of pharmacological agents ²⁹⁻³², or by a pan-neuronal agonist ³³. In addition, several other classifications have been proposed based on a single-cell PCR ³⁴, RNA-sequencing and microarray techniques ³⁵⁻³⁸. Recently, data from single-cell RNA-sequencing of DRG neurons became available ³⁹. Usoskin et al, have classified DRG neurons into 11 molecularly distinct subtypes. Another study by Li et al, 2016 that used a single-cell (high coverage) RNA-sequencing technique combined with in vivo electrophysiology suggested that DRG subpopulations are far more complex than what all the previous studies have described. The authors of this study proposed a new classification of the DRG neurons based on unbiased transcriptomic, functional and morphological data. Their classification consists of 10 main groups, and 14 sub-groups providing a new, more comprehensive catalogue of DRG neurons ⁴⁰. New DRG subtypes and new molecular

markers have been suggested by this study. C1 – C6 represents the small diameter neuron groups, while C7 – C9 groups are the large diameter neurons. Further subclassification of these groups was proposed based on detailed gene network analysis. C4-2 subgroup expresses high levels of both *Mrgpra3* and *Mrgpra4* genes while C4-1 expresses only *Mrgpra3*. Gene cluster analysis of C2 reveals some interesting neuronal subgroups where C2-2 subgroup expresses characteristic functional genes of C2 (*Ntrk1*, *Gfra3* and *Nppb*) along with other functional genes from other groups (*Pvalb* and *S100b* – genes that are predominantly expressed in large diameter neuron), therefore a “hybrid state” is referred to this C2-2 subcluster since its gene expression pattern is a hybrid of small and large diameter neurons. Similarly, C6 cluster represents a “hybrid state” where both *Mrgprd* and *S100b* are expressed; characteristic genes for small diameter and large diameter neurons, respectively. C7 and C8-1 are new groups that have not been described previously. Cells within these clusters express genes like *Nxph1* and *Ntrk3*, which makes them highly sensitive to noxious and innocuous mechanical stimuli (i.e. large-diameter mechanoheat nociceptors). C10 group also showed a high level of overlap with the other clusters. Cells in C10 group express *Gal* and *Adcyap1* (representative genes for C1), *Rspo1* (a representative gene for C4) in addition to other genes from C3 (e.g. *TH*) and large diameter neuron (e.g. *Cpne6*). Overall Li et al., study has revealed the degree of overlap in the traditional classification and shed light on the importance of integrating morphological, functional as well as transcriptional data while studying DRG neurons.

1.1.2. EXCITABILITY OF DORSAL ROOT GANGLIA (DRG) AND PAIN SIGNALING:

Neurons, as other cells in the body, display a negative membrane potential at resting state (resting membrane potential) due to the differences in the electrochemical gradient of ions, particularly sodium and potassium ions. Na^+ / K^+ ATPase pump and K^+ -leak channels are primarily involved in maintaining high K^+ / low Na^+ intracellular concentrations ⁴¹. Sensory neurons are mostly quiescent, but they fire action potentials on the presence of peripheral stimuli - mechanical, thermal or chemical. The specific expression and the subcellular localization of specific ion channels, ion exchangers and receptors are what determine neuronal excitability ¹⁰.

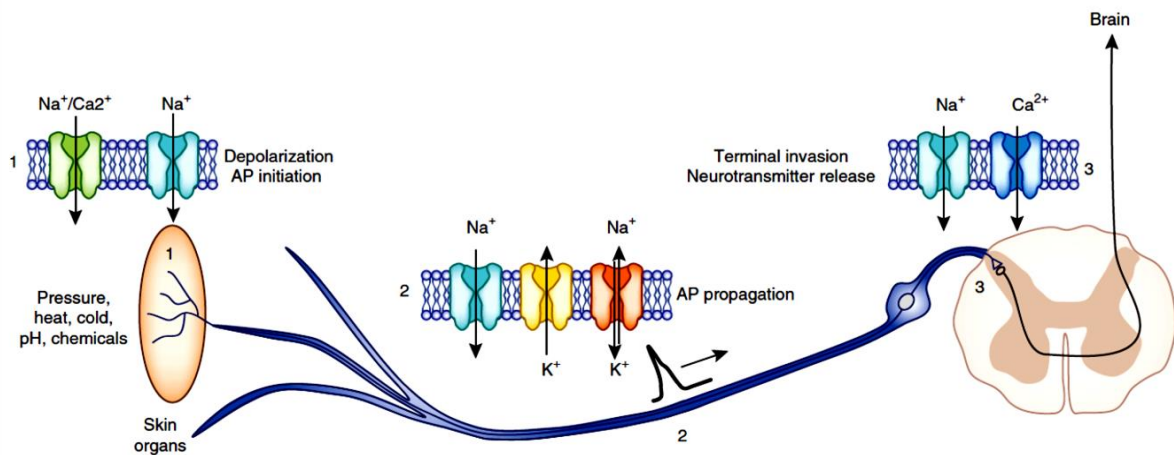


Figure 1.2: Demonstration of the generation and conduction of action potential signals in afferent pain pathway. (Site 1) Terminals of DRG neurons sense noxious stimuli, activate nonselective cation channels and VGSC. (Site 2) Propagation of the action potential through the axon is mediated by VGSC and voltage-gated K channels. (Site 3) activation of DRG somata mediate the signal transmission to the synaptic nerve terminals, where VGSC and voltage-gated calcium channels cooperate to facilitate the release of neurotransmitters such as glutamate and substance P that mediate the transmission of signals to the CNS. Source (Waxman et al., 2014) ¹⁰.

Detection of noxious peripheral stimuli occur at the level of the peripheral nerve terminals of primary afferent nociceptive fibres, where the activation of ion channels and receptors in the nerve terminals elicit action potentials that propagate along the nociceptive fibres to the dorsal horn of the spinal cord. At the spinal cord, neurotransmitter release (e.g. glutamate and substance P) from the presynaptic terminals of the primary afferent fibres result in activation of the second-order neurons that project and send the signal to the higher brain levels producing the painful sensation, Fig.1.2. Such organized signal transduction requires proper expression and distribution of specific ion channels, receptors, ion exchangers along the nerve terminals, axons and presynaptic terminals, accompanied by specific neurotransmitter synthesis and release mechanism. Dysregulation of any of these components, as in chronic pain conditions, results in an increased sensitivity to peripheral stimuli (reduced threshold), inappropriate action potential firing and neuronal hyperexcitability ^{10,42}.

Animal and genetic studies and human mutations have highlighted several ion channels and receptors as important players in regulating neuronal excitability, some of which are voltage-gated ion channels (sodium, potassium and calcium), Transient-receptor potential (TRP) channels, leak channels and ligand-gated channels.

Voltage-gated sodium channels (VGSC) are essential for the generation and initiation of action potential. They are involved in setting the resting membrane potential and contribute to the upstroke, initiation and propagation of the action potential, as well as synaptic transmission^{10,43,44}. Interestingly, specific VGSCs subtypes are preferentially expressed in the peripheral nervous system and are strongly implicated in chronic pain conditions (discussed in details later). The preferential expression of some VGSC subtypes in the peripheral nervous system as well as their pivotal role in regulating sensory neuron excitability under (patho)- physiological conditions make them potential candidates for pain relief strategies with minimum central side effects.

In the next few sections, I will mainly focus on the VGSC as key regulator of DRG excitability with a particular interest in VGSC subtypes that are involved in the nociceptive pathway.

1.2. Voltage-gated sodium channels (VGSC) in DRG neurons

1.2.1. VGSC structure:

VGSC family includes nine alpha-VGSC (Nav1.1 to Nav1.9) encoded by SCN1A, SCN2A, SCN3A, SCN4A, SCN5A, SCN8A, SCN9A, SCN10A and SCN11A, respectively, and four beta subunits (β 1- β 4) encoded by (SCN1B – SCN4B). The α -VGSC subunit forms the functional Na-conducting channel ⁴⁵, while the β -subunits are predominantly involved in regulating the channels' kinetics and biophysical properties⁴⁶.

As demonstrated in figure 1.3, the α -VGSC is composed of four homologous domains (DI-DIV), that are connected by three intracellular loops (L1-L3). Each domain consists of six transmembrane segments (S1-S6). The four domains come together to form two distinctive regions: the ion-conducting pore domain (PD) and the voltage-sensor domain (VSD). S1-S4 form the voltage-sensor domain that senses any changes in the membrane potential by virtue of the positively charged S4 segment. The other two segments (S5-S6) and their connecting loops form the PD. The PD is formed of four main regions: the outer vestibule (hole) that allow ion influx, the Na⁺-ion selectivity filter which is formed by the interaction of specific amino acids in the PD-loops to govern Na-selectivity, a central cavity filled with water and finally the intracellular activation gate which is formed as a result of S6 segment passing through the intracellular surface of the membrane. Opening and closing of the channel's pore is controlled by changes in VSD conformation ^{47,48}, Fig. 1.3.

Four different genes encode four different types of β -subunits. β -subunits (30 – 40 KDa) share a common structure of an extracellular N-terminus that is connected to the intracellular C-terminus via a single transmembrane segment. The extracellular N-terminus consists of an immunoglobulin-like domain that is believed to play a role in localization and stabilization of VGSC in specific locations within the cell membrane ⁴⁶, Fig. 1.3. β 1 and β 3 interact with VGSC by non-covalent bonds, where the interaction occur via multiple charged residues ^{49,50}. In contrast, β 2 and β 4 interact with VGSC by forming disulphide bonds through their extracellular domain ^{49,51,52}. It is believed that the association of β -subunit with VGSC influences the S4 voltage-sensor and subsequently modifies the biophysical properties of the VGSC. SCNB knock-out

animals demonstrated an attenuation of sodium current while upregulation of SCN8A is associated with neuronal hyperexcitability in various pain models like neuropathic pain⁵³⁻⁵⁷. These studies highlight the role of β -subunit in regulating neuronal excitability under normal and pain conditions.

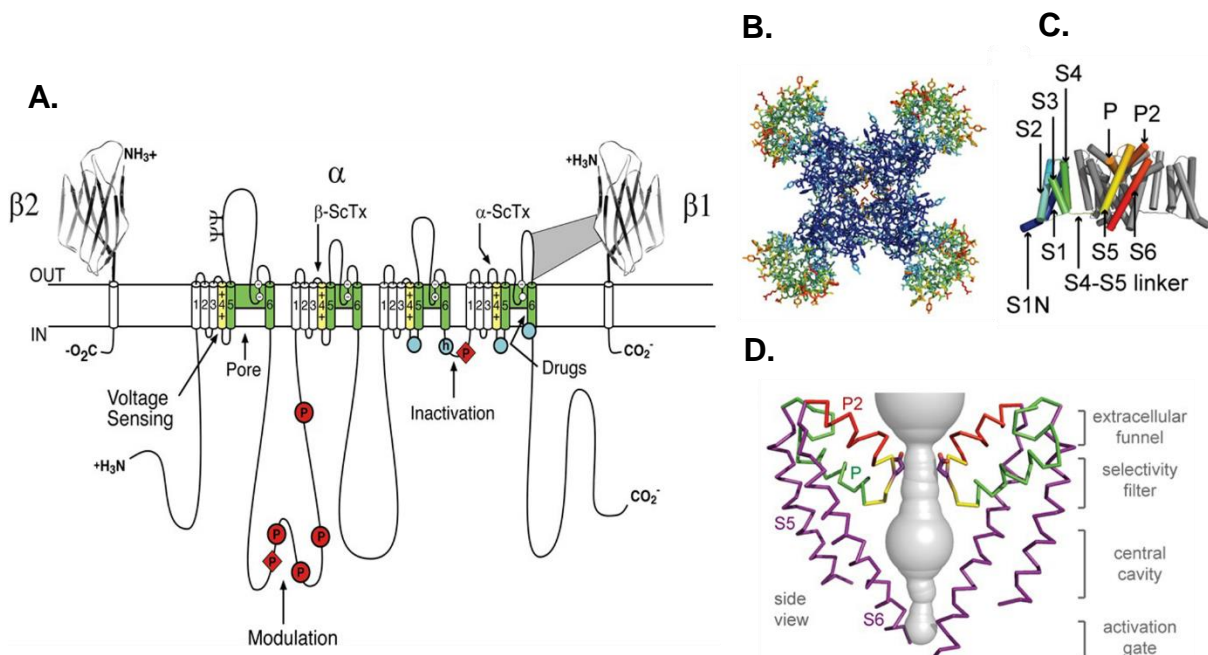


Figure 1.3: Structure of voltage-gated sodium channel (VGSC). **A.** schematic representation of α -subunit of VGSC and the associated β -subunits ($\beta 1$, $\beta 2$; on the edges). α -VGSC consists of four domains (DI-DIV) connected by three intracellular loops (L1 – L3). Each domain consists of six transmembrane domains (S1-S6). S1-S4 form the voltage-sensor domain (VSD). S4 (voltage sensing particle) consists of several positive amino acids (yellow). S5 and S6 and their connecting loops form the pore-domain (PD, green). Both C- and N- termini are intracellular. Several phosphorylation sites in L1 & L3 are indicated (P; red circles and diamonds for PKA and PKC, respectively). ψ – sites for N-linked glycosylation. **B.** subunits consist of one transmembrane domain with an intracellular C-terminus and an extracellular immunoglobulin-like N-terminus. **B.** top view of the extracellular side of bacterial α -VGSC (*Arcobacter butzleri*, NavAb) that serve as a model for eukaryotic α -VGSC. The blue coloured central part are rigid segments and form the PD, while the edges (warmer colours) are more mobile segments and represent the VSD of each domain. **C.** side-view of NavAb, highlighting S1-S6 segments of DI. **D.** Side view of the structure of NavAb pore. PD consist of four regions: extracellular funnel, selectivity filter, central cavity and activation gate. Figure is adopted (and modified) from William A. Catterall, Alan L. Goldin, Stephen G. Waxman. Voltage-gated sodium channels, introduction. IUPHAR/BPS Guide to PHARMACOLOGY, <http://www.guidetopharmacology.org/GRAC/FamilyIntroductionForward?familyId=82>.

1.2.2. The voltage-dependence gating of VGSC:

VGSC gating is governed by the conformational changes that occur in VSD upon changes in membrane potential. S4 consists of multiple positively charged amino acids. At resting membrane potential, the negatively charged field created by the interior transmembrane segments, particularly S2 and S3, attracts and pulls S4 toward the interior of the channel. Upon depolarization, S4 is released from its original position and moves outward causing conformational changes in VSD that opens the channel pore; The sliding helix model⁵⁸ or the helical screw model⁵⁹. Within a few milliseconds of pore opening and as a consequence of S4 outward movement, the inactivation gate (which is the short intracellular loop between D3 and D4), Fig. 1.3, is pulled toward the channel pore and closes it from the inside while the extracellular side of the pore is still open, such movements result in open state inactivation [OSI], Fig.1.4. Upon strong depolarization, the four S4 segments in each domain move outward which initiates inactivation coupled activation [OSI]. Hyperpolarized potentials or modest depolarization is sufficient to cause an outward movement of only DIII- and DIV- S4. This movement is sufficient to cause inactivation by pulling the inactivation gate toward its binding site but without producing sufficient force to open the extracellular side of the channel pore (Closed state inactivation [CSI]), Figure 1.4.

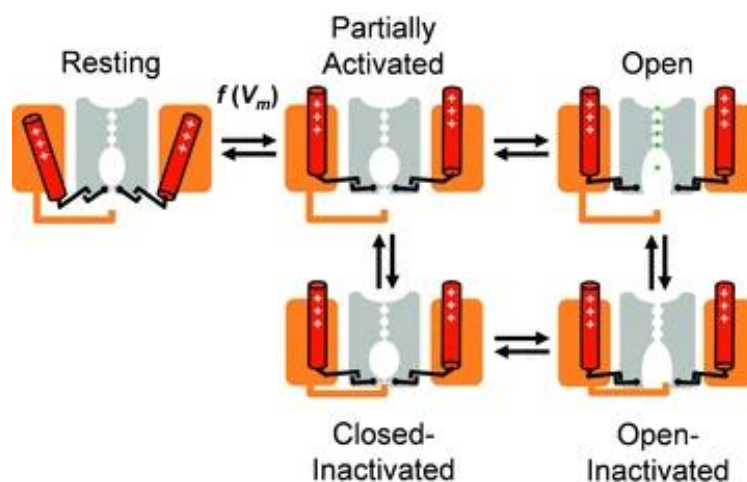


Figure 1.4: Schematic representation of inactivation coupled activation of VGSC. At resting membrane potential, the S4 segment is pulled toward the inside of the cell. Upon depolarization, the S4 moves outward, causing conformational changes in the VSDs which results in pore opening and ion conduction (open conformation). S4 movement initiates inactivation within few milliseconds where the inactivation gate pulled toward the intracellular side of the pore and closes it (Open-state inactivation). However, at moderate depolarization or at hyperpolarized potential, S4 of DIII and DIV can move outward causing sufficient force to pull the inactivation gate to its binding site but without opening the extracellular side of the pore (Closed-state inactivation). Source (Bahrina et al., 2011)⁸

1.2.3. VGSC tissue expression and biophysical properties:

VGSC have diverse biophysical properties, binding affinity to tetrodotoxin (TTX) toxin and expression pattern. Four VGSC (Nav1.1, Nav1.2, Nav1.3 and Nav1.6) are highly expressed in the CNS. Nav1.4 and Nav1.5 are primarily expressed in skeletal and cardiac muscles, respectively. While the remaining three VGSC (Nav1.7, Nav1.8 and Nav1.9) are preferentially expressed in the PNS. Nav1.8 and Nav1.9 are selectively expressed in nociceptive neurons, particularly in non-peptidergic nociceptors in case of Nav1.9^{42,60-66}, (Nav1.7 expression pattern is discussed in details later). Nav1.3 is mainly detected during embryogenesis in the PNS, however, the channel is upregulated in the DRG after nerve injury⁶⁷. Reports have also shown that Nav1.3 can be detected in adult sympathetic neurons and to a lesser extent in adult brain⁶⁸. Nav1.6 and Nav1.1 are also expressed in the DRG^{69,70}, Nonetheless, the preferential expression of Nav1.7, Nav1.8, and Nav1.9 - (as well as Nav1.3) in nociceptors make them good targets for novel analgesics with minimum central side effects.

VGSCs differ in their binding sensitivity to nanomolar concentration of the pore-blocking toxin tetrodotoxin (TTX). Accordingly, VGSC have been classified into TTX-sensitive and TTX-resistant channels. VGSC in the CNS are TTX-S channels with varying degree in channel activation and inactivation threshold and kinetic⁷¹, while VGSC in the PNS are both TTX-S and TTX-R channels⁷². The biophysical properties of the sodium currents produced by these two VGSC classes have been extensively studied. In general, fast activating and fast inactivating sodium currents are characteristic of TTX-S channels. While, slowly activating and slowly inactivating currents are characteristic of TTX-R channels. Similar sodium current features are conserved in human VGSC⁷³⁻⁷⁵.

Electrophysiological studies have also indicated differences in Na-current properties within each class. For instance, Nav1.7, is characterised by rapid activation and rapid inactivation a common characteristic of TTX-S current. However, in contrast to other TTX-S channels, Nav1.7 has a distinctly slow recovery rate from fast inactivation, which indicates that the channel does not contribute to the high firing frequency of action potential^{76,77}. In addition, Nav1.7 exhibit a significantly slower rate of inactivation at negative potentials, which means that the channel remains open at

longer times at membrane potentials that are close to the resting membrane potential which contribute to sodium influx (ramp current). These two main features of Nav1.7, together with its high localization at the nerve terminals, place the channel as an action potential “generator”, i.e. “threshold channel” ^{16,76,78}, Fig. 1.5.

A similar variation is found within the TTX-R class. Both Nav1.8 and Nav1.9 belong to the TTX-R VGSC class, yet each produces a characteristic sodium current that serves a distinct physiological function. Nav1.9 is characterized by generating a persistent current which is activated at negative potentials (- 60 to - 70 mV). Therefore, it has been proposed; due to its low voltage activation and persistent current generation, that Nav1.9 play an essential role in setting resting membrane potential of small DRG neurons ⁷⁹. While, Nav1.8 exhibit a more depolarized activation and fast-inactivation threshold, typically 30 – 40 mV than Nav1.9 and TTX-S ion channels ^{61,80}. This means that Nav1.8 channel opens only subsequent to TTX-S channel activation, hence Nav1.8 is unlikely to be involved in setting threshold for VGSC activation ⁸¹. On the other hand, the depolarized slow inactivation allows the channel to contribute to the bulk of the sodium current during depolarization as well as the ability to continuously fire action potentials at sustained depolarization ⁸², Fig. 1.5.

As mentioned earlier, peripheral VGSCs have got the attention of many researchers. In this study, I investigated the functional significance of one of the Nav1.7 interacting proteins. Therefore, in the next few sections, I will only focus on Nav1.7 unique properties, functional significance, and its protein interactors.

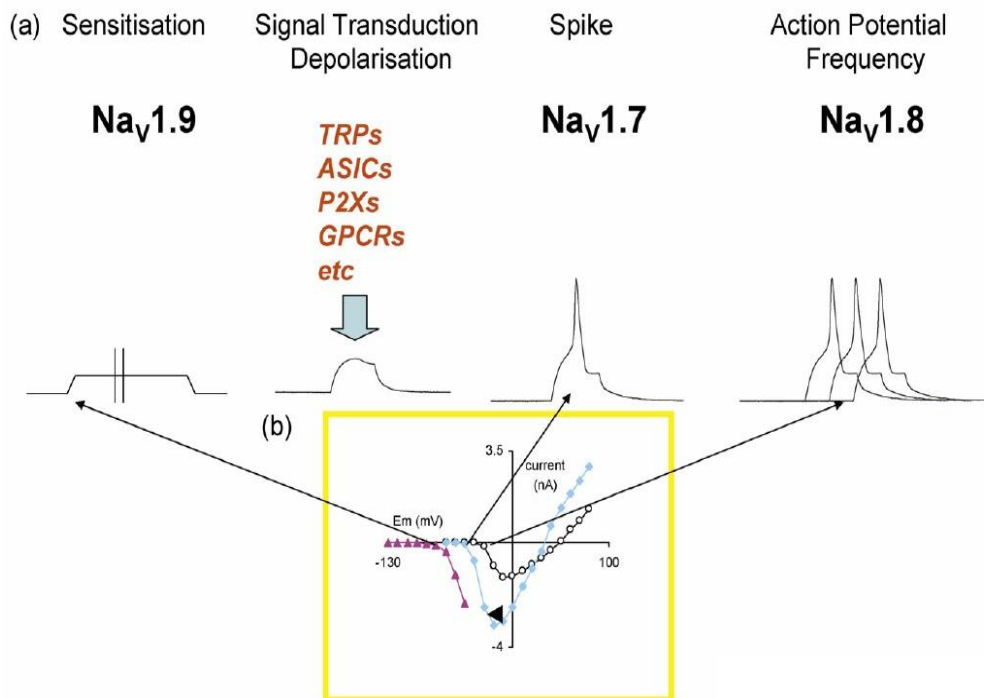


Figure 1.5: The sodium current biophysical properties and activation potential of peripheral VGSC (Nav1.7, Nav1.8 and Nav1.9). Nav1.9 activates at $\sim -70\text{mV}$, close to resting membrane potential and produces persistent current which plays a role in setting the membrane potential. Nav1.7 inactivates slowly at potentials close to resting membrane potentials, therefore, Nav1.7 contributes to sodium currents at these potentials (ramp currents) which is essential for recruiting other VGSC to elicit action potential (particularly Nav1.8), Nav1.7 is known as “threshold channel” or “generator channel”. Nav1.8 activates at a more depolarized potential (usually recruited by Nav1.7) and contributes to the bulk of sodium current during action potential. The inactivation of Nav1.8 is also more depolarized, hence the channel contributes to the continuous firing during persistent depolarization. B. the voltage-dependence for activation of Nav1.9 (triangle), Nav1.7 (closed diamonds) and Nav1.8 (open circles). Source: Momin et al., 2008⁵.

1.3. Nav1.7 VGSC subtype:

1.3.1. Nav1.7 expression pattern:

α -Nav1.7 is encoded by SCN9a gene. Nav1.7 is highly expressed in the PNS including DRG sensory neurons, sympathetic neurons and trigeminal ganglia⁸³. Nav1.7 is expressed in all cell sizes of DRG neurons, with a higher expression level in nociceptors^{74,84}. Nav1.7 is also found along the peripheral and central terminals, which suggests a role for the channel in the initiation and the transmission of action potential^{43,83}. In the CNS, Nav1.7 is reported to be expressed in some areas in the rodent brain, but not in the human^{85,86}. Furthermore, Nav1.7 mRNA and protein has been reported in tissues outside the nervous system, for example, human sperm⁸⁷, vascular endothelium in human⁸⁸ and mouse pancreatic beta-cells⁸⁹, however, the functional role of Nav1.7 in these tissues is still not very clear.

1.3.2. Evidence for Nav1.7 implications in pain

1.3.2.1. Human mutations:

Over the past several years, three human pain disorders have been genetically mapped to mutations in SCN9A (discussed below). Therefore, Nav1.7 has received a particular interest as a potential target for pain relief in human.

- **Channelopathy-associated insensitivity to pain (CIP):**

Channelopathy-associated insensitivity to pain (CIP) is a rare congenital recessive mutation in SCN9a gene that was first reported in three families from northern Pakistan. Patients whom carry this mutations seem normal except for their inability to sense all types of painful stimuli in all parts of their bodies (complete congenital analgesia)⁹⁰. Several other non-sense mutations have been mapped to SCN9a from individuals of different backgrounds. Most of the reported SCN9A mutations result in the formation of a truncated version of the Nav1.7 channel⁹⁰⁻⁹². Two, however, are non-truncated mutations that subsequently alter one amino acid at the pore of the channel (S5-S6 extracellular loop of either DIII or DII). These two mutations result in a significant reduction of Nav1.7 membrane expression with a consequent loss of Nav1.7 current and a complete loss of function of the protein⁹³. More recently, two additional SCN9a mutations have been described that affect the C-terminus part of Nav1.7 channel. Interestingly, although the patients carrying these mutations have similar phenotype to CIP patients, but unlike the other mutations, the channel is functional in this case. Electrophysiological characterization revealed a depolarizing shift in the activation threshold of the mutated channels which result in a significant, yet incomplete, reduction in the Nav1.7 current⁹⁴. These mutations are extremely useful in reinforcing the idea that inhibition of Nav1.7 is effective for pain relief in humans.

To better understand the role of Nav1.7 in CIP phenotype, a recent study by Minett et al., 2015 has proposed a link between loss-of-function mutation in SCN9A and opioid upregulation, where both SCN9A KO mice and a SCN9A-CIP patient regain pain sensitivity after administration of naloxone (a non-specific opioid antagonist). Nav1.7 KO mice, but not Nav1.8 or Nav1.9 KO, showed a significant upregulation of the enkephalin precursor *Penk* mRNA and the protein met-enkephalin in the DRG.

However, the opioid level in the human subject was not tested. While the mechanism involved in gene alteration is still unclear, it was hypothesised that the intracellular sodium level could act as a second messenger and regulates opioid peptide expression⁹⁵. Although it is unclear why changes in intracellular sodium levels mediated by Nav1.7, but not by the other VGSCs, could regulate gene expression. It is plausible to speculate that the role of sodium as a second messenger could be tightly regulated by the physiological pattern of sodium influx (i.e. quantitative and qualitative sodium influx properties) via each VGSC subtype and by the transient concentration of sodium at specific microenvironment. Future studies may give better mechanistic insights to CIP phenotype and to the role of sodium in gene regulation in sensory neurons.

- **Inherited erythromelalgia:**

Inherited erythromelalgia (IEM), also known as “primary erythromelalgia”, is a rare autosomal dominant disease. Unlike CIP, patients with IEM usually suffer from severe burning pain episodes in the extremities associated with skin erythema⁹⁶. The extent, period and frequency of the episodes differ among patients. Some patients reported pain even between the episodes. Some responded to sodium channel blockers like carbamazepine, while others use cooling (ice, cold water, cold air fans) to reduce the pain – although exposure to cold temperature sometimes lead to skin lesions. The trigger of the attacks is not clear; attacks can start without any defined trigger, or by exercise, temperature change, humidity and clothing⁹⁷. Several IEM mutations have been mapped to SCN9A gene. Most of the mutations are gain of function mutations that lead to enhanced channel activity by producing a hyperpolarizing shift in the activation potential while some cause a depolarizing shift in the inactivation potential. These changes will generally result in an increased ramp or persistent current. Given that Nav1.7 is a “threshold channel”, such mutations are likely to contribute to augmented neuronal responses to small “innocuous” stimuli which result in DRG neuron hyperexcitability and pain⁹⁷⁻⁹⁹, Fig. 1.6.

- **Paroxysmal extreme pain disorder (PEPD)**

Paroxysmal extreme pain disorder (PEPD), previously known as familial rectal pain syndrome, is another type of gain-of-function mutations in the SCN9A gene. The clinical presentation of PEPD differ from that of IEM, in which patients with PEPD suffer

from severe rectal, ocular and submandibular burning pain and skin erythema. Pain can be triggered mostly by mechanical stimuli like walking, eating, yawning, and defecation¹⁰⁰. PEPD mutations are mainly located at DIII and DIV and usually result in a depolarizing shift in the voltage-dependence fast inactivation as well as an incomplete inactivation. This ultimately result in an increased persistent current (also called tail current) which results in increased DRG hyperexcitability and pain^{100,101}, Fig. 1.6.

- **Small fibre neuropathy (SFN)**

Small fibre neuropathy (SFN) is disorder that involves degeneration of both the thinly myelinated A δ - fibres and the unmyelinated C-fibres¹⁰². Patients with SFN suffer from sensory symptoms that are usually starts from the lower leg and foot and extend proximally (symmetrical length-dependent pattern). The most common sensory symptoms are burning sensation, pain and itching that are accompanied sometimes with cramps and tingling sensations¹⁰³. SFN is associated with several diseases; Diabetes mellitus is one of the major reasons for SFN, however, other metabolic conditions (e.g. hyperlipidaemia¹⁰⁴, hypothyroidism¹⁰⁵), immune-mediated conditions (e.g. Sarcoidosis¹⁰⁶, inflammatory bowel diseases¹⁰⁷) and infectious diseases (e.g. HIV¹⁰⁸ and hepatitis C¹⁰⁹) are also associated with SFN. Gain of function mutation in SCN9a gene, that encodes Nav1.7 ion channel, is also found to be associated with almost 30 % of patients with idiopathic SFN¹¹⁰. Introducing the SCN9a mutations (Fig. 1.6) in DRG culture resulted in an excitatory effect, most likely by impairing Nav1.7 inactivation and enhancing resurgent current. Although the mechanism of the nerve degeneration is not well understood, it was hypothesized that the spontaneous firing activity and the hyperpolarizing shift in action potential threshold is what might ultimately lead to fibre degeneration in patients. Current treatment strategy of SFN patients include symptomatic treatment of the neuropathic pain (e.g. Tricyclic antidepressant and serotonin-norepinephrine reuptake inhibitors)¹¹¹. Nevertheless, these treatment strategies provide only a suboptimal pain relief. A better understanding of the pathophysiology of SFN and the advances in specific targeting of Nav1.7 might provide better treatment strategies in the future.

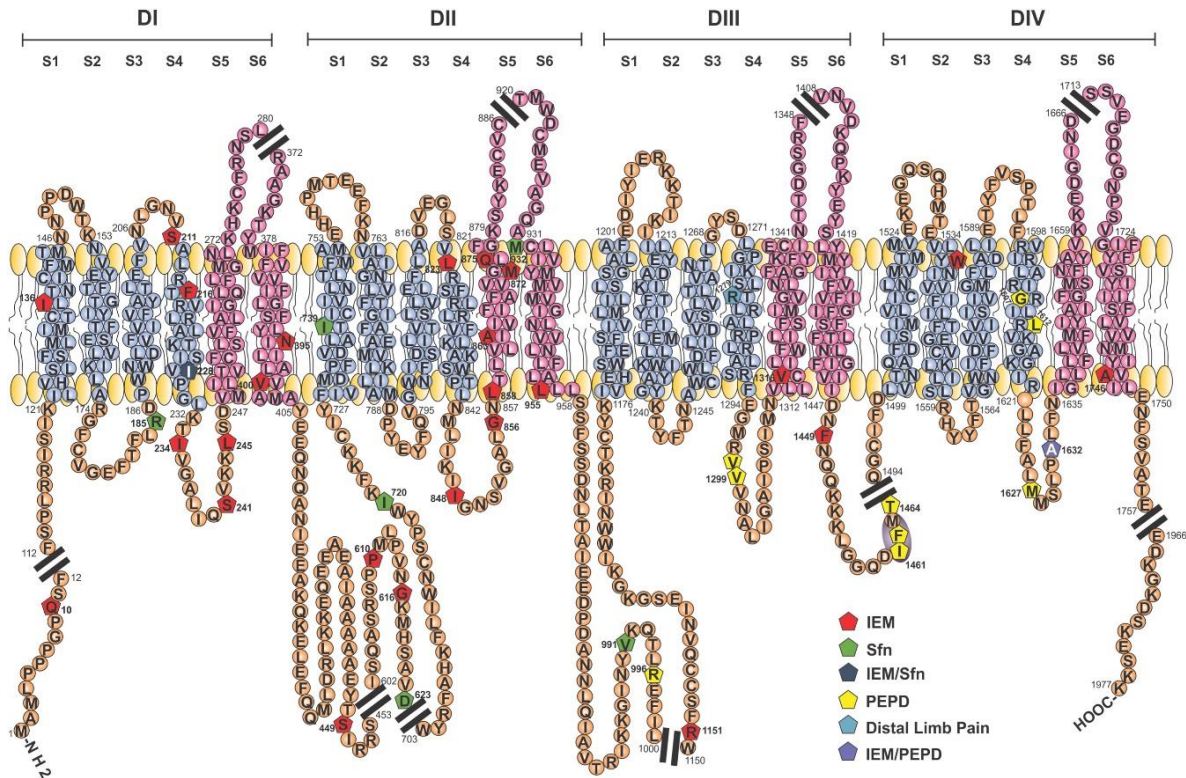


Figure 1.6: Illustration of the gain-of-function mutations of Nav1.7 channel. Several gain-of-function mutations that result in pain in humans are indicated on the secondary structure of α -Nav1.7 structure. VSD and PD are presented in blue and pink colours, respectively. Inherited erythromelalgia (IEM, red), small-fibre neuropathy (Sfn, green), paroxysmal extreme pain disorder (PEPD, yellow), Distal limb pain (turquoise), A mutation that is implicated in IEM and Sfn (dark blue), and a mutation implicated in IEM and PEPD (purple). Source: Vetter et al., 2017²

1.3.2.2. Animal knock-out (KO) studies:

Nav1.7 KO mice provide useful tools to study in details Nav1.7 mechanisms in pain. The first attempt to obtain a global SCN9A deletion mutant failed because Nav1.7^{-/-} pups died shortly after birth due to the inability to feed ¹¹². To overcome this problem, an alternative method was undertaken to generate tissue-specific SCN9A deletion mutants, taking advantage of the Cre-recombinase-loxP system. Several tissue-specific promoters have been utilized to drive cre- in specific neuronal population. Example of the promoters used are as follows: Nav1.8 (Nav1.7^{Nav1.8} KO; ablation of Nav1.7 in small-diameter nociceptors ¹¹²), Advillin (an actin-binding protein, specifically expressed in trigeminal and DRG neurons, Nav1.7^{Advil} KO; ablation of Nav1.7 in all sensory neurons ¹¹³), Wnt1 (neural crest cells, Nav1.7^{Wnt1} KO; ablation of Nav1.7 in sensory and autonomic neurons ¹¹³). Each of these animal models provided evidence for Nav1.7 role in pain. Nav1.7^{Nav1.8} KO showed loss of mechanosensitivity and a significant reduction in inflammatory pain. Similarly, Nav1.7^{Advil} KO showed abolished mechanosensitivity, inflammatory pain and reflex withdrawal responses to heat. But thermosensitivity and neuropathic pain remained unaffected in those Nav1.7 KO animal models ^{112,113}. In contrast, Nav1.7^{Wnt1} KO mice recapitulated CIP-phenotype and showed a significant attenuation in neuropathic pain ¹¹³. All of these studies are crucial in highlighting the role of different neuronal subsets in the development of different types of pain.

Since the original Nav1.7^{-/-} global KO report, studies have shown that Nav1.7 is expressed in the olfactory neurons in rodents ¹¹⁴, giving an explanation why Nav1.7^{-/-} pups died, most likely because they born blind and depend on smell sensation to feed ². Based on that, a global Nav1.7 KO has been successfully produced, recently ¹¹⁵. To overcome the lethality problem, extra animal husbandry measures and care were taken to increase the survival of the mutants. Pups were fed by hand with an in-house modified artificial mouse milk formula plus subcutaneous dextrose injections multiple times a day until P14, where the mice become able to feed. Interestingly, the phenotype was stronger than any of the other VGSC global KO (Nav1.8 ¹¹⁶, Nav1.3 ¹¹⁷ and Nav1.9 ¹¹⁸) as Nav1.7^{-/-} animals exhibited CIP-like phenotype with significant loss of thermo- and mechano- sensation ¹¹⁵.

Altogether, these studies highlight the critical role of Nav1.7 in pain. They also demonstrate that multiple neuronal types (sympathetic and sensory neurons) are involved in pain signalling, as deletion of Nav1.7 in all of these cell types is essential to obtain a complete pain-free phenotype. In addition, they validate the use of animal models in studying pain mechanisms. Future studies using the global Nav1.7^{-/-} mice may shed light on the role of the Nav1.7 in other types of pain, like neuropathic and cancer pain particularly because no data is currently available from human CIP patients.

1.3.3. Nav1.7 interacting protein partners:

Several interacting proteins have been shown to regulate VGSC subcellular targeting, surface density and activity. Therefore, VGSC-protein partners may play an important role in modulating the channels cellular and functional kinetics under pathological conditions. Relatively few number of Nav1.7 interacting proteins have been reported so far. The next few paragraphs briefly describe the current knowledge of Nav1.7 protein interactions in sensory neurons.

- **ERK1/2 Mitogen-Activated Protein Kinase:**

ERK1/2 mitogen-activated protein kinase (ERK1/2 MAPK) is expressed in medium and small size rat DRG neurons, but not in large diameter neurons.

ERK1/2 MAPK is activated “phosphorylated” by neurotrophic factors (NGF and GDNF) and proinflammatory cytokines, and has been implicated in pain hypersensitivity¹¹⁹⁻¹²¹. ERK1/2 MAPK has been shown to interact and directly phosphorylate Nav1.7 in DRG neurons. Nav1.7 intracellular loop (L1) contains four ERK1/2 MAPK phosphorylation sites. Mutations in three sites are critical for inhibition of ERK1/2 MAPK action. Modulation of Nav1.7 by ERK1/2 MAPK results in hyperpolarized shift in activation and fast inactivation threshold, without affecting the current density, suggesting that the enhanced Nav1.7 gating is via direct post-translational modification of the channel and not via enhanced trafficking to the cell membrane. This interaction provides a plausible explanation for the link between increased pERK1/2 MAPK and increased excitability of DRG neurons and suggest that modulation of Nav1.7 gating could contribute the ERK1/2 pathway-induced hyperalgesia¹²².

- **Fibroblast growth factor-13 (FGF-13):**

FGF-13 belongs to the intracellular, non-secretory class of FGF family. FGF-13 is expressed in DRG neurons¹²³, particularly in small diameter neurons¹²⁴. FGF-13 is highly co-localised with Nav1.7 expressing DRG neurons and its subcellular distribution resembles that of Nav1.7 channel, (soma, peripheral and central terminals of DRG neurons). Pull-down experiments as well as co-IP in mouse DRG neurons showed a direct interaction between FGF-13 and the C-terminus of Nav1.7. To elucidate the functional role of this interaction, FGF-13 KO mice were produced. FGF-13 KO exhibited normal developmental, behavioural and physiological phenotypes except for an enhanced tolerance to noxious heat (> 43 °C). Patch-clamp electrophysiology experiments performed before and after noxious heat stimulation from both WT and FGF-13 KO animals demonstrated a reduction in the TTX-S current density but not in the current properties. In accordance with patch-clamp results, surface biotinylation experiments showed a reduction in Nav1.7 surface expression in FGF-13 KO only after noxious heat stimulation. The phenotype was fully reversed by exogenous FGF-13. Interestingly, the stabilization of Nav1.7 at the cellular membrane by FGF-13 is not mediated by microtubules or actin cytoskeleton even though FGF-13 has been shown to act as a microtubule-stabilizing protein in cortical neurons. therefore, the molecular mechanism of Nav1.7-FGF-13 interaction remains to be elucidated. Altogether, this study demonstrates Nav1.7-FGF-13 complex as an important factor in regulating noxious heat sensation by increasing Nav1.7 density at the cell membrane, and propose a role for Nav1.7 in mediating inflammatory induced thermal hyperalgesia¹²⁴.

- **Ubiquitin protein ligases Nedd4 and Nedd4-2:**

Neuronal precursor cell expressed developmentally downregulated type 4 and type 4-2 (Nedd4 and Nedd4-2) are members of the E3-ubiquitin Ligase family that bind via an interaction of the Nedd(x) – multiple WW domain with a PY motif on the target protein. Both Nedd4 and Nedd4-2 interact with the PY motif in the C-terminus of Nav1.7. However, only Nedd4-2 can directly ubiquitinate Nav1.7, despite the fact that both Nedd4 and Nedd4-2 reduced Na-current in exogenous expression system. This suggest a direct role for Nedd4-2 and an indirect role for Nedd4 in regulating Nav1.7

membrane expression, probably via ubiquitination of other proteins that can subsequently reduce Nav1.7 surface density ¹²⁵.

In agreement, an *in vivo* study in neuropathic mouse model (spared nerve injury model “SNI”) in control and in Nedd4-2 KO animals was carried out to investigate the role of Nedd4-2 in regulating VGSC in pathological conditions. SNI is known to increase Na-current and DRG excitability. SNI in control animals caused a two-fold increase in Nav1.7 current density accompanied by a downregulation in Nedd4-2 expression level. Moreover, Nedd4-2 KO animals demonstrated an increased basal levels of Nav1.7 current density. Interestingly, acute mechanical nociception was unchanged, while Nedd4-2 KO were more sensitive to noxious heat stimuli (hot plate and plantar test, > 50 °C) under both basal and SNI conditions - an observation that fits the previously discussed role of Nav1.7 in regulating neuron response to noxious heat ¹²⁴. Future studies will reveal whether FGF-13 level is elevated in Nedd4-2 KO mice. In general, these studies demonstrate direct association and ubiquitination of Nav1.7 channel by Nedd4-2 that results in subsequent endocytosis and reduction of Nav1.7 surface density. Therefore, Nedd4-2 provides an alternative target for novel analgesics, where Nav1.7 surface density can be regulated by indirect targeting of specifically interacting proteins instead of targeting the channel itself ¹²⁶.

- **β1- and β3- subunits:**

As discussed earlier, β-subunits interacts and regulate VGSC activity in a cell-specific and VGSC-specific manner. Mature α-VGSC channels are found at the membrane, while, most of the α-VGSC pool is distributed intracellularly between the endoplasmic reticulum, Golgi and the secretory pathways. These “immature channels” are believed to serve as a “reservoir” ready to be exported to the plasma membrane when needed ¹²⁷. The various post-translational modifications (PTM) of α-VGSC can determine the fate of the intracellular α-VGSC. For example, α-VGSC intracellular pool undergoes an extensive glycosylation process in the endoplasmic reticulum and Golgi which can regulate VGSC membrane density, gating and Na-current biophysical properties ¹²⁸⁻¹³¹. Co-expression of α-hNav1.7 with individual β-subunits in HEK293 cell line revealed that β1- or β3- subunits increases the current density with modest effect on the current biophysical properties. Furthermore, Nav1.7 membrane density was also increased in surface biotinylation experiments when co-expressed with β1 or β3 – subunits, in

agreement with the patch-clamp experiments. The study also suggests that each β -subunit can differentially modify the glycosylated form of the channel. Even though this study highlighted the critical role of $\beta 1$ and $\beta 3$ in regulating Nav1.7 membrane expression level¹²⁸. Several questions remain to be investigated. For example, where does the β -mediated modulation of the channel take place? And how and to which extent does the differential glycosylation affects Nav1.7 current density? To what degree the results from HEK293 cells match that of DRG neurons? and finally, how would $\beta 2$, and $\beta 4$ modulate Nav1.7?

A previous Y2H data obtained from Nassar lab showed an interaction of Nav1.7 baits with several proteins. A systematic co-IP experiments have been carried out by myself and other colleagues in the lab to validate these interactions in mammalian cells. One of the positive interactors was the light-chain of microtubule associated protein 1A (MAP1A). Details for this interaction are in chapter 5 of this thesis. A brief background to the microtubules and microtubule-associated proteins and their functional importance in neurons are described in the next few sections. With a particular focus on MAP1A family.

1.4. Neuronal Microtubule Cytoskeleton and Microtubule-Associated Proteins.

The cytoskeleton is composed of an intricate filamentous network consist of three major groups: microtubules, microfilaments and intermediate filaments (IF). Each consists of distinct proteins, tubulin, actin and various IF proteins, respectively. The structure, function and interactions of one of the cytoskeleton major components, the microtubules, are mentioned below.

1.4.1. Microtubules : composition, structure and organisation.

Microtubules (MT) are formed of several hollow cylinders (~ 24 nm outer diameter) that are usually organized in bundles of varying thickness^{132,133}. Individual microtubule is formed by lateral alignment of the linear α - and β - tubulin heterodimers. Organisation of α - and β - tubulin usually occur in head-to-tail fashion, where β -tubulin of the heterodimer is aligned toward the plus end (fast-growing, exterior), and the α -tubulin toward the minus end (slow growing, interior), Fig. 1.7, A.

Microtubules are characterised by their abilities to rapidly alternate between polymerisation (growth) and depolymerisation (shrinkage) states^{134,135}. This is known as “dynamic instability” and it provides the MT the flexibility to expand and retreat within the 3-dimensional cytoskeleton inside the cell according to the cellular needs and to the cues available within the internal and external micro-environment¹³⁶. The dynamic instability of the MT depends on the presence of GTP. MT growth and elongation can occur at both ends, however it is significantly faster at the plus-end. MT growth occur between the β -subunit in the plus-end and the α -subunit from newly unbound heterodimer (α , β -tubulin heterodimer). β -tubulin at the tip of the MT plus-end is usually bound to GTP via the nucleotide exchangeable site (β -tubulin E-site). Upon polymerization, the GTP gets hydrolysed by the catalytic site of the α -subunit of the unbound heterodimer, this consequently result in addition of the heterodimer to the plus end of the MT (MT polymerisation)^{12,137}. In this case, the addition of the heterodimer will always be in a specific orientation (i.e. α -subunit facing the minus-end

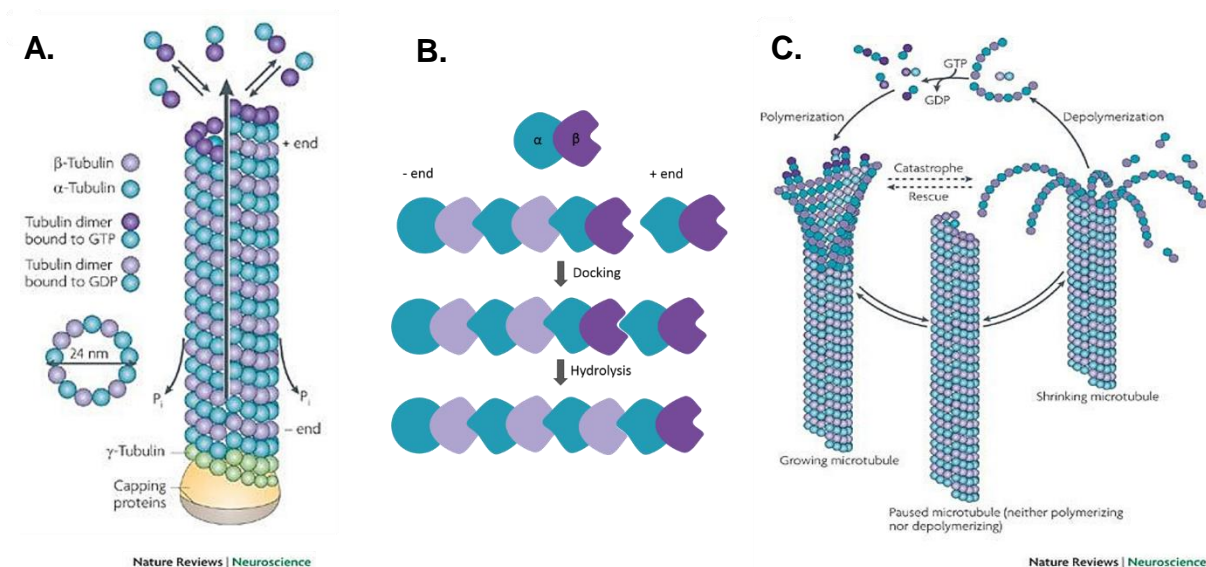


Figure 1.7: Schematic representation of the microtubules structure and MT dynamic instability. **A.** Individual microtubule (MT) protofilament is formed of a hollow cylinder (24 nm in diameter). It consists of lateral alignment of α -tubulin (blue) and β -tubulin (purple). γ -tubulin (green) and γ -tubulin ring complex (yellow-capping proteins) form MT-nucleation sites. MT has two ends, the minus-end (- end); toward the nucleation site, slow-growing and the plus-end (+ end); toward the periphery, fast-growing. **B.** illustration of MT polymerization. free tubulin heterodimer consists of α and β tubulin. The catalytic site of the α -tubulin binds to the GTP- β -tubulin at the tip of the plus-end (dark purple) [docking], followed by immediate hydrolysis of GTP to GDP (interior GDP- β -tubulin, light purple and exterior GTP- β -tubulin, dark purple). **C.** the dynamic instability of MT. upon stochastic hydrolysis of the outer GTP- β -tubulin, MT depolymerisation (shrinkage) takes place. Panels A, C are adopted from Conde et al., 2009¹², panel B is based on Howard et al., 2003¹⁵

and β -subunit facing the plus-end). Therefore, only the outer layer of the plus-end has β -tubulin-GTP and able to bind new heterodimers and grow. The rest of the MT filament is composed of GDP-tubulin and is stable, Fig. 1.7-B. Upon stochastic loss of this GTP-outer layer, MT become highly unstable, and depolymerisation events happen, Fig.1.7, C. Another tubulin isoform is the γ - tubulin which is usually found at the MT nucleation sites along with other proteins that associate together to form the γ - tubulin ring (γ -TuRC) complex which serve as the base for MT elongation and distal extension ^{138,139}.

Several other factors and proteins are involved in the regulation of microtubules dynamics, assembly, organisation, composition, stability and function. For examples, the presence of specific α - and β -tubulin isotypes, MT post-translational modifications, motor proteins (kinesin and dynein), as well as the microtubules-associated proteins (MAPs) ^{12,137}.

Differences in the MT arrangement can be noticed at different neuronal regions. In the soma, MT are uniformly organised in a radial orientation where the stable minus-end aligned toward the interior while the fast growing plus-ends are aligned toward the exterior. In the axons, microtubules bundles run in parallel with their plus-ends mostly aligned distal to the soma ¹⁴⁰. Whereas in the dendrites, microtubules have been shown to have a mixed orientation with different polarity and directionality ¹⁴¹, Fig. 1.8. Moreover, the relative abundance of the microtubule-associated proteins at different neuronal regions also contribute to regional differences in the MT lattice. For example, Tau proteins are mainly found in the axonal region ¹⁴², while MAP1B protein is mainly localised at the somatodendritic region ¹⁴³. More examples regarding MAPs distribution will be discussed in details in later sections.

The presence of various tubulin isotypes (5 α) and (6 β) also account for the heterogeneity of MT and account for its biological functions in different types of cells ^{144,145}. For example, β -III tubulin isotype is exclusively expressed in the nervous system ^{146,147}, while β -IV tubulin is the main isotype found in the ciliary axoneme ^{148,149}. The differential expression and the relative abundance of the various tubulin isotypes

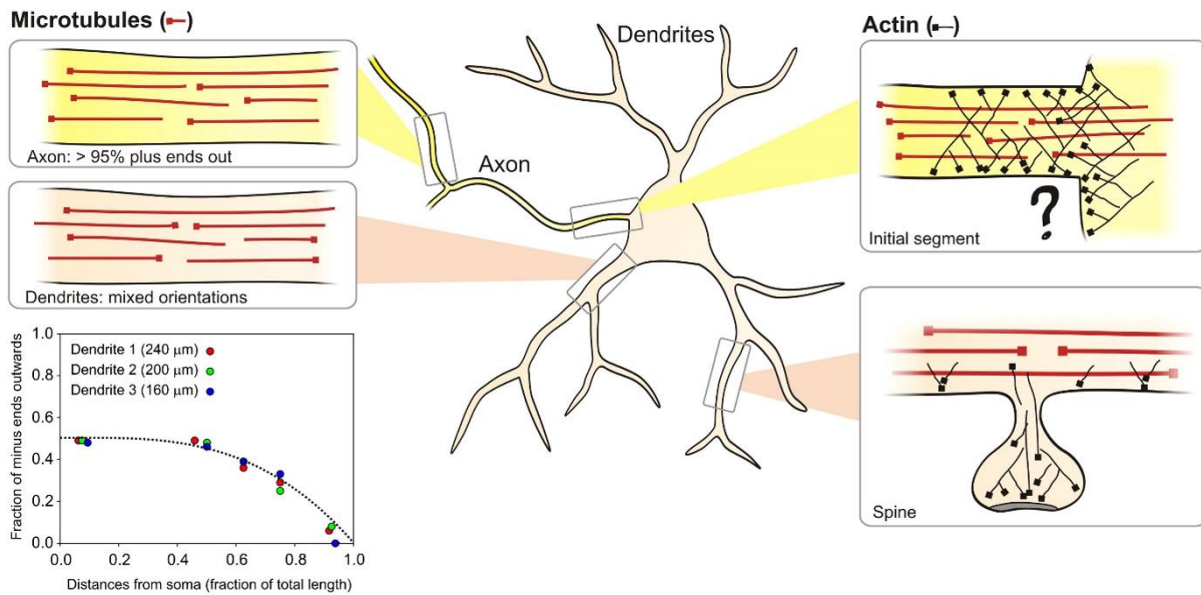


Figure 1.8: Schematic representation of the microtubule orientations at different neuronal sites. MT and actin plus-ends are indicated by filled squares. In the soma and the axonal initial segments, MT plus-ends are arranged distal from the cell centre. Similarly, in the axon, majority of MT plus-ends are arranged distally. In contrast, MT have mixed orientation in the dendrites. The figure demonstrates the correlation between the fraction of the distal minus-ends and the dendrite length. (the further the distance from the soma, the more the opposite orientation to occur – minus end outward). In the dendritic spine, microfilament is the prevalent cytoskeleton structure. Source: Kapitein et al., 2010 ¹¹

at different developmental stages, different cell types and different regions within the cell suggest an important biological significance for such heterogeneity. With the advances in technology, several mutations in single tubulin isotypes have been mapped to various disorders ¹⁵⁰⁻¹⁵⁴. This enforces the idea of the significance of tubulin isotypes that has been long considered as redundant proteins, and also shed light on how subtle changes in the MT composition and diversity can directly affect the basic cellular functions.

1.4.2. Biological functions of the microtubules.

MT cytoskeleton proteins play a pivotal role in neuronal development, plasticity, maturation and maintenance. MT along with actin microfilament and intermediate filaments allow neurons to go through all these dynamic and functional changes as they develop. MT provides the mechanical and structural support for the neurons. They are essential for developing new axons, neurites and dendrites and establishing new synapses via coordination with the actin cytoskeleton. They form a highly intricate

and well connected structural tracks whereby motor proteins like dynein and kinesin can translocate with their cargoes to virtually any site within the neurons. They provide an enormous surface area that covers the three-dimensional architecture of the neuron which in turns make them ideal places for docking cytoplasmic proteins and organelles. They also play a significant role in regulating intracellular signalling pathways. All of these functions are achieved by having a highly complexed and interconnected organisation of cytoskeleton proteins ¹⁵⁵.

There are several lines of evidence that cytoskeleton proteins play a role in regulating cell signalling pathways and intracellular calcium levels ^{156,157}, as well as modulating ion channel functions either indirectly by affecting ion channel transport, targeting, clustering, membrane retention, anchoring and internalisation ¹⁵⁸⁻¹⁶⁰, or by directly affecting the activation / inactivation of the ion channels. For instance, it has been shown that disruption of actin filaments by cytochalasin results in activation of sodium channels and inactivation of potassium channels ¹⁵⁵. On the other hand, disruption of microtubules by pharmacological agents like colchicine or nocodazole has been shown to activate L-type calcium channels ¹⁶¹.

1.4.3. Microtubule-Associated Proteins (MAPs)

Microtubule-associated proteins include all the proteins that binds and modulate microtubule structure and function ^{137,162}. Based on their main function, MAPs are generally classified into five main groups: First: proteins that specifically associate with either tip of the microtubules to control MT dynamics and MT interactions with other proteins and signalling factors (specialized MAPs) ¹³⁴. Examples of proteins in this groups are: plus-end tracking proteins (+TIPS) and minus-end targeting proteins (-TIPS). Second: proteins that directly control MT density and number; which include proteins that are involved in the initiation of MT nucleation (MT density regulators)¹³⁸ as well as MT severing proteins (MT number regulators)¹⁶³. MT severing proteins (katanin, spastin and fidgetin) are able to cut pre-existing microtubules and start a new nucleation site. They have been shown to be essential for axonal regeneration, dendrite formation, neuromuscular junction development and microtubule nucleation ^{137,164,165}. Third: kinesin and dynein superfamily of motor proteins that are involved in directional cargo transport across the neuronal axon, dendrites and synapses. Motor proteins are involved in anterograde and retrograde transport of synaptic vesicles,

organelles, mRNA and neurotransmitters between different regions of neurons. Motor proteins have been shown to play an essential role in maintaining normal neuronal cellular functions, plasticity and survival¹⁶⁶. Fourth: proteins that are involved in tubulin modification. A group of MT bundles can be distinctly marked and modified by post-translational modifications (PTM). Tubulin undergo a wide range of PTM such as acetylation, phosphorylation, detyrosination / tyrosination, polyglutamylation, and polyglycylation. Such modifications are believed to regulate other MAPs binding and consequently affect MT stability, properties and functions^{167,168}. Fifth: protein that are primarily involved in stabilizing and cross-linking MT as well as in determining MT shape (structural MAPs)^{6,169}. This group is of special interest and will be discussed in details in the next sections.

The diversity of MAPs and their spatiotemporal expression are additional factors that contribute to MT complexity and heterogeneity. Advances in microscopy and genetic techniques have revealed new molecular structures and functions of critical components in the MT cytoskeleton. However, a comprehensive understanding of the molecular mechanisms involved in MT diverse functions, dynamics and modulations are yet to be understood.

1.4.4. Structural Microtubule-Associated Proteins (Structural MAPs)

The two major cytoskeleton networks, the actin microfilaments and the microtubules each were believed to bring a unique feature to the cell. Actin was thought to be mainly involved in the more dynamic cellular events including force generation and cell contraction due its plastic and flexible properties. While the microtubules were believed to bring the rigidity, stiffness and stability to the cell and to provide stable tracks for microtubule-based cargo transport, in addition to their central role in cell division. However, a compelling body of evidence suggests that there is actually an overlap in the function of these two major networks. Actin microfilaments were shown to be involved in cell division and trafficking, while microtubules were found to be involved in neurites formation and plasticity as well as in force generation. This largely suggest that these two networks work cooperatively to achieve specific cellular needs. Structural MAPs are believed to play a central role in networks cross-talk due to their ability to bind and cross-link both microtubules and microfilaments to each other and

to other cellular components. In addition, structural MAPs are known to associate with the whole length of the microtubules and regulate MT stability, bundling, correct spacing and binding to signalling molecules ¹⁶².

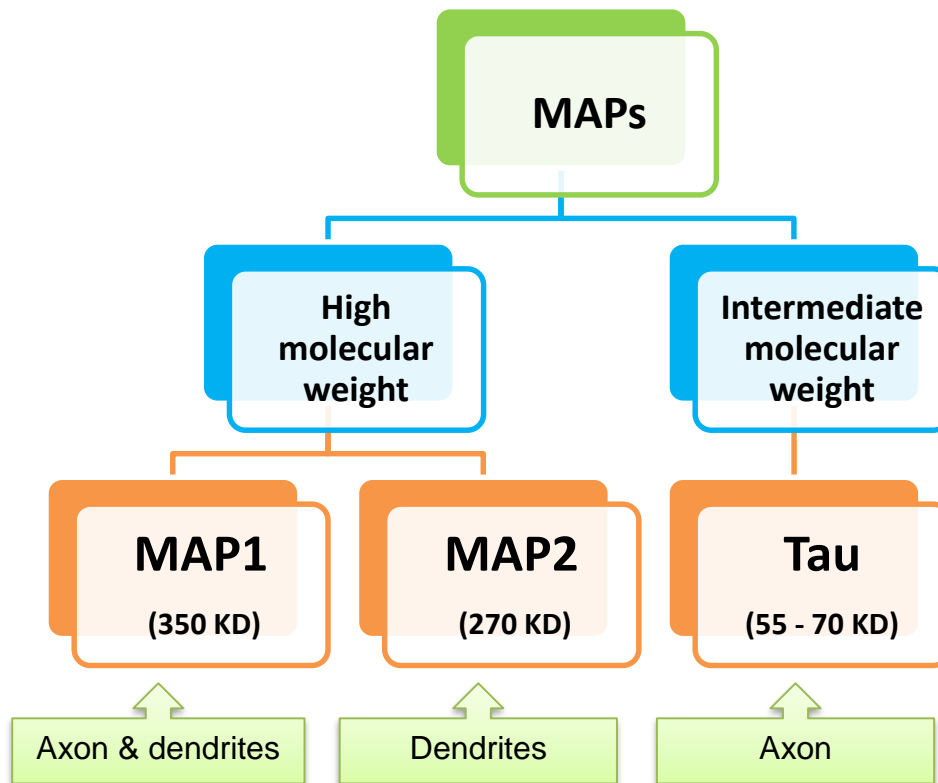


Figure 1.9: Classification of different types of structural MAPs. Diagram showing the classification of structural MAPs based on their molecular weight. MAP1 and MAP2 belong to the high-molecular weight category, while Tau protein belongs to the intermediate molecular weight. Each MAP type show a distinct subcellular localization, MAP1 is localized to the axons and dendrites, MAP2 is mainly found in the dendrites and Tau is mainly localized to the axon. This diagram was based on Matus et al., 1988 ⁷

MAPs are heterogeneous family of proteins that differ in their structure, molecular weight, differential expression, cellular distribution and function. Based on their molecular weight, they are roughly classified into two main categories: high molecular weight MAP (e.g. MAP1 and MAP2) and intermediate molecular weight MAP (e.g. tau protein), Fig. 1.9.

The expression of MAPs is under tight spatiotemporal regulation. Different types of MAPs are expressed at various levels in different cell types. For example, MAP1A is the main MAP1 type in adult rat brain. MAP1A can be found in the soma, axon and

dendrites of the neuronal cells, although some reported MAP1A expression in glial cells as well as in neurons ^{170,171}. In contrast, MAP2 is exclusively expressed in neuronal cells and mainly found in the dendrites ¹⁷². While MAP3 and MAP4 are mainly expressed in glial cells ^{173,174}.

Electron microscopy examination of polymerised MT with purified MAPs *in vitro* showed that the decoration of MT by various MAPs corresponds to distinct MT morphology. MAP1 and MAP2 are long, filamentous proteins forming side-projections that decorate the full length of the MT ¹⁷⁵, tau on the other hand produced smooth-surfaced MT with no side-projections ¹⁴, Fig. 1.10.

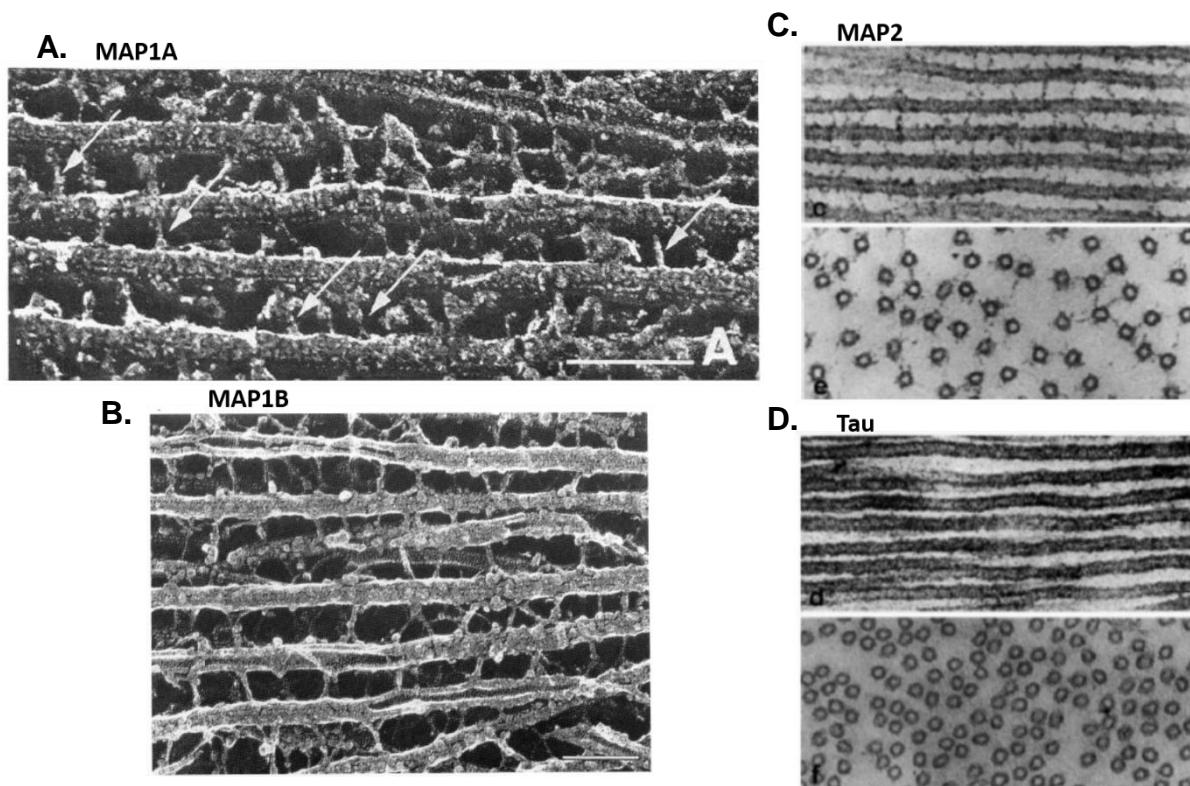


Figure 1.10: Morphological differences of various types of MAPs. Electron microscopy of *in vitro* polymerized MT in the presence of: **A.** MAP1A, **B.** MAP1B, **C.** MAP2 & **D.** tau protein. In **A.** MT are connected by long, thin, filamentous side projections of MAP1A, (arrows). **B.** MT are connected by long, filamentous projections of MAP1B. Small spherical structures are found on the surface of the MT which could be part of MAP1B molecule. **C.** MT-decorated with MAP2 has long filamentous side projections (top panel is longitudinal section and bottom panel is transverse section). **D.** MT-decorated with MAP2 is smooth without any side projections (top panel is longitudinal section and bottom panel is transverse section). Source: **A.** Shiomura et al., 1987 ³, **B.** Sato-Yoshitake et al., 1989 ⁴, **C & D.** Herzog et al., 1978 ¹⁴

Post-translational modification of MAPs also plays an important role in determining MAP properties and function. For example, unphosphorylated tau protein is known to predominantly associate with the axonal MT¹⁴², while the phosphorylated form seems to localize in the soma and dendrites¹⁷⁶. Importantly, while phosphorylated tau is critical for axonal and synaptic plasticity during development, (hyper)phosphorylated tau is implicated in Tauopathies in adults (e.g. Alzheimer disease and frontotemporal dementia). Several efforts have been made to identify various phosphorylation sites of Tau protein and to investigate their pathophysiological consequences in humans¹⁷⁷. MAPs post-translational modifications have been also shown to determine MAPs binding affinity and function. The binding affinity of MAP1 proteins is affected by the phosphorylation state. MAP1A and MAP1B association with the microtubules is enhanced upon phosphorylation¹⁷⁸, while dephosphorylated MAP1B has a higher binding affinity to the microfilaments¹⁷⁹. Also, even though that both phosphorylated and unphosphorylated MAP2 bind to MT and actin microfilaments, the phosphorylated form appears to have a higher binding affinity for actin microfilament over MT in *in vitro* experiments. Interestingly, only the unphosphorylated MAP2 can promote actin microfilament bundling, while the phosphorylated form binds actin without causing any structural modifications¹⁸⁰.

Several questions remain to be answered? for example, How would the various kinases influence MAPs dynamic distribution and function? How does the phosphorylated state of an individual MAP affect its interaction with the other cellular components? What are the consequences of glycosylation, oxidation and other PTM on the various MAPs? How do all these modifications contribute to cellular activity regulation under normal and pathological conditions? All of the previous examples highlight the fact that the diversity in MAPs expression levels, subcellular distribution patterns and PTM at the level of cell type, cell compartment and splice variant must contribute to a wide and diverse functional significance that has not been fully explored.

1.4.5. MAP1 family of proteins

1.4.5.1. Structural features of MAP1 proteins:

MAP1 family of proteins include three major types (MAP1A, MAP1B and MAP1S) that are found in most vertebrates and are encoded by distinct genes. No MAP1 ortholog has been found in *Caenorhabditis elegans* or primitive organism. MAP1 in teleosts fish shares only 25 % of the size of mammalian MAP1. *Drosophila melanogaster* expresses MAP1-related protein called Futsch, which shares 60 % similarity to rat MAP1A and 1B but differs in having an extra domain that shares sequence homology to mammalian neurofilaments ⁶.

MAP1A and MAP1B are closely related proteins. They are prominently expressed in the nervous system and share almost similar structural and functional features. Electron examination of hippocampal dendrites as well as of in vitro polymerised MT preparation have shown that both MAP1A and 1B are long, filamentous molecules that heavily cross-linked MT to each other, to other cellular organelles and to the plasma membrane, Fig. 1.10. Slight structural differences have been observed between the two molecules. MAP1B is characterized by having a small rounded structure at one end ⁴, while MAP1A is a highly flexible molecule that lacks the spherical domain ³, Fig. 1.10.

MAP expression levels vary at different developmental stage. MAP1A expression level is undetectable in rat embryo, it only starts to appear 48 h after birth and gradually increases until the end of the third week after which its level is kept constant ¹⁸¹. In contrast, MAP1B is highly expressed at early developmental stages where its level decreases gradually in adult brain ¹⁸² - probably replaced by MAP1A. In contrast to the central nervous system, MAP1B in DRG neurons preserves the same expression level during the lifespan of peripheral neurons which highlight further regional, and probably functional, differences in MAP expression pattern ¹⁸³⁻¹⁸⁵.

Both MAP1A and MAP1B form a polyprotein precursor, that undergo proteolytic cleavage at a conserved site near the C-terminus. This in turn result in the formation of two subunits: MAP1A, MAP1B heavy (HC) and light chain, LC2 and LC1, respectively ¹⁸⁶⁻¹⁸⁸. The light chains are interchangeable; LC1 exhibit non covalent

association with the heavy chain of both MAP1 members, the same applies for LC2 but with a higher affinity toward MAP1A-HC^{143,189}. Additionally, another light chain (LC3) which is encoded by a distinct gene is also capable of binding to MAP1 heavy chains, as illustrated in Fig. 1.11.¹⁹⁰

MAP1A and MAP1B contain a highly conserved region in the N-terminus. This region is not involved in microtubules binding¹⁹¹, rather it is mainly for light chains binding^{186,192}. Another important structural domain is the MT-binding domain. MT-binding domain of MAP1B consists of 19 basic repeats of KKE motif¹⁹¹. Similarly, a shorter region consisting of only 3 repeats of KKE motif in the N-terminus of MAP1A (aa 300 – 500, SS1 domain) in MAP1A is also shown to function as the MT-binding domain^{186,192,193}, Fig. 1.11 & 1.12.

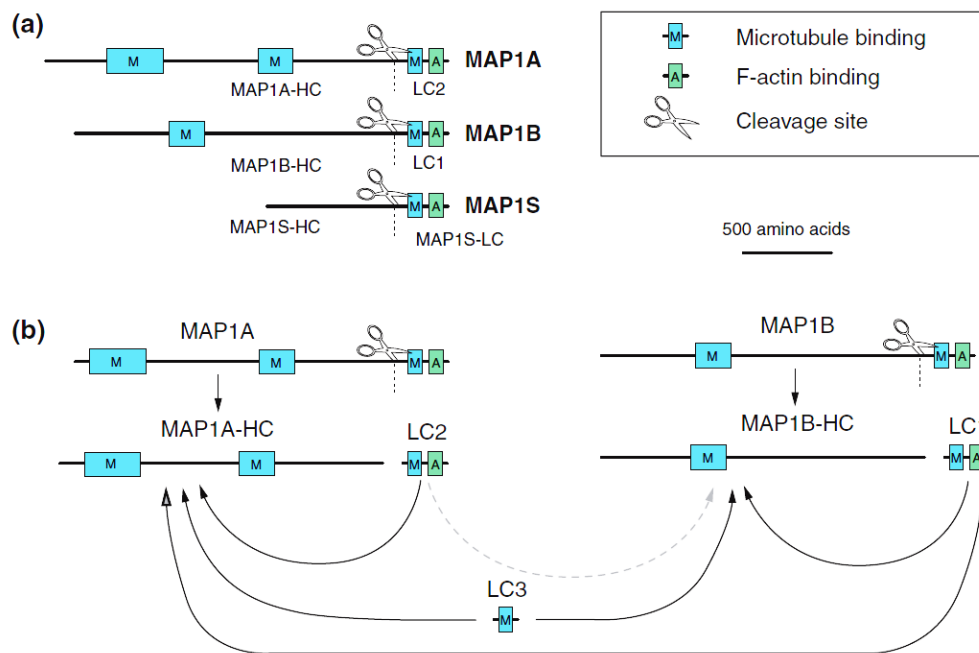


Figure 1.11: MAP1A and MAP1B structural features. **A.** MAP1A and MAP1B are highly homologous proteins. MAP1S is another member of the MAP1 family that is not very well characterized. MAP1A, 1B and 1S undergo proteolytic cleavage into two parts (heavy chain (HC) and light chain (LC)). LC2 and LC1 are the light chains of MAP1A and MAP1B, respectively. **B.** Once cleaved, light chains can bind to either HC. LC3 is another light chain that is encoded by a different gene. LC3 can also bind to the HC. Microtubule-binding domain is indicated as (M, blue square), Actin-binding domain (A, green square), cleavage site (scissor). Source: Halpain et al., 2006⁶

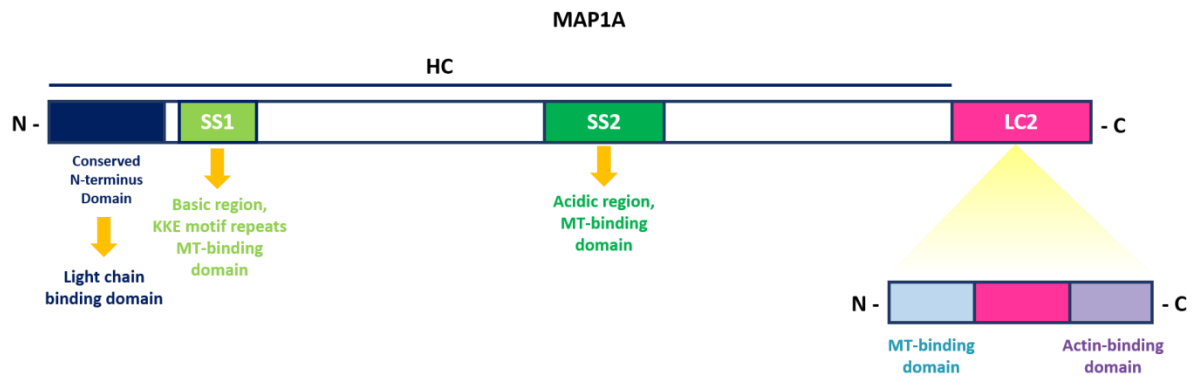


Figure 1.12: Schematic representation of MAP1A structure. Self-similarity domains SS1 and SS2 are believed to act as microtubule-binding domains (green). A highly conserved region in the N-terminus of MAP1A protein is believed to be the light-chain binding domain (dark blue). LC2 region in the C-terminus of MAP1A protein (pink). Structural analysis of LC2 reveal two major regions; N-terminus is the microtubule-binding domain (light blue) and C-terminus is the actin binding domain (purple). This figure is adopted and modified from Cravchick et al., 1994⁹

Additional domain on the C-terminus of MAP1A heavy chain was also suggested to function as a MT-binding domain (aa 1300 – 1600, SS2 domain). This domain differs from all the previously characterised MT-binding domains in having acidic composition with no known sequence repeats⁹, Fig.1.11 &1.12. However, when overexpressed, it co-localized and stabilized the microtubules in HeLa cells⁹ but failed to do so in COS7 and N2a cells¹⁹². The reason behind this contradicting results is unclear but could be related to differences in the MT properties of the cell models used in these studies as well as to differences in the endogenous level of MAP1A protein that might compete with the overexpressed domain for MT binding.

A MT-binding domain was also mapped to the N-terminus of the light chains, Fig. 1.11 &1.12. The amino acid sequence of this domain varied between the different light chains. Despite the structural differences, overexpression of the N-terminus of either LC1 and LC2 in PtK2 cells showed a significant MT co-localization, in vitro MT polymerization and MT protection against depolymerizing agents (e.g. colchicine and nocodazole). Hence, it was proposed that the light chains (LC1 and LC2) can bind, protect and modulate the MT network in a HC-independent manner¹⁸⁹.

Finally, a highly-homologous actin-binding domain is found in the C-terminus of both LC1 and LC2 of MAP1B and MAP1A, respectively, Fig.1.11 &1.12. This domain was shown to directly bind the microfilament network and suggested to mediate the cross-

talk between MT and microfilaments ¹⁸⁹, although there is no direct evidence for a concurrent binding of a single light chain to the two networks available so far.

1.4.5.2. Functional roles of MAP1 heavy and light chains.

Despite all the advances in research techniques, it is technically challenging to identify the functional significance of individual MAP due to the presence of several isoforms and splice variants that share similar functions and/or could compensate for the genetic deletion of a particular MAP. For instance, animals lacking either MAP2 or tau were viable. Isolated cells from these animals were able to produce normal axons and neurites *in vitro*. However, when crossed to MAP1B KO animals, severe neurodevelopmental defects were observed in MAP2/MAP1B and tau/MAP1B double knock-out (DKO) animals, which indicates a functional redundancy between MAP1B and MAP2 / tau proteins. Intriguingly, cells isolated from the DKO animals were still able to produce axons and neurites *in vitro*, suggesting the involvement of additional proteins and pathways in the MT formation, neurites initiation and formation ¹⁹⁴⁻¹⁹⁶.

In addition, it was argued that the use of different gene deletion strategies could influence the severity of the phenotype, which in turn influence the true assessment of the physiological role of the protein of interest. For example, MAP1B KO mice generated by three different studies produced a very different phenotypic severity levels. One targeting strategy resulted in very severe developmental defects in the heterozygous while the homozygous animals did not survive beyond postnatal day 8. The gene targeting strategy in that study resulted in the formation of a truncated product of MAP1B (571-amino acids), therefore the phenotype was proposed to arise from dominant negative effect of this truncated version of the protein rather than from actual MAP1B gene deletion ¹⁹⁷. In the contrary, another MAP1B^{-/-} mutant produced by Takei et al. concluded that MAP1B is not critical for survival, but it is important in an accurate time-course of the development of the nervous system. This conclusion was based on the fact that heterozygous mice had no aberrant phenotype while homozygous animals suffered from mild decrease in brain weight with delayed development of the nervous system. Reduced axonal diameter and myelin sheath thickness were observed in the peripheral nervous system in these animals ¹⁹⁸. A third study produced further contradicting results to the two aforementioned studies. The

study showed that only homozygous animals suffer from corpus callosum malformation and a defected axon guidance in a specific subset of neurons. In addition, the peripheral nervous system of the homozygous animals exhibited a smaller axon diameter size with reduced myelination levels of peripheral axons, consistent with the reported PNS findings from the previous study ¹⁸⁵.

In contrast to MAP1B, MAP1A is less extensively studied, the first MAP1A KO animal was reported while conducting this study. A spontaneous mouse mutation, nm2719 disrupts MAP1A gene and results in the deletion of 297 amino acids from the C-terminus (including the complete deletion of LC2). Aged homozygous animals suffered from degeneration of Purkinje fibres (18 months old) which can be rescued by transgenic expression of full MAP1A but not LC2, suggesting the importance of MAP1A-HC in the survival of Purkinje cells. In addition, earlier phenotypes included axonal dystrophy, disturbance in MT organisation at different cellular compartment particularly in the somatodendritic region and at the axonal initial segment (AIS) of Purkinje cells. There was also a drastic reduction in the levels of MAP1B and post-synaptic density-93 (PSD-93) proteins in the soma and dendrites. All of these changes led to ataxia and tremors in older animals (1 year) and consequently resulted in Purkinje fibres degeneration and cell death ¹⁹⁹. No double knockout studies with MAP1A gene have been published so far.

Overall, in vivo and in vitro studies have highlighted MAP1B as a key factor in the proper development of the central nervous system as well as in controlling both the extent and the direction of neurite and axonal outgrowth, while MAP1A is more involved in maintaining adult neuron shape and function by stabilizing MT and maintaining its proper organisation. Nonetheless, it has been shown that MT stabilization by MAP1A protein might not be as prominent as for MAP2 and tau proteins ^{192,200}. This in fact led many researchers to investigate other MT-independent functions of this ubiquitously expressed family of proteins (MAP1). In agreement, light chain pool of both MAP1A and MAP1B was shown to be much higher than that of HC, also a large proportion of the LC2 and LC1 are distributed in a HC/MT-independent manner. Which further enforces the idea that the function of these proteins and their light chains extend beyond the classical “structural” views. In the next few sections I will briefly describe the current knowledge regarding MAP1A and MAP1B additional

potential functions in regulating various ion channels and receptors in the nervous system. Summary of all of the interactions can be found in Table 1.1.

- **LC1 interaction with 5-HT_{3A} receptor:**

5-HT_{3A} is a ligand-gated ion channel that is expressed in the central and peripheral nervous system. 5-HT_{3A} receptor has been shown to co-localise with LC1 in hippocampal neurons as well as in HEK-293 co-transfected cells. LC1 is shown to reduce the membrane receptor density when co-transfected with 5-HT_{3A} receptor in HEK-293 cells. In addition, 5-HT_{3A} receptor desensitisation process was increased in the presence of LC1 in transfected HEK293 cells without affecting the ligand-binding kinetics. Taken together, it has been suggested that LC1 may play a role in reducing 5-HT_{3A} surface expression by targeting the receptor to MT or actin cytoskeleton²⁰¹. The exact molecular mechanism of this interaction and whether it involves other proteins remain unclear.

- **LC1 interaction with voltage-gated sodium channel Nav1.6**

LC1 has been reported to interact with the N-terminus of Nav1.6 channel in heterologous system and in the mouse brain. LC1 is shown to enhance Nav1.6 current density in ND7/23 cells without affecting other parameters. This suggests that LC1 might be involved in increasing the number of Nav1.6 ion channels at the ND7/23 cell membrane. The authors of this study proposed a potential role for LC1 as an adaptor protein that mediates Nav1.6 targeting to AIS and node of Ranvier in the neurons, in addition to its involvement in MT-mediated trafficking of Nav1.6 to the cell membrane²⁰². Yet, there are no available subsequent studies that investigate the molecular mechanism of this interaction and its functional significance in primary neurons.

- **Interaction of LC1 with NMDA receptor subunit NR3A.**

N-methyl-d-aspartate receptor (NMDAR) is a heterotetramer receptor that is usually composed of two NR1 and two NR2 subunits in which they cooperatively increase NMDAR calcium current. Alternatively, incorporation of a third subunit (NR3A) into the receptor usually produce an opposite effect which result in a reduction of the NMDAR calcium current. LC1 is found to interact with NR3A subunit in rat brain. MAP1B^{-/-} mice demonstrated an elevated level of NR3A subunit in parallel to reduced levels of NR1 subunit. The molecular mechanism of this interaction is not clear, however, it was

hypothesised that this interaction might be involved in regulating the number of NR3A containing NMDAR receptors at the plasma membrane between synaptic and extrasynaptic sites, which as a result would affect the development of proper dendritic organisation as well as neuronal synaptic plasticity ²⁰³.

- **LC1 interaction with voltage-gated calcium channel (Cav2.2)**

The N-terminus part of LC1 was shown to interact with the C-terminus of N-type voltage-gated calcium channel Cav2.2 α 1 (pore-forming subunit) in heterologous system (HEK293) and in mice cerebral cortex. Co-expression of LC1 and Cav2.2 (α , & β) subunits in HEK293 cells resulted in a significant reduction in the calcium current density as well as in the total surface expression level of the channel – detected by surface biotinylation experiment. In accordance, LC1 knock-down (KD) in mouse DRG neurons resulted in increased Cav2.2 current density. Such effects indicated that LC1 could play a role in Cav2.2 internalisations. A subsequent study has supported this hypothesis by demonstrating that UBE2L3 (E2 ubiquitin conjugase) can associate with Cav2.2 channel and promote channel ubiquitination only in the presence of LC1. Additionally, MAP1B^{-/-} KO animals showed a significant increase in the level of ubiquitinated Cav2.2 channels. Altogether, these studies suggested that LC1 acts as a scaffold protein that links Cav2.2 channel to UBE2L3 and mediate the channel ubiquitination and subsequent internalization via clathrin-dependent pathway ^{204,205}.

- **MAP1A and MAP1B interact with an orphan G-protein coupled receptor (GPCR) in vivo.**

Y2H assay, co-localisation and co-IP experiments have showed an in vivo interaction of ee3 GPCR with both MAP1A and MAP1B and their light chains in mouse brain. Interestingly, ee3 protein level, but not mRNA, was completely abolished in MAP1B^{-/-} mice, which suggests that the interaction might be important for proper ee3 protein expression, folding, targeting and stabilization in neuronal cells ²⁰⁶. The molecular mechanism of this interaction and evidence for its physiological significance remain poorly understood.

- **MAP1A interaction with BKCa potassium channel**

LC2 is found to interact with the C-terminus of calcium-activated potassium channel (BKCa) in the rat brain. Both proteins were shown to co-localize in the rat cerebral Purkinje cells of the cerebellum by immunostaining. MAP1A-HC was also found to associate with the BKCa-LC2 complex in rat brain. The functional aspect of this macromolecular interaction is yet to be identified. However, based on the fact that BKCa activity can be modulated by actin cytoskeleton²⁰⁷, it has been proposed that LC2 might play a role in the regulation of BKCa channel by the actin cytoskeleton²⁰⁸.

- **LC2 interacts with Stargazin-AMPA receptor complex**

Stargazin protein interacts with AMPA receptor GluR1, 2 and 4 subunits as well as with PDZ-domain containing proteins like postsynaptic density proteins (PSD-93 and PSD-95). Accordingly, it was suggested that stargazin is involved in the regulation of AMPA receptor trafficking and anchoring to the cytoskeleton network (stargazin-AMPA, and stargazin-PSD proteins)²⁰⁹⁻²¹².

LC2 has also been reported to directly interact with stargazin in mouse cerebellum. In addition, AMPA receptor subunit (GluR2) was also found to interact with LC2. When fully glycosylated, GluR2 co-associate with LC2-stargazin protein complex, implying a role for this tripartite (LC2-Stargazin-GluR2) complex in regulating AMPA intracellular trafficking prior to synaptic targeting and anchoring (e.g. Golgi to plasma membrane)²¹³. Interestingly, PSD-93 is reported to interact with LC2 in cerebellar Purkinje neurons²¹⁴, which raises the possibility that LC2 might be involved in the regulation of AMPA receptor trafficking as well as in AMPA receptor synaptic targeting and anchoring via its differential interaction with multiple protein complexes at different cellular compartments, (*LC2-Stargazin-GluR2* and *PSD-93-LC2-stargazin-GluR2*), respectively.

- **LC2 interaction with voltage-gated calcium channel (Cav2.2)**

The N-terminus of LC2 is shown to interact with the C-terminus of Cav2.2 channel at the presynaptic boutons of rat hippocampal neurons. By using various molecular techniques; co-IP, pull-down and immunostaining using antibody that recognizes the extracellular epitope of Cav2.2 channel, it was shown that LC2 is critical for Cav2.2

trafficking, targeting and surface anchoring at the presynaptic terminals of hippocampal neurons. Furthermore, the fact that only the full length LC2, but not the N-terminus part (MT-binding domain), resulted in Cav2.2 membrane anchoring suggest the importance of the C-terminus part of LC2 (actin-binding domain) for Cav2.2 anchoring, which is most likely mediated via the actin cytoskeleton ²¹⁵. Although, the mechanism by which LC2 retains surface Cav2.2 is not clear, it might involve selective targeting and stabilization of the channel along with other protein partners at the presynaptic terminals, or it might involve inhibition of the channel internalization (which is known to take place as a result of disrupting channel-actin interaction) ²¹⁶, in contrast to the previously mentioned interaction of LC1 with Cav2.2.

From all of the previously described interactions, it is clear that MAP1A and MAP1B are involved in several cellular processes along with their classical MT stabilization and organization roles. They are involved in regulating membrane trafficking, targeting, anchoring and internalisation of various ion channels and receptors. Additionally, it seems that the function of the reported protein complexes varies according to the type of interacting protein (e.g. LC1 or LC2), phosphorylation state, cellular compartment and cell type. To date, most of the molecular mechanisms of these interactions have been poorly described, probably due to the overlap between MAP1A, MAP1B (as well as other MAPs) structure and function that might obscure the dissection of the functional significance of a specific interaction.

Table 1.1: Summary of MAP1A and MAP1B protein interactions

MAP1 protein	Interacting partner	Cell type	Proposed functional effect	Reference
LC1	5-HT _{3A}	HEK293	↓ 5-HT _{3A} surface expression	Sun et al. 2008 ²⁰¹
LC1	Nav1.6	ND7/23	↑ Nav1.6 surface trafficking	O'Brien et al., 2012 ²⁰²
LC1	NR3A	Rat brain	↓ NR3-containing NMDAR at the cell membrane	Eriksson et al., 2010 ²⁰³
LC1	Cav2.2	HEK293 & mouse brain	↓ Cav2.2 surface expression by promoting ubiquitination (Cav2.2-LC1-UBE2L3 complex)	Gandini et al., 2014 ^{204,205}
MAP1A & MAP1B	GPCR	Mouse brain	Regulation of protein expression, protein folding and targeting	Maurer et al., 2004 ²⁰⁶
MAP1A	BKCa	Rat brain	Mediate BKCa-actin interaction	Park et al., 2004 ²⁰⁸
LC2	Stargazin-AMPA receptor complex	Mouse brain	Regulate AMPA receptor trafficking to the cell membrane	Ives et al., 2004 ²¹³
LC2	PSD-93	Mouse brain	Regulate AMPA receptor anchoring	Brenman et al., 1998 ²¹⁴
LC2	Cav2.2	Rat brain	Regulation of Cav2.2 trafficking, targeting and surface anchoring the the presynaptic terminals of hippocampal neurons	Leenders et al., 2008 ²¹⁵

To characterise the functional significance of LC2-Nav1.7 interaction, several functional assays were explored (as discussed in chapter 5). One of the explored options was calcium imaging using veratridine as VGSC activator. The rationale behind using this particular technique and veratridine to investigate the functional consequences on DRG neurons and the advantages and potential applications of using this assay are presented in chapter 3 and 4. Hence, in the last section of this chapter, I will describe calcium imaging technique and discuss its most recent applications in studying DRG neurons.

1.5. Calcium imaging assay for assessing DRG excitability

Considerable efforts have been done in the field to better understand the complexity of DRG neurons and to isolate the molecular components that regulate neuronal excitability in normal and pathological conditions. Electrophysiology is considered the gold-standard in our current understanding of neuronal excitability. Its highly sensitive temporal resolution enable researcher to extract valuable information regarding the action potential frequency, duration and conduction velocity. However, the diversity and heterogeneity of the DRG neurons make it more difficult, laborious and nearly impossible to obtain a representative sample for each and every cell subtype by electrophysiology where, most of the times, action potential from a single cell is recorded at a time. Therefore, there is an increasing need for a high-throughput assay that can simultaneously monitor the activity of a large number of neurons such as calcium imaging assay.

1.5.1. Calcium imaging indicators:

Calcium imaging assay is widely used by neuroscientist to study neuronal regulatory mechanisms and calcium signalling pathways. Many of the advances made in the neuroscience today have not been possible without the important contribution of the Tsien laboratory where they developed highly sensitive calcium indicators for in vitro use^{217,218} and discovered the genetically encoded calcium indicator (GECIs) for in vivo use²¹⁹.

One of the most widely used in vitro calcium indicator is the high-affinity calcium indicator Fura-2. Fura-2 molecule is composed of two main parts, a highly-selective calcium chelator and a fluorescent chromophore (fluorophore). Fura-2 is considered the standard chemical dye for in vitro calcium imaging experiments. It has a wide calcium sensitivity range (~100 nM – 100 μ M), with a high calcium affinity (K_d ~ 145 nM) which is comparable to the intracellular calcium levels²²⁰. The ester form of Fura-2-acetoxymethyl ester (Fura-2AM) is membrane permeable that can easily and readily enter the cytosolic compartment of the cell. Once there, the ester bond gets degraded by cytoplasmic esterase, which render the dye membrane impermeable. Upon binding to intracellular calcium, Fura-2 undergoes intramolecular conformational changes that shift its excitation wavelength (380 nm, calcium free) to a shorter wavelength (340 nm,

calcium bound), while the emission wavelength of the two forms is usually between 505 – 520 nm. When intracellular calcium concentration is increased it results in an increase in the calcium-bound fura-2 excitation efficiency at 340 nm, that is accompanied by a simultaneous decrease in the calcium-free fura-2 excitation efficiency at 380 nm. Therefore, a ratiometric measurement of fura-2 excitation wavelengths (340 / 380) gives a quantitative measure of the intracellular calcium concentration independently of the fura-2 concentration within the cells ^{218,220}. Ratiometric measurement of fura-2 excitation has also the advantage to overcome problems of dye leaking, photobleaching and unequal tissue / cells thicknesses. Finally, the micromolar concentration of fura-2 is bright and stable enough for relatively lengthy imaging protocols with minimum photobleaching and cellular phototoxicity ²²⁰.

Genetically encoded calcium indicators (GECIs) are protein-based calcium indicators that have the advantage of selective expression in a specific tissue, cell population or even specific intracellular compartment. GCaMPs proteins are a group of GECIs composed of a circular permuted enhanced green fluorescent protein (eGFP) that is linked to calmodulin on its C-terminus side and to calmodulin binding peptide (M13) on the N-terminus side. In calcium free condition, minimum fluorescent is detected by the fluorophore. Upon increased intracellular calcium level, calcium binds to the calmodulin, which in turn binds to the M13. The formation of Ca-calmodulin-M13 complex induces conformational changes to the eGFP molecule which results in a significantly enhanced fluorescent activity ²²¹. Several GCaMPs have been developed so far to enhance the signal-to-noise ratio, the dynamic range (the ratio of differences in intensity between the free-calcium form to the bound-calcium form) and the response kinetics ²²².

1.5.2. In vitro calcium imaging of DRG neurons:

Profiling of DRG neurons based on their unique calcium responses to a series of algogenic markers (e.g. Capsaicin, AITC, ATP, histamine, menthol, veratridine, bradykinin and acetylcholine) has been introduced by the Olivera research group, a concept termed “constellation pharmacology” ^{29,223}. Constellation pharmacology provides an elaborate catalogue of DRG neurons based on their functional phenotypes. In addition, it allows for the identification of unique and rare neuronal

subtypes that were usually missed by classical techniques - due to their infrequent occurrence³⁰⁻³². Constellation pharmacology can also be used in drug screen, where comparison of calcium responses from treated and untreated cultures can reveal the primary target of the drug as well as its potential off-target effects²²⁴. Another application of constellation pharmacology approach in drug screen is that cells are challenged with multiple pulses of high potassium external solution. The effect of the test compound on the neuronal excitability was judged by the degree of distortion / inhibition it produces on one of the KCl pulses. The effect of the test compound is then compared to pre-determined effects obtained by known specific and non-specific ion-channel blockers^{29,30,224}. However, the lengthy protocol, the need for a pre-determined, species-specific response-templates for comparison as well as the use of high-potassium solution (a non-specific neuronal depolarizing agent) in the assessment of the specificity of ion channel blockers are all limiting factors that are associated with this particular assay.

1.5.3. In vivo calcium imaging of DRG neurons:

GCaMP3 and GCaMP6 are common examples of GECI that are used to study DRG neurons in vivo. They are genetically expressed in sensory neurons under the control of phosphoinositide-binding protein (*pirt*) promoter, (*pirt* gene is selectively expressed in the DRG and trigeminal ganglia, but not in the sympathetic ganglia and CNS)²²⁵. This unique expression in DRG neurons combined with the development of a novel in vivo DRG imaging technique have allowed scientists today to monitor large number of sensory neurons in their native environment to several physiological / pharmacological stimuli and reveal interesting information regarding neuron types, communication with surrounding cells and pain signalling²²⁶⁻²²⁹.

One study has investigated the neuronal coupling upon peripheral injury. Neuron-satellite glial cell coupling as well as neuron-neuron coupling events are shown to be significantly higher in injured animals compared to controls. Interestingly, neuronal coupling was noticed between all cell sizes, which suggest that in the presence of peripheral insult, nociceptive neurons as well as non-nociceptive neurons can be activated via coupling. This “hijacking” of the large-diameter neurons by small nociceptive neurons could have potential implications in injury-induced mechanical

allodynia. Neuronal coupling has been suggested to be directly mediated via gap junction formation, although chemical communication was not ruled out ²²⁷.

A different study that used GCaMP3-expressed in all cell types by means of adenoviral E11A-driven Cre has showed that inflammation can alter the sensitivity of neurons to mechanical stimuli where, unexpectedly, some cells loses mechanical sensitivity while others showed similar or enhanced sensitivity. Intriguingly, the study also reports that not all action potentials from large to medium neurons can elicit calcium responses in their animal model. Conversely, some calcium responses are elicited independently of the propagated action potential ²²⁸.

Another study has looked at the responses of sensory neurons to various physiological modalities (mechanical, heat and cold) applied directly to the plantar surface of the hind paw of an anesthetized animal. The study suggests that under normal conditions > 85 % of the responsive DRG neurons are modality-specific, in contrast to what have been demonstrated previously by in vitro and in vivo electrophysiology studies in which majority of DRG neurons are polymodal. Interestingly, the study also shows that upon PGE2-induced inflammation, several neurons switch from unimodal to polymodal responses with an increased response intensity to noxious physiological stimuli. It also shows that almost 48 % of the primarily unresponsive neurons (silent neurons) become responsive upon injury ²²⁶. In contrast, a large-scale in vivo study by Chisholm et al, 2017 using similar technique with three different methods of GCaMP6 expression (intrathecal AAV9 virus injection, Pan-neuronal transgenic GCaMP6 expressing mice and sensory neuron specific GCaMP6 expressing mice) demonstrates that polymodality is an inherent feature to DRG neurons under normal conditions in consistence with the classical view of the DRG polymodality ²²⁹.

Altogether, each of the previous studies has suggested new and interesting hypotheses that would not be possible to propose without the simultaneous and high-throughput capacity of the in vivo calcium imaging. Importantly, such technique is limited to a very few number of laboratories around the world and its application is still an evolving process. It is not unexpected that several technical aspects including GCaMP choice (sensitivity, dynamic range and expression methods), microscopy (type, acquisition rate and resolution), stimulation (type, application method, intensity,

application site), surgery of exposing the DRG, the choice of the anaesthetic agent and the sample size used in the analysis are only few out of many other factors that could lead to the generation of some controversial and contrasting results from these studies. Nonetheless, given the amount of data that can be obtained by such technique, it is undoubtedly that several efforts will be invested and more laboratories will adapt the technique in the next few years to resolve pain pathways in an sophisticated, more physiological and comprehensive way.

1.5.4. The use of Veratridine to activate neurons in calcium imaging assay.

In vitro calcium imaging experiments are classically performed by applying a specific pharmacological agent to activate neurons. However, majority of these agents are subtype specific. For example, capsaicin specifically activates TRPV1 expressing neurons, NGF activates TRKA expressing neurons, and mustard oil and cinnamaldehyde specifically activate TRPA expressing neurons. In order to activate the whole population of neurons, electrical stimulation or high-potassium extracellular solution are used to alter membrane potential and elicit depolarization in all neurons. Importantly, the use of high potassium or electrical stimulation to reflect VGSC activity is precluded by the fact that multiple ion channels can be activated, hence contribute to neuronal depolarization (e.g. VGSC and VGCC) ²³⁰⁻²³³.

In the current study, I was mostly interested in examining VGSC activity and neuronal excitability upon direct modification of VGSC or VGSC-interacting proteins. Therefore, I used veratridine (instead of high-potassium solution) in calcium assay to directly measure VGSC activity and neuronal excitability.

Veratridine is a natural alkaloid produced by the lilaceous plants as a part of a many other related alkaloids named (veratrum alkaloids). The seeds of these plants contain mixture of ester alkaloids named "veratrine" and was used as insecticides ²³⁴. Goldstein was the first who purified veratridine from the veratrine mixture and provide several investigators with the pure alkaloid. On the 1970s, a pure form of veratridine became commercially available ²³⁵. Early experiments with the pure veratridine alkaloid has shown that the drug causes characteristic change in sodium permeability

as a result of keeping the sodium channels open for relatively longer time ²³⁶. Moreover, experiments on myelinated frog nerve fibres and on single nerve fibres suggested that the presence of sodium ions in the external medium is critical for veratridine-induced depolarization ²³⁷. All of these observations were consolidated by extensive patch-clamp electrophysiology experiments ^{235,238,239}. Now, veratridine is widely accepted as “VGSC activator /agonist”. Veratridine predominantly binds TTX-S VGSC with a higher preference to open VGSC. It binds S6 in DI and DIV of VGSC, locks the channel in its active state and delays fast inactivation, with subsequent increase in sodium influx and membrane depolarization ²⁴⁰. Due to its action on VGSC and its ability to elicit robust depolarization in excitable cells, veratridine has been long used as a pharmacological tool to activate neurons in multiple drug screen assays ^{30,241}.

1.6. Aims:

The expression pattern of MAP1A and its light chain (LC2) was mostly studied in the CNS. Several MAP1A-protein partners have been identified, but in most cases left with no clear description of the functional consequence in native tissue. Therefore, the main aims of this study were:

Aim 1: To develop a high throughput assay based on calcium imaging to assess neuronal excitability in general and Nav1.7 function in particular, in primary cultures of DRG sensory neurons.

Aim 2: Investigate the effect of MAP1A knock-down on Nav1.7 function and neuronal excitability.

Therefore, the following objectives were carried out:

Aim 1:

- Characterize VTD calcium responses in DRG neurons, (Chapter 3).
- Characterize the effect of sodium channel blocker on VTD calcium responses in DRG neurons, (Chapter 4).
- Optimization and investigation of the functional differences between long-term and short-term DRG cultures, (Chapter 5).

Aim 2: (Chapter 5)

- Confirm LC2-Nav1.7 interaction in DRG neurones.
- Investigate MAP1A-HC and LC2 distribution patterns in DRG culture.
- Achieve high-efficiency MAP1A KD in DRG neurons.
- Characterize the functional significance of MAP1A KD on Nav1.7 and neuronal excitability.
- Identify the binding domains involved in LC2-Nav1.7 interaction.

CHAPTER 2

MATERIALS & METHODS

Chapter 2: Materials and Methods

2.1. Materials:

2.1.1. Animals:

Tissues and cells were freshly obtained from 3-4 months old (adult) male C57/BL6 mice purchased from Charles River (Margate, UK). All mice had a free access to food and water before sacrifice.

2.1.2. Mammalian cell lines:

Cell line	Details
N2a	Mouse neuroblastoma cell line, adherent
HEK-293	Human Embryonic Kidney cell line, adherent.
SH-SY5Y	Human neuroblastoma cell line, adherent and suspension
HeLa	human cervical cancer cell line, adherent
Caco-2	Human colon colorectal adenocarcinoma epithelial cell line; adherent

2.1.3. Bacterial strains:

Strain	Details
DH5 α TM	Genotype: <i>F- Φ80lacZΔM15 Δ(lacZYA-argF) U169 recA1 endA1 hsdR17(rk-, mk+) phoA supE44 thi-1 gyrA96 relA1 λ-</i> Source: Invitrogen (cat.no. 18265-017)
E.coli Nova Blue (XL1)	Genotype: <i>recA1 endA1 gyrA96 thi-1 hsdR17 supE44 relA1 lac [F' proAB lacIqZΔM15 Tn10 (TetI)]</i> Source: Dr. Erdmann lab (Stratagene GmbH)
E.coli XL10-Gold ultracompetent cells	Genotype: <i>TetrD(mcrA)183 D(mcrCB-hsdSMR-mrr)173 endA1 supE44 thi-1 recA1 gyrA96 relA1 lac Hte [F' proAB lacIqZDM15 Tn10 (Tetr) Amy Camr</i> Source: Dr. Erdmann lab (Agilent)

2.1.4. Cell culture reagents:

Reagent name	Supplier	Cat. no.
Accumax	Innovative Cell Technologies	AM105
Albumin Bovine fraction V (BSA)	Melford	A1302
B27 supplement (without insulin)	Gibco™ life technologies	05-0129SA
Collagenase Type XI, 100X (0.6 mg/mL)	Sigma	C9407
Dispase, 100X (1 mg/mL)	Sigma	D4693
Dulbecco's phosphate buffered saline (DPBS), without Ca ⁺⁺ and Mg ⁺⁺ , 0.0095 M (PO ₄)	Lonza	BE17-512Q
Dulbecco's Modified Eagle's Medium/F12 with Glutamax medium (DMEM/F-12 + Glutamax)	Gibco™ life technologies	31331-028
F12 Nutrient mix+GlutaMA	Gibco™ life technologies	31765-027
FBS (fetal bovine serum) – EU approved origin, origin: South America	Gibco™ life technologies	10500-064
MEM+Glutamax	Gibco™ life technologies	41090-028
MEM-NEAA(100x)	Gibco™ life technologies	11140-035
Opti-MEM® I Reduced Serum Medium, no phenol red	Gibco™ life technologies	11058021
Penicillin/Streptomycin 100X	Sigma	P0781
Polyethyleneimine (PEI), linear	Polysicene	23966
Poly-L-ornithine (20ug/mL)	Sigma	P3655
Trypsin-EDTA (10X) [0.5 % / 0.2 % in DPBS]	A&E scientific (PAA)	L11-003

2.1.5. Bacterial Culture and molecular cloning reagents:

Reagent name	Supplier	Cat. no.
Agar Granulated	Melford	GM1002
Agarose	Melford	MB1200
Ampicillin sodium salt (200 mg/mL)	Sigma	A0166
Glycerol	Fisher Scientific	G/0650/17
LB Broth, MILLER, Large granule	Fisher BioReagents	BPE9723-2
Spectinomycin dihydrochloride pentahydrate	Sigma	S4014
Terrific Broth Modified, Large granule	Fisher BioReagents	BPE9728-2
5x Green buffer	Promega	M791B
dNTP set	Thermo Scientific	R0186
Go Taq polymerase enzyme	Promega	M830C
SYBR® Safe DNA Gel Stain	Thermo Fisher Scientific	S33102
Antarctic phosphatase enzyme (ACP)	New England BioLabs	M0289S
T4 DNA ligase enzyme	New England BioLabs	M0202S
T4 DNA ligase buffer	New England BioLabs	B0202S

2.1.6. Restriction enzymes:

All endonuclease restriction enzymes and buffers used in this thesis were purchased from New England BioLabs (NEB).

2.1.7. Pharmacological compounds:

Reagent name	Vehicle	Stock conc.	Supplier	Cat. no.
A-803467	DMSO	10 mM	Abcam	Ab120282
Allyl isothiocyanate (AITC)	-	100 μ M	Sigma	377430
ATP	Water	10 mM	Sigma	A2383
Bradykinin	0.1 M acetic acid	10 mM	Sigma	B3259
Capsaicin	Ethanol	10 mM	Tocris	0462
Isoflurane (IsoFlo®)	Abbott	100 %	Abbott	B506
PF-04856264	DMSO	10 mM	Sigma	11916
Recombinant mNGF beta	0.1 % BSA/PBS	20 μ g/mL	R&D	1156-NG
Tetradotoxin (TTX)	Citrate buffer	30 μ M	Abcam	Asc-054
TNP-ATP triethylammonium salt	Water	10 mM	Tocris	2464
Veratridine	Ethanol	5 mM	Abcam	Ab120279
α,β -methylene ATP	Water	10 mM	Sigma	M6517

2.1.8. Reagents, Chemicals and Solvents:

Reagent name	Supplier	Cat. no.
2-Mercaptoethanol	Sigma	M-3148
4 % PFA + 3 % Sucrose	Alfa Aesar	J61984
Acetic acid glacial	Fisher Scientific	A/0400/PB17
Albumin Standard 2mg/mL	Thermo Scientific	23210
Ammonium Chloride	Sigma	A9434
Ammonium Persulphate (APS)	Melford	A1512
Bio-Rad protein assay	Bio-Rad	500-0006
Bromophenol Blue	Fisher BioReagents	BP115-25
Calcium Chloride (anhydrous)	Melford	C1103
DAPI (4,'6-Diamidino-2-Phenylindole)	Fisher Scientific	D1306
D-glucose (anhydrous)	Fisher Scientific	G/0500/53

Dimethylsulfoxide (DMSO)	Sigma-Aldrich	276855
EDTA (Diaminoethanetetra-acetic acid disodium salt)	Fisher Scientific	D/0700/53
Ethanol, absolute (HPLC grade)	Fisher Scientific	E/0665DF/17
Fura-2,AM (20 X 50 µg unit)	Molecular Probes	F1221
Gelatin from cold water fish skin	Sigma	G7765
Gene Ruler 100bp DNA Ladder plus, 0.5 µg/µL	Fermentas	SM0321
Gene Ruler 1Kb DNA Ladder plus, 0.5 µg/µL	Fermentas	SM0311
Glycine	Acros organics	220910050
HEPES	Sigma	H3375
Hydrochloric acid S.G. 1.18 (~ 37 %)	Fisher Scientific	H/1200/PB17
Magnesium chloride (Anhydrous)	Melford	M0535
Methanol	Fisher Scientific	M/3950/17
Normal Goat Serum	Gibco™ life technologies	16210-064
OCT embedding matrix	LAMB/OCT	03661650
PageRuler™ Plus Prestained Protein Ladder	Thermo Scientific	26619
Paraformaldehyde	TAAB Laboratories	P001
Poropan-2-ol (Analytical grade reagent)	Fisher Scientific	P/7500/17
Potassium chloride	Melford	P0515
ProLong® Gold antifade mounting reagent	Life Technologies	P36930
Protease Inhibitor Cocktail (PIC) 100 X	Sigma	P8340
Protein G sepharose®, fast flow	Sigma	P3296
ProtoGel® [Acrylamide 30 % (w/v): 0.8 % (w/v) Bis-Acryl-amide stock solution (37.5:1)]	Ultra Pure	EC-890
Sepharose® 6B	Sigma-Aldrich	6B100
Skim milk powder	70166	Fluka
Sodium Azide	Aldrich	438456
Sodium Chloride	Fisher Scientific	S/3160/65

Sodium chloride	Fisher Scientific	S/3160/65
Sodium dihydrogen orthophosphate dehydrate	Fisher Scientific	S/3760/53
Sodium dodecylsulphate	Fisher Scientific	S/5200/53
Sodium hydroxide	Fisher Scientific	S/4920/53
TEMED	Melford	T3100
Tetraethylammonium chloride	Sigma	T2265
TRIS	Melford	B2005
Triton® X-100	Sigma-Aldrich	T9284
Tryptone granulated	Melford	GT1332
Tween-20	Melford	P1362
Yeast extract (large granules)	Fisher Bioreagents	BPE9727-500

2.1.9. Commercial Kits:

Reagent name	Supplier	Cat. no.
Block-it™ Pol II miR RNAi Expression Vector Kit with EmGFP	Invitrogen	45-1102
Direct-zol™ RNA Miniprep	The Epigenetics company	R2050
GenElute™ Plasmid Miniprep Kit	Sigma-Aldrich	PLN350-1KT
Genopure Plasmid Maxi Kit	Roche	03143422001
Genopure Plasmid Midi Kit	Roche	03143414001
High Capacity cDNA Reverse Transcription Kit	Applied Biosystems	4368814
Micro BCA™ Protein Assay Kit	Thermo Scientific	23235
Pierce® Cell Surface Protein Isolation Kit	Thermo Scientific	89881
Pierce® ECL Western Blotting Substrate	Thermo Scientific	32106
Qiaex II® Gel Extraction Kit	Qiagen	20021
Qiagen® Plasmid Plus Mega Kit	Qiagen	12981
Western bright™ ECL Kit	Advansta	K-12045-D20

2.1.10. Primary Antibodies:

Antibody	Host	Application	Supplier	Cat.no.
Anti-ac- α -Tubulin	Rabbit	WB (1:1000)	Cell signaling	5335S
Anti-Na/K ATPase α (H-300)	Rabbit	WB (1:1000)	SantaCruz	Sc-28800- E1412
Anti-Actin	Rabbit	WB (1:1000), IF (1:1000)	Biorbyt	Orb10033
Anti-cmyc (A-14)	Rabbit	WB (1:1000), IF (1:1000)	SantaCruz	Sc-789
Anti-GAPDH	Rabbit	WB (1:5000)	Biorbyt	Orb66644
Anti-GFAP	Rabbit	IF (1:500)	Sigma	G9269
Anti-GFAP	Mouse	IF (1:500)	Sigma	G3893
Anti-HuD (H-300)	Rabbit	WB (1:500)	SantaCruz	Sc-25360
Anti-LC2	Rabbit	WB & IF (1:1000)	Gift from Dr. Friedrich Propst	
Anti-MAP1A (HC)	Rabbit	WB (1:500), IF (1:200)	SantaCruz	Sc-25728
Anti-MAP1B (LC1)	Mouse	WB (1:500)	SantaCruz	Sc-136472
Anti-MAP1LC3A	Rabbit	WB (1:500)	LSBio	LS-C165699
Anti-NaV 1.7	Mouse	WB (1:1000), co-IP (1:100), IF (1:400)	Neuromab	75-103
Anti-NF200	Rabbit	IF (1:500)	Sigma	N4142
Anti-Peripherin	rabbit	IF (1:500)	Abcam	Ab4666
Anti- β III-Tubuin	Mouse	WB & IF (1:1000)	R&D	MAB1195
IgG	Mouse	co-IP	Sigma	I5381

2.1.11. Secondary Antibodies:

Antibody	Host	Application	Supplier	Cat.no.
Alexa Fluor 647, Anti-Mouse Fab fragment	Goat	IF (1:2000)	Molecular Probe	A21237
AlexaFluor 488 Anti-mouse Fab2	Goat	IF (1:2000)	Life Technologies	A11017
AlexaFluor 594 Anti-mouse	Goat	IF (1:2000)	Life Technologies	A11032
AlexaFluor 594 Anti-rabbit	Goat	IF (1:2000)	Life Technologies	A11037
AlexaFluor488 Anti-mouse	Goat	IF (1:2000)	Life Technologies	A11029
Anti-mouse IgG (H+L) DyLight 680	Goat	WB (1:10000)	Thermo Scientific	35518
Anti-mouse HRP	Goat	WB (1:2000)	Life Technologies	G21234
Anti-Rabbit HRP	Goat	WB (1:2000)	Invitrogen	1148960
Anti-rabbit IgG (H+L) DyLight 800	Goat	WB (1:10000)	Thermo Scientific	SA5-35571
Clean blot IP detection reagent		WB (1:100)	Thermo Scientific	21230
GFP booster Atto-488		IF (1:1000)	Chromotek	Gba488-100

2.1.12. DNA Plasmids:

Plasmid Name	Details
pcDNA3-cmyctag	Dr. Nassar plasmids library
pcDNA™6.2-GW/EmGFPmiR	Block-it™ Pol II miR RNAi Expression Vector Kit
pcDNA™ 1.2/V5-GW/lacZ control plasmid	Block-it™ Pol II miR RNAi Expression Vector Kit
pcDNA™ 6.2-GW/EmGFP-miR-neg control plasmid	Block-it™ Pol II miR RNAi Expression Vector Kit
SIN-PGK-cPPT-GDNF-WHV	Obtained from Prof. Mimoun Azzouz plasmid library at (SiTran).
SIN-CMV-EmGFP-miR	miR containing vector that is used in LV particle. Made by cloning “CMV-EmGFPmiR” fragment

	from pcDNA™6.2-GW/EmGFPmiR vector into SIN-PGK-cPPT-GDNF-WHV by using SpeI and XhoI restriction enzymes.
pMAX-green	Dr. Nassar plasmids library

2.1.13. Primers:

Primer name	Sequence (5' - 3')	Length [bp]	Details
EmGFP forward	ggcatggacgagctgtacaa	20	Sequencing (Block-it™ kit)
miRNA reverse	ctctagatcaaccactttgt	20	Sequencing (Block-it™ kit)
T7 forward	taatacgactcactataggg	20	Sequencing (UoS - Core genomic facility)
SP6 promoter	atttagtgacactatag	18	Sequencing (UoS - Core genomic facility)
mLC2-PCR17s	aaaggtaccaccatggctgatgagacacccccaca	36	cDNA synthesis by PCR to produce (LC2 deletion mutants), Figure 2.4, Sigma-Aldrich
mLC2-PCR18s	aaaggtaccaccatggctgaccccgaggggctcagc	36	
mLC2-PCR19s	aaaggtaccaccatggttgcatggctgaccccgag	36	
mLC2-PCR20s	aaaggtaccatgcctcctgtgtatgtggatcttgc	35	
mLC2-PCR21s	aaaggtaccatgcctcctgtgtatgtggatcttgcct	37	
mLC2-PCR12a	tttctcgaggaactcaatctgcaggctggaaag	34	
mLC2-PCR16a	tttctcgaggccagagctacccttgacccca	32	
mLC2-PCR15a	tttctcgagcaaacatccggctcggggaggggg	32	

2.1.14. MAP1A miRNA sequences:

Sequence_1	<i>tgctGTCCAATACCTGACTTCCTGCTGTTTTGGCCACTGACTGACAGCAGGAACAGGTATTGGA</i> <i>cagg</i>
Sequence_2	<i>tgctGAATCCTTCAAATCCGAGGCCCGTTTTGGCCACTGACTGACGGGCCTCGTTTTCAAGGATT</i> <i>cagg</i>
Sequence_3	<i>tgctGATTAGTACCATCATCCCAGTGGTTTTGGCCACTGACTGACCACTGGGAATGGTACTAAT</i> <i>cagg</i>
Sequence_4	<i>tgctGATCAGAATCTGATTGTGAGGAGTTTTGGCCACTGACTGACTCCTCACACAGATTCTGAT</i> <i>cagg</i>

2.1.15. Tools and labware:

Name	Supplier	Cat. no.
Calcium imaging perfusion chamber	Warner instruments	RC-25F
Cell scraper, 220 mm Long, 11 mm blade, Sterile	CytoOne	CC7600-0220
Cellview™ cell culture dish, PS, 35/10MM (Glass bottom, one compartment)	Greiner Bio-One GmbH	627861
Cover glass ø16 mm (0.13-0.17 mm thick)	Scientific Laboratory Supplies LTD	
Disposable Scalpels (Surgical steel blades)	Swann-Morton	0505
DNA LoBind Tube 1.5 mL	Eppendorf	0030108.051
Dumont #5 Forceps	Fine Science Tools, FST	15018-10
Glass homogenizer	Scientific limited	
Ground edges 90° frosted end slide	Thermo Scientific	BS7011/2
ImmEdge™ PEN	Vector Laboratories	H-4000
Luer-Lok syringes (50 mL)	Becton Dickinson (BD)	300865
Minisart® Syringe Filters (0.45 µm, Sartorius)	Appleton woods	25926

MP-8 Manifold	Warner instruments	64-0211
Portex Tubing ,30m non-sterile polythene tubing, [0.86 mm ID, 1.27 mm OD]	Fisher Scientific	800/110/260
SuperFrost® Plus Microscope Slide	VWR international	631-0108
Ultra-Clear centrifuge tubes (25X89 mm)	Beckman Coulter, Inc.	344058
VWR™ Pellet Mixer (pestle & mortar mixer)	VWR international	47747-370
Whatman™ Nitrocellulose membrane	GE Healthcare Life Sciences	10401196
X-ray Amersham Hyperfilm™ ECL film	GE Healthcare Life Sciences	28906835

2.1.16. Buffer, solution and medium recipes:

- **DRG enzyme digestion mixture**

1 X Collagenase XI,
1 X Dispase II,
DMEM/F-12 + Glutamax

- **Standard Extracellular Ringer Solution**

140 mM Sodium Chloride,
4 mM Potassium Chloride,
2 mM Calcium Chloride,
1 mM Magnesium Chloride,
10 mM HEPES,
pH = 7.4 at 25 °C, PH is adjusted with Sodium Hydroxide

- **High Potassium Ringer Solution**

104 mM Sodium Chloride,
40 mM Potassium Chloride,
2 mM Calcium Chloride,
1 mM Magnesium Chloride,

10 mM HEPES,
pH = 7.4 at 25 °C, PH is adjusted with Sodium Hydroxide

- **TAE Buffer (10 X)**

2 M Tris Base,
50 mM EDTA,
0.95 M Glacial acetic acid

- **Gel buffers**

- Resolving gel buffer – 1.5 M Tris-HCl, pH 8.8
- Stacking gel buffer – 0.5 M Tris-HCl, pH 6.8

- **TBS Buffer (10 X)**

200 mM Tris Base,
1.37 M Sodium Chloride,
PH = 7.4, PH is adjusted with HCl

- **Western Blot Running Buffer (10 X)**

250 mM Tris Base,
1.92 M Glycine,
1 % SDS

- **Western Blot Transfer Buffer (10 X)**

250 mM Tris Base,
1.92 M Glycine

- **Laemmli sample Buffer (4 X)**

250 mM Tris-HCl pH 6.8,
40 % Glycerol,
20 % β -mercaptoethanol,
8 % SDS,
1 % bromophenol blue

- **Blocking buffer for Western blot**
 - 5 % skim milk powder in TBS-0.1 % Tween-20 (TBST)
- **Buffer A (Blocking buffer for LC2 antibody in WB)**
 - 150 mM Sodium Chloride,
 - 0.25 % Tween-20,
 - 2 % BSA,
 - 1 X PBS
- **Blocking Solution for Immuno-fluorescence**
 - 2 % BSA,
 - 2 % Fish skin gelatin,
 - 0.1 % Tween-20,
 - 0.5 % Sodium Azide,
 - 2 % Normal goat serum,
 - 1 X PBS
- **HEPES Lysis Buffer**
 - 50 mM HEPES, pH 7.5,
 - 150 mM Sodium chloride,
 - 1.5 mM Magnesium chloride,
 - 1 mM EDTA,
 - 10 % Glycerol,
 - 1 % Triton X-100
 - 1 X Protease Cocktail Inhibitor
- **HEPES Wash Buffer (Immunoprecipitation)**
 - 50 mM HEPES, pH 7.5,
 - 150 mM Sodium chloride,
 - 1.5 mM Magnesium chloride,
 - 1 mM EDTA,
 - 0.1 % Triton X-100

10 % Glycerol,
1 X Protease Cocktail Inhibitor

- **SOB Medium**

2 % Tryptone,
1 % Yeast Extract,
2 mM Sodium Chloride,
0.7 mM Potassium Chloride,
1 mM Magnesium Chloride

- **LB – agar plates**

25 g LB broth
10 – 15 g Agar granules
Antibiotic (ampicillin 100 μ L/mL or spectinomycin 50 μ L/mL)
dH₂O up to 1 L,
Media was autoclaved before use, plates were stored at 4 °C.

2.2. METHODS:

CELL CULTURE RELATED METHODS:

2.2.1. Mouse dorsal root ganglia primary culture:

2.2.1.1. DRG isolation:

At the day of the dissection, the animal was first anesthetized with isoflurane and then humanly killed by cervical dislocation in accordance with Schedule 1 procedures of UK Animals (Scientific Procedures) Act 1986. The spinal column was then carefully cut off longitudinally and isolated out of the animal. Muscles were gently scraped off the bones. The bones were opened longitudinally into two hemi sections with a sharp scalpel to expose the spinal cord. Spinal cord was gently scraped off under the microscope to expose the DRGs. DRGs were then isolated one by one from the root and placed in a 35-mm dish containing ice-cold PBS.

2.2.1.2. DRG digestion:

PBS was replaced with 1 mL Dulbecco's Modified Eagle's Medium/F12 (DMEM/F12) with Glutamax medium containing Dispase (1 mg/mL) and Collagenase Type XI (0.6 mg/mL). DRGs were left for digestion for 60 min at 37 °C and 5 % CO₂.

2.2.1.3. DRG dissociation and culture preparation:

After incubation with the digestive enzyme mix, cells were triturated with P1000 pipette 10 times to ensure full dissociation of the tissue. Cell suspension was carefully layered on top of 15 % Bovine Serum Albumin in DMEM/F12 and centrifuged at 800 g [2000 rpm (rotor no. 4624/ Hettich Rotina 46R centrifuge)], for 10 min at room temperature with the minimum deceleration speed. The cell pellet was then washed in excess culture medium composed of DMEM/F12 plus 10 % Fetal Bovine Serum, 100 units/mL penicillin and 100 µg/mL streptomycin (Gibco). Cells were pelleted again, re-suspended in DRG culture medium and plated on glass coverslips coated with L-polyornithine (20 µg/mL). Cells were incubated at 37 °C / 5 % CO₂ for 24 h for recovery before experiments.

2.2.2. Mammalian cell lines:

2.2.2.1. Cell line types and culture media:

N2a-neuroblastoma, HeLa and HEK293 cells were maintained in DMEM-F12/Glutamax supplemented with 10 % Fetal Bovine Serum (FBS), 100 units/mL penicillin and 100 µg/mL streptomycin at 37°C in 5 % CO₂. SH-SY5Y neuroblastoma cells were maintained in medium that consists of 42 % F-12 + Glutamax, 42 % MEM + GlutaMax, 15 % heat inactivated FBS, 10 % MEM-NEAA. HEK-293 cells for lentivirus production and Caco-2 cells for immunofluorescence experiments were maintained in DMEM with 4.5 g/L glucose, L-glutamine, without Na Pyruvate) supplemented with 10 % FBS and 1 % penicillin/Streptomycin.

2.2.2.2. Cell line sub-culturing:

When 80 % cell confluency was reached, cells were washed twice with PBS and then incubated with Trypsin EDTA (0.05 % in PBS) at a sufficient volume that covered the cells for 3 min at 37 °C. Flasks were gently tapped to speed up cells detachment and frequently checked under the microscope to avoid over-trypsinization. Cells were collected in the standard culture medium, to inactivate trypsin, and pelleted at RT. Cell pellet was re-suspended in culture medium and re-seeded at the desired passage ratio in a new flask (1:10 ratio for N2a, Hela and HEK293 cell lines, 1:5 ratio for SH-SY5Y cell line and 1:5 Caco-2 cell line).

2.2.3. Cell line DNA transfection:

One day prior to transfection, cells were counted and seeded at the same cell densities recommended by Invitrogen (cell culture protocols - useful numbers for cell culture) – Table 2.1. The desired volume of DNA and PEI were diluted separately in Opti-MEM® - Reduced Serum Medium (usually at 1:3 ratio, but large DNA constructs (e.g. Scn9a-GFP overexpression constructs) needs higher ratio 1:7. DNA concentration is optimized per construct but it is usually between 1 – 2 µg / mL, Table 2.2. Diluted PEI was added to the DNA, the DNA-PEI mixture was left to stand for 10 min at RT. Culture medium in the wells was replaced with a fresh serum free and antibiotic free medium. DNA-PEI mixture was then added to each well and left for 6 h at 37 °C incubator. DNA-

PEI containing medium was replaced with a fresh DMEM/F12-Glutamax medium supplemented with 10 % FBS and 1 % Penicillin/Streptomycin. Cells were then processed after 48 h for overexpression experiments or 96 h for KD experiments.

Table 2.1: Mammalian cell line seeding density. Numbers are adopted from Invitrogen cell culture protocols - useful numbers for cell culture.

[<https://www.thermofisher.com/uk/en/home/references/gibco-cell-culture-basics/cell-culture-protocols/cell-culture-useful-numbers.html>]

	Surface area (cm ²)	Seeding density	Cells at confluency	Growth medium (mL)
Dishes				
35 mm	9	0.3 X 10 ⁶	1.2 X 10 ⁶	2
60 mm	21	0.8 X 10 ⁶	3.2 X 10 ⁶	3
100 mm	55	2.2 X 10 ⁶	8.8 X 10 ⁶	10
150 mm	152	5 X 10 ⁶	20 X 10 ⁶	20
Culture plates				
6-well	9	0.3 X 10 ⁶	1.2 X 10 ⁶	3-5
12-well	4	0.1 X 10 ⁶	0.4 X 10 ⁶	1-2
24-well	2	0.05 X 10 ⁶	0.2 X 10 ⁶	0.5-1
Flasks				
T-25	25	0.7 X 10 ⁶	2.8 X 10 ⁶	3-5
T-75	75	2.1 X 10 ⁶	8.4 X 10 ⁶	8-15
T-160	162	4.6 X 10 ⁶	18.4 X 10 ⁶	15-30

Table 2.2: The concentration of DNA ($\mu\text{g}/\text{mL}$) of different constructs used in transfection experiments

DNA construct	Concentration ($\mu\text{g} / \text{mL}$)
MAP1A miR sequence 1 to 4	1.6
MAP1A miR chained sequences	1.2
Full length LC2-myc	2
LC2-myc deletion constructs	1

2.2.4. DRG neuron LV transduction:

DRG neurons were counted before the final seeding step using hemocytometer. The desired number of neurons (> 1200 neurons) were seeded per well and left to recover at 37 °C incubator for 24 h. At the day of transduction, the required volume of LV virus for the desired multiplicity of infection (MOI) was calculated according to the formula:

$$MOI = \frac{\text{Volume of LV (mL)} \times \text{LV Titre}}{\text{Number of cells}}$$

and added to a serum free / antibiotic free culture medium. DRG culture medium was then replaced with virus containing medium and left at 37 °C for 6 h. Next, the virus containing medium was replaced with a fresh DMEM/F-12 –Glutamax medium supplemented with B27 (1X) and 0.5 ng/mL NGF. At day 5 or 6 post-transduction, culture was used for experiment. Cultures were closely observed during the incubation period, and culture medium were replenished and topped up when needed.

PROTEIN RELATED METHODS:

2.2.5. Western blot:

2.2.5.1. Sample lysis and protein extraction:

DRG from all spinal levels were collected in ice-cold PBS. Once the collection was over, DRGs were pelleted and PBS was replaced with 500-700 µL of the desired lysis buffer (ice-cold) supplemented with protease inhibitor cocktail (PIC,1X). In case of cultured cells, cells were first washed twice with ice-cold PBS then ice-cold lysis buffer plus PIC was added directly to the cells. The volume of the lysis buffer used varied according to the flask/dish size as in Table 2.3. Cells were detached using a cell scraper. DRGs or cell suspensions were homogenized with an electric or manual homogenizer for 1- 2 min on ice. The suspension was incubated for 60 min at 4 °C with continuous rotation. During the incubation period, DRGs or cell suspension was vortexed for 1 min every 15 min to increase the lysis efficiency. Soluble protein lysate was then collected into new Eppendorf tubes after centrifugation at 130000 rpm (Micro Centaur MSE, UK), 4 °C for 15 min. The pellet of the insoluble fraction was usually discarded but sometimes were kept for further analysis by western blot to determine the efficiency of extraction for the desired protein.

Table 2.3: Lysis buffer volumes used for sample lysis and protein extraction in different experiments.

Well size	Type	Lysis buffer volume (μL)
12-well plate	Cell lines	50
35 mm Dish	Cell lines	150
60 mm Dish	Cell lines	200 - 250
	DRG culture	depending on the number of wells per culture. e.g. All DRGs from one animal cultured in one dish = 150 μL .
	DRG tissue	200 – 500 μL depending on the type of the experiment and the strength of lysis buffer used.

2.2.5.2. Protein quantification:

Protein concentration was measured by Bradford protein assay according to the manufacturer instructions. Samples lysed in RIPA buffer were measured with BCA protein assay according to the manufacturer instructions. Blank, BSA control and sample absorbance were measured by a spectrophotometer at 595 nm absorption wavelength.

2.2.5.3. Sample preparation:

Proteins were reduced and denatured by mixing the desired volume of sample with the required volume of Laemmli buffer (4X) to make 1x final concentration. Samples were then heated at 95 °C for 5 min or at 37 °C for 30 min if Nav1.7 protein detection is required. Samples were either loaded directly into SDS-PAGE acrylamide gel or stored at -20 C for later use.

2.2.5.4. SDS-PAGE sample loading and running:

Samples were loaded into SDS-polyacrylamide gel that consist of a resolving layer (varied acrylamide concentration) and a stacking layer (4 % acrylamide concentration). Both layers contained fixed volumes of gel buffer, SDS, APS and TMED but differed in the acrylamide and water ratios as shown in Table 2.4, (adopted from Bio-Rad protocols / per 10 mL). The desired sample volumes were loaded carefully with gel-loading tips to avoid over-spillage to neighbouring wells. Sample running through the

SDS-PAGE gel usually started at low power (75 V) and increased later (100 – 120 V) once the samples migrate through the resolving layer.

Table 2.4: SDS-PAGE recipe (Bio-Rad protocols)

Percent gel (%)	dH ₂ O (mL)	30 % Degassed Acrylamide/Bis (mL)	Gel buffer (mL)	10 % w/v SDS (mL)	10 % APS (μL)	TEMED (μL)
4	6.1	1.3	2.5	0.1	50	5
6	5.4	2	2.5	0.1	50	10
8	4.7	2.7	2.5	0.1	50	10
10	4.1	3.3	2.5	0.1	50	10
12	3.4	4	2.5	0.1	50	10
15	2.4	5	2.5	0.1	50	10

2.2.5.5. Transfer:

Migrated protein on the SDS-PAGE gel was then transferred to nitrocellulose membrane (0.45 μm) overnight at 4 °C / 20 V for large size proteins (> 50 KD) or for 90 min / RT / 250 A for smaller proteins (< 50 KD). Transfer buffer supplemented with 10 % or 20 % methanol was used for large and small molecular weight proteins, respectively.

2.2.5.6. Blocking and primary antibody incubation:

Membranes then were blocked with 5 % non-fat milk in TBS-0.1 % Tween (TBST) buffer for 1 h at RT with continuous rotation. Antibodies were added to 1 – 2 mL of the blocking buffer at the recommended dilution. Membranes were incubated with the primary antibody in small plastic pouch overnight at 4 °C with continuous rotation. In case of LC2 protein detection, membranes were blocked and incubated with the LC2 polyclonal antibody using a different blocking buffer (Buffer A) prepared as detailed in section 2.1.16.

2.2.5.7. Protein signal revelation:

Membranes were washed 3 times, 10 min each, with TBST buffer. Secondary antibodies were added to the appropriate blocking buffer at 1:2000 dilution for HRP conjugated or at 1:10000 for fluorescently tagged secondary antibodies. Membranes

were incubated for 1 h at RT with continuous rotation, washed 3 times / 10 min each with TBST buffer and processed to membrane development for HRP-conjugated antibodies or left to dry in the dark for the fluorescently tagged secondary antibodies. For protein band revelation, Pierce™ ECL Western Blotting Substrate and X-ray films were used for HRP-conjugated secondary antibody according to the manufacturer instructions. Odyssey Sa® infrared imaging system from LI-COR was used for the fluorescently tagged secondary antibodies.

2.2.6. Co-immunoprecipitation (co-IP):

Sample lysate was prepared with 0.3 to 1 % Triton HEPES buffer containing PIC as described earlier. 100 µL Sepharose beads per sample were washed with ice-cold washing buffer (0.1 % Triton HEPES buffer) and then centrifuged at 1000 rpm/ 30 sec / RT. Washing process was repeated 3 times. Protein samples were precleared by incubation with the washed Sepharose beads for 1 h at 4 °C with continuous rotation. Samples were then centrifuged at 1000 rpm / 30 sec / RT and left to stand for an extra 1 – 2 minutes on ice for a complete sedimentation of the beads by gravity. The cleared protein sample was then transferred into a new Eppendorf tube. Pellet was usually discarded, but sometimes was saved for further analysis by WB to ensure that the desired proteins were not non-specifically bound to the Sepharose beads. 10 – 20 % of the sample was saved as an input control. The rest was equally divided into two equal volumes; one was incubated with 100 µL monoclonal Nav1.7 antibody and the other half was incubated with 1.5 µL (1 mg/mL) monoclonal IgG antibody. Both tubes were topped up to 1 mL with the same lysis buffer + PIC used for each experiment. Samples were incubated with the antibodies overnight at 4 °C with continuous end to end rotation. Two tubes containing 25 µL G-protein linked Sepharose beads were washed three times as described earlier. Samples were then added to G-protein beads and incubated for 4 h at 4 °C with continuous end-to-end rotation. Samples were then washed with washing buffer and pelleted by both centrifugation and gravity as described earlier, the washing step was repeated 5 times to ensure complete removal of the supernatant (unbound protein fraction). Protein bound to the beads was then eluted by mixing each pellet with 50 µL of 2X Laemmli buffer containing 100 µM DDT. Samples were then heated at 37 °C for 30 min, centrifuged and loaded (without the

beads) into SDS-PAGE gel for protein detection by WB as described under section 2.2.5.

2.2.7. Cell surface biotinylation:

Cells were seeded in 60 mm dish at the recommended seeding density, Table 2.1. When the cells reached 80 % confluency, they were washed once with ice-cold PBS provided by the Pierce® Cell Surface Protein Isolation kit, and then incubated with 2 mL of solubilized EZ-Link Sulfo-NHSSS-Biotin (0.5 mg / mL) made in ice-cold PBS (Pierce® Cell Surface Protein Isolation kit) for 45 min on ice at 4 °C. Cells were then washed once with ice-cold PBS and then with 200 mM glycine in PBS for 5 min / 3 times / 4 °C / on ice to quench and inactivate the unbound biotin, followed by washing with ice-cold PBS twice. Dishes were briefly left on ice at a slanted position to remove excess PBS before cell lysis. 200 µL of HEPES lysis buffer (1 % Triton X-100) plus PIC was added to the dish. Cell lysate was collected with the aid of cell scrapers and processed as described earlier under sample lysis (2.2.5.1) and protein quantification (2.2.5.2) sections. 10 – 20 % of the sample was saved as an input control, the rest was incubated with 50 µL of NeutrAvidin agarose beads per sample for 1 hour at 4 °C under continuous rotation. Samples were washed 5 times with washing buffer HEPES buffer (0.1 % Triton-X100) at 1000 rpm/ 30 sec / RT and left to stand for 1 - 2 min on ice to allow full sedimentation of the beads by gravity. Beads were resuspended in 50 µL of 2X Laemmli buffer containing 100 mM DDT, heated at 37 °C for 30 min, centrifuged and loaded (without the beads) into SDS-PAGE gel for protein detection by WB as described under section 2.2.5.

2.2.8. Immunofluorescence (IF):

2.2.8.1. Immunocytochemistry (ICC):

Cells were seeded at the desired seeding density on L-polyornithine coated coverslips. At the day of the experiment, cells were placed on ice and washed twice with ice-cold PBS. Cells were then fixed with either 4 % paraformaldehyde (PFA) solution for 10 – 15 min on ice or with cold 100 % methanol for 10 min at – 20 °C. Fixative solution then was removed and washed twice with excessive PBS. PFA fixed cells were quenched with 50 mM ammonium chloride in PBS solution for 20 min to inactivate and quench

residual PFA and reduce PFA background fluorescence, followed by excessive PBS washing and permeabilization with 0.1 % Triton-X100 PBS three times, 10 min each. Next, cells were blocked with a blocking buffer (section 2.1.16) for 1 h. Methanol fixes and permeabilizes the cells at the same time, so the previous few steps were skipped in case of methanol fixation, and cells were immediately blocked with the blocking buffer after washing out methanol. Labelling solution of the desired primary antibodies was made in the blocking buffer at the recommended dilution. Blocking buffer was removed and replaced with 300 – 700 μ L of labelling solution (according to the well size) and incubated overnight at RT. Next, cells were washed three times, 10 min each with PBS solution, and incubated for 1 h at RT in the dark with a mixture of secondary antibodies (1:2000) and DAPI (1:5000) in blocking solution. Cells were washed three times, 10 min each with PBS. During the washing period, slides were cleaned with tissues and appropriately labelled. Cells were finally washed with dH₂O to remove residual salt precipitation from PBS and mounted on the slides with ProLong®Gold mounting medium. Slides were kept in the dark at RT to dry for one day, then saved at 4 °C until being imaged.

2.2.8.2. Immunohistochemistry (IHC):

2.2.8.2.1. Cryo-sectioning:

One to three DRGs were fully embedded in OCT blocks and allowed to snap freeze on dry ice. Blocks were sectioned in a cryostat (Bright Instrument, OTF5000, Huntingdon, UK) at 10 μ m. The cryostat was set up at -20 °C at the specimen area and -15°C at the chamber. Sections were collected on a pre-coated glass slides, air-dried at RT for 30 min and then stored at -20 °C.

2.2.8.2.2. Immuno-labelling:

Specimen slides were thawed down at RT for 10 to 20 min, then immersed in PBS to rehydrate the tissues for 10 min. The tissues were surrounded with a hydrophobic barrier using the barrier pen, then fixed with 4 % PFA for 10 min. Specimen slides were then washed and permeabilized with 0.1 % Triton-X100 PBS three times / 10 min each and blocked with blocking buffer for 1 h. Specimen slides were then incubated with blocking buffer containing the desired dilution of primary antibodies for 3 h or overnight depending on the antibody used. A thin layer of parafilm was placed

on top of the specimen to prevent dehydration during antibody incubation and to ensure homogenous distribution of the antibody mixture throughout the DRG section. Next, the slides were washed three times / 10 min each with 0.1 % Triton-X100 PBS and incubated with secondary antibodies and DAPI in blocking buffer for 45 min in the dark. After the incubation time, the slides were washed three times / 10 min each with 0.1 % Triton-X100 PBS and mounted with glass coverslips using ProLong®Gold mounting medium, left to dry overnight at RT in the dark and then processed to microscopy and stored at 4 °C.

NUCLEIC ACID RELATED METHODS:

2.2.9. Plasmid preparation:

2.2.9.1. Bacterial transformation:

50 - 100 µL of competent bacterial cells (section 2.1.3) were transformed with the DNA plasmid by heat shock at (42 °C / 45 s) to disrupt bacterial membrane and allow DNA uptake, followed by an immediate cooling to retain the plasmid inside the bacteria (tubes were placed on ice / 2 min). Transformed bacteria were then allowed to recover in 1 mL SOB medium for 1 h at the 37 °C in the shaking incubator (230 rpm). The entire 1 mL (ligation reaction) or a small fraction (10 % - in case of plasmid amplification) was spread on LB agar plate + antibiotic specific for the plasmid in use (ampicillin 100 µg/mL or spectinomycin 50 µg/mL) for overnight at 37 °C.

2.2.9.2. Amplification, isolation and purification of plasmid DNA:

One single bacterial colony was inoculated into 2 mL (mini-prep), 20 mL (medi-prep), 50 mL (maxi-prep), 250 mL (mega-prep) of TB medium containing the plasmid specific antibiotic at the recommended concentration. Culture was incubated in the shaking incubator overnight (37 °C / 220 rpm). DNA was then isolated and purified according to the protocol provided by each kit.

2.2.9.3. Qualitative and quantitative DNA analysis:

Quantity and purity of the purified DNA was usually assessed by NanoDrop Lite Spectrophotometer (Thermo Scientific). The ratio of absorbance at 260 nm and 280 nm ($A_{260}/A_{280} = \sim 1.8$) was used as an estimation of the purity of the DNA preparation.

In addition, the quality of the DNA samples was also determined by agarose gel electrophoresis after DNA digestion with specific restriction enzymes (section 2.2.10.1). Finally, DNA samples were sent to the core genomic facility at the university of Sheffield for sequencing.

2.2.10. Molecular cloning:

2.2.10.1. Restriction enzyme digestion and gel electrophoresis:

Single digestion is used to linearize the plasmid, while double digestion is used for cloning and sub-cloning. DNA constructs (plasmid vectors and PCR products) were mixed with specific endonuclease enzymes with the appropriate buffer at an optimized temperature condition for cloning purposes. Serial Cloner software was utilized to identify all the possible digestion sites for several restriction enzymes. Selected enzymes were then used to digest the DNA constructs as predicted by the software. For cloning, two DNA constructs (backbone and insert) were usually treated with the same enzyme mixture to produce adhesive ends that can be ligated afterwards (section 2.2.10.2) to produce a new DNA construct. In addition, restriction enzyme digestion was also used as a quick quality check for DNA constructs by subsequent analysis of the product size on gel-electrophoresis. Double Digest Finder by NEB, an online tool, <https://www.neb.com/tools-and-resources/interactive-tools/double-digest-finder> was used to predict the optimal conditions for the double digest reaction: enzyme compatibility, buffer selection, temperature conditions and any required supplements to optimize the reaction. The enzyme concentration was calculated as every 1 enzyme unit digests 1 µg DNA in 1 h. Typically, the digestion reaction was carried on in a 50 µL total volume; the volume of the individual components (dH₂O, BSA, and buffers) were calculated accordingly. To prevent vector self-ligation after digestion and to increase the ligation efficiency with the recombinant DNA insert, linearized vectors (backbone) were treated with Antarctic phosphatase enzyme (ACP) and ACP buffer for 30 min at 37 °C to dephosphorylate the 5' phosphate end which is essential for self-ligation. Digested DNA fragments were analysed by agarose-gel electrophoresis. Agarose was dissolved in 1 X TEA buffer at different concentrations according to the molecular size of the DNA fragments (0.5 – 1 %). Syber®safe (1:10000) was used to bind to DNA fragments. Gel Doc™ EZ system was used for DNA revelation.

2.2.10.2. DNA ligation:

After gel-electrophoresis, backbone and insert fragments were isolated from the agarose gel and purified by Qiaex II® Gel Extraction kit according to the manufacturer instructions. Ligation of the purified dephosphorylated vector and DNA insert molecule was performed with T4-ligase enzyme for 4 h at 25 °C or overnight at 16 °C. For 1:1 ratio of vector to insert, the following formula was used:

$$\text{ng of insert for 1:1 ratio} = \text{ng of vector} \times \frac{\text{length of insert (Kb)}}{\text{length of vector (Kb)}}$$

A 1:5 ratio (vector: insert) was usually chosen to increase the ligation efficiency. The ligation reaction was usually carried out in a 20 µL total volume; the volume of T4 ligase buffer and dH₂O were calculated accordingly.

2.2.11. MAP1A miRNA preparation:

2.2.11.1. Design and structure of MAP1A pre-miRNA sequences:

MAP1A miRNA oligonucleotide sequences (mature miRNA) were designed by the use of Invitrogen RNAi designer, an online tool that helps to design a pre-miRNA sequences for the target gene. (www.invitrogen.com/rnai). MAP1A accession gene number used was (NM_001173506). The online software produced multiple design outputs that were scored according to the predicted knock-down efficiency of the target gene (five stars being the highest predicted KD efficiency). The sequences were then carefully checked with NCBI blast to identify any potential off-target effect. Four sequences (with high star-scoring and no off-target effect in mus musculus species) were selected for miRNA design, Fig. 2.1, section 2.1.14. Once selected, the software engineered a pre-miRNA sequences that targets the gene of interest. The pre-miRNA design is based on the murine miR-155 sequence but optimized by the supplier to achieve higher KD efficiency. The structure of the designed pre-miRNA is demonstrated in Fig. 2.2.

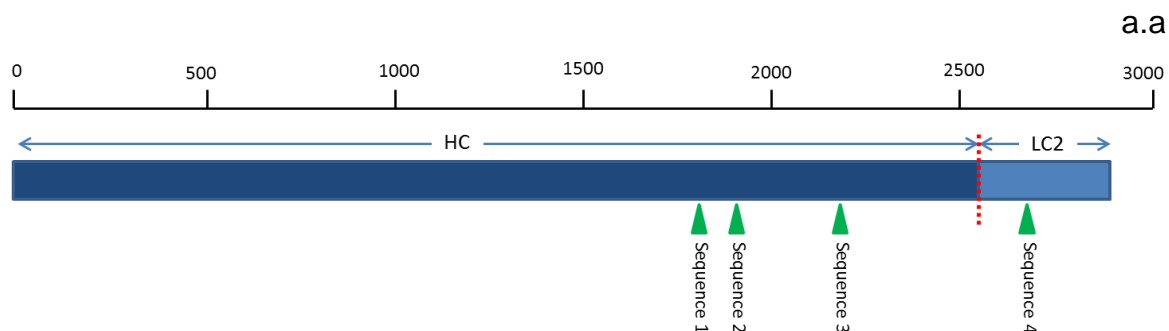


Figure 2.1: Representation of the sites where each of the four MAP1A miRNA sequences targets. 3 of the designed miRNA sequences target the heavy chain region, and only sequence 4 targets the light chain (LC2) region.



Figure 2.2: The structure of the designed pre-miRNA. Source: Invitrogen™, catalog nos. K4935-00 to K4938-00.

2.2.11.2. Cloning MAP1A pre-miRNA sequence into BLOCK-iT™ Pol II miR RNAi expression vector:

Cloning of the four selected sequences into pcDNA™ 6.2-GW/EmGFP-miR vector was performed according to the manufacturer instructions. An experimental outline is demonstrated in Figure 2.3. Bacterial transformation, DNA isolation, quantification, sequencing and amplification was performed as described under section (2.2.9).

2.2.11.3. Chaining of miRNAs:

Multiple miRNAs can be expressed as one long primary transcript driven by RNAPoll, the pre-miRNA transcript is processed later on in the cell ²⁴². The BLOCK-iT vector allows for chaining two miRNAs (co-cistronic expression) to produce one primary transcript that consists of two pre-miRNAs to increase KD efficiency with less transfection variabilities. MAP1A miRNA-sequence 2 (backbone) was chained to the rest of three sequences: 1, 3 and 4 (inserts) as demonstrated in Fig. 2.4. The backbone and insert vector were sequentially digested; first with SmaI followed by a second digestion of the backbone and insert with BglII and BamHI-HF restriction enzymes, respectively, as described under section (2.2.10). The two digested DNA fragments (backbone: 4459 bp) and (insert: 1318 bp) were then ligated, transformed into

bacteria, and followed by DNA isolation, quantification, sequencing and amplification as described under sections (2.2.9 and 2.2.10).

Flow Chart

The figure below illustrates the major steps necessary to produce a pcDNA™ 6.2-GW/miR or pcDNA™ 6.2-GW/EmGFP-miR expression clone using the BLOCK-iT™ Pol II miR RNAi Expression Vector Kits.

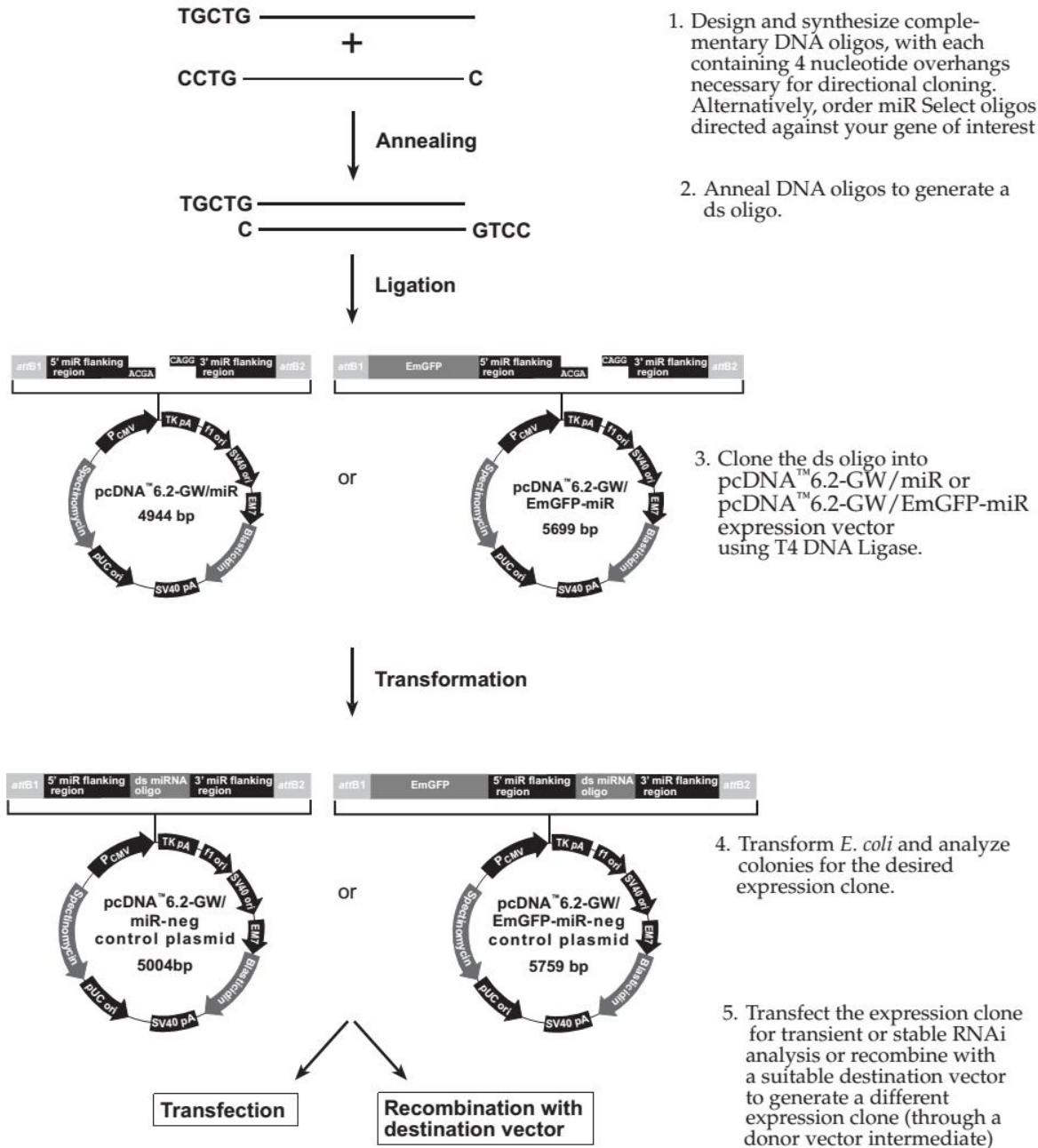


Figure 2.3: An illustration the steps required to produce pcDNA™ 6.2-GW/EmGFP-miR expression clone as recommended by the manufacturer. Source: Invitrogen™, catalog nos. K4935-00 to K4938-00.

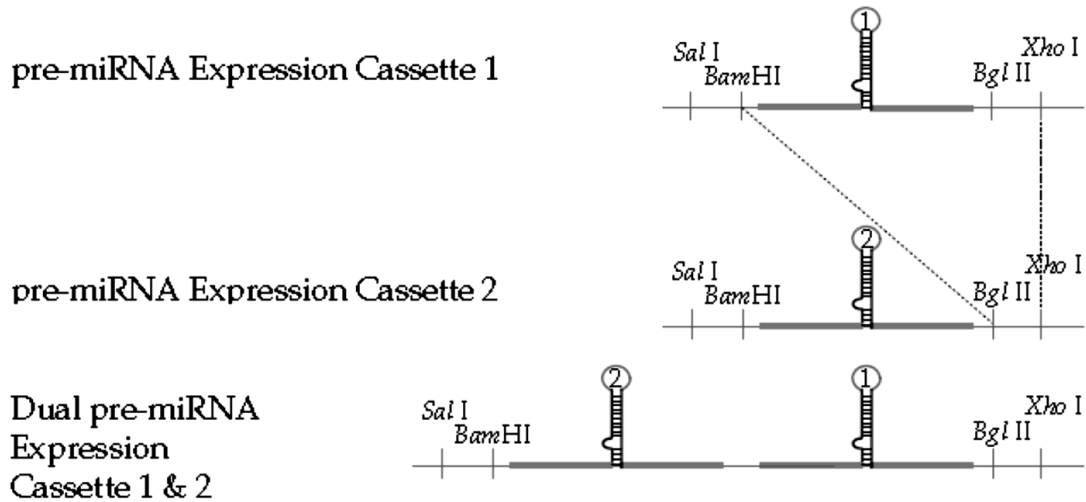


Figure 2.4: An illustration of the steps required to chain two miRNAs into one expression vector. In this example, miRNA sequence 1 is being sub-cloned into miRNA sequence 2 (backbone) using the restriction sites demonstrated in the figure as recommended by the manufacturer. Source: Invitrogen™, catalog nos. K4935-00 to K4938-00.

2.2.12. Production of LC2-myc (full length and deletion constructs):

2.2.12.1. Primers:

Sense and antisense primers were designed (by Dr. Nassar) using Serial cloner software to bind different regions of the LC2 protein. LC2 cDNA sequence published in Langkopf et al., 1992¹⁸⁶ was used as guide for the different regions in the LC2 protein (Tubulin-binding domain and actin-binding domain).

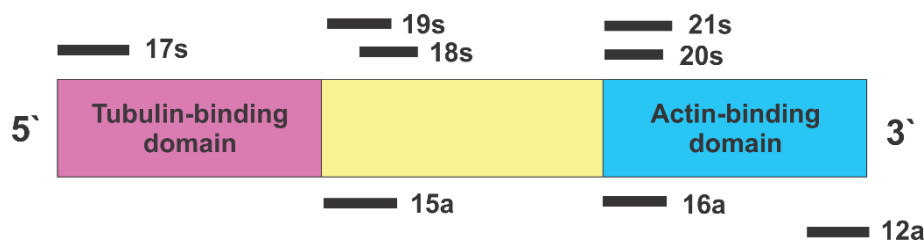


Figure 2.5: Schematic representation of the primer positions on MAP1A-light chain (LC2). LC2 (300 amino acids) consists mainly of three major areas: Tubulin-binding domain on the N-terminus, Actin-binding domain on the C-terminus and a middle area with unknown functional features. Primers were given numbers for identification. "s" indicates (sense, forward primer), "a" indicates (anti-sense, reverse primer).

2.2.12.2. Polymerase Chain Reaction (PCR):

RNA was extracted from mouse DRGs using Direct-zol™ RNA Miniprep kit and then converted into cDNA by RT-PCR using High Capacity cDNA Reverse Transcription Kit (Applied Biosystems) with random hexamers, (these two steps were performed according to the manufacturer instruction and were carried out by Dr. Nassar). Different regions of the LC2 gene were amplified by PCR using Go Taq polymerase in a mixture of mouse DRG cDNA library (template), primers (listed in section 2.1.13), dNTP and buffers as demonstrated in Table 2.5.

First step in the reaction was the initial denaturation (94 °C for 2 min), followed by 35 cycles of: denaturation (94 °C / 30 s), annealing ($T_m - 3$ °C / 30 s), and elongation (72 °C / 1 min) and a final extension step (72 °C / 5 min). The optimized annealing temperature for each pair of primers is listed in Table 2.6.

Table 2.5: Description of the PCR mixture components

PCR component	Amount
5 X green buffer (+MgCl ₂)	5 µL
5 mM dNTPs	1 µL
Primer 1: Sense primer (10 µM)	1 µL
Primer 2: Anti-sense primer (10 µM)	1 µL
Go Taq polymerase enzyme	0.125 µL
cDNA template (mouse DRG cDNA library)	1 µL
dH ₂ O	16 µL
Total reaction volume	25 µL

Table 2.6: Optimized annealing temperature used for different primer pairs

Primer pairs	Annealing temperature (°C)
17 s – 12 a	63
19 s – 12 a	65
18 s – 12 a	65
20 s – 12 a	61
21 s – 12 a	61
17 s – 16 a	70
19 s – 16 a	63
18 s – 16 a	65

Next, PCR products were separated on agarose gel by electrophoresis, isolated and purified by Qiaex II® Gel Extraction kit according to the manufacturer instructions. DNA concentration was measured by NanoDrop Lite Spectrophotometer (Thermo Fisher), followed by insertion into pcDNA3-myc tag plasmid as described in section 2.2.10 and transformed into competent bacteria for mini and medi-preparation as described in section 2.2.9.

LENTIVIRUS RELATED METHODS:

2.2.13. Production of lentivirus particles:

2.2.13.1. Preparation of LV DNA constructs:

Bacterial stocks of LV packaging system (pCMVΔ8.92, pRSV-Rev) and envelope element (pMD.G) were kindly provided by Prof. Azzouz group at SiTran. 500 mL of TB growth medium was inoculated for each construct and incubated overnight at 37 °C with continuous shaking at 220 rpm. Next day, bacterial lysis, DNA extraction and purification was carried out using Mega-kit Plasmid Plus (Qiagen) according the manufacturer instructions.

2.2.13.2. Sub-cloning of miRNA cassette into lentivirus vector:

Lentivirus vector plasmid (SIN-PGK-cPPT-GDNF-WHV) was a kind gift from Prof. Azzouz (SiTran). Both pcDNA™6.2-GW/EmGFP-miR and SIN-PGK-cPPT-GDNF-WHV vectors were digested with SpeI and XhoI restriction enzymes (as described under in section 2.2.10) to isolate CMV+EmGFP+miR from the block-it kit vector and transfer it to the SIN-PGK-cPPT-GDNF-WHV by replacing PGK promoter with CMV in the new LV vector. Plasmid was transformed into competent DH5α, isolated, purified and sequenced as described under section 2.2.9.

2.2.13.3. Seeding HEK-293 cells for transfection:

Freshly thawed HEK-293 cells were used for every LV batch production. Cells were seeded into 20 petri dishes (10 cm) at 3×10^6 cells per dish. Cells were incubated for 24 h at 37 °C / 5 % CO₂ incubator. Cells were incubated with DMEM full medium (DMEM with 4.5 g / L glucose, L-glutamine, without Na Pyruvate) supplemented with 10 % FBS and 1 % penicillin / Streptomycin.

2.2.13.4. DNA transfection of HEK-293 cells:

Calcium phosphate method is used for transfection. A mixture of the four plasmids at the specified concentration (pCMV Δ 8.92 (260 μ g), pRSV-Rev (60 μ g), pMD.G (75 μ g) and SIN-CMV-EmGFP-miR (260 μ g)) were mixed together in a falcon tube and topped up with dH₂O to 5 mL. 5 mL of 0.5 M CaCl₂ was added to the DNA mixture drop-wise and thoroughly mixed. CaCl₂-DNA mixture then added drop-wise to 10 mL of warm, air-bubbled 2X HBS buffer. The mixture was left to stand for 10 min at RT to form DNA / calcium phosphate co-precipitate (solution becomes cloudy). 1 mL of the DNA complex was added drop-wise to each plate of HEK-293 cells (20 mL for 20 dishes). Cells were incubated for 6 h, medium was then replaced with a fresh DMEM full medium supplemented with 10 % FBS and 1 % Penicillin / Streptomycin. Cells were incubated for 48 h to allow for the cells to produce the LV particles.

2.2.13.5. Harvesting lentivirus particles:

Medium was carefully collected from HEK-293 dishes, filtered with 0.45 filters and spun down with Beckman coulter ultracentrifuge (SW28 Ti Rotor) at 19000 rpm/ 4 °C for 90 min. At the end of the centrifugation step, a pale pellet of concentrated LV particles was formed at the bottom of each tube. Each pellet was gently resuspended in 300 μ L of 1 % BSA in PBS buffer and left to dissolve for 1 h on ice. LV suspensions from all tubes were combined, aliquoted into 50 μ L volume and stored at -80 °C.

2.2.13.6. Lentivirus titre measurement:

A 12-well plate of HeLa cells was seeded at 75000 cell per well in DMEM/F12-Glutamax culture medium supplemented with 10 % FBS and 1 % Penicillin / Streptomycin antibiotic one day prior to LV transduction. At the day of transduction, one well was used to count the number of cells which is essential for titre calculation later on. The rest of the cells were transduced with a serial dilution of the LV virus (1:100, 1:1000 and 1:10000) in duplicates, some wells were left un-transduced to be used as negative control. Cells were incubated with the virus for 6 h, medium was then replaced with a fresh culture medium and incubated for 48 h at 37 °C / 5 % CO₂. Cells were washed with PBS, trypsinized (250 μ L 1X Trypsin/EDTA), collected in Eppendorf tubes with excess complete culture medium (750 μ L) to stop trypsin activity and pelleted at 2000 rpm for 5 min. Medium was removed and the cell pellets were fixed with 200 μ L of 4 % PFA for 15 min at RT. Cells were pelleted again, PFA was removed

and pellets were re-suspended in 200 μ L PBS. Samples were stored at 4 °C until processed by FACS. Samples were analysed by LSRII machine at the university of Sheffield flow-cytometry core-facility. Untransduced samples were used as negative control for adjusting the background autofluorescence. The gate threshold was set according to both the negative control as well as to the highly transduced samples (high GFP signal). Vector titre is then estimated by the following formula:

$$\text{Vector Titre (TU/mL)} = \% \text{ positive cells} \times \text{no. of cells at the transduction day} \times \text{dilution factor} \times 2$$

To avoid underestimation of the vector titre, it is recommended to use the dilution that give 1 – 20 % positive cells (by assuming in this case that there is only one viral particle per cell). LV titre measurement was repeated every time a new LV batch was produced. Multiplicity of infection into DRG was calculated based on LV titre as described in section 2.2.4.

FUNCTIONAL ASSAY:

2.2.14. Calcium Imaging:

2.2.14.1. Seeding cells for calcium imaging experiment:

DRG culture for calcium imaging were prepared as described under section 2.2.1. However, for calcium imaging experiments, DRG pellet in the final step were resuspended in 60 – 120 μ L culture medium and were seeded on L-polyornithine coated 16 mm coverslips as one small drop (5 – 10 μ L) in the centre of the coverslip. Cells were left to adhere for 1 h at 37 °C / 5 % CO₂ incubator and gently flooded by DRG culture medium. Cells were incubated for 24 h before any intervention (e.g. Fura-2AM loading and LV transduction).

2.2.14.2. Cell loading with Fura-2AM calcium dye:

Fura-2AM (2 μ M) was prepared by diluting Fura-2AM stock (1 μ L) into 1 mL standard extracellular solution. The solution was vigorously mixed in the dark by P1000 pipette to ensure sufficient solubilisation of the dye into the aqueous solution. Culture medium were aspirated, cells were washed with standard extracellular solution once, and then

incubated with Fura-2AM in extracellular solution for 30 min at 37 °C and 5 % CO₂. Fura-2AM dye was then washed with 1 mL standard extracellular solution and incubated to recover for 15 min in the 37 °C incubator followed by another 15 min at RT to allow for temperature adaptation.

2.2.14.3. Experimental set-up and image acquisition:

Coverslips were mounted onto the recording chamber (RC-25F, Warner instruments) and placed on top of an inverted microscope (Olympus, IMT-2) fitted with a 40 X oil immersion objective (Olympus, 160/-, DPlanApo40UVPL). The coverslip was scanned to find a good field of view (good number of single cells at the centre of the coverslip) and ROI for each cell and for the background were selected using Simple PCI 6 software. Cells were alternatively excited with 350 and 380 nm at 1.6 s intervals for a ratiometric measurement of intracellular calcium using Cairn Dual OptoLED system. Images were acquired using a Hamamatsu C4742-95 camera. The cells were superfused with standard extracellular solution for at least 5 min to establish stable baseline. All recordings were performed at room temperature (23 + 1 °C). Drugs were superfused in a laminar flow manner by gravity-fed system at a flow rate of 3 mL/min. High potassium extracellular solution (104 mM NaCl, 40 mM KCl, 2 mM CaCl₂, 10 mM HEPES, 5 mM glucose, pH = 7.4 with NaOH) was superfused at the end of the recordings, unless mentioned otherwise, as a depolarizing agent to identify viable neurons. Simple PCI 6 software was used for data acquisition, background subtraction and Fura-2 AM ratiometric measurement (F350/380 nm).

2.2.15. Data processing and statistical analysis:

2.2.15.1. Calcium imaging data:

Neurons were identified by their responsiveness to 40 mM KCl. A response was defined as an increase in (F350/380) ratio of > 6 SD above the baseline. Fractional difference in fluorescence ($\Delta F/F_0$) was calculated in GraphPad Prism 7 software according to the following formula:

$$\text{fractional difference } (\Delta F/F_0) = \frac{F_{350/380} - \text{Baseline}}{\text{Baseline}}$$

Baseline was calculated as the mean value of the 30 frames before any drug application. The area under the curve was calculated from ($\Delta F/F_0$) data sheet by an

integrated function in GraphPad Prism 7 software (using the trapezoid rule for measuring the area under the curve). Since the VTD calcium responses differed in their shapes and decay rates, the area under the curve was calculated for the 10 min period from VTD application onset. Statistical analysis was performed by calculating the mean percentage of responsive neurons from multiple coverslips in each DRG culture preparation (N). Sample mean of each set of experiments was calculated from DRG cultures from multiple animals (as specified in the result section) and compared to each other by one-way analysis of variance (ANOVA) with Sidaks' post-test. Cell diameter measurements were performed using ImageJ software; cell area was obtained from a hand-drawn line delineating the soma. Soma diameter was then calculated using the following formula, $\text{Diameter} = \sqrt{(4 \cdot \text{Area} / \pi)}$. For cell size comparison, two-tailed unpaired Student's t-test was used for comparisons. For experiments where a treated sample was compared to a control sample (VGSC blockers and KD experiments), two-tailed paired Student's t-test was used for comparison. All statistical analysis and comparisons were performed by GraphPad Prism software (version 7.00 for Windows). Area-proportional Venn diagrams were generated by BioVenn software 11²⁴³ and colour edited by CorelDRAW X8 software.

2.2.15.2. Western Blot data analysis:

Image-studio™ lite software was used for signal quantification and image processing of membranes detected with Li-Cor system. For knock-down quantification and membrane protein level, signals were first normalized to the area of the region of interest, and then normalized to the loading control signal in each experiment. Data was statistically compared by t-test using GraphPad Prism (version 7 for Windows) as described under each experiment.

2.2.15.3. Immunofluorescence data analysis:

Control and treated samples were acquired at the same microscope setup. Exposure time and laser power were optimized using negative control samples (no primary antibody), to minimize background signals. At the start of the image acquisition process for every experiment, image acquisition setups were optimised and saved for each antibody based on the minimum background signal in the negative control samples, Fig. 2.6.

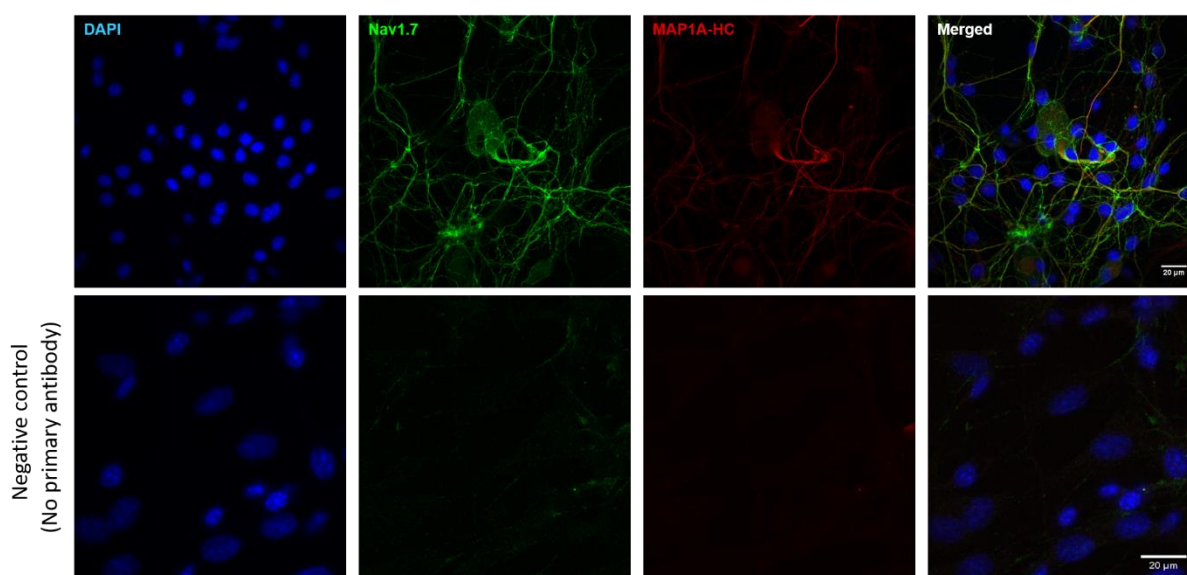


Figure 2.6: An example of unmodified raw images of Nav1.7 and MAP1A-HC immunostaining and their negative control in mouse DRG culture.

DRG neurons in long-term culture (>5 DIV) were fixed and co-immunostained with Nav1.7 (top panel, green) and MAP1A-HC (top panel, red). Cells nuclei were stained with DAPI (blue). Bottom panel represents the negative control (no primary antibody) of each channel. The signal intensity is significantly stronger in the presence of primary antibody than the negative control, which indicates minimum non-specific activity of the secondary antibody. Images were acquired with conventional confocal microscopy, 40 X objective. Images represent one z-plane (middle of the cells).

Image J software was utilized to select a region of interest (whole cell or only the membrane of the cell) and measure different parameters for the selected region like mean grey value, area and integrated density. Because of the shape of the neurons and heterogeneity of the DRG culture, the middle z-plane (for each cell) was usually used to measure the different parameters. For membrane selection, cells were first thresholded, selected with the wand tool to outline the cell perimeter. 1.25 µm width band was then calculated by the software to identify cell membrane and measure its protein signal, Fig. 2.7, (Various width of membrane bands were tested and 1.25 µm was found to be the most appropriate representation of the cell membrane). Data was statistically compared by t-test using GraphPad Prism (version 7 for Windows).

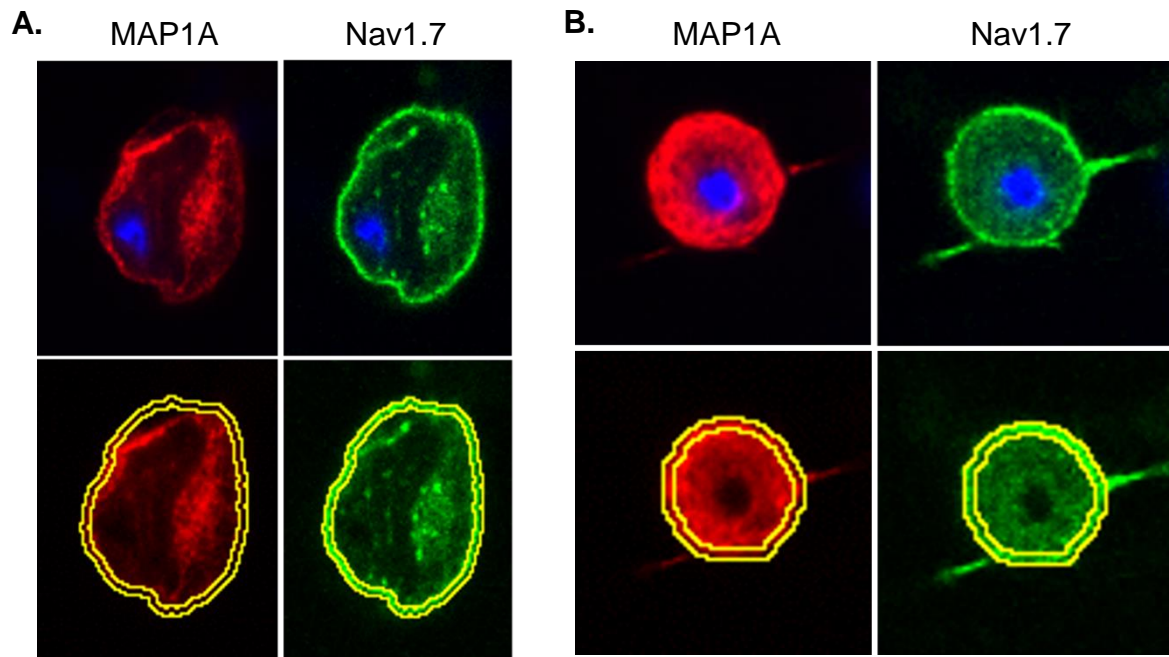


Figure 2.7. Illustration of the Nav1.7 membrane quantification method by ImageJ software. The middle z-plane of each cell was selected. The ROI of the whole cell was selected first, followed by a band of 1.25 μm width to fit the cell membrane. Integrated density of both the whole cell (total) and the membrane were computed by imageJ software. A and B are examples of two different cells.

CHAPTER 3
CHARACTERIZATION OF THE
DISTINCT VERATRIDINE
CALCIUM RESPONSE PRPFLES
IN MOUSE DRG NEURONS

Chapter 3: Characterization of Veratridine distinct calcium response profiles in mouse DRG neurons

The work presented in this chapter has been published under the title:

“Veratridine produces distinct calcium response profiles in mouse Dorsal Root Ganglia neurons”

Authors: Zainab A. Mohammed, Ciara Doran, David Grundy, Mohammed A. Nassar.

Scientific Reports. **7**, article number: 45221; doi: 10.1038/srep45221,

Date: 24 March 2017.

This article was published under the creative commons CC-BY license.

Author contribution:

I co-designed, carried out and analysed all experiments. I prepared all figures and wrote the first draft of the manuscript and have contributed to the corrected versions.

Mohammed Nassar conceived, designed and supervised experiments and wrote the manuscript.

David Grundy contributed reagents and equipment and commented on manuscript.

Ciara Doran trained me on calcium imaging, advised on some experiments and commented on manuscript.

SCIENTIFIC REPORTS

OPEN

Veratridine produces distinct calcium response profiles in mouse Dorsal Root Ganglia neurons

Received: 09 December 2016

Accepted: 20 February 2017

Published: 24 March 2017

Zainab A. Mohammed, Ciara Doran, David Grundy & Mohammed A. Nassar

Nociceptors are a subpopulation of dorsal root ganglia (DRG) neurons that detect noxious stimuli and signal pain. Veratridine (VTD) is a voltage-gated sodium channel (VGSC) modifier that is used as an "agonist" in functional screens for VGSC blockers. However, there is very little information on VTD response profiles in DRG neurons and how they relate to neuronal subtypes. Here we characterised VTD-induced calcium responses in cultured mouse DRG neurons. Our data shows that the heterogeneity of VTD responses reflects distinct subpopulations of sensory neurons. About 70% of DRG neurons respond to 30–100 μ M VTD. We classified VTD responses into four profiles based upon their response shape. VTD response profiles differed in their frequency of occurrence and correlated with neuronal size. Furthermore, VTD response profiles correlated with responses to the algescic markers capsaicin, AITC and α , β -methylene ATP. Since VTD response profiles integrate the action of several classes of ion channels and exchangers, they could act as functional "reporters" for the constellation of ion channels/exchangers expressed in each sensory neuron. Therefore our findings are relevant to studies and screens using VTD to activate DRG neurons.

Dorsal Root Ganglia (DRG) contain a heterogeneous population of sensory neurons that detect noxious and innocuous stimuli. DRG neurons that respond to noxious stimuli are known as nociceptors. Inflammation and nerve injury sensitise sensory neurons and result in hyperalgesia and allodynia^{1,2}. Understanding the physiology and pathophysiology of nociceptors is important for the development of analgesic drugs. Nociceptors express multiple subtypes of voltage-gated sodium channels (VGSCs) which are a key determinant of their excitability. Inflammation and injury-induced sensitisation of nociceptors is in part mediated through changes in expression and/or properties of VGSCs^{1–3}.

Drug screens for VGSC blockers use functional assays to test their sensitivity. These include FLIPR, calcium imaging and patch clamp electrophysiology; and employ Veratridine (VTD) as a VGSC "agonist" to test the pharmacological properties of candidate VGSC ligands⁴. VTD is a natural, lipid-soluble alkaloid from the Liliaceae family that binds to the S6 in Domain I and IV of VGSCs; a site-2 neurotoxin^{4–6}. VTD binds to open VGSCs and prevents the channels from entering into the inactivated state^{7–9}. VTD acts predominantly on tetrodotoxin-sensitive (TTX-S) VGSCs¹⁰. Despite its wide use there is little information on how VTD responses relate to the different subpopulations of DRG neurons; particularly nociceptors. Given the functional and molecular heterogeneity of DRG neurons we hypothesised that VTD produces heterogeneous responses in primary sensory neurons. A better characterisation of the VTD responses in DRG neurons may provide a novel functional classification of sensory neurons.

Results

Veratridine produces TTX-sensitive responses. VTD elicited heterogeneous calcium responses that differed in their profile and onset in sensory neurons, Fig. 1A. This is in contrast to the homogenous response profile elicited in the neuroblastoma cell lines N2a¹¹ and SH-SY5Y¹², which are commonly used mouse and human neuronal cell lines (respectively), Fig. 1B,C. Different concentrations of VTD ranging from 15 to 200 μ M have been used to activate VGSCs in a variety of cell types^{7,10,13–15}. We therefore examined a wide range of VTD concentrations (0.001, 0.1, 1, 10, 30, and 100 μ M) on cultured mouse DRG neurons. Since 200 μ M VTD has been shown to inhibit voltage-gated potassium channels (VGKCs)¹³ we did not use concentrations greater than 100 μ M. There was a concentration dependent increase in the number of responding neurons from a threshold of

Biomedical Science, University of Sheffield, Sheffield S102TN, UK. Correspondence and requests for materials should be addressed to M.A.N. (email: m.nassar@sheffield.ac.uk)

www.nature.com/scientificreports/

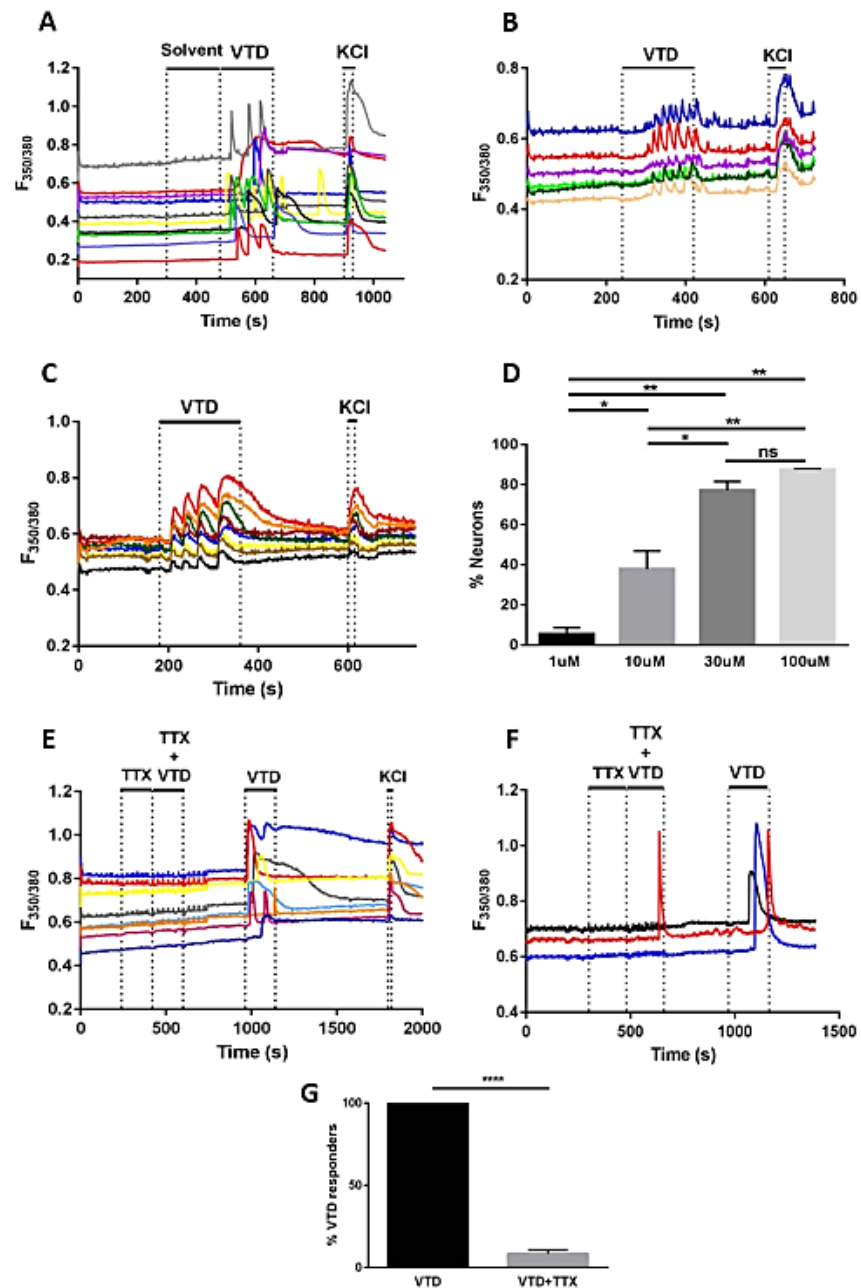


Figure 1. Veratridine elicits TTX-sensitive calcium responses in DRG neurons. (A) Example traces of ratiometric (F350/380) increases in Fura-2 fluorescence following application of 30 μM veratridine (VTD) and 40 mM KCl to cultured DRG neurons, Neuroblastoma-2a (N2a) cells (B) and SH-5Y5 cells (C). Each trace represents the response of a single cell. VTD but not solvent (ethanol) elicited responses of heterogeneous profiles in DRG neurons but not in any of the cell lines. (D) Percentages of neurons activated by a range of VTD concentrations from potassium responsive neurons. Response rates are 5.4 ± 3 for 1 μM (20/303 cells), 37.8 ± 9 for 10 μM (131/325 cells), 77.2 ± 4 for 30 μM (119/151 cells) and 87.5 ± 0.3 for 100 μM (272/311 cells); from N = 2 mice. One-way analysis of variance with Tukey's post-test, * $P < 0.05$, ** $P < 0.01$ and *** $P < 0.001$. (E) Example traces of response to 30 μM VTD in presence and then absence of 0.3 μM Tetrodotoxin (TTX). (F) An example trace of a neuron responding to VTD in the presence of 0.3 μM TTX. (G) TTX blocked 92% of VTD responses. Only 8 ± 2 (10/98 cells) of neurons responded to VTD in the presence of TTX. Data shown are mean \pm SEM, Two-tailed paired Student's t-test, **** $P < 0.0001$.

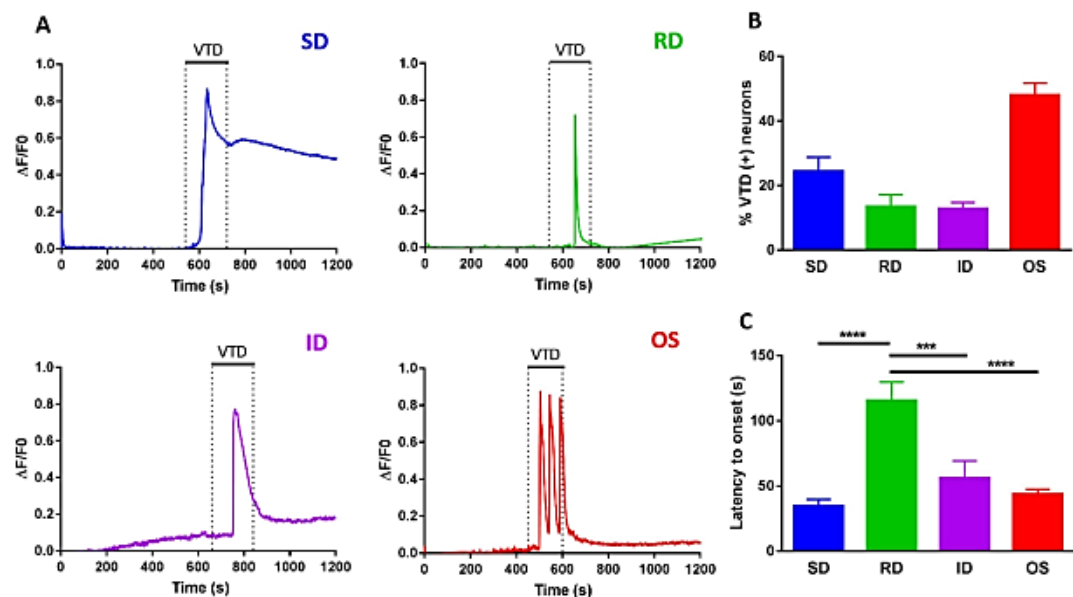


Figure 2. Veratridine produces four calcium response profiles that differ in their frequency of occurrence and latency to peak. (A) Representative traces of the four VTD response profiles observed in cultured DRG neurons. SD (slow decay) in blue has the slowest decay rate of calcium signal, followed by ID (intermediate decay) in purple and then RD (rapid decay) in green. Responses with two or more peaks are called oscillatory (OS) in red. (B) Frequency of occurrence of the four VTD response profiles in VTD-responsive neurons (N = 8 mice, 494 cells). The OS profile is the most frequent ($48 \pm 4\%$), followed by the SD profile ($24.4 \pm 4\%$). The RD ($13.4 \pm 4\%$) and ID ($12.7 \pm 2\%$) profiles have similar frequencies. (C) Mean response latency for the four VTD response profiles (N = 3 mice, 143 cells). Only neurons that have the same onset to KCl were included in this analysis to exclude differences due to rate of perfusion. The RD (115.4 ± 15 s) profile has the longest latency while the SD (34.2 ± 5 s), ID (55.8 ± 13 s) and OS (43.5 ± 4 s) profiles have similar latencies. Data shown are mean \pm SEM. One-way analysis of variance with Tukey's post-test, ***P < 0.001 and ****P < 0.0001.

1 μ M to which 5% of neurons responded. 10 μ M elicited a response in 38% of neurons while 30 μ M and 100 μ M VTD elicited responses in 77% and 88% of neurons, respectively, Fig. 1D. Subsequent experiments were performed using 30 μ M VTD because of the robust response at this concentration and to minimise potential effects on VGKCs. Responses to 30 μ M VTD varied in latency from 30 to 150 seconds as shown in the example traces in Fig. 1A. Therefore, we standardised the period of VTD application to three minutes. Pre-treatment of neurons with TTX (0.3 μ M) blocked VTD responses in 92% of VTD-responsive neurons, Fig. 1E–G. Of note, VTD responses elicited in the presence of TTX had a response profile characterised by a single peak with a delayed onset (towards the end of the 3 minutes of VTD application period), Fig. 1E.

Veratridine produces four distinct calcium response profiles that occur at different frequencies.

We classified VTD responses into four distinct profiles, Fig. 2A. Three profiles were characterised by a single peak with a rapid rise in intracellular calcium $[Ca]_i$ levels but differed in their decay rate. The Slow Decay (SD) profile returned to baseline over 15–40 min following VTD washout, Fig. 2A (blue). In the Intermediate Decay (ID) profile, calcium responses returned to baseline within 2–5 min, Fig. 2A (purple). The Rapid Decay (RD) profile was characterised by a transient $[Ca]_i$ peak which returned to baseline during the application period, Fig. 2A (green). The fourth profile was characterised by a multi-peak response which we thus called the Oscillatory profile (OS), Fig. 2A (red). In some OS neurons the response ended prior to the end of VTD application while in others it continued to oscillate during the wash. The four VTD response profiles varied in their frequency of occurrence. The OS profile was the most frequent accounting for 48% of all VTD-responsive neurons, followed by the SD profile (24%) and equal frequencies for the ID and RD profiles (13% each), Fig. 2B. Furthermore, the four profiles differed in their onset, calculated as the latency to peak from the start of VTD application. The RD profile had the longest latency which was twice that of the other three profiles, Fig. 2C. The onset difference was inherent to neurons and not due to variation in the rate of perfusion since all neurons responded with the same latency to high potassium. A very small number of VTD-responsive neurons had a “ramp” like profile characterised by a very slow rise and decay of $[Ca]_i$ levels (not shown). These neurons were classified as “undefined” in further experiments and were not included in our characterisation because they were too infrequent (less than 1%) to include in our analysis and draw any conclusions about.

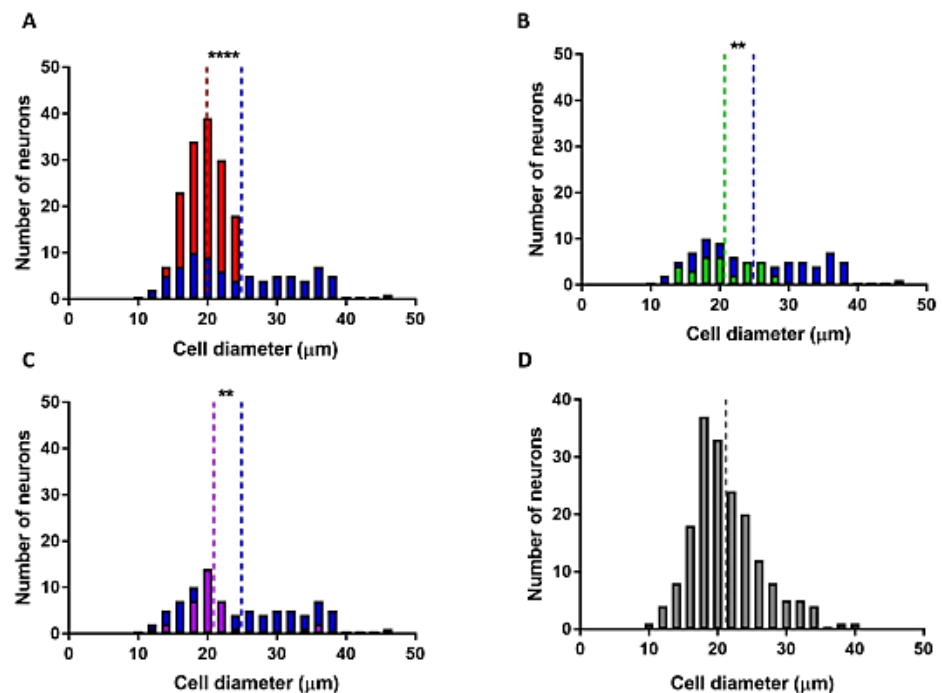


Figure 3. Veratridine OS, RD and ID response profiles occur in neurons smaller than 30 μm in diameter. (A) Histogram of soma diameter distribution of neurons with the SD profile in blue (mean 42.9 ± 1 , median = $23.1 \mu\text{m}$; 79 cell) with superimposed distribution of neurons with the OS profile in red (mean $19.9 \pm 0.3 \mu\text{m}$, median = $19.7 \mu\text{m}$; 161 cell). (B) Histogram of soma diameter of neurons with the SD profile versus neurons with the RD profile in green (mean $20.7 \pm 0.8 \mu\text{m}$, median = $20.1 \mu\text{m}$; 33 cell). (C) Histogram of soma diameter of neurons with the SD profile versus neurons with the ID profile in purple (mean $20.9 \pm 0.8 \mu\text{m}$, median = $20.1 \mu\text{m}$; 35 cell). (D) Histogram of soma diameter of VTD-unresponsive neurons (mean $21.2 \pm 0.4 \mu\text{m}$, median = $20.4 \mu\text{m}$; 181 cell). Histograms are in $2 \mu\text{m}$ bins. Vertical dotted line indicates the mean value for each distribution. All diameter measurements were taken from $N = 8$ mice and compared by Two-tailed paired Student's t-test, * $P < 0.05$ and **** $P < 0.0001$.

The Veratridine SD response profile is enriched in large diameter neurons. DRG neurons are classified according to their soma size into small, medium and large diameter neurons^{16–18}. Soma size of DRG neurons correlates with functional modalities. Small and medium sized neurons tend to be nociceptors and innocuous thermoreceptors, while large diameter neurons are more likely to be proprioceptors and low threshold mechanoreceptors^{19,20}. Neuronal soma size in our DRG cultures ranged from 10 to $45 \mu\text{m}$. Analysis of soma size and VTD response profiles showed that although the SD profile occurs in all neuronal sizes (mean $25 \mu\text{m}$), it was the most prevalent profile in neurons larger than $30 \mu\text{m}$ in diameter (82% of these neurons had the SD profile). Neurons with the RD, OS and ID profiles had the narrowest size range with almost all smaller than $30 \mu\text{m}$ in diameter (100, 99 and 91%, respectively). The mean soma diameter of neurons with the RD, OS and ID VTD response profiles was smaller than that of SD neurons (RD $21 \mu\text{m}$, OS $20 \mu\text{m}$ and ID $21 \mu\text{m}$), Fig. 3A–C. Of note, the majority (94%) of VTD-unresponsive neurons were smaller than $30 \mu\text{m}$ (mean $21 \mu\text{m}$), Fig. 3D.

The Veratridine SD and RD response profiles are under-represented in capsaicin sensitive neurons. We next investigated how the four VTD response profiles correlate with a commonly used functional marker of nociceptors. Capsaicin is a TRPV1 agonist used to activate peptidergic nociceptors²¹. In order to examine the relationship between VTD response profiles and sensitivity to capsaicin we applied them sequentially in a single calcium imaging protocol as illustrated in Fig. 4A. The order in which the two agonists were applied did not influence the proportion of responding neurons nor the frequency of occurrence of VTD response profiles, Supplementary Fig. S1. Therefore, we combined results from both experiments in subsequent analysis, Fig. 4B. The frequency of occurrence of the four response profiles in these neurons was in the same order as obtained without capsaicin, Fig. 4C. The percentage of capsaicin sensitive neurons in our cultures (32%) is comparable to published reports²². Capsaicin sensitive neurons were approximately twice as likely to respond to VTD (156 of 223, 70%) than not (67 of 223, 30%), Fig. 4B. We next examined VTD-responsive neurons for the relationship between each of the four VTD response profiles and capsaicin sensitivity. The proportions of capsaicin-sensitive

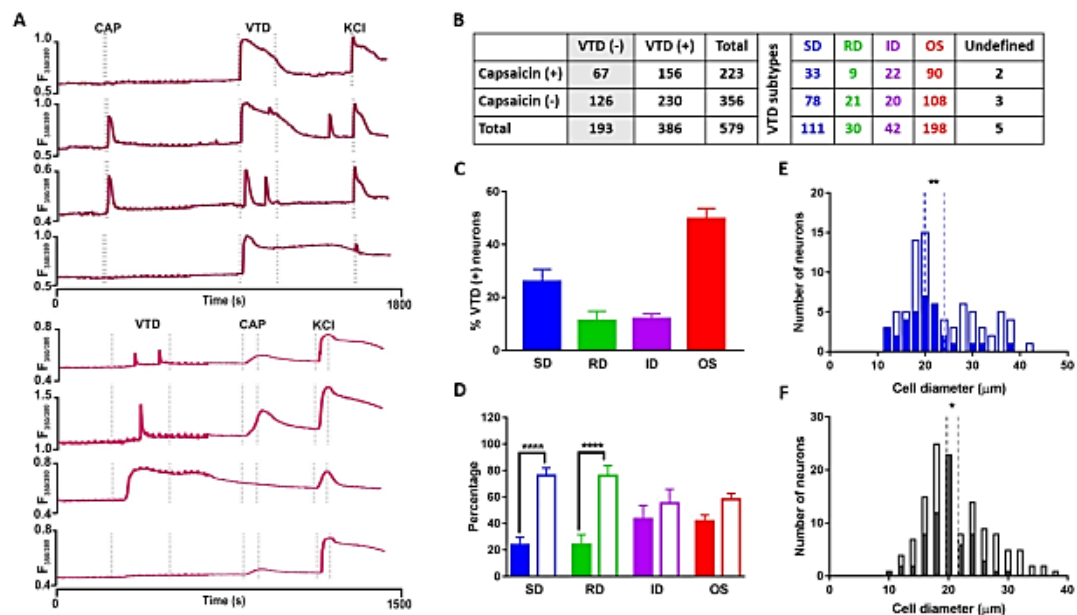


Figure 4. Veratridine SD and RD response profiles are under-represented in capsaicin-sensitive neurons. (A) Example traces from the two drug application protocols used. Top four traces from experiments where VTD was applied after 200 nM capsaicin. Bottom traces from experiments where VTD was applied before 1 μ M capsaicin. In the former case, a lower capsaicin concentration was used to avoid potential indirect suppression of VGSC by capsaicin⁴² (B). Capsaicin sensitivity and VTD response profiles of 579 neurons from N = 8 mice (combined from the two protocols in A). (C) The frequency of occurrence of the four VTD response profiles in the 386 VTD-responsive neurons shows the same order as in Fig. 2B. The OS profile is the most frequent ($49.7 \pm 4\%$) then the SD ($26 \pm 5\%$) followed by the ID ($12 \pm 2\%$) and the RD ($11.1 \pm 4\%$). (D) The proportion of capsaicin-sensitive neurons (closed bars) and capsaicin-insensitive neurons (open bars) within the four VTD response profiles. A larger proportion of SD (76.2 vs. $23.8 \pm 6\%$) and RD neurons (76 vs. $24 \pm 8\%$) is insensitive to capsaicin. OS (58.1 vs. $41.9 \pm 5\%$) and ID neurons (55.3 vs. $43.4 \pm 10\%$) show no difference. Frequency was from total number of neurons in each profile ($n_{SD} = 111$, $n_{RD} = 30$, $n_{ID} = 42$, and $n_{OS} = 198$ neurons). Data shown are mean \pm SEM. One-way analysis of variance with Sidak's post-test, **** $P < 0.0001$. (E) Diameter of SD neurons sensitive to capsaicin is smaller (closed bars, mean $19.9 \pm 0.9 \mu\text{m}$, median $19.3 \mu\text{m}$, $n = 33$ cell) than diameter of capsaicin insensitive neurons (open bars; $24 \pm 0.8 \mu\text{m}$, median $21 \mu\text{m}$, $n = 78$ cell). (F) Diameter of VTD-unresponsive neurons showing capsaicin-sensitive (closed bars, mean $19.7 \pm 0.4 \mu\text{m}$, median $19.8 \mu\text{m}$, $n = 67$ cell) and capsaicin-insensitive populations (open bars, mean $21.6 \pm 0.5 \mu\text{m}$, median $20.3 \mu\text{m}$, $n = 126$ cell). In (E,F), dotted lines represent the mean. Two-tailed unpaired Student's t-test, * $P < 0.05$ and ** $P < 0.01$.

and insensitive neurons within the OS and ID profiles were not significantly different. However, there was a clear bias in neurons with the SD and RD profiles towards capsaicin insensitivity, Fig. 4D.

As the SD profile occurred in a wide range of neuronal sizes, we examined the relationship between neuronal size and capsaicin sensitivity in the 111 neurons with the SD profile. Capsaicin-sensitive SD neurons had a smaller mean diameter than capsaicin-insensitive SD neurons, Fig. 4E, which is consistent with the known tendency of capsaicin sensitive neurons to be small to medium in diameter. Interestingly, capsaicin activated 35% (67 of 193) of VTD-unresponsive neurons which were all smaller than $30 \mu\text{m}$, Fig. 4F. From all the above, the SD and RD profiles are enriched in capsaicin-insensitive neurons.

The Veratridine SD and RD response profiles are under-represented in α , β -methylene ATP sensitive neurons.

We next investigated how the four VTD response profiles correlate with sensitivity to another commonly used marker for nociceptors. α , β -methylene ATP is a specific agonist for $P2 \times 3$ receptors that marks the non-peptidergic population of nociceptors^{23–26}. A preliminary experiment showed that responses to $1 \mu\text{M}$ α , β -methylene ATP (the EC_{50} for $P2 \times 3$) can be completely inhibited by TNP-ATP, a selective $P2 \times 3$ antagonist²⁷ (data not shown). Therefore, we applied $1 \mu\text{M}$ α , β -methylene ATP with VTD to examine the relationship between the four VTD response profiles and sensitivity to α , β -methylene ATP. We applied the two agonists in alternate order, Fig. 5A. As with capsaicin, the order in which VTD and α , β -methylene ATP were applied did not significantly influence the proportion of responding neurons nor the frequency of occurrence of VTD profiles, Supplementary Fig. S2. The frequency of occurrence of the four VTD response profiles was as obtained previously, Fig. 5C. The percentage of α , β -methylene ATP-responsive neurons (26%) was comparable to percentage of $P2 \times 3$ positive neurons reported in immunolabelling studies^{23,26}. α , β -methylene ATP-responsive neurons are approximately five times more likely to respond to VTD ($289/344$, 84%) than not ($55/344$, 16%), Fig. 5B. We next

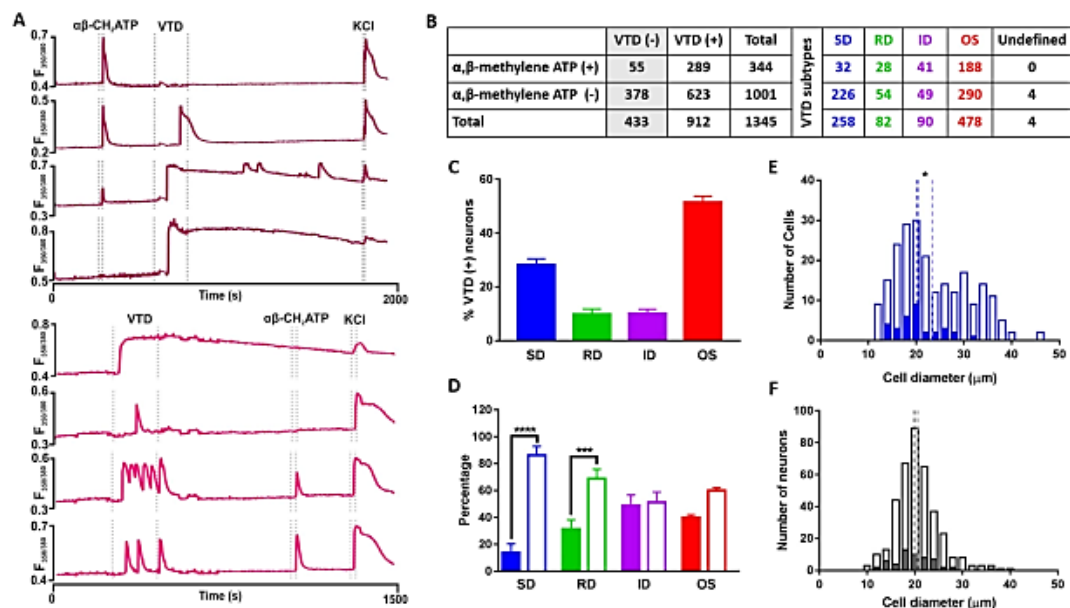


Figure 5. Veratridine SD and RD response profiles are under-represented in α,β -methylene ATP-sensitive neurons. (A) Example traces from the two drug application protocols used. (B) α,β -methylene ATP sensitivity and types of VTD response profile of the 1345 neurons sampled from $N = 9$ mice (combined from the two protocols in A). (C) The frequency of occurrence of VTD profiles in the 912 VTD-responsive neurons shows the same order as in Fig. 2B. The OS profile is the most frequent ($51.4 \pm 2\%$) then SD ($28.1 \pm 2\%$) followed by ID ($10.1 \pm 2\%$) and RD ($9.8 \pm 2\%$). (D) The proportion of α,β -methylene ATP-sensitive neurons (closed bars) and α,β -methylene ATP-insensitive neurons (open bars) within each of the four VTD response profiles. A larger proportion of SD (86.3 vs. $13.7 \pm 6.6\%$) and RD neurons (68.9 vs. $31.1 \pm 7\%$) is insensitive to α,β -methylene ATP. Neurons with the OS (60 vs. $40 \pm 2\%$) and ID (51.1 vs. $48.9 \pm 8\%$) profile show no difference in the proportion of α,β -methylene ATP-sensitive and -insensitive neurons. Frequency was calculated from total number of neurons in each profile ($n_{(SD)} = 258$, $n_{(RD)} = 82$, $n_{(ID)} = 90$, and $n_{(OS)} = 478$ neurons). Data shown are mean \pm SEM. One-way analysis of variance with Sidak's post-test, $***P < 0.001$ and $****P < 0.0001$. (E) Histogram of diameter of neurons with the SD response profile showing that α,β -methylene ATP-sensitive neurons (closed bars, mean $20.2 \pm 0.8 \mu\text{m}$, median $19.9 \mu\text{m}$, $n = 32$ cell) are significantly smaller than α,β -methylene ATP-insensitive neurons (open bars; mean $23.4 \pm 0.5 \mu\text{m}$, median $21.3 \mu\text{m}$, $n = 226$ cell). (F) Histogram of diameter of neurons unresponsive to VTD showing α,β -methylene ATP-sensitive population (closed bars, mean $19.9 \pm 0.6 \mu\text{m}$, median $19.2 \mu\text{m}$, $n = 55$ cell) and α,β -methylene ATP-insensitive population (open bars, mean $20.6 \pm 0.2 \mu\text{m}$, median $20.2 \mu\text{m}$, $n = 378$ cell). In (E,F), dotted lines represent the mean. Two-tailed unpaired Student's t-test, $*P < 0.05$ and $**P < 0.01$.

examined the 912 VTD-responsive neurons for a relationship between each of the four VTD response profiles and α,β -methylene ATP sensitivity. The proportions of α,β -methylene ATP-sensitive and insensitive neurons within the OS and ID profiles were not significantly different, Fig. 5D. However, like with capsaicin, there was a clear bias in neurons with the SD and RD profiles towards α,β -methylene ATP insensitivity.

The SD subpopulation of neurons sensitive to α,β -methylene ATP had a smaller mean size ($20 \mu\text{m}$) compared to the subpopulation insensitive to α,β -methylene ATP ($23 \mu\text{m}$), Fig. 5E. Interestingly, 98% of VTD-unresponsive but α,β -methylene ATP-sensitive neurons were less than $30 \mu\text{m}$ in diameter, Fig. 5F. From all the above, the SD and RD profiles are enriched in α,β -methylene ATP-insensitive neurons.

The Veratridine OS, ID and RD response profiles are enriched in nociceptors. Both the SD and RD response profiles were enriched in neurons insensitive to the two nociceptive markers; capsaicin and α,β -methylene ATP. This led us to hypothesize that these two response profiles could be functional markers for non-nociceptors, while the OS and ID response profiles could be functional markers for nociceptors. However, The OS and ID profiles did not occur preferentially in neurons sensitive to the nociceptive markers capsaicin (Fig. 4D) and α,β -methylene ATP (Fig. 5D). Nevertheless, it is possible that the OS neurons insensitive to capsaicin are the same neurons that are sensitive to α,β -methylene ATP and vice versa. To test this hypothesis, it was necessary to apply VTD, capsaicin and α,β -methylene ATP sequentially in the same protocol. We also wanted to profile VTD responses in C-low threshold mechanoreceptors because it was reported that this population is required for injury induced mechanical hypersensitivity²⁸. This population expresses TRPA1 but not TRPV1 nor P2 \times 3²⁹; therefore we included allyl isothiocyanate (AITC, a specific TRPA1 agonist^{30–32}) in our protocol. We applied the five agents in the calcium imaging protocol in two orders, Fig. 6A. The order of agents in the

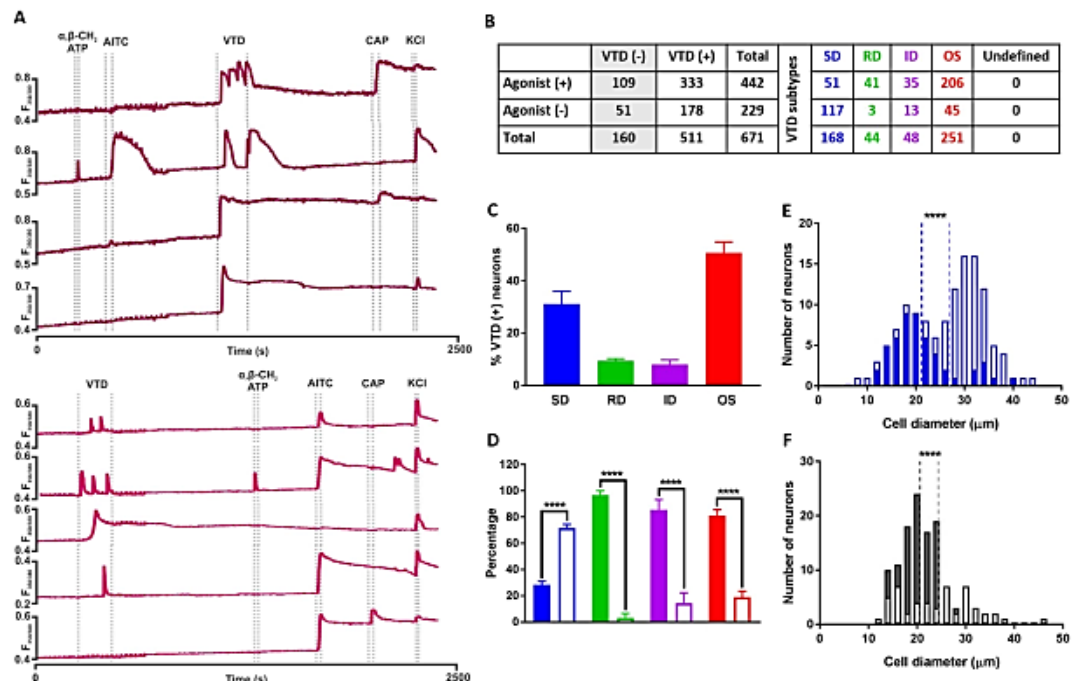


Figure 6. The Veratridine OS, ID and RD response profiles are enriched in nociceptors. (A) Example traces from the two drug application protocols used. (B) Drug sensitivity and VTD response profiles of 671 neurons from $N = 7$ mice. (C) The frequency of occurrence of VTD profiles in the 511 VTD-responsive neurons shows the same order as in Fig. 2B. The OS profile is the most frequent ($50.6 \pm 4.2\%$) then the SD profile ($31.2 \pm 4.8\%$) followed by RD ($9.4 \pm 0.8\%$) and ID ($8 \pm 1.8\%$). (D) The proportion of neurons sensitive to at least one agonist (closed bars) and neurons insensitive to any (open bars) within the four VTD response profiles. Larger proportion of SD neurons (71.6 vs. $28.4 \pm 2.9\%$) is insensitive to any of the three agonists. In contrast, larger proportion of RD neurons (96.7 vs. $3.3 \pm 3.3\%$), ID (85.5 vs. $14.5 \pm 7.7\%$) and OS (81 vs. $19 \pm 4.6\%$) neurons are sensitive to at least one of the three agonists. Percentages were calculated from total number of neurons in each profile ($n_{(SD)} = 168$, $n_{(RD)} = 44$, $n_{(ID)} = 48$, and $n_{(OS)} = 251$ neuron). Data shown are mean \pm SEM. One-way analysis of variance with Sidak's post-test, $***P < 0.001$ and $****P < 0.0001$. (E) Diameter of SD neurons that are sensitive to at least one of the three agonists (closed bars, mean $21.2 \pm 0.9 \mu\text{m}$, median $19.6 \mu\text{m}$, $n = 51$ cell) is significantly smaller than that of neurons insensitive to any of the three agonists (open bars; mean $26.9 \pm 0.7 \mu\text{m}$, median $28.3 \mu\text{m}$, $n = 117$ cell). (F) Diameter of VTD-unresponsive neurons sensitive to at least one agonist (closed bars are, mean $20.6 \pm 0.4 \mu\text{m}$, median $20.7 \mu\text{m}$, $n = 109$ cell) and VTD-unresponsive neurons insensitive to any of the three agonists (open bars, mean $24.4 \pm 1 \mu\text{m}$, median $24.3 \mu\text{m}$, $n = 51$ cell). In (E,F), dotted lines represent the mean. Two-tailed unpaired Student's t -test, $*P < 0.05$.

first protocol was; α , β -methylene ATP ($1 \mu\text{M}$), AITC ($100 \mu\text{M}$), VTD ($30 \mu\text{M}$), capsaicin (200 nM) and 40 mM KCl. The order of agents in the second protocol was VTD, ATP, AITC, capsaicin and KCl. As with previous experiments (Figs 4 and 5), there was no significant difference in the proportion of responding neurons nor the frequency of occurrence of VTD profiles in both protocols, Supplementary Fig. S3.

Neurons sensitive to any of the three agonists were three times more likely to respond to VTD ($333/442$, 75%) than not ($109/442$, 25%), Fig. 6B. The frequency of occurrence of the four response profiles, Fig. 6C, was similar to previous values in Figs 3C, 4C and 5C. We next examined the 511 VTD-responsive neurons for a relationship between each of the four VTD response profiles and sensitivity to any of the three agonists. The three agonists divided the four VTD profiles into two groups. In one group is the SD response profile which continued to show a bias towards insensitivity to any of the three agonists, Fig. 6D. In the other group are the OS, ID and now the RD response profiles all showing a significant bias towards sensitivity to any of the three agonists, Fig. 6D.

The SD subpopulation of neurons sensitive to any of the three agonists have a smaller mean size ($21 \mu\text{m}$) compared to the subpopulation insensitive to any of the three agonists ($26 \mu\text{m}$), Fig. 6E. Interestingly, all neurons unresponsive to VTD but sensitive to any of the three agonists are smaller than $30 \mu\text{m}$ in diameter, Fig. 6F. The percentage of responsive neurons to $100 \mu\text{M}$ AITC (54%) is consistent with published findings³¹. The relationship between VTD response profiles and sensitivity to AITC alone matches that for the three agonists combined (Supplementary Fig. S4). From all the above, the OS, ID and RD response profiles are enriched in neurons sensitive to the nociceptive markers whereas the SD response profile is enriched in neurons insensitive to the nociceptive markers, Fig. 7.

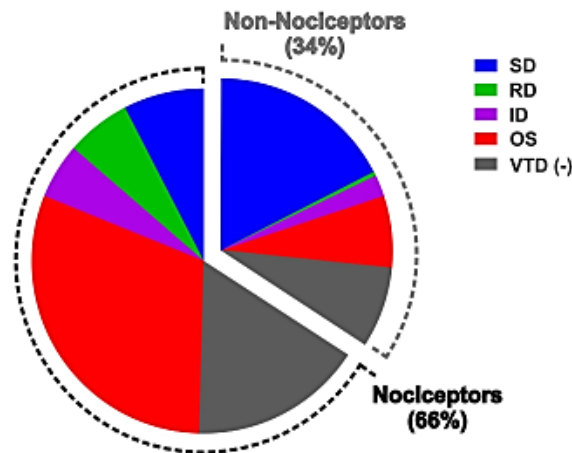


Figure 7. VTD response profiles correlate with classical functional markers of nociceptors. Neurons responding to at least one of the three agonists represent nociceptors and constitute 66% (442/671) of all DRG neurons in culture. Nociceptors with the OS, ID or RD VTD response profiles constitute 64% (282/442) of nociceptors (equivalent $282/671 = 42\%$ of all neurons) compared to 12% (51/442) of nociceptors with the SD profile (equivalent to $51/671 = 8\%$ of all neurons). Neurons insensitive to any of the three agonists represent non-nociceptors and constitute 34% (229/671) of all DRG neurons in culture. Non-nociceptors with the SD VTD response profile constitutes 51% (117/229) of non-nociceptors (equivalent to $117/671 = 17\%$ of all neurons) compared to non-nociceptors with the OS, ID or RD VTD response profiles which constitute 27% (61/229) of non-nociceptors (equivalent $61/671 = 9\%$ of all neurons).

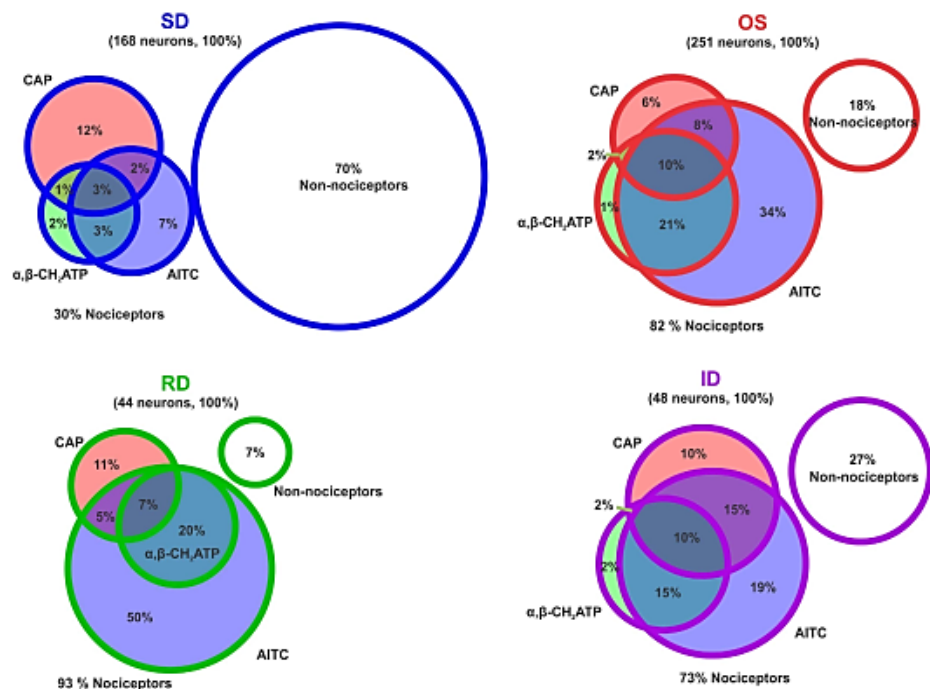


Figure 8. Distribution of sensitivity to the three nociceptive markers within the four VTD response profiles. Venn diagram of the mean percentage of neurons with the SD, OS, RD and ID profiles that responded to allyl isothiocyanate (AITC, blue), capsaicin (CAP, red) and α, β -methylene ATP (α, β -CH₂ATP, green). The percentage of neurons in each profile that did not respond to any of the agonists comprises the fourth non-overlapping circle (white). Percentages were calculated from the total number of neurons in each VTD profile (SD: 168 cell, OS: 251 cell, RD: 44 cell, and ID: 48 cell) in experiment shown in Fig. 6B.

We also examined the distribution of sensitivity to the three agonists among neurons with the four VTD profiles, Fig. 8. AITC sensitivity was the commonest feature of neurons that responded to one or more of the three agonists with the OS (88%), RD (86%), ID (81%) profiles but not the SD response profile (52%). Neurons with the SD response profile were approximately equally as likely to be capsaicin-sensitive (56%) or AITC-sensitive (52%).

Discussion

The present study examined VTD-elicited calcium responses in cultured adult mouse DRG neurons. VTD responses were heterogeneous. We categorised VTD responses into four distinct profiles based on the number of peaks and their decay rate. We report that VTD response profiles correlated with soma size and with commonly used pharmacological markers of nociceptor. To our knowledge this is the first detailed characterisation of VTD responses in DRG neurons.

What do VTD response profiles represent? Most of the studies that looked at the effect of VTD on voltage-gated ion channels used patch-clamp electrophysiology to examine the effect of VTD on sodium^{8,9}, calcium³³ and potassium¹³ currents separately. In calcium imaging the measured response occurs in non-clamped neurons and is indirect to sodium entry. Therefore, the observed VTD response profiles are the net effect of VTD action on VGSCs at the resting membrane potential and the subsequent activation of other ion channel/exchanger classes. Therefore, it is important to keep in mind that although the response is initiated by VTD's action on VGSCs, the overall response is shaped by; 1) Qualitative and quantitative differences in the "constellation" of sodium, potassium and calcium voltage-gated ion channels subtypes in each DRG neuron. 2) Variations in calcium buffering mechanisms within each neuron which includes calcium efflux pathways, intracellular stores as well as calcium binding proteins³⁴.

Our data shows that 30 μ M VTD evoked robust responses in approximately 70% of sensory neurons. A higher dose of 100 μ M VTD did not significantly increase the percentage of responding cells, Fig. 1D. Considering that higher doses of VTD are reported to have inhibitory effects on potassium channels, 30 μ M seems to be the most suitable concentration to use for an action primarily on VGSCs. VTD predominantly activates TTX-S VGSCs and our results are in agreement with this as TTX blocked most VTD responses (Fig. 1E–G). Voltage-clamp experiments on rat DRG neurons showed that VTD binds TTX-R VGSCs but dissociates at much faster rate than with TTX-S VGSCs¹⁰, which might explain why the TTX-R VTD responses we observed are transient in nature, Fig. 1F. It remains to be determined which of the TTX-R channels expressed in DRG neurons (i.e. Nav1.8 and Nav1.9) underlie the observed TTX-R VTD responses. We speculate that Nav1.9 is the most likely candidate because its expression is more restricted in DRG than Nav1.8 and this fits with low incidence of TTX-R VTD responses. Secondly, Nav1.9 activation potential is hyperpolarised allowing it to be open at the resting membrane potential which would allow VTD to act on the open channel. In contrast Nav1.8 activation potential is more depolarised and is unlikely to be open at resting membrane potential for VTD to affect it. In fact, it was reported that VTD did not activate a stable cell line expressing Nav1.8³⁵. Therefore, the contribution of Nav1.8 to VTD responses will be dependent upon prior action of VTD on TTX-S subtypes to depolarise the membrane. Since this would not happen in the presence of TTX; it is thus unlikely that Nav1.8 produces the TTX-R VTD responses in our experiment.

Importantly, the inability of VTD to activate stable cells expressing Nav1.8 may explain the about 25–30% of DRG neurons that are unresponsive to up to 100 μ M VTD, Fig. 1D. We suggest that VTD-unresponsive neurons are so because they express mostly TTX-R and little TTX-S channels. In support of this the majority of neurons in this population are less than 30 μ m in diameter, Figs 3D, 4F, 5F and 6F. Additionally, the majority of neurons in this population (109/160, 68%) responded to at least one of the three nociceptor markers; capsaicin, AITC and α , β -methylene ATP, Fig. 6B. These 109 neurons constitute 25% of nociceptors (109/442, Fig. 6B). These neurons are likely to represent the small diameter, Nav1.8-rich and high-threshold neurons known as "silent nociceptors"^{36,37}. Interestingly, silent nociceptors were estimated to be about 30% of all DRG neurons which is about the same percentage as the VTD-unresponsive population. This finding has significant implications for studies using veratridine to activate DRG neurons as it means that up to 25% of nociceptors would not be assayed and their contribution would be unknown.

We categorised VTD calcium responses in cultured DRG neurons into four profiles which we named SD, ID, RD and OS. The four profiles were observed in similar relative frequencies from cultures prepared over many months, from different patches of mice and by different researchers. Furthermore, the frequency of occurrence of VTD profiles was not affected by the order of applications of agonists in our experiments, Supplementary Figs 1–3. The stability of these profiles supports their suitability for use as functional signatures of subpopulations of DRG neurons in drug screens.

The most abundant response type is the OS (47–51% of VTD-responsive neurons) where VTD elicited oscillatory changes in [Ca]_i levels. Interestingly, this is the only response profile VTD elicited in N2a and SH-SY5Y cells, Fig. 1B,C. A similar response profile was also reported in bovine chromaffin cells where VTD induced [Ca]_i oscillations were dependant on the activation of TTX-S VGSC²⁵. The oscillatory response in bovine chromaffin cells were long lasting (up to 40 min) even after VTD wash. A proportion of the OS responses in DRG neurons were persistent but most returned to baseline after VTD wash (not shown). Although SH-SY5Y, N2a and chromaffin cells^{12,38,39} all express Nav1.7, it is unlikely that the OS profile is a characteristic of Nav1.7 expressing cells as Nav1.7 is expressed in all DRG neurons whereas the OS profile occurs in about 50% of DRG neurons.

The other three types of VTD response profiles shared a profile characterised by a single peak but differed in their decay rate. The difference in the rate of signal decay could be due to a difference in the disassociation rates of VTD from the different VGSC subtypes. In addition, it has been shown that DRG neurons (particularly large-diameter neurons) produce calcium responses with slow decay rates (SD-like responses) when treated with VGKC blockers⁴⁰. Therefore, differences in the decay rates of the VTD response profiles might be in part due to

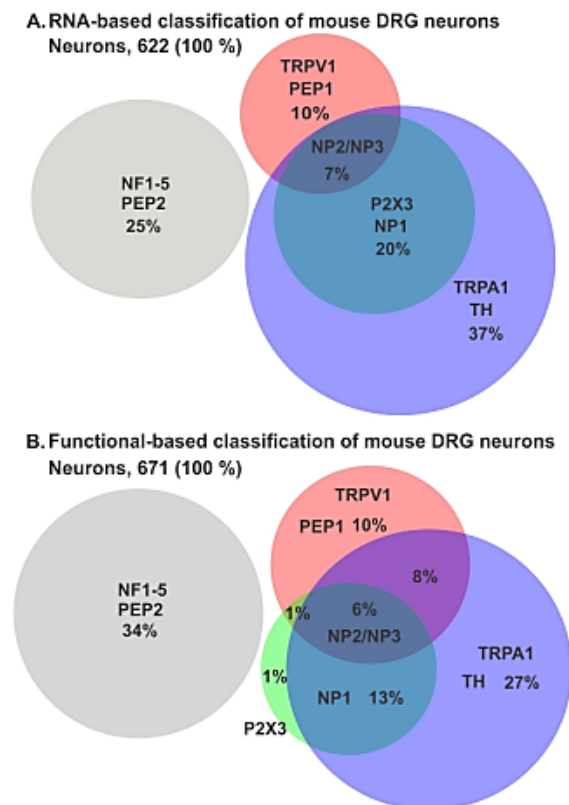


Figure 9. Comparison of the sensitivity to the three nociceptive markers based on published RNASeq and our functional imaging data. (A) Venn diagram of the percentage of neurons expressing mRNA for receptors for the three agonists used according to data from Figs 2 and 4 of ref. 29. (B) Percentage of neurons responding to the three agonists from our experiment in Fig. 6. The classification of neuronal subpopulations is as per that in ref. 29. NP is non-peptidergic, PEP is peptidergic, NF is neurofilament heavy chain and TH for tyrosine hydroxylase.

some inhibitory effect of 30 μ M VTD on VGKCs. However, this is unlikely to be the main determinant of decay rates as it takes a much higher concentration of VTD (200 μ M) to inhibit VGKCs¹³.

A recent paper classified DRG neurons into 11 groups based on their mRNA profile²⁹. Using their data (Figs 2 and 4 in ref. 29) we predicted the distribution of sensitivity of DRG neurons to the three agonists used in this study based on the expression of their receptors, Fig. 9A. We compared this to the distribution of sensitivity we obtained from applying the concentrations of agonists we used, Fig. 9B. The two distributions have many similarities. For example, all non-peptidergic neurons (represented by groups NP1–3 in ref. 29) are predicted to respond to AITC and in agreement we found that almost all α , β -methylene-ATP responded to 100 μ M AITC. Another similarity is that the TRPA1 positive population is the largest of the three agonists being 64% of DRG neurons by mRNA expression of TRPA1 and 54% by response to AITC. The percentage of AITC responders (54%) is almost identical to that reported by Barabas, M.E. *et al.*³¹ (55%). Therefore, the 10% higher percentage of TRPA1 expressing neurons must be due to the higher sensitivity of mRNA detection compared to functional imaging. The same reason is likely to explain the 9% higher percentage of neurons not responding to any of the agonists in our hands compared to what is predicted by mRNA expression. Capsaicin activated 25% DRG neurons in our experiments as opposed to a predicted 17% based on expression of TRPV1 receptor. The percentage of capsaicin responders in our experiments is in agreement with others (e.g.ref. 22). The higher percentage in our and others' experiments could be due increased TRPV1 expression in cultured DRG neurons (>1 day) compared to dissociated but non-cultured neurons as used for the mRNA sequencing study.

The data presented here raises several interesting questions. One question is what are the key molecular determinants of each of the four VTD response profiles? Answering this allows the use of VTD profiles as readout for these ion channels and exchangers in high throughput functional screens on primary DRG neurons. Considering that 25–30% of nociceptors do not respond to 30 μ M VTD and that these are likely to be “silent” nociceptors, a second question is does the sensitization of DRG neurons by inflammation and nerve injury affect the number of VTD responsive neurons and their response profiles? Answering this question would allow the use of VTD

response profiles as readout of drugs' ability to cause or reverse sensitisation of DRG neurons in high throughput screens. Such screens have the advantage of showing the net effect of a drug on the various classes of ion channels that give rise to VTD response profiles.

In conclusion, the present study shows that VTD induces calcium responses with heterogeneous profiles in TTX-S rich sensory neurons. VTD response profiles reflect distinct subpopulations of sensory neurons. These subpopulations overlap but are not identical to the subpopulations identified by classical functional nociceptive markers, Fig. 7. The OS and RD profiles are particularly enriched in nociceptors (neurons sensitive to at least one of the three agonists), while the SD profile is enriched in non-nociceptors (neurons insensitive to any of the three agonists). Our findings provide a detailed characterisation of VTD action on the different subsets of DRG neurons. Our work is relevant to studies and screens using VTD to activate DRG neurons.

Methods

DRG culture. Adult male C57BL/6 mice were sacrificed according to Schedule 1 of the Animal (Scientific procedure) Act 1986. DRG from all spinal levels were isolated and collected in PBS. PBS was then replaced with 1 mL Dulbecco's Modified Eagle's Medium/F12 (DMEM/F12) with Glutamax medium (Gibco) containing Dispase (1 mg/mL, Sigma) and Collagenase Type XI (0.6 mg/mL, Sigma) and left for 60 min at 37 °C and 5% CO₂. DRGs were then triturated with a P1000 pipette tip. The cell suspension was carefully layered on top of 15% Bovine Serum Albumin (Melford) in DMEM/F12 and centrifuged at 800g, for 10 min at room temperature with the minimum deceleration speed. The cell pellet was then washed in culture medium composed of DMEM/F12 plus 10% Fetal Bovine Serum (FBS, Gibco), 100 units/ml penicillin and 100 µg/ml streptomycin (Gibco). Cells were pelleted again, re-suspended in DRG culture medium and plated on glass coverslips coated with polyornithine (20 µg/mL, Sigma). Cells were imaged 24 h after plating.

Calcium imaging. DRG neurons were loaded with 2 µM Fura-2, AM (Molecular Probes) in standard extracellular solution (140 mM NaCl, 4 mM KCl, 2 mM CaCl₂, 10 mM HEPES, 5 mM glucose, pH = 7.4 with NaOH) and incubated for 30 min at 37 °C. Coverslips were then washed with standard extracellular ringer solution and left for 15 min at 37 °C and 5% CO₂ and then for another 15 min at room temperature. Cells were excited with 350 and 380 nm for ratiometric measurement of intracellular calcium using Cairn Dual OptoLED system. Cells were viewed using a 40X oil immersion objective. Images were acquired using a Hamamatsu C4742-95 camera. The cells were perfused with standard extracellular solution for at least 5 min to establish stable baseline. All recordings were performed at room temperature (23 ± 1 °C). Drugs were perfused at a flow rate of 3 mL/min. High potassium extracellular solution (104 mM NaCl, 40 mM KCl, 2 mM CaCl₂, 10 mM HEPES, 5 mM glucose, pH = 7.4 with NaOH) was perfused at the end of the recordings, unless mentioned otherwise, as a depolarizing agent to identify viable neurons. *Simple PCI 6* software was used for data acquisition, background subtraction and Fura-2,AM ratiometric measurement (F350/380 nm).

Compounds. All drugs were made to the required working dilution in standard extracellular ringer solution from stock solutions of the following concentrations: VTD (5 mM in ethanol, Abcam ab120279), Capsaicin (10 mM in ethanol, Tocris 0462), α , β -methylene ATP (10 mM in water, Sigma M6517), TTX (30 µM in citrate buffer, Abcam Asc-054), TNP-ATP triethylammonium salt (10 mM in water, Tocris 2464), and allyl isothiocyanate (AITC; 100 µM, Sigma 377430).

Data and statistical analysis. Neurons were identified by their responsiveness to 40 mM KCl. We defined a response as an increase in (F350/380) ratio of > 6 SD above the baseline. Differences in fluorescence ($\Delta F/F_0$) were calculated according to the following formula: F350/380 ratio in the presence of drug (F) during drug application – the mean of F350/380 ratio of the 2.5 min prior to drug application (F₀). Statistical analysis was performed by calculating the mean percentage of responsive neurons (n) from the indicated number of mice for each figure (N). Sample mean of each set of experiments was calculated from multiple independent experiments (as specified in the result section) and compared to each other by one-way analysis of variance (ANOVA) with Sidaks' post-test. Cell diameter measurements were performed using ImageJ software; cell area was obtained from a hand-drawn line delineating the soma. Soma diameter was then calculated using the following formula, Diameter = $\sqrt{(4 \cdot \text{Area} / \pi)}$. For cell size comparison, two-tailed unpaired Student's t-test was used for comparisons. All statistical analysis and comparisons were performed by *GraphPad Prism* software (version 7.00 for Windows). Area-proportional Venn diagrams were generated by *BioVenn* software⁴¹ and colour edited by *CorelDRAW X8* software.

References

1. Wood, J. N. *et al.* Ion channel activities implicated in pathological pain. *Novartis Foundation symposium* **261**, 32–40, discussion 40–54 (2004).
2. Lai, J., Porreca, F., Hunter, J. C. & Gold, M. S. Voltage-gated sodium channels and hyperalgesia. *Annual review of pharmacology and toxicology* **44**, 371–397, doi: 10.1146/annurev.pharmtox.44.101802.121627 (2004).
3. Waxman, S. G. The molecular pathophysiology of pain: abnormal expression of sodium channel genes and its contributions to hyperexcitability of primary sensory neurons. *Pain Suppl* **6**, S133–140 (1999).
4. Felix, J. P. *et al.* Functional assay of voltage-gated sodium channels using membrane potential-sensitive dyes. *Assay and drug development technologies* **2**, 260–268, doi: 10.1089/1540658041410696 (2004).
5. Cao, Z. *et al.* Influence of lipid-soluble gating modifier toxins on sodium influx in neocortical neurons. *The Journal of pharmacology and experimental therapeutics* **326**, 604–613, doi: 10.1124/jpet.108.138230 (2008).
6. Stevens, M., Peigneur, S. & Tytgat, J. Neurotoxins and their binding areas on voltage-gated sodium channels. *Frontiers in pharmacology* **2**, 71, doi: 10.3389/fphar.2011.00071 (2011).
7. Ulbricht, W. Effects of veratridine on sodium currents and fluxes. *Reviews of physiology, biochemistry and pharmacology* **133**, 1–54 (1998).

8. Ulbricht, W. The effect of veratridine on excitable membranes of nerve and muscle. *Ergebnisse der Physiologie, biologischen Chemie und experimentellen Pharmakologie* **61**, 18–71 (1969).
9. Barnes, S. & Hille, B. Veratridine modifies open sodium channels. *The Journal of general physiology* **91**, 421–443 (1988).
10. Farrag, K. J., Bhattacharjee, A. & Docherty, R. J. A comparison of the effects of veratridine on tetrodotoxin-sensitive and tetrodotoxin-resistant sodium channels in isolated rat dorsal root ganglion neurons. *Pflügers Archiv: European journal of physiology* **455**, 929–938, doi: 10.1007/s00424-007-0365-5 (2008).
11. Augusti-Tocco, G. Neuroblastoma culture: an experimental system for the study of cellular differentiation. *Trends in Biochemical Sciences* **1**, 151–154, doi: 10.1016/0968-0004(76)90416-3.
12. Biedler, J. L., Roffler-Tarlov, S., Schachner, M. & Freedman, L. S. Multiple neurotransmitter synthesis by human neuroblastoma cell lines and clones. *Cancer research* **38**, 3751–3757 (1978).
13. Verheugen, J. A., Oortgiesen, M. & Vijverberg, H. P. Veratridine blocks voltage-gated potassium current in human T lymphocytes and in mouse neuroblastoma cells. *The Journal of membrane biology* **137**, 205–214 (1994).
14. Sigel, E. Effects of veratridine on single neuronal sodium channels expressed in *Xenopus* oocytes. *Pflügers Archiv: European journal of physiology* **410**, 112–120 (1987).
15. Teichert, R. W. *et al.* Characterization of two neuronal subclasses through constellation pharmacology. *Proceedings of the National Academy of Sciences of the United States of America* **109**, 12758–12763, doi: 10.1073/pnas.1209759109 (2012).
16. Snider, W. D. & McMahon, S. B. Tackling pain at the source: new ideas about nociceptors. *Neuron* **20**, 629–632 (1998).
17. Lawson, S. N., Caddy, K. W. & Biscoe, T. J. Development of rat dorsal root ganglion neurones. Studies of cell birthdays and changes in mean cell diameter. *Cell and tissue research* **153**, 399–413 (1974).
18. Rambourg, A., Clermont, Y. & Beaudet, A. Ultrastructural features of six types of neurons in rat dorsal root ganglia. *Journal of neurocytology* **12**, 47–66 (1983).
19. Lawson, S. N. Phenotype and function of somatic primary afferent nociceptive neurones with C-, Delta- or Alpha/beta-fibres. *Experimental physiology* **87**, 239–244 (2002).
20. Harper, A. A. & Lawson, S. N. Conduction velocity is related to morphological cell type in rat dorsal root ganglion neurones. *J Physiol* **359**, 31–46 (1985).
21. Cavanaugh, D. J. *et al.* Restriction of transient receptor potential vanilloid-1 to the peptidergic subset of primary afferent neurons follows its developmental downregulation in nonpeptidergic neurons. *The Journal of neuroscience: the official journal of the Society for Neuroscience* **31**, 10119–10127, doi: 10.1523/jneurosci.1299-11.2011 (2011).
22. Ren, A. J. *et al.* ZBTB20 regulates nociception and pain sensation by modulating TRP channel expression in nociceptive sensory neurons. *Nature communications* **5**, 4984, doi: 10.1038/ncomms5984 (2014).
23. Chen, C. C. *et al.* A P2X purinoceptor expressed by a subset of sensory neurons. *Nature* **377**, 428–431, doi: 10.1038/377428a0 (1995).
24. Collo, G. *et al.* Cloning OF P2X5 and P2X6 receptors and the distribution and properties of an extended family of ATP-gated ion channels. *The Journal of neuroscience: the official journal of the Society for Neuroscience* **16**, 2495–2507 (1996).
25. Lewis, C. *et al.* Coexpression of P2X2 and P2X3 receptor subunits can account for ATP-gated currents in sensory neurons. *Nature* **377**, 432–435, doi: 10.1038/377432a0 (1995).
26. Bradbury, E. J., Burnstock, G. & McMahon, S. B. The expression of P2X3 purinoreceptors in sensory neurons: effects of axotomy and glial-derived neurotrophic factor. *Molecular and cellular neurosciences* **12**, 256–268, doi: 10.1006/mcne.1998.0719 (1998).
27. Virginio, C., Robertson, G., Surprenant, A. & North, R. A. Trinitrophenyl-substituted nucleotides are potent antagonists selective for P2X1, P2X3, and heteromeric P2X2/3 receptors. *Molecular pharmacology* **53**, 969–973 (1998).
28. Seal, R. P. *et al.* Injury-induced mechanical hypersensitivity requires C-low threshold mechanoreceptors. *Nature* **462**, 651–655, doi: 10.1038/nature08505 (2009).
29. Usoskin, D. *et al.* Unbiased classification of sensory neuron types by large-scale single-cell RNA sequencing. *Nature Neuroscience* **18**, 145–153, doi: 10.1038/nn.3881 (2015).
30. Jordt, S. E. *et al.* Mustard oils and cannabinoids excite sensory nerve fibres through the TRP channel ANKTM1. *Nature* **427**, 260–265, doi: 10.1038/nature02282 (2004).
31. Barabas, M. E., Kossyeva, E. A. & Stucky, C. L. TRPA1 is functionally expressed primarily by IB4-binding, non-peptidergic mouse and rat sensory neurons. *PloS one* **7**, e47988, doi: 10.1371/journal.pone.0047988 (2012).
32. Paulsen, C. E., Armache, J. P., Gao, Y., Cheng, Y. & Julius, D. Structure of the TRPA1 ion channel suggests regulatory mechanisms. *Nature* **520**, 511–517, doi: 10.1038/nature14367 (2015).
33. Romey, G. & Lazdunski, M. Lipid-soluble toxins thought to be specific for Na⁺ channels block Ca²⁺ channels in neuronal cells. *Nature* **297**, 79–78 (1982).
34. Lu, S. G., Zhang, X. & Gold, M. S. Intracellular calcium regulation among subpopulations of rat dorsal root ganglion neurons. *J Physiol* **577**, 169–190, doi: 10.1113/jphysiol.2006.116418 (2006).
35. Liu, C. J. *et al.* A high-capacity membrane potential FRET-based assay for Nav1.8 channels. *Assay and drug development technologies* **4**, 37–48, doi: 10.1089/adt.2006.4.37 (2006).
36. Djouhri, L. *et al.* The TTX-resistant sodium channel Nav1.8 (SNS/PN3): expression and correlation with membrane properties in rat nociceptive primary afferent neurons. *J Physiol* **550**, 739–752, doi: 10.1113/jphysiol.2003.042127 (2003).
37. Schmidt, R. *et al.* Novel classes of responsive and unresponsive C nociceptors in human skin. *The Journal of neuroscience: the official journal of the Society for Neuroscience* **15**, 333–341 (1995).
38. Lou, J. Y. *et al.* Fibroblast growth factor 14 is an intracellular modulator of voltage-gated sodium channels. *J Physiol* **569**, 179–193, doi: 10.1113/jphysiol.2005.097220 (2005).
39. Wada, A., Yanagita, T., Yokoo, H. & Kobayashi, H. Regulation of cell surface expression of voltage-dependent Nav1.7 sodium channels: mRNA stability and posttranscriptional control in adrenal chromaffin cells. *Frontiers in bioscience: a journal and virtual library* **9**, 1954–1966 (2004).
40. Teichert, R. W. *et al.* Functional profiling of neurons through cellular neuropharmacology. *Proceedings of the National Academy of Sciences of the United States of America* **109**, 1388–1395, doi: 10.1073/pnas.1118833109 (2012).
41. Hulsen, T., de Vlieg, J. & Alkema, W. BioVenn – a web application for the comparison and visualization of biological lists using area-proportional Venn diagrams. *BMC Genomics* **9**, 1–6, doi: 10.1186/1471-2164-9-488 (2008).
42. Onizuka, S. *et al.* Capsaicin indirectly suppresses voltage-gated Na⁺ currents through TRPV1 in rat dorsal root ganglion neurons. *Anesthesia and analgesia* **112**, 703–709, doi: 10.1213/ANE.0b013e318204ea5b (2011).

Acknowledgements

The authors would like to thank Dr. Elizabeth Seward and Dr. Claudia Bauer for their critical comments on manuscript. Keith Woodley for his help with *BioVenn* software and all the members of Grundy and Seward labs for their comments and discussions.

www.nature.com/scientificreports/

Author Contributions

M.A.N., conceived, designed and supervised experiments. Z.A.M., co-designed, carried out and analysed all experiments. D.G., contributed reagents and equipment. C.D., trained Z.A.M. on calcium imaging and advised on some experiments. M.A.N. and Z.A.M. wrote the manuscript. D.G. and C.D. commented on manuscript.

Additional Information

Supplementary information accompanies this paper at <http://www.nature.com/srep>

Competing Interests: The authors declare no competing financial interests.

How to cite this article: Mohammed, Z. A. *et al.* Veratridine produces distinct calcium response profiles in mouse Dorsal Root Ganglia neurons. *Sci. Rep.* 7, 45221; doi: 10.1038/srep45221 (2017).

Publisher's note: Springer Nature remains neutral with regard to jurisdictional claims in published maps and institutional affiliations.



This work is licensed under a Creative Commons Attribution 4.0 International License. The images or other third party material in this article are included in the article's Creative Commons license, unless indicated otherwise in the credit line; if the material is not included under the Creative Commons license, users will need to obtain permission from the license holder to reproduce the material. To view a copy of this license, visit <http://creativecommons.org/licenses/by/4.0/>

© The Author(s) 2017

Veratridine produces distinct calcium response profiles in mouse Dorsal Root Ganglia neurons

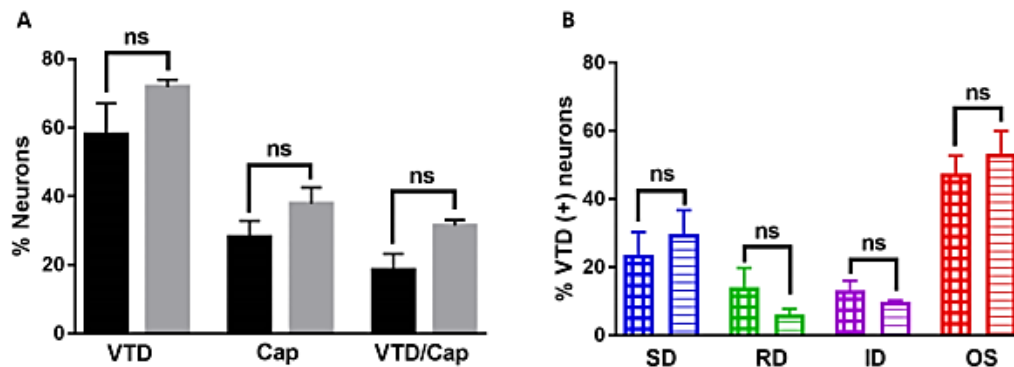
Zainab A Mohammed, Ciara Doran, David Grundy and Mohammed A Nassar*

Biomedical Science, University of Sheffield, Sheffield S102TN, UK

*Corresponding Author m.nassar@sheffield.ac.uk

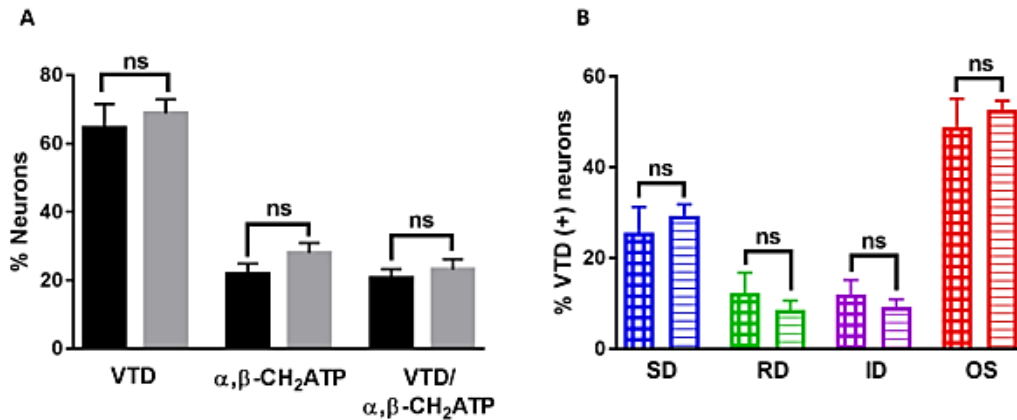
Supplementary figures to Zainab et al

Figure S1:

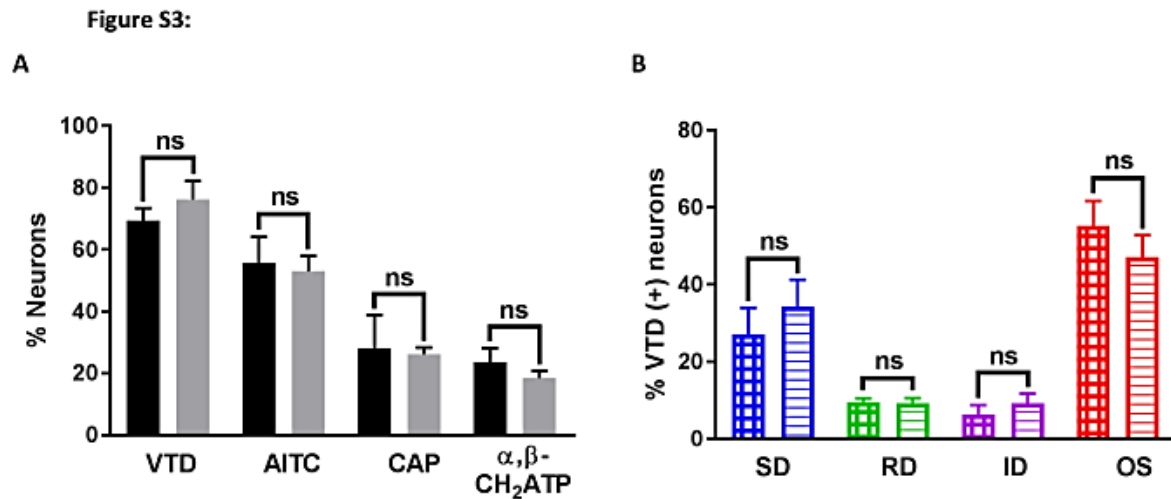


Supplementary S1: Order of veratridine and capsaicin application does not affect VTD response profiles. A. Percentage of neurons that responded to VTD, capsaicin (CAP) and VTD plus capsaicin (VTD+/CAP+) when VTD was applied before 1 μ M capsaicin (black bars; N = 5 mice, n = 200 cell) and when VTD was applied after 200 nM capsaicin (grey bars; N = 3 mice, n = 379 cell). Percent responses between VTD first and VTD second protocols were not significantly different. Percent of neurons responsive to VTD (58 ± 9 %, 112 cell vs. 71.8 ± 2 %, n = 274 cell); percent of neurons sensitive to capsaicin (28.1 ± 5 %, n = 59 cell vs. 37.9 ± 4.6 %, n = 164 cell) and percent of neurons responsive to both VTD and capsaicin (31.5 ± 1.6 %, n = 119 cell vs. 18.5 ± 5 %, n = 37 cell) were not different. **B.** The frequency of occurrence of the four VTD profiles is not different when VTD is applied first (crossed bars, N = 3 mice) and second (horizontal lines, N = 3 mice). The frequencies for SD response profile are (23.6 ± 7 %, n = 29 cell vs. 29.7 ± 7 %, n = 82 cell), for RD response profile are (14.1 ± 6 %, n = 13 cell vs. 6.3 ± 2 %, n = 17 cell), for ID response profile are (13.2 ± 3 %, n = 15 cell vs. 9.8 ± 0.4 %, n = 27 cell) and for OS response profile are (47.5 ± 5 %, n = 53 cell vs. 53.3 ± 7 %, n = 145 cell). Data shown are mean \pm SEM. One-way analysis of variance with Sidak's post-test.

Figure S2:



Supplementary S2: the order of veratridine and α, β -methylene ATP application does not affect VTD response profiles. **A.** Percentage of neurons that responded to VTD, α, β -methylene ATP (α, β -CH₂ATP) and VTD plus α, β -methylene ATP (VTD/ α, β -CH₂ATP) when VTD was applied before α, β -methylene ATP (black bars; N = 3 mice, n = 294 cell) and when VTD was applied after α, β -methylene ATP (grey bars; N = 6 mice, n = 1051 cell). Percent responses between VTD first and VTD second protocols were not significantly different. Percent of neurons responsive to VTD (64.7 ± 7 , n = 201 cell vs. 68.8 ± 4 %, n = 711 cell); percent of neurons sensitive to α, β -methylene ATP (21.8 ± 3 %, n = 69 cell vs. 27.9 ± 3 %, n = 275 cell); and percent of neurons sensitive to both VTD and capsaicin (20.7 ± 3 %, n = 65 cell vs. 23.2 ± 3 %, n = 224 cell) are not different. **B.** The frequency of occurrence of the four VTD profiles is not different when VTD is applied first (crossed lines, N = 3 mice) and second (horizontal lines, N = 6 mice). The frequencies for the SD response profile are (25.6 ± 6 , n = 50 cell vs. 29.4 ± 3 %, n = 208 cell), for the RD response profile are (12.3 ± 5 %, n = 20 cell vs. 8.6 ± 2 %, n = 62 cell), for the ID response profile are (12 ± 3 %, n = 20 cell vs. 9.2 ± 2 %, n = 70 cell) and for the OS response profile are (48.9 ± 6 %, n = 108 cell vs. 52.7 ± 2 %, n = 370 cell). Data shown are mean \pm SEM. One-way analysis of variance with Sidak's post-test.



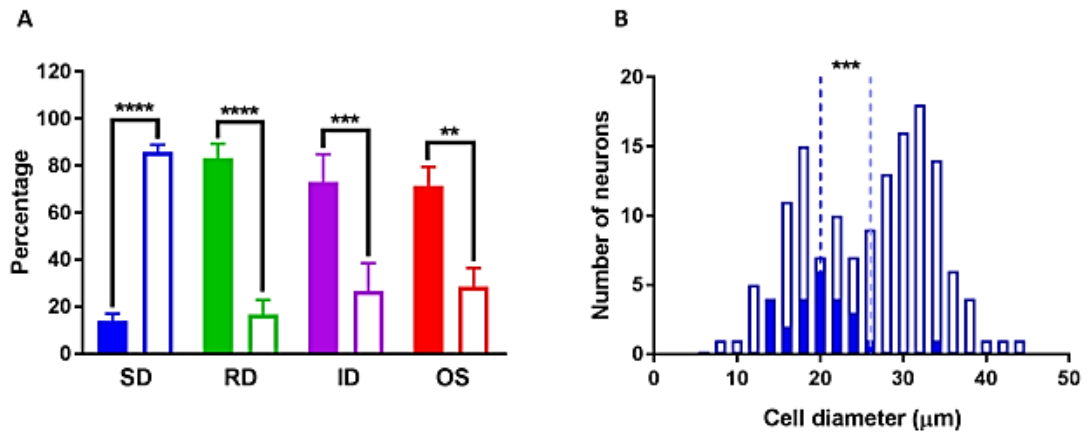
Supplementary S3: The order of Veratridine, α, β-methylene ATP, capsaicin and AITC application

does not affect VTD response profiles. A. Percentage of neurons responding to VTD,

allysiothiocyanate (AITC), capsaicin (CAP), and α, β-methylene ATP (α, β-CH₂ATP) when VTD was applied first (black bars; N = 3 mice, n = 220 cell) and when VTD was applied third (grey bars; N = 4 mice, n = 451 cell). Percent responses between VTD first and VTD second protocols were not significantly different. Percent of neurons responsive to VTD ($69.4 \pm 4\%$, n = 150 cell vs. $76.3 \pm 6\%$, n = 361 cell), AITC ($55.7 \pm 8.5\%$, n = 128 cell, vs. $53.1 \pm 5\%$, n = 229 cell), CAP ($28 \pm 11\%$, n = 58 cell vs. $26.2 \pm 2.1\%$, n = 115), and α, β-methylene ATP ($23.7 \pm 4.4\%$, n = 54 cell vs. $18.5 \pm 2.3\%$, n = 87 cell) are not different.

B. The frequency of occurrence of the four VTD profiles is not different when VTD is applied first (crossed bars, N = 3 mice) and third (horizontal lines, N = 4 mice). The frequencies for the SD response profile are ($27.1 \pm 6.9\%$, n = 13 cell vs. $34.3 \pm 7\%$, n = 38 cell), for the RD response profile are ($9.5 \pm 1\%$, n = 15 cell vs. $9.3 \pm 1.3\%$, n = 26 cell), for the ID response profile are ($6.3 \pm 2.5\%$, n = 9 cell vs. $9.3 \pm 2.5\%$, n = 26 cell) and for the OS response profile are ($55.2 \pm 6.5\%$, n = 71 cell vs. $47.2 \pm 5.6\%$, n = 135 cell). Data shown are mean ± SEM. One-way analysis of variance with Sidak's post-test.

Figure S4:



Supplementary S4: Relationship between AITC sensitivity and the four veratridine profiles. A. This data is extracted from data presented in figure 6. The proportion of AITC-sensitive (closed bars) and AITC-insensitive neurons (open bars) within each of the four VTD response profiles. Significantly a larger proportion of neurons with the SD (86 vs. 14 + 3 %) profile is insensitive to AITC. In contrast, significantly a larger proportion of neurons with the RD (83.2 vs. 16.8 + 6.2 %), ID (73.2 vs. 16.8 + 11.7 %) and OS (71.5 vs. 28.5 + 8 %) profiles are sensitive to AITC. Percentages were calculated from total number of neurons in each profile ($n_{(SD)} = 168$, $n_{(RD)} = 44$, $n_{(ID)} = 48$, and $n_{(OS)} = 251$ neuron). Data shown are mean \pm SEM. One-way analysis of variance with Sidak's post-test, $^{**}P < 0.01$, $^{***}P < 0.001$ and $^{****}P < 0.0001$. **B.** Histogram of diameter of neurons with the SD response profile showing that neurons sensitive to AITC (closed bars; mean $20 \pm 0.9 \mu\text{m}$, median $19.5 \mu\text{m}$, $n = 25$ cell) are significantly smaller than neurons insensitive to AITC (open bars; mean $26.1 \pm 0.6 \mu\text{m}$, median $27.9 \mu\text{m}$, $n = 143$ cell). Dotted lines indicate the mean. Two-tailed unpaired Student's t-test, $^{*}P < 0.05$.

CHAPTER 4

DIFFERENTIAL EFFECTS OF
VGSC BLOCKERS ON VTD
CALCIUM RESPONSE PROFILES
IN MOUSE DRG NEURONS

Chapter 4: Differential effects of VGSC blockers on VTD calcium response profiles in mouse DRG neurons

4.1. Introduction:

The previous results demonstrated the potential use of the VTD response profiles as nociceptor markers. The interplay between VGSC and other receptors and ion channels resulted in such distinct calcium responses, however, the contribution of the different ion channel classes is unknown. Genetic and pharmacological approaches are both beneficial to dissect the role of individual component in shaping VTD responses. However, each approach has its own limitation. Pharmacological blockers are widely available, affordable, faster and produces minimum changes to the ion channel/receptor constellation of the neurons than the genetic approaches, but unfortunately the specificity of the pharmacological blocker in hands is always questionable due to the high degree of homology between the ion channel subtypes and due to species differences. Therefore, this approach is highly limited by the availability of validated specific ion channel subtype blockers. On the other hand, gene ablation is specifically targeted but it might be accompanied by upregulation / downregulation of other ion channels that could also contributes to the VTD responses¹¹². Nevertheless, none of the two approaches are dispensable and marrying the two (if applicable) in the same study would clearly elucidate the role of the ion channel of interest.

In this chapter I focused on the contribution of two major VGSC subtypes in eliciting distinct VTD calcium responses. Nav1.7 and Nav1.8 are the main TTX-S and TTX-R VGSC subtypes expressed in mouse sensory neurons, respectively. Nav1.7 is widely expressed in all sensory neurons while Nav1.8 is mainly expressed in nociceptor³⁹. Both subtypes play an essential role in eliciting peripheral pain signals as discussed previously. Arylsulfonamide inhibitor (PF-04856264) was used as a specific Nav1.7 blockers, while A803467 compound was used as a specific Nav1.8 blocker.

- **Arylsulfonamide (PF-04856264)**

PF-04856264 is a selective Nav1.7 inhibitor that belongs to the arylsulfonamide family. PF-04856264 is 1000 folds more selective to hNav1.7 than other VGSC subtypes (hNav1.3, hNav1.8, hNav1.4 and hNav1.5), 100 folds higher than Nav1.1 and 10 folds higher than hNav1.2 and Nav1.6 in HEK293 cells ^{244,245}. PF-04856264 shows high state-dependence mode of action. Upon activation of the channel, an outward movement of the voltage-sensor domain 4 (VSD4) translocates a critical arginine group on the S4 and expose it to the extracellular binding cleft which acts as a clamp-shell that traps PF-04856264 within the binding site, Fig. 4.1. Subsequent to S4 outward movement, the inactivation gate closes the intracellular channel pore which result in an open-state inactivation (as described previously in Fig. 1.4). The binding of PF-04856264, however, locks the VSD4 in its inactivated conformation and delays its recovery to the resting conformation. i.e. stabilizes the channel in a non-conducting conformation. This state-dependency is evident by crystallographic ¹ as well as electrophysiological methods ²⁴⁴⁻²⁴⁶, where PF-04856264 preferentially binds to the channel in its inactivated conformation 1000 folds higher than its resting conformation [IC50: 11 nM vs. 10 μ M], respectively ²⁴⁵. Voltage-sensor trapping mechanism is also shared by other site-3 toxins like α -scorpion and sea anemone. However, unlike arylsulfonamides, site-3 toxins bind the channel in its resting conformation, preventing the outward movement of the S4 which results in inhibition of channel activation.

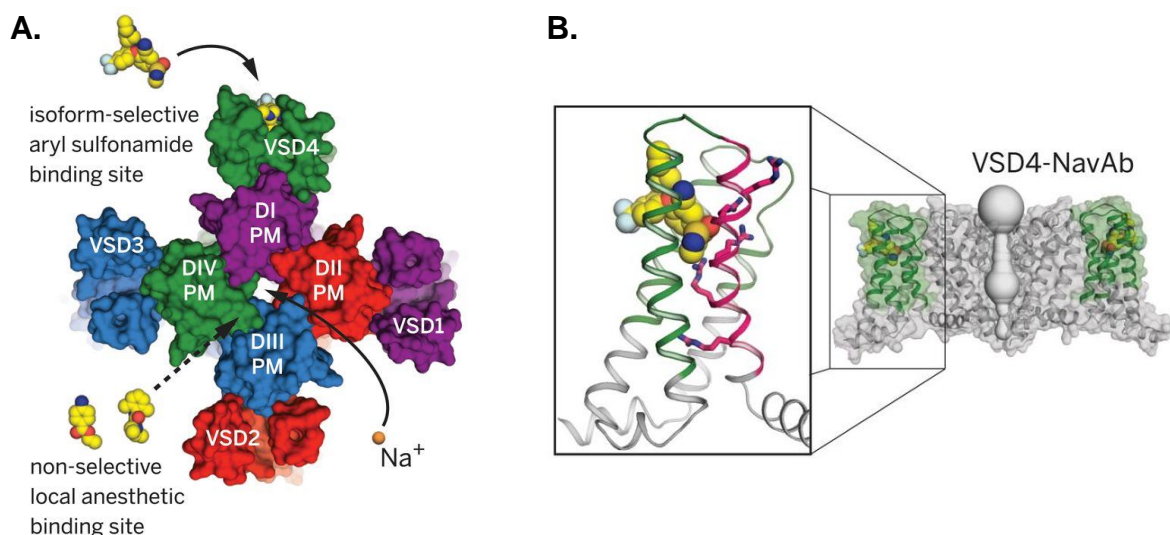


Figure 4.1: Aryl sulfonamide binding site in α -subunit of VGSC. A. Illustration of the binding site of arylsulfonamide to VSD4 in top view. B. Side view of the VSD4 domain that illustrates the interaction of aryl sulfonamides with S4 transmembrane helix (positively charged arginine containing segment, pink color). Source: (Ahuja et al, 2015) ¹.

- **A-803467:**

Nav1.8 has higher activation threshold than TTX-S VGSC. Nav1.8 contribution to the VTD response profiles is likely secondary to TTX-S channel activation or, less likely, by direct binding and activation by VTD. In either case, inhibition of Nav1.8 channel by a specific blocker would reveal its contribution to VTD response profiles.

A-803467 [5-(4-Chlorophenyl) furan-2-carboxylic acid (3,5-dimethoxyphenyl) amide] was identified via structure-activity relationship studies of TTX-R VGSC inhibitors at Abbott Laboratories. The presence of the furan-amide structure is essential for Nav1.8 selectivity. A-803467 was tested in patch-clamp electrophysiology on rat DRG neurons and recombinant hNav1.8. The drug shows a high level of selectivity toward recombinant hNav1.8 over the other VGSC subtypes (>100 folds). It shows a preferential binding affinity toward the inactivated state of the VGSC, nevertheless, it blocked both open and inactivated states of the channel at nanomolar concentration²⁴⁷.

4.2. Aim:

To investigate the contribution of the two major VGSC subtypes in DRG neurons; Nav1.7 (TTX-S) and Nav1.8 (TTX-R) in shaping VTD calcium response profiles by using specific pharmacological blockers, PF-04856264 and A-803467.

4.3. Methods:

PF-04856264 is a potent inhibitor of Nav1.7 at nanomolar concentration ($IC_{50} = 28 \pm 5$ nM), mostly used at 1 μ M in in vitro assays²⁴⁴. However, it has been shown that co-application of PF-04856264 with OD-1 (VGSC agonist) decreases PF-04856264 potency in CHO cells²⁴⁸. Therefore, to overcome the potential loss of potency due to co-application of the blockers with VTD, two concentrations of PF-04856264 (1 μ M and 5 μ M) and two concentrations of A-803467 (100 nM and 300 nM) were tested to examine the contribution of Nav1.7 and Nav1.8 in eliciting VTD response profiles, respectively.

DRG neurons were incubated with the intended concentration of the drug or the vehicle (control) during Fura-2AM wash period. Cells were superfused with standard extracellular solution containing the working dilution of the drug or its vehicle during

field and ROI selection and baseline recording to ensure consistent concentration level of the drug. 30 μ M of VTD + Drug/vehicle were perfused for 3 min and then washed away with standard extracellular solution for at least 10 min. At the end of each experiment, high potassium (40 mM) extracellular solution was perfused as a positive control to identify viable cells as well as an indicator for immediate onset to response, Fig. 4.2.

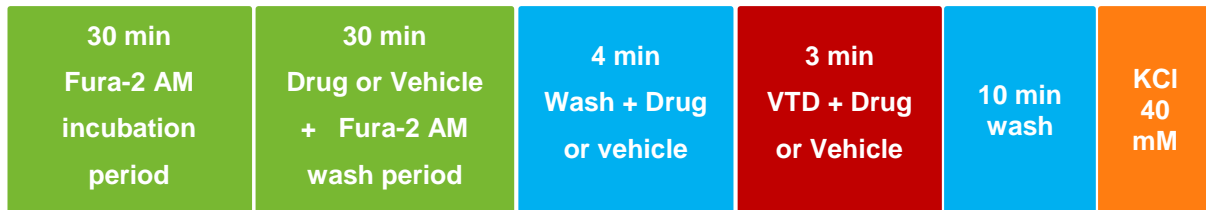


Figure 4.2: Illustration of the calcium imaging protocol used in the experiments presented in this chapter. Fura-2AM was incubated with the cells for 30 min, followed by wash period and drug incubation for another 30 min. application of VTD and the drug mixture started after achieving a stable baseline. VTD wash period took usually 10 min followed by application of high potassium solution to identify viable cells.

4.4. Results:

Nav1.7 BLOCKER (PF-04856264) RESULTS:

4.4.1. PF-04856264 (5 μ M) reduces all VTD response profiles.

Analysis of the inhibitory effect of the two PF-04856264 concentrations in the presence of VTD showed a dose-dependent inhibition in the percentage of VTD responding neurons, in which almost 30 % and 50 % of the VTD responses were inhibited by 1 μ M and 5 μ M PF-04856264 concentrations, respectively, Fig. 4.3. Next, I examined the percentage of occurrence of each of the VTD response profiles in the presence of PF-04856264, calculated from the total number of neurons. The data showed a small but significant reduction only in the OS responses in the presence of 1 μ M of the blocker (OS_{CTR} 27.2 % vs OS_{PF-048} 16.9 %), Fig. 4.4 (A-C), whilst higher concentration (5 μ M) produced a significant inhibition in three of the VTD response profiles (SD_{CTR} 13.2 vs SD_{PF-048} 6.3; OS_{CTR} 28.1 vs OS_{PF-048} 12.4; ID_{CTR} 7.9 vs ID_{PF-048} 5.8), and non-significant reduction in the RD response profile, (RD_{CTR} 7.7 vs RD_{PF-048} 4.3), Fig. 4.4 (D-F).

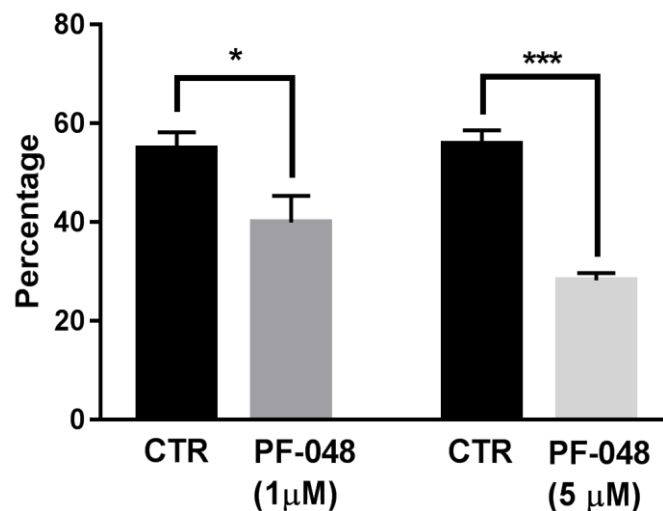


Figure 4.3: The effect of PF-04856264 on the total number of VTD responding neurons. The percentage of VTD responses were significantly inhibited in the presence of PF-04856264. The mean percentage of VTD responding neurons in the presence of 1 μ M of PF-04856264. Control = 55 \pm 3.2 %, PF-048 = 40 \pm 5.4 %. The mean percentage of VTD responding neurons in the presence of 5 μ M of PF-04856264. Control = 56 \pm 2.7 %, PF-048 = 28.2 \pm 1.5 %.

Two-tailed paired Student's t-test, * P < 0.05 and *** P < 0.001. For 1 μ M experiments: N = 5 DRG cultures, $n_{(CTR)}$ = 490 cells, $n_{(PF-048)}$ = 508 cells. For 5 μ M: N = 5 DRG cultures, $n_{(CTR)}$ = 605 cells, $n_{(PF-048)}$ = 338 cells. Error bars represent SEM.

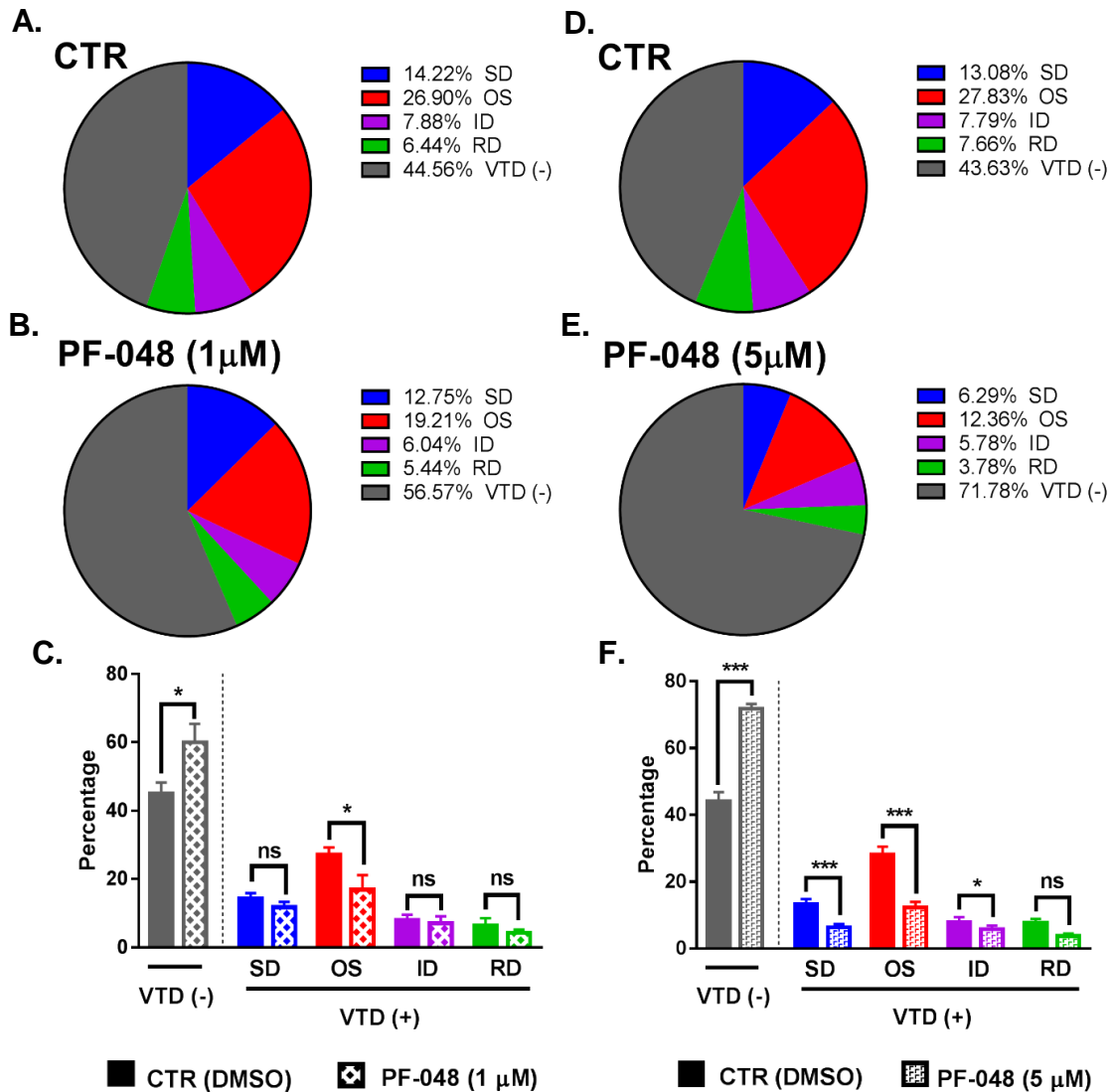


Figure 4.4: Analysis of the inhibitory effect of PF-04856264 on VTD response profiles. PF-04856264 showed a significant inhibition of OS response profiles at low concentration (1 μM) and significant inhibition of all VTD response profiles, except RD, at a higher concentration (5 μM).

A and B. Pie chart representation of the mean percentage of VTD responding (coloured) and non-responding (grey) neurons in control (A) and 1 μM PF-048 (B).

C. Comparison between the number of VTD responding and non-responding neurons in (A & B). Only OS response profile is significantly inhibited. Percentages were calculated from the total number of neurons. $VTD(-)_{CTR} = 45 \pm 3.2$, $VTD(-)_{PF-048} = 60.1 \pm 5.4$; $SD_{CTR} = 14.4 \pm 1.5$, $SD_{PF-048} = 11.7 \pm 1.6$, $OS_{CTR} = 27.2 \pm 2.1$, $OS_{PF-048} = 16.9 \pm 4.3$, $ID_{CTR} = 8 \pm 1.6$, $ID_{PF-048} = 7 \pm 2$, $RD_{CTR} = 6.5 \pm 2$, $RD_{PF-048} = 4.8 \pm 1$ %.

D and E. Pie chart representation of the mean percentage of VTD responding (coloured) and non-responding (grey) neurons in control (E) and 5 μM PF-048564 (F).

F. Comparison between the number of VTD responding and non-responding neurons in (D & E).

All VTD responses are significantly inhibited except for the RD response profile. Percentages were calculated from the total number of neurons. $VTD(-)_{CTR} = 44.1 \pm 2.7$, $VTD(-)_{PF-048} = 71.8 \pm 1.5$; $SD_{CTR} = 13.2 \pm 1.6$, $SD_{PF-048} = 6.3 \pm 1$, $OS_{CTR} = 28.1 \pm 2.4$, $OS_{PF-048} = 12.4 \pm 1.6$, $ID_{CTR} = 7.9 \pm 1.6$, $ID_{PF-048} = 5.8 \pm 1.1$, $RD_{CTR} = 7.7 \pm 1.2$, $RD_{PF-048} = 3.8 \pm 0.7$ %.

Two-tailed paired Student's t-test, * $P < 0.05$, ** $P < 0.01$ and *** $P < 0.001$. For 1 μM experiments: $N = 5$ DRG cultures, $n_{(CTR)} = 490$ cells, $n_{(PF-048)} = 508$ cells. For 5 μM: $N = 5$ DRG cultures, $n_{(CTR)} = 605$ cells, $n_{(PF-048)} = 338$ cells. Error bars represent SEM.. Error bars represent SEM.

4.4.2. PF-04856264 (5 μ M) reduces the relative frequency of the OS response profile.

To examine the relative change in frequency of occurrence of each VTD response profile between control and PF-04856264, VTD response profiles were calculated as a percentage from the total number of VTD responding neurons. The analysis showed that at the lower concentration of the blocker (1 μ M), VTD responses were equally affected with no obvious inhibitory preference toward any particular profile, Fig.4.5,A. However, in the presence of 5 μ M concentration of the blocker, a significant reduction in the OS response profile with a concomitant increase in the ID response profile (OS_{CTR} 50.2 vs OS_{PF-048} 43.5; ID_{CTR} 14.7 vs ID_{PF-048} 20.9), Fig. 4.5,B. Altogether, these results suggest that although PF-04856264 application resulted in reduced VTD responding neurons of all types, the OS-responding neurons were the most affected among all the other response profiles.

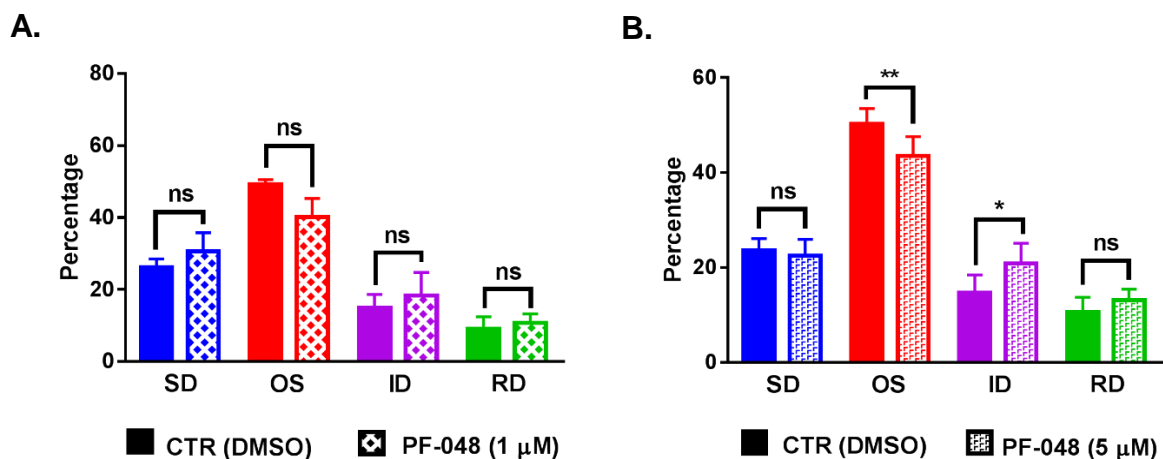


Figure 4.5: Comparison of the relative frequency of each VTD response profile in the presence of PF-04856264.

A. Comparison between the number of VTD responding and non-responding neurons. Low concentration of the blocker (1 μ M) equally inhibited all VTD response profiles with no particular preference. Percentages were calculated from the total number of neurons. VTD(-)_{CTR} = 44.1 \pm 2.7, VTD(-)_{PF-048} = 71.8 \pm 1.5; SD_{CTR} = 13.2 \pm 1.6, SD_{PF-048} = 6.3 \pm 1, OS_{CTR} = 28.1 \pm 2.4, OS_{PF-048} = 12.4 \pm 1.6, ID_{CTR} = 7.9 \pm 1.6, ID_{PF-048} = 5.8 \pm 1.1, RD_{CTR} = 7.7 \pm 1.2, RD_{PF-048} = 3.8 \pm 0.7 %.

B. Comparison between the relative change in the VTD response profiles. Higher concentration of the blocker (5 μ M) showed a significant inhibition of the OS responses with a concomitant increase in the ID responses. Percentages were calculated from the total number of VTD responding neurons. SD_{CTR} = 23.6 \pm 2.4, SD_{PF-048} = 22.5 \pm 3.4, OS_{CTR} = 50.2 \pm 3.3, OS_{PF-048} = 43.5 \pm 4.1, ID_{CTR} = 14.7 \pm 3.8, ID_{PF-048} = 20.9 \pm 4.3, RD_{CTR} = 10.7 \pm 3, RD_{PF-048} = 13.2 \pm 2.3 %.

Two-tailed paired Student's t-test, *P < 0.05, **P < 0.01 and ***P < 0.001. For 1 μ M experiments: N = 5 DRG cultures, n_(CTR) = 490 cells, n_(PF-048) = 508 cells. For 5 μ M: N = 5 DRG cultures, n_(CTR) = 605 cells, n_(PF-048) = 338 cells. Error bars represent SEM.. Error bars represent SEM.

To further characterize the OS profile, I classified the OS responses into two main classes: responses that continued to elicit in the wash period after the end of VTD application (persistent oscillations), and responses that elicited only during VTD application (Non-persistent oscillations), Figure 4.6, (A). Analysis of the percentages of the two classes in the presence of both concentrations of PF-04856264 showed no significant differences between the two OS subtypes, Figure 4.6, (B). This data suggests that PF-04856264 at both concentrations partly inhibits the initiation of the OS responses but has no further consequences on the oscillatory pattern of the “uninhibited” OS responses.

4.4.3. PF-04856264 has no effect on the maximum peak amplitude and on the area under the curve (AUC) of VTD responses.

To further investigate the effect of PF-04856264 on VTD response profiles. Various parameters were investigated including the maximum peak amplitude and the area under the curve of the responses as described in section (2.2.15.1). Analysis of the maximum peak amplitude of each VTD response profile showed no significant difference between control and PF-04856264 at both concentrations, Fig.4.7, (A & B). Similarly, the area under the curve of the VTD responses were also unchanged, Fig. 4.7, (C & D). Notably, there was no significant difference in the peak amplitudes of all the responses between PF-04856264 treated and control group.

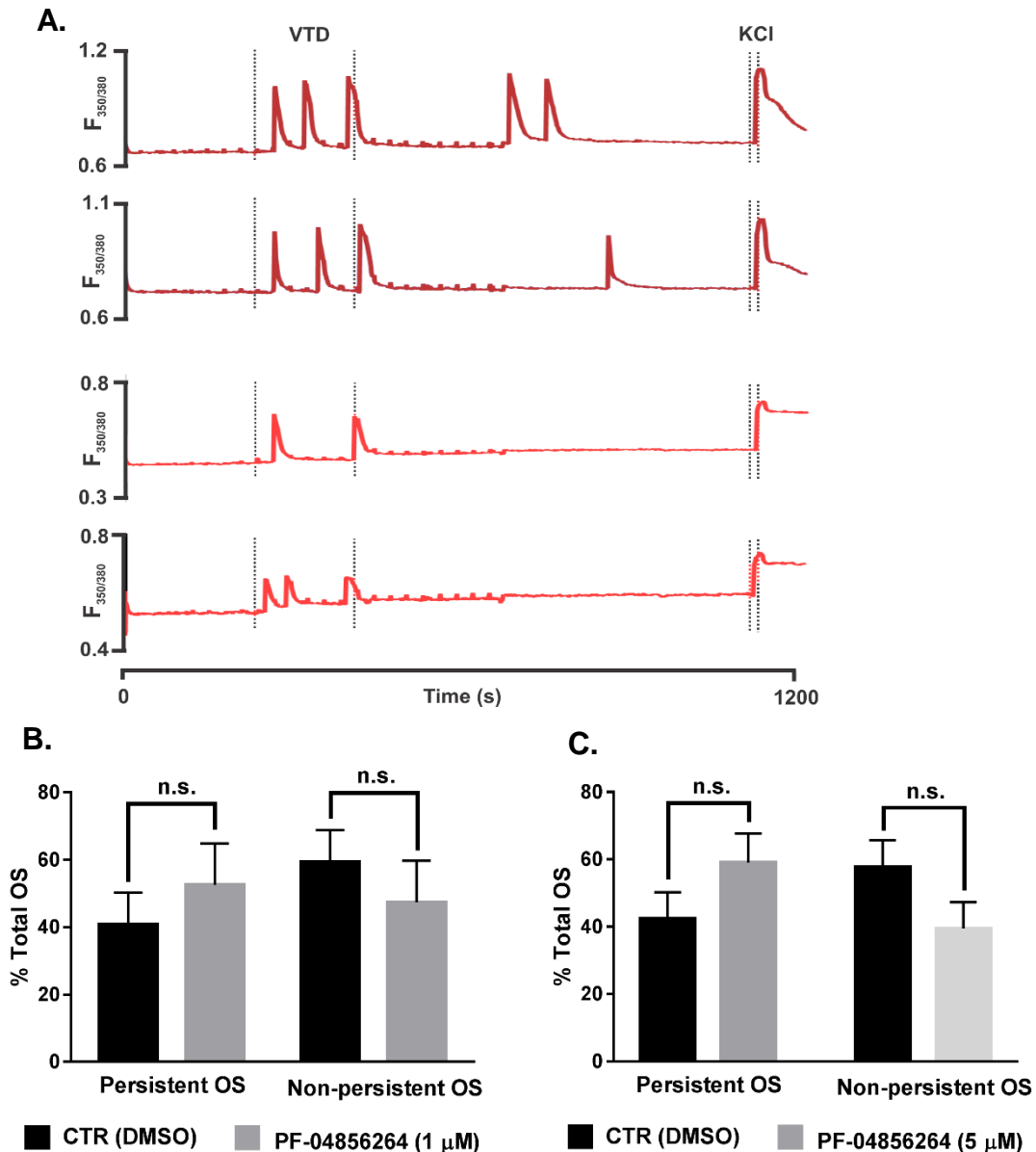


Figure 4.6: Analysis of the effect of PF-04856264 on the oscillatory pattern of OS responding neurons.

A. Example traces of the two classes of OS response profile. Top two traces represent the class of persistent oscillation (P_{OS}) where the oscillatory peaks persisted even after the end of the VTD application period, while the bottom two traces represent the non-persistent oscillation class (NP_{OS}) where the oscillatory peaks stopped immediately after the end of the VTD application. Each trace represents the response of a single neuron. Dotted lines indicate the start and the end of the stimulus application (VTD and KCl).

B. Comparison of the mean percentage of OS subtypes (Persistent & Non-persistent) between control and 1 μM PF-04856264 showed no significant difference between the drug and the control group. $P_{OS, CTR} = 40.7 \pm 9.5\%$, $P_{OS, PF-048} = 52.6 \pm 12.3\%$; $NP_{OS, CTR} = 59.3 \pm 9.5\%$, $NP_{OS, PF-048} = 47.4 \pm 12.3\%$.

C. Comparison of the mean percentage of OS subtypes (Oscillatory and stable) between control and 5 μM PF-04856264 showed no significant difference between the drug and the control group. $P_{OS, CTR} = 42.3 \pm 7.9\%$, $P_{OS, PF-048} = 59 \pm 8.7\%$; $NP_{OS, CTR} = 57.7 \pm 7.9\%$, $NP_{OS, PF-048} = 39.4 \pm 7.8\%$. Two-tailed paired Student's *t*-test, $*P < 0.05$. For 1 μM experiments: $N = 5$ DRG cultures, $n_{(CTR)} = 490$ cells, $n_{(PF-048)} = 508$ cells. For 5 μM : $N = 5$ DRG cultures, $n_{(CTR)} = 605$ cells, $n_{(PF-048)} = 338$ cells. Error bars represent SEM.. Error bars represent SEM.

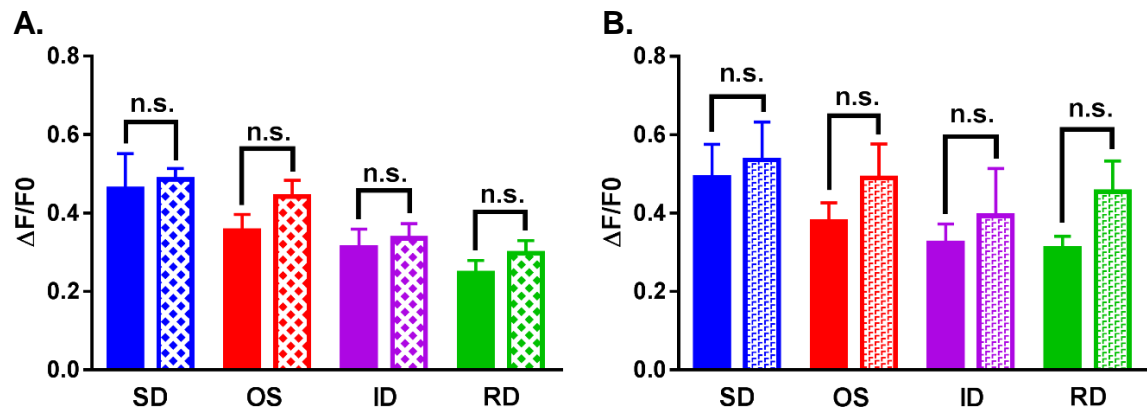
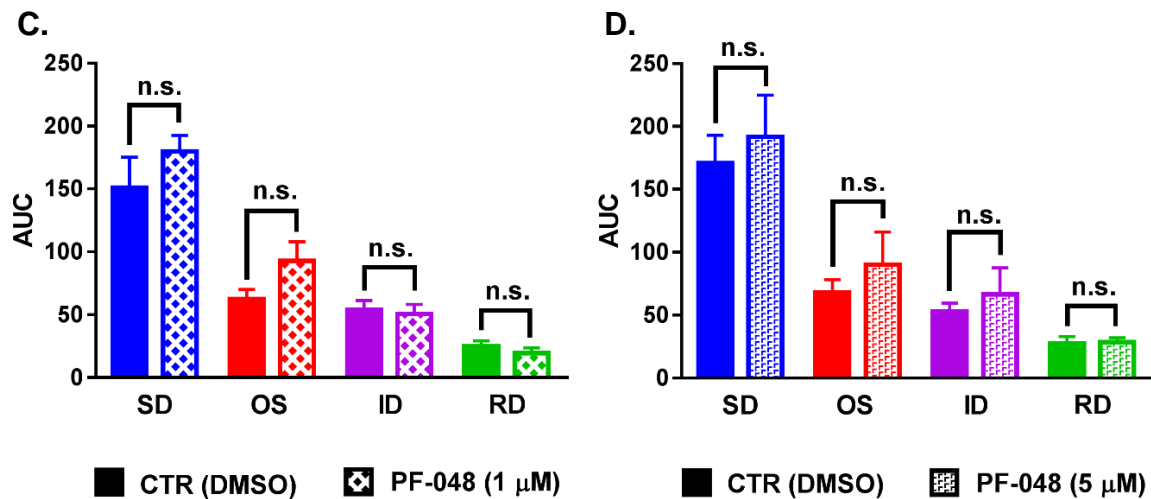
Maximum VTD peak amplitude**Area under the curve**

Figure 4.7: Analysis of the effect of PF-04856264 on the maximum VTD peak responses and their area under the curve.

A & B show no effect of PF-04856264 on VTD peak amplitude in each response profile. C&D show no effect of PF-04856264 on VTD area under the curve in each response profile.

A. Comparison of the VTD peak amplitude in each response profile between control and 1 μM PF-04856264. $SD_{CTR} = 0.46 \pm 0.09$, $SD_{PF-048} = 0.49 \pm 0.03$, $OS_{CTR} = 0.35 \pm 0.04$, $OS_{PF-048} = 0.44 \pm 0.04$, $ID_{CTR} = 0.31 \pm 0.05$, $ID_{PF-048} = 0.33 \pm 0.04$, $RD_{CTR} = 0.25 \pm 0.03$, $RD_{PF-048} = 0.3 \pm 0.03$.

B. Comparison of the VTD peak amplitude in each response profile between control and 5 μM PF-04856264. $SD_{CTR} = 0.5 \pm 0.09$, $SD_{PF-048} = 0.54 \pm 0.1$, $OS_{CTR} = 0.38 \pm 0.05$, $OS_{PF-048} = 0.49 \pm 0.09$, $ID_{CTR} = 0.32 \pm 0.05$, $ID_{PF-048} = 0.39 \pm 0.12$, $RD_{CTR} = 0.31 \pm 0.03$, $RD_{PF-048} = 0.45 \pm 0.08$.

C. Comparison of the area under the curve (AUC) of the VTD responses in each response profile between control and 1 μM PF-04856264. $SD_{CTR} = 151.1 \pm 24.2$, $SD_{PF-048} = 180 \pm 12.9$, $OS_{CTR} = 62.4 \pm 7.6$, $OS_{PF-048} = 92.9 \pm 15.1$, $ID_{CTR} = 53.9 \pm 7.4$, $ID_{PF-048} = 50.8 \pm 7.5$, $RD_{CTR} = 24.7 \pm 4.6$, $RD_{PF-048} = 19.4 \pm 4.2$.

D. Comparison of the area under the curve (AUC) of the VTD responses in each response profile between control and 5 μM PF-04856264. $SD_{CTR} = 171 \pm 22.2$, $SD_{PF-048} = 191.7 \pm 33.3$, $OS_{CTR} = 68.1 \pm 10.1$, $OS_{PF-048} = 90.2 \pm 26$, $ID_{CTR} = 52.9 \pm 6.6$, $ID_{PF-048} = 66.4 \pm 21.3$, $RD_{CTR} = 27.5 \pm 5.6$, $RD_{PF-048} = 28.4 \pm 6.7$.

Two-tailed paired Student's t-test, * $P < 0.05$. For 1 μM experiments: $N = 5$ DRG cultures, $n_{(CTR)} = 490$ cells, $n_{(PF-048)} = 508$ cells. For 5 μM: $N = 5$ DRG cultures, $n_{(CTR)} = 605$ cells, $n_{(PF-048)} = 338$ cells. Error bars represent SEM., Error bars represent SEM.

4.4.4. PF-04856264 (5 μ M) causes delayed RD responses.

Analysis of the latency to peak of the VTD responses between control and PF-04856264 showed no statistically significant difference at both concentrations of the blocker except for the RD profile where the mean latency of the RD profile was significantly delayed in the presence of 5 μ M PF-04856264 (RD_{CTR} 119 vs RD_{PF-048} 174.5 s), Fig. 4.8,B. However, a trend of increased latencies was also observed while conducting the experiments in OS and ID, Fig. 4.8,B.

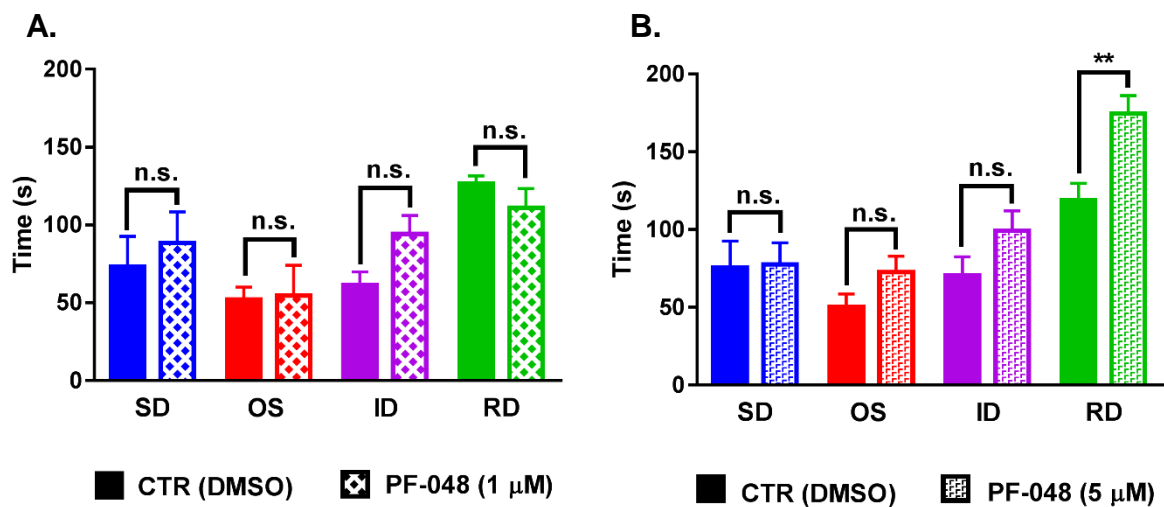


Figure 4.8: Analysis of the effect of PF-04856264 on latency of VTD response profiles.

A. Comparison of the VTD latency in each response profile between control and 1 μ M PF-04856264. $SD_{CTR} = 73.3 \pm 19.5$, $SD_{PF-048} = 88.5 \pm 20$, $OS_{CTR} = 52.1 \pm 8$, $OS_{PF-048} = 54.7 \pm 19.4$, $ID_{CTR} = 61.4 \pm 8.5$, $ID_{PF-048} = 94.2 \pm 11.9$, $RD_{CTR} = 126.4 \pm 5.2$, $RD_{PF-048} = 110.9 \pm 12.6$.

B. Comparison of the VTD latency in each response profile between control and 5 μ M PF-04856264. $SD_{CTR} = 75.4 \pm 17.2$, $SD_{PF-048} = 77.5 \pm 13.9$, $OS_{CTR} = 50.3 \pm 8.4$, $OS_{PF-048} = 72.6 \pm 10.3$, $ID_{CTR} = 70.8 \pm 11.6$, $ID_{PF-048} = 99.4 \pm 12.8$, $RD_{CTR} = 119 \pm 10.7$, $RD_{PF-048} = 174.5 \pm 11.6$.

Only neurons that had an immediate onset to KCl were included in this analysis to exclude differences due to rate of perfusion. Two-tailed paired Student's t-test, * $P < 0.05$. For 1 μ M experiments: $N = 5$ DRG cultures, $n_{(CTR)} = 490$ cells, $n_{(PF-048)} = 508$ cells. For 5 μ M: $N = 5$ DRG cultures, $n_{(CTR)} = 605$ cells, $n_{(PF-048)} = 338$ cells. Error bars represent SEM., Error bars represent SEM.

Nav1.8 BLOCKER (A-803467) RESULTS:

4.4.5.A-803467 preferentially reduces the percentage of the OS response profile.

Analysis of the inhibitory effect of the two A-803467 concentrations in the presence of VTD showed no inhibitory effect on the total number of VTD responding neurons at low concentration (100 nM), while the higher concentration of the inhibitor (300 nM) resulted in ~ 60 % reduction in the number of VTD responding neurons (CTR = 61.2 vs A-80 = 35.1 %), Fig. 4.9.

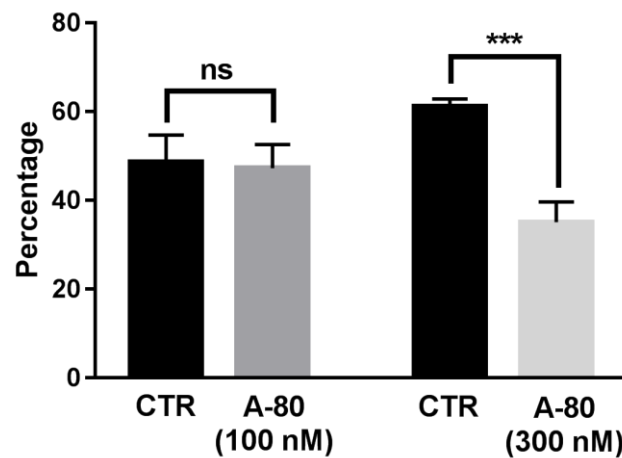


Figure 4.9: The effect of A-803467 on the total number of VTD responding neurons. The percentage of VTD responses were unaffected at the lower concentration of the drug (100 nM), while the higher concentration (300 nM) produced a significant reduction in the total percentage of VTD responding neurons. The mean percentage of VTD responding neurons in the presence of 100 nM of A-803467. Control = 48.69 ± 6 %, A-80 = 47.3 ± 5.4 %. The mean percentage of VTD responding neurons in the presence of 300 nM of A-803467. Control = 61.2 ± 1.7 %, A-80 = 35.1 ± 4.6 %. Two-tailed paired Student's *t*-test, ****P* < 0.001. For 100 nM experiments: *N* = 5 DRG cultures, $n_{(CTR)}$ = 522 cells, $n_{(A80)}$ = 514 cells. For 300 nM: *N* = 5 DRG cultures, $n_{(CTR)}$ = 502 cells, $n_{(A80)}$ = 571 cells. Error bars represent SEM.. Error bars represent SEM.

Next, I examined the percentage of occurrence of each of the VTD response profiles in the presence of A-803467, calculated from the total number of neurons. Despite that 100 nM of the blocker did not change the total number of the VTD responding neurons, Fig. 4.10, (A & B), the percentage of occurrence of the OS response profile was significantly reduced (OS_{CTR} 24 vs OS_{A80} 12.7), Fig. 4.10,C. Similarly, the percentage of the OS response profile was significantly inhibited in the presence of 300 nM of the blocker, (OS_{CTR} 29.7 vs OS_{A80} 11), Fig. 4.10,G, without any change in the other response profiles.

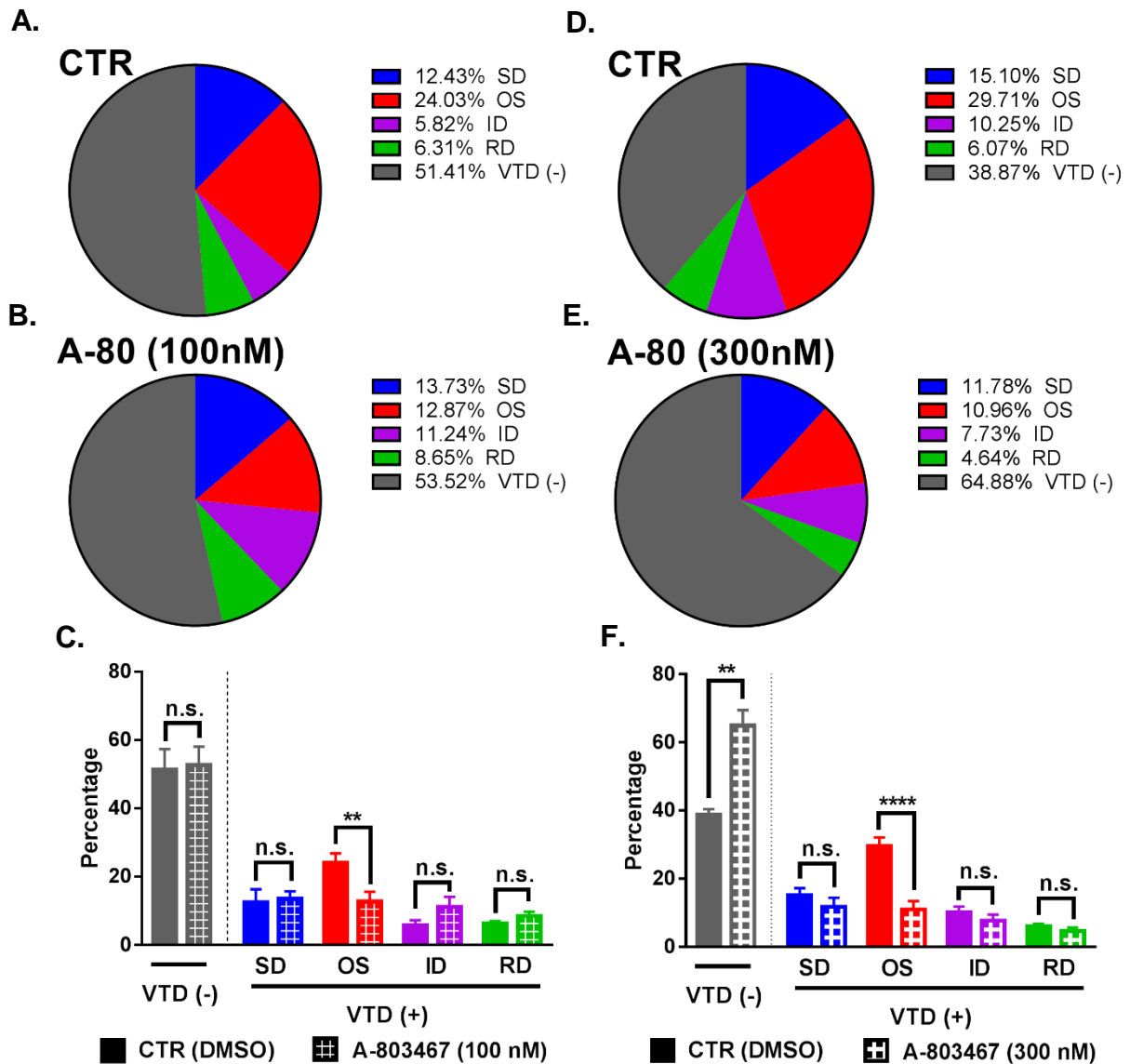


Figure 4.10: Analysis of the inhibitory effect of A-803467 on VTD response profiles.

A and B. Pie chart representation of the mean percentage of VTD responding (coloured) and non-responding (grey) neurons in control (A) and 100 nM A-803467 (B). At low concentration of A-803467 (100 nM) the total number of VTD responding neurons was unchanged,

C. Comparison between the number of VTD responding and non-responding neurons in (A and B). The figure shows a preferential inhibition of the OS response profile in the presence of the blocker. Percentages were calculated from the total number of neurons. $VTD(-)_{CTR} = 51.3 \pm 6$, $VTD(-)_{A80} = 52.7 \pm 5.4$; $SD_{CTR} = 12.4 \pm 3.9$, $SD_{A80} = 13.5 \pm 2.2$, $OS_{CTR} = 24 \pm 2.9$, $OS_{A80} = 12.7 \pm 2.9$, $ID_{CTR} = 5.8 \pm 1.4$, $ID_{A80} = 11.1 \pm 3$, $RD_{CTR} = 6.3 \pm 0.6$, $RD_{A80} = 8.5 \pm 1.2$ %.

D and E. Pie chart representation of the mean percentage of VTD responding (coloured) and non-responding (grey) neurons in control (D) and 300 nM A-803467 (E). At a higher concentration (300 nM) the total number of VTD responding neurons was significantly reduced.

F. Comparison between the number of VTD responding and non-responding neurons in (D and E). the figure shows a preferential inhibition of the OS response profile in the presence of the blocker. Percentages were calculated from the total number of neurons. $VTD(-)_{CTR} = 38.8 \pm 1.7$, $VTD(-)_{A80} = 64.9 \pm 4.6$; $SD_{CTR} = 15.1 \pm 2.1$, $SD_{A80} = 11.8 \pm 2.7$, $OS_{CTR} = 29.7 \pm 2.4$, $OS_{A80} = 11 \pm 2.5$, $ID_{CTR} = 10.2 \pm 1.6$, $ID_{A80} = 7.7 \pm 1.8$, $RD_{CTR} = 6.1 \pm 0.7$, $RD_{A80} = 4.6 \pm 1.1$ %.

Two-tailed paired Student's t-test, * $P < 0.05$, ** $P < 0.01$ and **** $P < 0.0001$. For 100 nM experiments: $N = 5$ DRG cultures, $n_{(CTR)} = 522$ cells, $n_{(A80)} = 514$ cells. For 300 nM: $N = 5$ DRG cultures, $n_{(CTR)} = 502$ cells, $n_{(A80)} = 571$ cells.. Error bars represent SEM.

4.4.6.A-803467 reduces the relative frequency of the OS response profile and its persistent subtype.

To examine the relative change in frequency of occurrence of each VTD response profile between control and A-803467, VTD response profiles were calculated as a percentage from the total number of VTD responding neurons. The analysis showed that at the lower concentration of A-803467 (100 nM) resulted in a significant reduction in the OS response profile (OS_{CTR} 50.4 vs OS_{A80} 26.6) with a concomitant increase in the ID response profile (ID_{CTR} 11.5 vs ID_{A80} 22.2). SD and RD profiles were slightly, but non-significantly increased. Fig. 4.11,A. Similarly, in the presence of a higher concentration of A-803467 (300 nM), a significant reduction in the OS response profiles was observed (OS_{CTR} 48.4 vs OS_{A80} 31.2) with a concomitant slight, non-significant, increase in all of the other responses (ID, RD and SD), Fig. 4.11,B.

Furthermore, analysis of the percentages of the two OS classes in the presence of a 100 nM concentration of the blocker showed a significant reduction in the oscillatory baseline subtype that was accompanied by an increase in the non-persistent oscillatory responses compared to the control group, Fig. 4.12,A. Which further suggests that the application of A-803467 not only inhibited the oscillatory responses but also reduced the neuronal excitability which is evident by the reduced number of elicited OS peaks during and after VTD application, ($P_{OS, CTR} = 50.1 \pm 4.6 \%$, $P_{OS, A80} = 30.6 \pm 5.8 \%$; $NP_{OS, CTR} = 49.9 \pm 4.6$, $NP_{OS, A80} = 69.4 \pm 5.8 \%$). In contrast, the higher concentration of A-803467 (300 nM) did not show any significant changes between the two OS subclasses, if anything, it showed a small but non-significant increase in the persistent subtype and a decrease in the non-persistent oscillatory subtypes. The effect of the 100 nM better fits the role of Nav1.8 in neuronal excitability. However, the effect of the 300 nM could be due to its action on other ion channel classes (i.e. non-specific effect). Altogether, these results suggest a preferential inhibitory effect of A-803467 on the OS response profile and most likely on neuronal excitability.

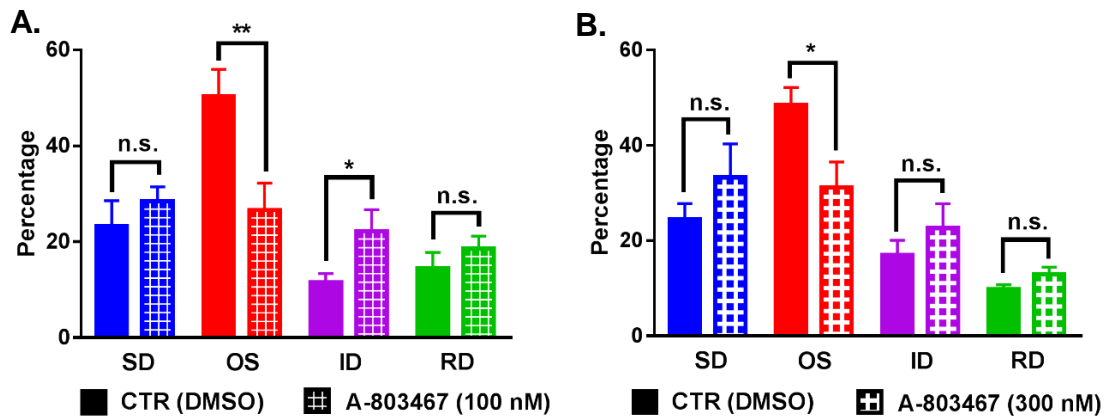


Figure 4.11: Comparison of the relative frequency of each VTD response profile in the presence of A-803467.

A. Comparison between the relative change in the VTD response profiles. Low concentration of A-803467 (100 nM) significantly reduced the OS response profile and increased the ID response profile. Percentages were calculated from the total number of VTD responding neurons. $SD_{CTR} = 23.3 \pm 5.3$, $SD_{A80} = 28.5 \pm 3$, $OS_{CTR} = 50.4 \pm 5.6$, $OS_{A80} = 26.6 \pm 5.6$, $ID_{CTR} = 11.5 \pm 1.8$, $ID_{A80} = 22.2 \pm 4.5$, $RD_{CTR} = 14.5 \pm 3.3$, $RD_{A80} = 18.6 \pm 2.6$ %.

B. Comparison between the relative change in the VTD response profiles. Higher concentration of A-803467 (300 nM) significantly reduced the OS response profile with a small, non-significant increase in all other three VTD profiles. Percentages were calculated from the total number of VTD responding neurons. $SD_{CTR} = 24.5 \pm 3.3$, $SD_{A80} = 33.3 \pm 7$, $OS_{CTR} = 48.4 \pm 3.7$, $OS_{A80} = 31.2 \pm 5.4$, $ID_{CTR} = 17 \pm 3.1$, $ID_{A80} = 22.6 \pm 5.1$, $RD_{CTR} = 9.8 \pm 0.9$, $RD_{A80} = 12.9 \pm 1.5$ %.

Two-tailed paired Student's *t*-test, **P* < 0.05, ***P* < 0.01 and *****P* < 0.0001. For 100 nM experiments: *N* = 5 DRG cultures, $n_{(CTR)} = 522$ cells, $n_{(A80)} = 514$ cells. For 300 nM: *N* = 5 DRG cultures, $n_{(CTR)} = 502$ cells, $n_{(A80)} = 571$ cells. Error bars represent SEM.

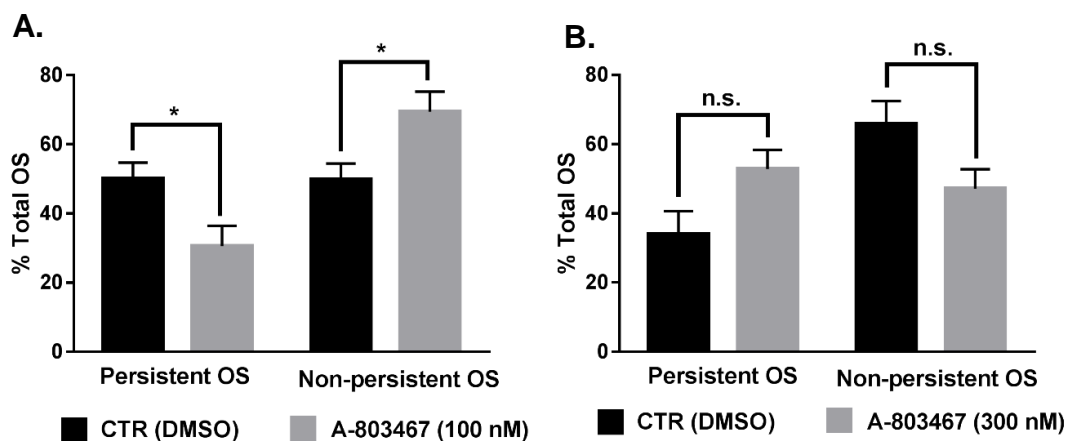


Figure 4.12: Analysis of the effect of A-803467 blocker on the oscillatory pattern of OS responding neurons.

A. Comparison of the mean percentage of OS subtypes (Oscillatory and stable) between control and (100 nM) A-803467. Oscillatory $_{CTR} = 50.1 \pm 4.6$ %, Oscillatory $_{A80} = 30.6 \pm 5.8$ %; Stable $_{CTR} = 49.9 \pm 4.6$, Stable $_{A80} = 69.4 \pm 5.8$.

B. Comparison of the mean percentage of OS subtypes (Oscillatory and stable) between control and (300 nM) A-803467. Oscillatory $_{CTR} = 34.1 \pm 6.6$ %, Oscillatory $_{A80} = 52.8 \pm 5.6$ %; Stable $_{CTR} = 65.9 \pm 6.6$, Stable $_{A80} = 47.2 \pm 5.6$.

Two-tailed paired Student's *t*-test, **P* < 0.05. For 100 nM experiments: *N* = 5 DRG cultures, $n_{(CTR)} = 522$ cells, $n_{(A80)} = 514$ cells. For 300 nM: *N* = 5 DRG cultures, $n_{(CTR)} = 502$ cells, $n_{(A80)} = 571$ cells. Error bars represent SEM.

4.4.7. The effect of A-803467 on the maximum peak amplitude and area under the curve (AUC).

Application of A-803467 had no obvious effect on the maximum VTD peak response and on the area under the curves of the elicited responses at the lower concentration of the drug (100 nM), Fig. 4.13, (A & C). The SD response showed a slight, statistically non-significant, decrease in maximum peak values (SD_{CTR} 0.47 vs SD_{A80} 0.39) paralleled by a decrease in AUC (SD_{CTR} 180.9 vs SD_{A80} 153.8), Fig. 3.10, (A & C). Similar patterns were conserved with the higher concentration of A-803467 where almost similar effect on the VTD response profiles but with a more evident inhibition on the SD responses in this case (SD_{CTR} 0.6 vs SD_{A80} 0.46), Fig. 3.10, (B & D).

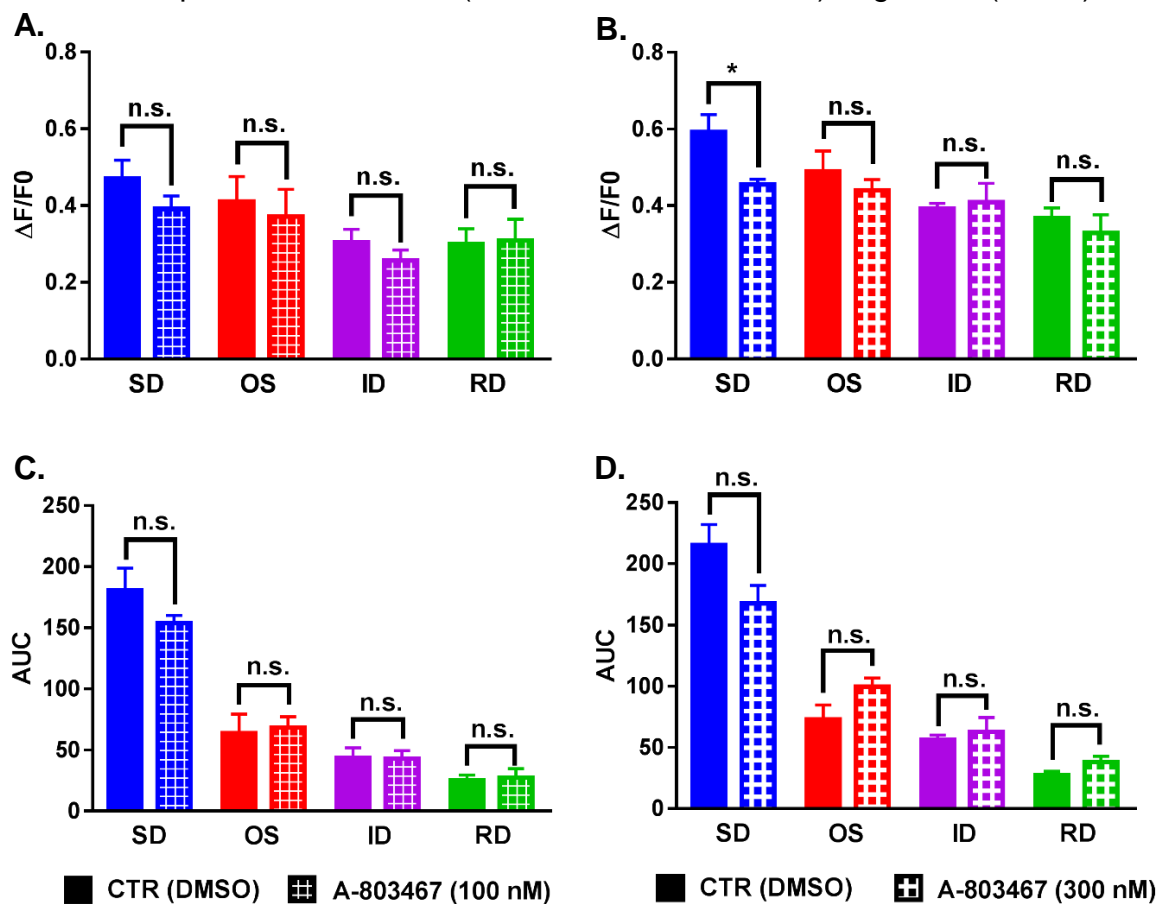


Figure 4.13: Analysis of the effect of A-803467 on the maximum VTD peak responses and their area under the curve.

A. Comparison of the VTD peak amplitude in each response profile between control and 100 nM A-803467. $SD_{CTR} = 0.47 \pm 0.05$, $SD_{A80} = 0.39 \pm 0.03$, $OS_{CTR} = 0.41 \pm 0.07$, $OS_{A80} = 0.37 \pm 0.07$, $ID_{CTR} = 0.3 \pm 0.03$, $ID_{A80} = 0.26 \pm 0.03$, $RD_{CTR} = 0.3 \pm 0.04$, $RD_{A80} = 0.31 \pm 0.06$.

B. Comparison of the VTD peak amplitude in each response profile between control and 300 nM A-803467. $SD_{CTR} = 0.6 \pm 0.05$, $SD_{A80} = 0.46 \pm 0.01$, $OS_{CTR} = 0.5 \pm 0.05$, $OS_{A80} = 0.44 \pm 0.03$, $ID_{CTR} = 0.4 \pm 0.02$, $ID_{A80} = 0.41 \pm 0.05$, $RD_{CTR} = 0.37 \pm 0.03$, $RD_{A80} = 0.33 \pm 0.05$.

Figure 4.13 (continued): Analysis of the effect of A-803467 on the maximum VTD peak responses and their area under the curve.

C. Comparison of the area under the curve (AUC) of the VTD responses in each response profile between control and 100 nM A-803467. $SD_{CTR} = 180.9 \pm 17.9$, $SD_{A80} = 153.8 \pm 6.3$, $OS_{CTR} = 63.7 \pm 15.6$, $OS_{A80} = 68.2 \pm 8.9$, $ID_{CTR} = 43.6 \pm 8.1$, $ID_{A80} = 43 \pm 6.4$, $RD_{CTR} = 25.4 \pm 4.1$, $RD_{A80} = 27.3 \pm 7.4$.

D. Comparison of the area under the curve (AUC) of the VTD responses in each response profile between control and 300 nM A-803467. $SD_{CTR} = 215.3 \pm 16.9$, $SD_{A80} = 167.8 \pm 14.6$, $OS_{CTR} = 72.9 \pm 11.9$, $OS_{A80} = 99.6 \pm 7.2$, $ID_{CTR} = 56.7 \pm 3.4$, $ID_{A80} = 62.8 \pm 11.6$, $RD_{CTR} = 27.4 \pm 3$, $RD_{A80} = 38.2 \pm 4.5$. Two-tailed paired Student's *t*-test, **P* < 0.05. For 100 nM experiments: *N* = 5 DRG cultures, $n_{(CTR)}$ = 522 cells, $n_{(A80)}$ = 514 cells. For 300 nM: *N* = 5 DRG cultures, $n_{(CTR)}$ = 502 cells, $n_{(A80)}$ = 571 cells, Error bars represent SEM.

4.4.8.A-803467 has no effect on the latency of VTD responses.

Analysis of the response latencies showed no statistical difference between control and A-803467 blocker (at both concentrations), Fig. 3.11. However, at 300 nM concentration, there was a slight, non-significant increase in latency in all VTD response profiles, Fig.4.14,B. Similar to the observation made earlier in the PF-0485 experiment, some neurons elicited responses during the wash period after the end of the VTD/blocker application. These responses were not included in the analysis and only the ones that were elicited during the co-application of the VTD and the blocker were included.

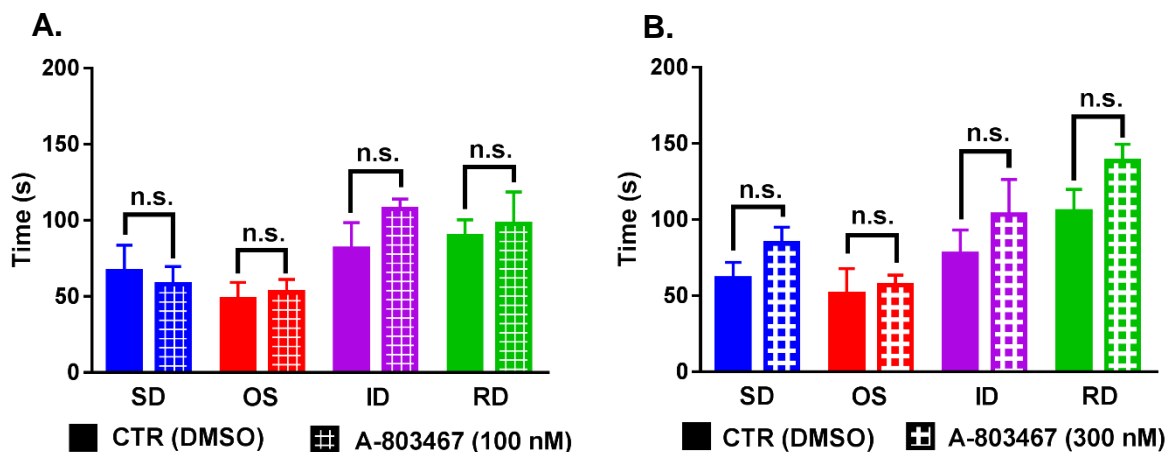


Figure 4.14: Analysis of the effect of A-803467 on latency of VTD response profiles.

A. Comparison of the VTD latency in each response profile between control and 100 nM A-803467. $SD_{CTR} = 66.5 \pm 17.29$, $SD_{A80} = 58 \pm 11.8$, $OS_{CTR} = 48.2 \pm 11$, $OS_{A80} = 52.8 \pm 8.4$, $ID_{CTR} = 81.3 \pm 17.3$, $ID_{A80} = 107.3 \pm 6.8$, $RD_{CTR} = 89.8 \pm 10.7$, $RD_{A80} = 97.8 \pm 21.1$.

B. Comparison of the VTD latency in each response profile between control and 300 nM A-803467. $SD_{CTR} = 61.3 \pm 10.7$, $SD_{A80} = 84.4 \pm 10.8$, $OS_{CTR} = 51.1 \pm 16.9$, $OS_{A80} = 56.9 \pm 6.8$, $ID_{CTR} = 77.5 \pm 15.7$, $ID_{A80} = 103.3 \pm 23$, $RD_{CTR} = 105.4 \pm 14.5$, $RD_{A80} = 138.5 \pm 11$.

Only neurons that had an immediate onset to KCl were included in this analysis to exclude differences due to rate of perfusion. Two-tailed paired Student's *t*-test, **P* < 0.05. For 100 nM experiments: *N* = 5 DRG cultures, $n_{(CTR)}$ = 522 cells, $n_{(A80)}$ = 514 cells. For 300 nM: *N* = 5 DRG cultures, $n_{(CTR)}$ = 502 cells, $n_{(A80)}$ = 571 cells, Error bars represent SEM.

4.5. Discussion:

The aim of the experiments in this chapter was to examine the contribution of the two main TTX-S (Nav1.7) and TTX-R (Nav1.8) channels expressed in mouse dorsal root ganglia neurons on VTD response profiles by using two specific pharmacological blockers, PF-0856264 and A-803467, respectively. Although these blockers are well documented and widely accepted as specific pharmacological blockers, their binding affinity, specificity and IC₅₀ were mostly determined by patch-clamp electrophysiology on VGSC channels expressed in heterologous system. The drug properties, however, can change under different experimental setups – for example, patched vs unpatched cells, native vs recombinant, single vs combined drugs and the drug application period/method. I tested two concentrations of each drug due to the lack of reports in the literature regarding the use of these two drugs in calcium imaging. The lower concentration was used to give the most specific action, while the higher concentration to give higher inhibition but with increased potential of non-specific effects.

Application of PF-04856264 to DRG neurons resulted in a dose-dependent inhibition of the total number of VTD responding neurons, which suggests that Nav1.7 is the key VGSC channel in eliciting VTD responses in all DRG neurons. In the presence of 5 μ M PF-04856264, almost half of the neurons failed to produce a VTD response in the presence of Nav1.7 blocker Fig. 4.3. These results agree with the notion that Nav1.7 is a key regulator of neuronal excitability in all DRG neurons. Nav1.7 channel is the major contributor to TTX-S current in nociceptors²⁴⁵. The “incomplete” inhibition of VTD responses (~ 50 %) by PF-04856462 in calcium imaging could be due to the state-dependence activity of both the blocker and VTD. This has been demonstrated in FLIPR assay where PF-04856462 (10 μ M) failed to achieve a complete inhibition of the VTD responses in Nav1.7 transfected HEK293 cells. The authors argued that the reason for such incomplete inhibition is due to the competition between VTD and PF-04856264, in which VTD binding to some VGSC will lock the VTD-bound channels in the open (active) state; a conformation that is highly unfavourable for PF-04856264 binding²⁴⁸. This does not exclude the contribution of the other TTX-S VGSC in eliciting VTD responses, but it only emphasizes a limitation in the current assay in which co-

application of VTD and the blocker could prevent the optimal Nav1.7 inhibition due to drug competition.

PF-04856462 (5 μ M) resulted in a significant reduction in the total number of VTD responding neurons, particularly on the OS responses (15 %), Fig.4.4,F and Fig. 4.5,B. This could suggest a more prominent role for Nav1.7 within this subgroup of neurons. Studies that use Nav1.7 pharmacological blockers²⁴⁵ or Nav1.7 KO animals²⁴⁹ in patch-clamp electrophysiology showed that Nav1.7 accounts for almost 70 % of the TTX-S current in the small-diameter neurons. Based on the data presented in Chapter 3, OS responses were mainly elicited by the small-diameter, TRPA1 expressing neurons (i.e. PEP and TH subtypes)²⁵⁰. These neurons are also characterised by a relatively higher levels of Nav1.7 mRNA³⁹. Further experiments with various algescic markers should be done to confirm the identity of the cells mostly affected by the Nav1.7 blocker.

Analysis of the other parameters of the elicited VTD responses in the presence of PF-04856264 showed no significant differences to the control, including oscillation frequency within the OS profile, VTD peak amplitude, area under the curve and VTD response latency which suggests that these parameters are independent of Nav1.7 channel. Note that VTD latency was not changed except in the RD profile at the higher concentration of the blocker, Fig.4.8,B; It was previously hypothesised that RD response profiles results from TTX-R, Nav1.9 in particular. Since VTD preferentially binds open/active confirmation of the VGSC, the resting membrane potential should shift to a more hyperpolarised potential in the presence of the blocker, which might explain why it took a longer time for the TTX-R channel to open.

Collectively, these results highlight the main role of Nav1.7 in eliciting all types of VTD response profiles, with a probably more prominent role of Nav1.7 in the small-diameter, PEP and TH nociceptor subtypes. In addition, the inhibition of Nav1.7 channel by PF-04856462 does not contribute to the VTD peak amplitude, area under the curve and latency to response which suggest that other ion channels could contribute to these parameters.

We hypothesized that VTD responses are the sum of an initial activation of TTX-S by VTD that lead to a consequent activation of TTX-R VGSC, particularly Nav1.8. To test

this hypothesis, I used A-803467, a specific Nav1.8 blocker (100 and 300 nM) to investigate the contribution of Nav1.8 to VTD response profiles. One important consistent phenotype that resulted from Nav1.8 inhibition is the specific reduction of the OS response profile, 47 % and 36 % at 100 and 300 nM, respectively. Fig. 4.11. The characterization of OS response profile (Chapter 3) showed that OS responses are mainly elicited by small-diameter nociceptor neurons which fits Nav1.8 expression pattern in DRG neurons. Furthermore, the OS peak frequency at 100 nM showed a significant reduction which further suggests a reduction in neuronal excitability, Fig.4.12,A. The increase in the ID profile that occurred along with the decrease in the OS profile in the presence of both Nav1.7 and Nav1.8 blockers, could be due to reduced ability of the cells to elicit multiple peaks. Therefore, most of the “originally OS” cells elicited a single-peak response in the presence of the blockers which caused an increase in the single peak category in general, and in the ID response profile in particular, Fig.4.5 and 4.11.

The higher concentration of the blocker not only inhibited the OS responses but also the total number of VTD-responding neurons, Fig.4.10, (D-F). Two reasons might account for this action, First, it is possible that the excitability of the affected cells are highly dependent on Nav1.8 activation which means that activation of TTX-S is not enough to drive VTD responses in these neurons. A second explanation might be due to the drug non-specific effect on TTX-S channels. A-803467 is a 100 fold selective to Nav1.8 therefore, theoretically, it should not interfere with the activation of TTX-S channels. However, it has been shown that part of the binding sites of A-803467 includes S6 in DIII and DIV. The amino acids residues at these sites are identical in all other VGSC subtypes²⁵¹. Since VTD also binds S6 in DI and DIV, it is possible that A-803467 might prevent VTD from reaching its binding site in the TTX-S VGSC which could explain the reduction in the total number of VTD responding neurons at only higher concentrations of the blocker (300 nM).

Analysis of the other parameters of the elicited VTD responses in the presence of A-803467 showed no differences in all the examined parameters (peak amplitude, area under the curve and latency to response), except for a noticeable decrease in the SD peak amplitude and the area under the curve that were consistent at both concentrations, although statistically significant only at 300 nM, Fig.4.13. This effect

of the Nav1.8 blocker is opposite to that produced by Nav1.7 blocker where peak amplitude and area under the curve were slightly elevated, Fig.4.7. The reason for the effects of both blockers on peak amplitude and area under the curve is unclear. It could be due to some off-target effect of these drugs on other ion channels (e.g. calcium channels), Further experiments might better address this issue.

The results obtained here demonstrated a link between Nav1.8 and VTD-elicited calcium oscillations. However, since other cell types that lacks Nav1.8 expression, like N2a cells (Fig. 1, chapter 3) and chromaffin cells²⁵² also showed calcium oscillation to VTD. Indicates that Nav1.8 triggers calcium oscillation in DRG neurons but it is not the determinant of the shape of the OS profile in general. Further experiments are needed to identify other ion channels and receptors that might also contribute to the oscillatory profile, as well as their expression pattern and relevance to different neuronal subtypes. This may also explain the variations in the oscillatory patterns between DRG neurons and may have significance in normal and pathological conditions that need to be explored in more details in future experiments.

The A-803467 results obtained here give an example on how the nature of each assay determines the experiment outcomes. In my experiments, a 100 nM of the blocker produced a robust inhibition of the OS response profile and OS peak frequency in mouse DRG culture. Whereas the same concentration was completely ineffective in blocking the action potential from rat DRG neurons in patch-clamp electrophysiology at both resting and depolarized states, and only the 300 nM concentration of the blocker showed a significant efficacy²⁴⁷. Also, in Jarvis et al, the authors used voltage-clamp electrophysiology with an acute application of the drug. However, in calcium imaging, neurons were intact and longer drug application periods were used (30 – 45 min) – which is somehow more relevant to an in vivo drug testing. Longer contact time with the cells might give a higher chance for the drug to bind the target (Nav1.8), therefore the enhanced response was seen at 100 nM in calcium imaging but not in patch-clamping, yet it might also give rise to potentially higher off-target effects that can be detected early on in the in vitro study. Such discrepancies in results highlight the importance of using different experimental approaches in testing and characterising novel drugs. Calcium imaging assay is particularly useful in investigating the general effect of the drug on neuronal excitability.

In conclusion, the results presented in this chapter examined the effect of Nav1.7 and Nav1.8 blockers on VTD responses. The data demonstrate a distinct contribution of each of the tested VGSC to VTD response profile. Nav1.7 inhibition resulted in a reduction in the number of VTD responding neurons. All of the VTD response profiles were affected by Nav1.7 inhibition, with the most evident inhibition on the OS response profile. On the other hand, Nav1.8 inhibition resulted in a significant reduction of the OS responses without affecting the other VTD response profiles. Finally, the data also showed that VGSC (Nav1.7 and Nav1.8, in particular) might not have a major influence on the other properties of the VTD responses. It is therefore most likely that VTD response properties measured in this study are mainly affected by other ion channel classes like VGCC and VGKC. Future characterization of other ion channel classes contribution to VTD responses may better address this point. Finally, the results presented in this chapter support the idea of the use of VTD responses as a potential read-out for Nav1.7 and Nav1.8 VGSC subtypes in DRG neurons and is relevant to VGSC drug screens and to various functional studies.

CHAPTER 5

THE ROLE OF MAP1A LIGHT
CHAIN (LC2) IN THE
EXCITABILITY OF SENSORY
NEURONS

Chapter 5: The role of MAP1A light chain (LC2) in the excitability of sensory neurons

5.1. Introduction:

Pathophysiological conditions can result in changes in the expression level of ion channels in the peripheral sensory neurons which can result in an altered ion channel activity. For example, in chronic inflammatory pain, the expression level of certain subtypes of voltage gated sodium channels (Nav1.8, Nav1.7, and Nav1.3) is increased, which result in an increased sensory neuron excitability and pain. The ability of the sensory neurons in general, and the nociceptors in particular, to immediately respond and adapt to the presence of noxious stimuli require the presence of a dynamic machinery which is capable of providing a dynamic regulation of ion channels at the plasma membrane under various conditions. Yet, the mechanism of transporting ion channels from the site of synthesis to the plasma membrane and vice versa is not fully understood.

Many factors have been reported to be involved in regulating ion channel trafficking. For example, microtubules and their associated proteins (MAPs) have been shown to be involved directly or / and indirectly in the transport of several ion channels in excitable cells. For example, The light chain of MAP1B (LC1) is shown to be involved in Nav1.6 trafficking to the cell membrane in ND7/23 cell line ²⁰². Cav2.2 is shown to interact with both MAP1A and MAP1B light chains in rodent brain ^{204,205,215}. Interestingly, the effect of LC2 on Cav2.2 membrane level is opposite to LC1, the former produces stabilization of Cav2.2 at the pre-synaptic membrane of hippocampal neurons while the latter promotes internalization and endocytosis of the ion channel.

In addition to ion channel trafficking, microtubules are also involved in the regulation of ion channel function. TRPV1 is classically known as a thermotransducer channel. However, an N-terminus truncated version of the channel is expressed in the osmosensory neurons in the brain and have been linked to mechanotransduction ²⁵³. By using high resolution microscopy (STORM), pharmacological tools (Nocadazole and taxol) and molecular assays, Prager-Khoutorsky et al., have demonstrated that the mechanical gating of TRPV1 isoform is directly mediated by MT. Disruption of MT

resulted in a loss of TRPV1 mechanotransduction only, without affecting its thermotransduction which indicates a specific role for the MT in TRPV1-mediated mechanotransduction in osmosensory neurons ²⁵⁴. What is the role of MT and its associated proteins in peripheral mechanosensors? and what are the roles of the MT and MAPs in the development of injury-induced mechanical hyperalgesia? are all interesting questions that need to be investigated.

Evidence for the contribution of the cytoskeleton networks in inflammatory pain has been previously demonstrated. Development of epinephrine-induced hyperalgesia (EPI-hyperalgesia) *in vivo*, mediated by activation of PKA, PKC and ERK pathways, is shown to be dependent on an intact cytoskeleton network. In contrast, PGE2-induced hyperalgesia, mediated by PKA activation, is shown to be cytoskeleton-independent ²⁵⁵. Again, these findings highlight the crucial role of cytoskeletal proteins in regulating cellular responses and mediating second-messenger pathways under normal and pathological conditions. These findings demonstrate that disruption of the cytoskeletal proteins does not necessarily result in a generalized effect, on the contrary, it seems that these networks are linked to specific pathways and even specific components within each particular pathway; indicated by the fact that both PGE2 and EPI – induced hyperalgesia are mediated by PKA activation, but only that induced by EPI seems to be dependent on the cytoskeleton network.

As described previously, MAP1A and MAP1B are closely related proteins that undergo post-translational proteolytic cleavage which result in the formation of two subunits: MAP1A, MAP1B heavy (HC) and light chain, LC2 and LC1, respectively ^{186,188,256}. MAP1A protein in neurons was shown to be an important element for the survival of adult neurons. Mice with a spontaneous mutation in the MAP1A gene are characterized by having a weak microtubule network with significant structural changes that ultimately result in degeneration and death of Purkinje cells, ¹⁹⁹. Which indicate that MAP1A is essential for the proper development of Purkinje cells in mouse brain. Overexpression of LC2-myc *in vivo* failed to rescue the phenotype which supports the notion that the light chains of the MAP proteins have independent functions that differ from that of the heavy chains ¹⁹⁹. However, the effect of MAP1A KO on the development and proper function of the peripheral neurons have not been investigated.

It was previously shown in my lab that Nav1.7 interacts with the light chain of microtubule associated protein A1 (LC2) in Y2H assay. Therefore, the work described in this chapter represents the steps to elucidate the role of MAP1A in DRG neurons.

5.2. Aims:

The aims of the work in this chapter were as follows:

1. To characterise MAP1A distribution in adult mouse sensory neurons
2. To confirm the interaction of LC2-Nav1.7 in mammalian cells by co-IP.
3. To study the physiological function of MAP1A on the excitability of sensory neurons in general and on Nav1.7 ion channels in particular.
4. To map the LC2 interaction site to Nav1.7 using LC2 deletion constructs.

5.3. Methods:

All the methods were done as described in the materials and methods chapter, except for calcium imaging where due to the nature of the experiment, I had to adopt some necessary modification as described below.

5.3.1. Calcium imaging:

Two main changes to calcium imaging protocol were adopted for the experiments in this chapter. First: DRG cultures were imaged at day 6 and 7 DIV, where LV transduced cells were maintained in culture for 5 days to achieve an efficient MAP1A KD. Protocol for maintaining the DRG culture was as described under materials and methods chapter.

Due to a technical limitation, no more than two light sources can be used in our calcium imaging setup. Such limitation precludes the use of an extra light source 488 nm to identify GFP signal in LV-transduced cells while performing a ratiometric fura-2 imaging with 350 and 380 nm light sources. Since the change in the fura2 fluorescence at 380 nm is much higher than the changes obtained at 350 nm, in fact the 380 nm signal usually represents a negative replica of the responses obtained by ratiometric measurement with a similar robustness of the responses. therefore, and given the fact the identification of GFP expressing neurons is critical for the interpretation of the results, it was decided to replace the 350 nm light source with 488 light source to be able to identify GFP signal in live imaging – i.e. using a single-wavelength measurement of fura-2 to observe the qualitative changes in intracellular calcium.

For data analysis, cells that showed homogenous distribution of GFP in the soma with a fluorescence intensity higher than 15 % of the background level were considered GFP positive cells (LV transduced neurons). Likewise, cells that had fluorescence signal intensity less than 15 % of the background, or does not have homogenous distribution of GFP signal in the whole cytoplasm of the soma (due to passing of GFP expressing neurites of other cells or non-neuronal cells through the ROI) were considered GFP negative neurons (LV untransduced neurons).

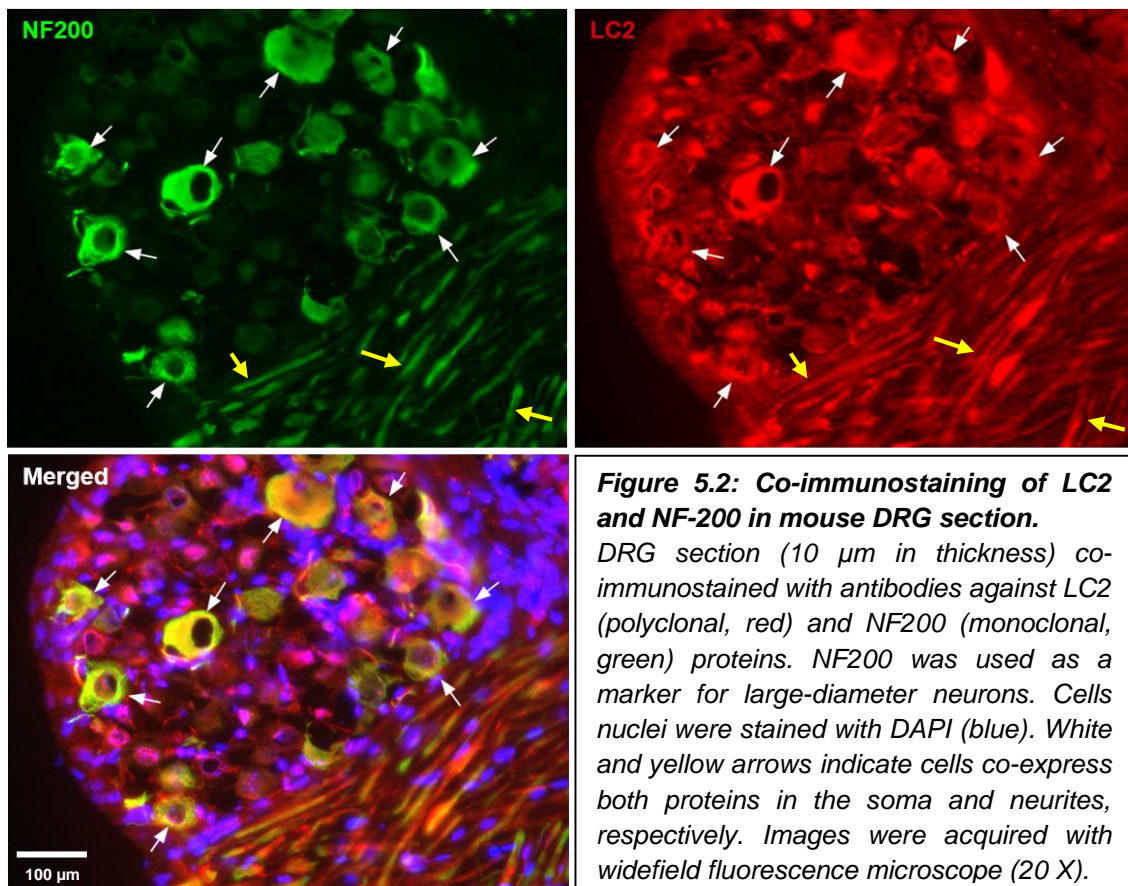
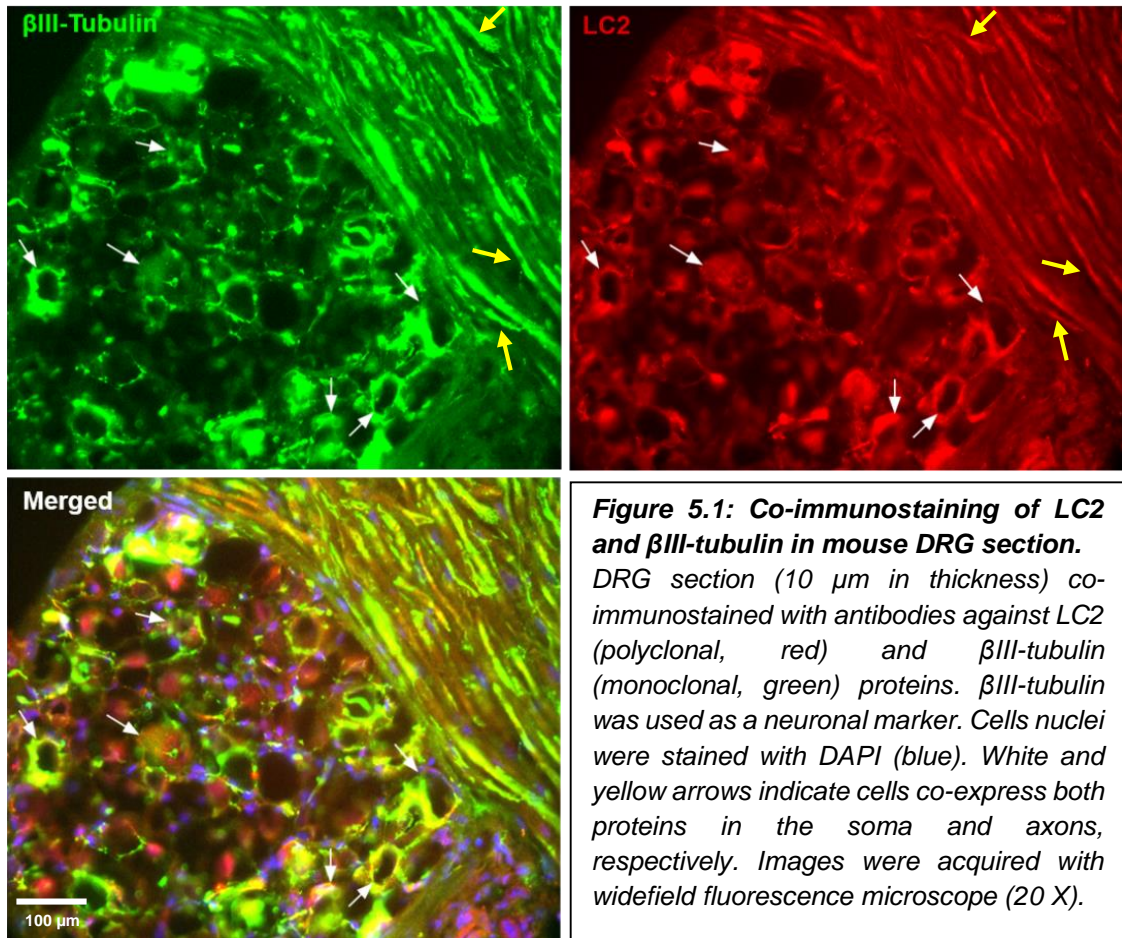
5.4. Results:

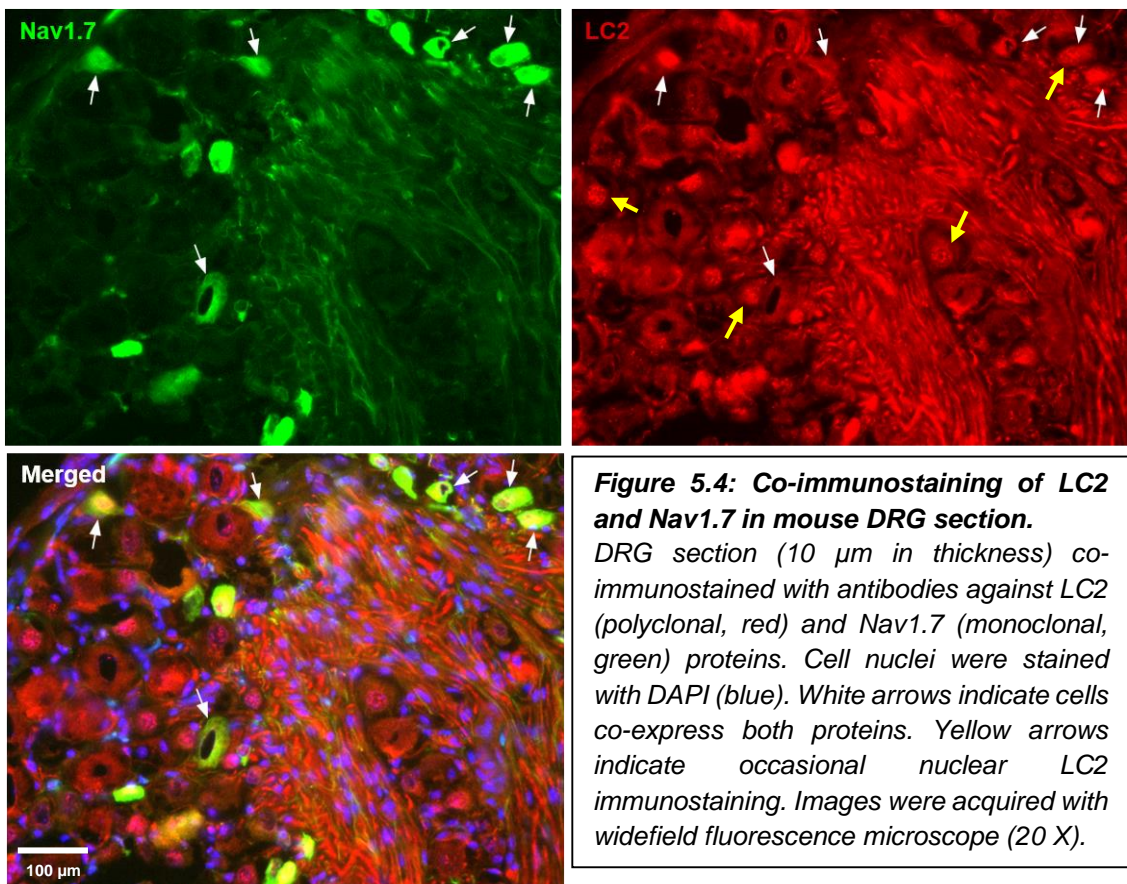
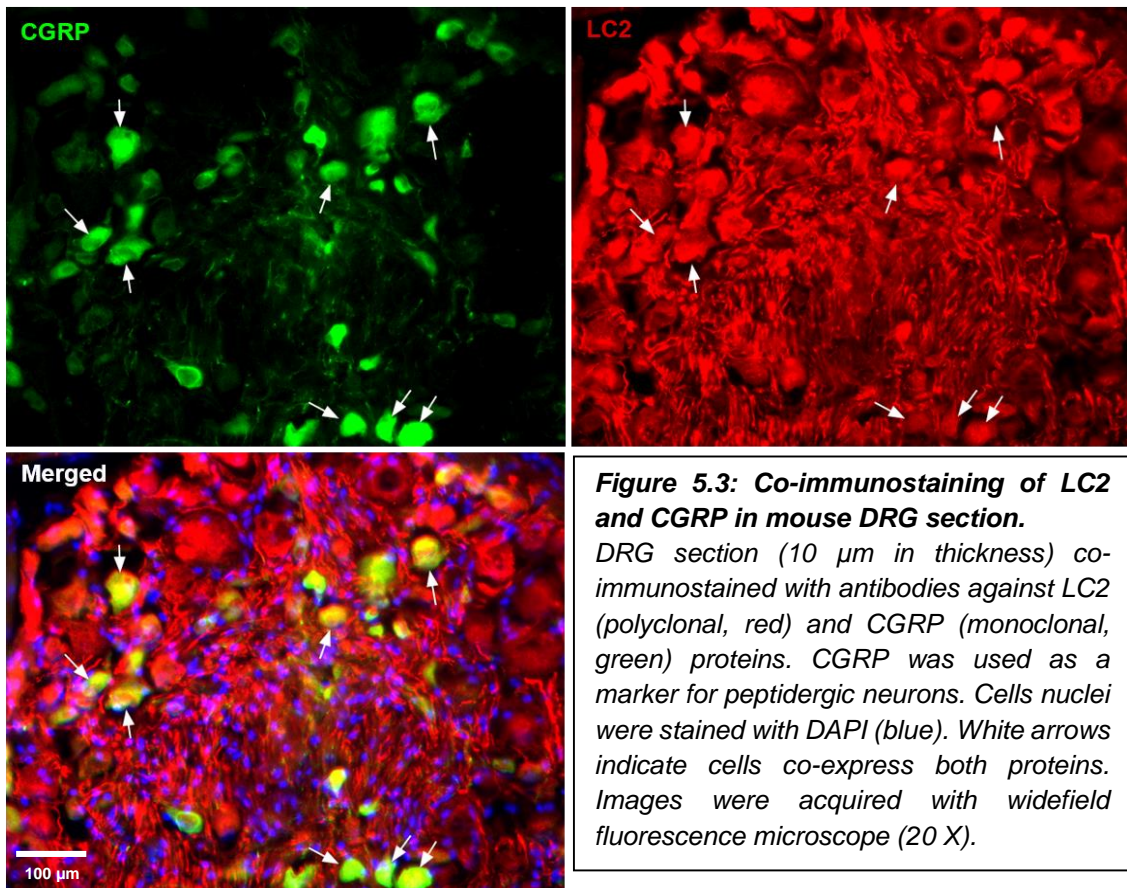
5.4.1. MAP1A expression pattern in adult mouse DRG neurons.

Expression of MAP1A in mouse DRG neurons has not been explored in details previously. Therefore, I used immunofluorescence to examine the distribution of MAP1A protein in both DRG sections and cultures. An antibody against LC2 is commercially unavailable. The experiments presented in this chapter were performed with a non-purified polyclonal LC2 antibody that was obtained as a kind gift from Dr. Friedrich Propst^{189,257}. The limited amount of the antibody restricted the number and the type of experiments done with the LC2 antibody. Fortunately, MAP1A-HC antibody is commercially available and it was used when appropriate to limit the use of the LC2 antibody.

In DRG sections, LC2 was ubiquitously distributed in all DRG neurons. LC2 was found to be co-expressed with cells labelled with β III-tubulin (neuronal marker), CGRP (small, unmyelinated, peptidergic neuron marker), NF200 (large-diameter, myelinated neuron marker) and Nav1.7, Fig.5.1 – 5.4, respectively. The expression level of LC2 did not seem to vary between the various subpopulations of neurons. DRG axons were also strongly labelled with LC2 antibody. Some occasional LC2 immunostaining was observed in the nucleus, Fig. 5.4. Co-expression of LC2 with several other markers, for example IB4 (small, unmyelinated, non-peptidergic neuron marker), GFAP (non-neuronal cells marker) and peripherin (small-diameter, C-fibre neuron marker) were also tested. However, the antibodies against these markers failed to produce a reliable immunostaining pattern in my hands, data not shown. In summary, LC2 was shown to be ubiquitously expressed in DRG neurons with no obvious variations in the expression level within the tested neuronal subpopulations.

LC2 is a product of MAP1A enzymatic cleavage and the distribution and degradation of LC2 may be different to the MAP1A-HC. Therefore, I examined both the MAP1A-HC and LC2 expression in dissociated DRG culture. Both MAP1A-HC and LC2 were expressed in neuronal and non-neuronal cells. The intensity of MAP1A-HC was stronger and more distinct in neurons than non-neuronal cells. In contrast, LC2 showed a profound distribution in both types of cells. In addition, LC2 was present in the neurites with some enrichment at the sites of contacts to other neurites, Fig. 5.5.





Interestingly, MAP1A-HC distribution pattern changed during the incubation period of the DRG culture. In short term DRG culture (2 DIV), MAP1A-HC was homogenously distributed in the cytoplasm of the soma and the neurites. While, in long term DRG culture (> 5 DIV), the expression pattern of MAP1A-HC changed to a distinct beaded pattern (i.e. a dashed line along the length of the neurites), Fig.5.5, top panel. The distinct beaded pattern of MAP1A-HC was evident in most but not all neurites. Also, there was no preference of MAP1A-HC beaded pattern in neurites of all thicknesses. This distribution pattern was independent of the culture condition (i.e. NGF, serum, virus transduction and inflammation) – data not shown. In contrast to neurons, non-neuronal cells showed a filamentous distribution of MAP1A-HC in both long and short term cultures. Unlike LC2, the beaded MAP1A-HC neuronal distribution pattern made it feasible to identify neurons from non-neuronal cells in further immunostaining experiments.

The characteristic pattern of MAP1A-HC in the axons and neurites led us to investigate whether MAP1A-HC beaded distribution localizes or overlaps with other proteins. I investigated the distribution of MAP1A-HC in relevance to other structural proteins (β III-tubulin and actin), as well as to Nav1.7 channel. β III-tubulin demonstrated a homogenous distribution within the axons and neurites and showed no specific relation to MAP1A-HC distribution. Likewise, the homogenous distribution of LC2 (Fig. 5.5) did not correlate with the distinct localization of MAP1A-HC. This indicates that both parts of MAP1A protein may have distinct subcellular distribution and function. Unfortunately, both LC2 and MAP1A-HC antibodies are polyclonal from same species and could not be combined in one experiment.

In case of actin, both neuronal and non-neuronal cells were immunolabelled with actin antibody, Fig. 5.6, which precluded the localization study and made the analysis and conclusion prone to errors.

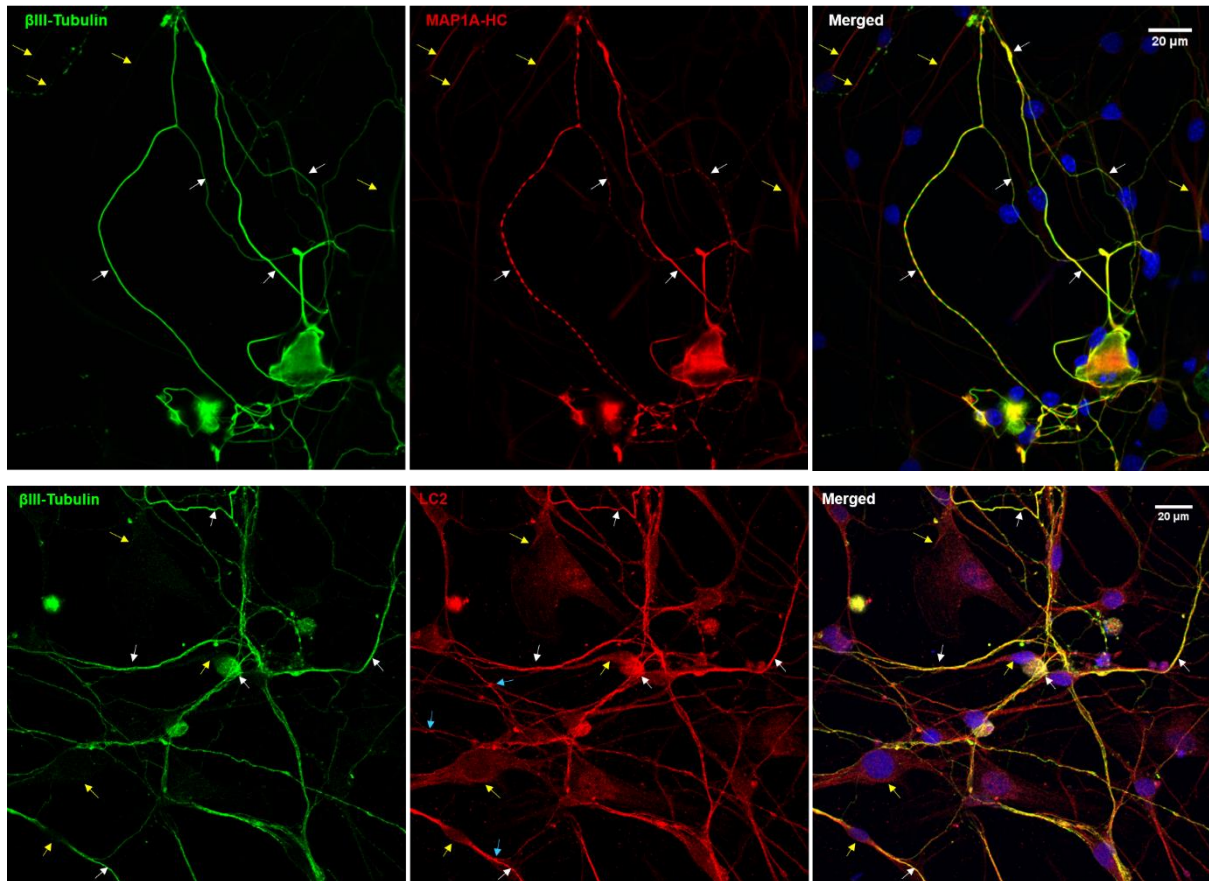


Figure 5.5: immunostaining pattern of MAP1A-HC and LC2 in mouse DRG culture.

DRG neurons in long-term culture (>5 DIV) were fixed and co-immunostained with β III-tubulin (neuronal marker, green) and MAP1A-HC (top panel, red), or LC2 (bottom panel, red). Cells nuclei were stained with DAPI (blue). MAP1A-HC demonstrated a distinct distribution pattern in some neurites (dashed lines), while both β III-tubulin and LC2 demonstrated a homogenous distribution along the soma, axons and neurites. White arrows indicate neurons (soma and fibres) while yellow arrows indicate non-neuronal cells. LC2 antibody showed a strong immunostaining intensity in all cells with a slight increase in intensity at the neurites contact sites (blue arrows), while MAP1A-HC antibody majorly immunolabelled neurons with a much lower intensity in non-neuronal cells. Images were acquired with conventional confocal microscopy, 40 X objective. Images represent one z-plane (near the bottom of the cells).

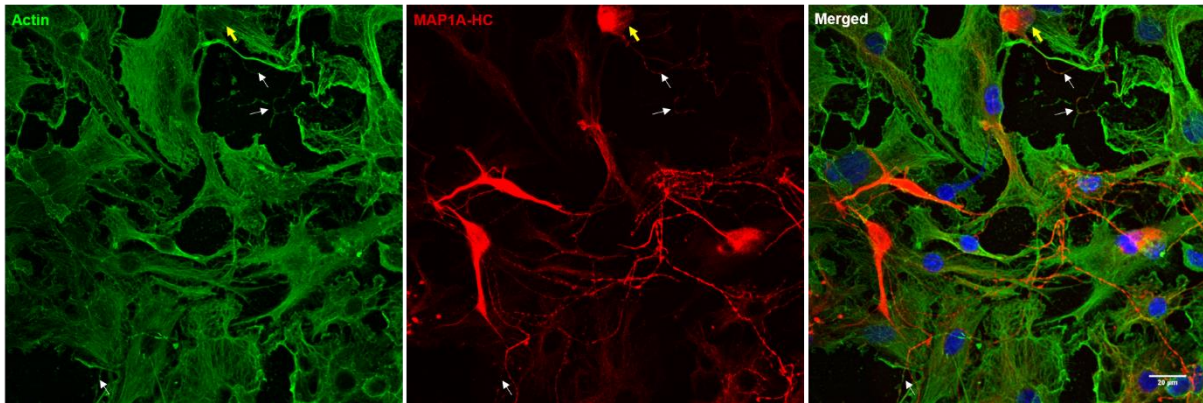


Figure 5.6: immunostaining pattern of MAP1A-HC and Actin in mouse DRG culture.

DRG neurons in long-term culture (>5 DIV) were fixed and co-immunostained with Actin (green) and MAP1A-HC (red). Cells' nuclei were stained with DAPI (blue). MAP1A-HC demonstrated a distinct distribution pattern in relatively thick and thin neurites (dashed lines), while actin was most visible in the non-neuronal cells, however some Actin immunostaining can be noticed in the neuronal soma periphery (yellow arrows) and in some neurites (white arrows). Images were acquired with conventional confocal microscopy, 40 X objective. Images represent one z-plane (near the bottom of the cells).

Nav1.7 showed a distinct beaded distribution pattern along the axons and neurites in DRG culture similar to what has been reported previously in sciatic nerve preparation and in the nerve terminals in the skin sections⁴³. analysis of the maximum intensity peaks of both MAP1A-HC and Nav1.7 clusters along the axons and neurites showed a clear overlap of the peak intensity of both proteins, which indicated a potential colocalization of Nav1.7 and MAP1A-HC in the axons and neurites of DRG cultures, Fig.5.7. This however remains as an interesting initial observation and should be further investigated with experiments using cell type markers (e.g. IB4, CGRP), ion channel clustering markers (e.g. ankyrin G, β II- and β IV-spectrin) and structural proteins (e.g. MAP2) by advanced imaging techniques as STORM microscopy.

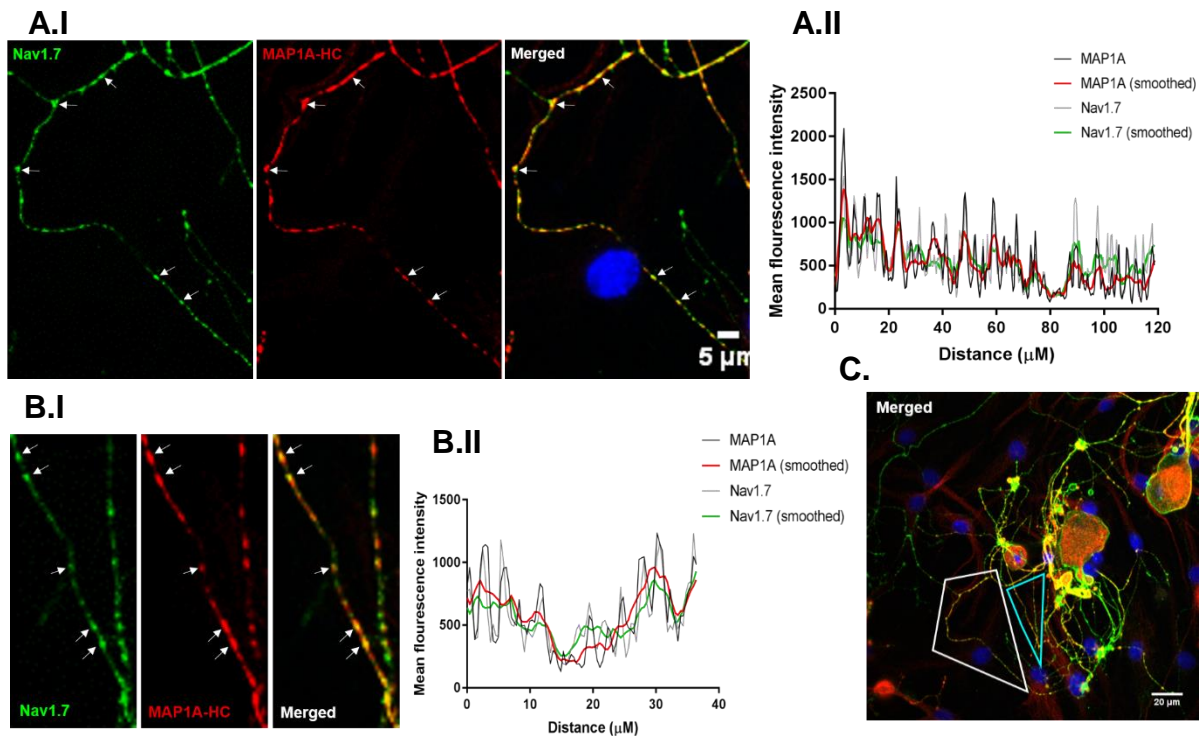


Figure 5.7: immunostaining pattern of MAP1A-HC and Nav1.7 in the neurites of DRG neurons.

DRG neurons in long-term culture (>5 DIV) were fixed and co-immunostained with Nav1.7 (green) monoclonal antibody and MAP1A-HC (red) polyclonal antibody. Cells' nuclei were stained with DAPI (blue).

A.I and B.I. demonstrate MAP1A-HC distinct distribution pattern in neurites (dashed lines) which overlapped with Nav1.7 clusters (white arrows), images are zoomed in from the two boxed areas shown in the original image in **C**.

A.II and B.II. demonstrate the overlap between the maximum intensity peaks detected along the neurite (by raw intensity peak values and smoothed peaks) between Nav1.7 and MAP1A-HC clusters.

Images were acquired with conventional confocal microscopy, 40 X objective. Images represent one z-plane (near the bottom of the cells). Maximum intensity peak values and smoothed peaks

A characteristic distribution of MAP1A-HC and LC2 was also observed in the soma of the DRG neurons. MAP1A-HC was usually found to be most enriched in two main areas: first, the perinuclear region where it spreads from there toward the plasma membrane. And second, the axonal initial segment (AIS) where it extends to fill the cytoplasm of the axons and neurites, Fig. 5.8. Co-immunostaining of actin and MAP1A-HC revealed no overlap between actin submembranous ring and MAP1A-HC in the soma of all neurons (this was more noticeable in large diameter neurons), Fig. 5.9. Detailed examination of Nav1.7 and MAP1A-HC distribution in the soma and the neurites suggested no direct overlap between Nav1.7 and MAP1A-HC at the plasma membrane, which suggests the need for an adaptor proteins linking both, Fig. 5.10.

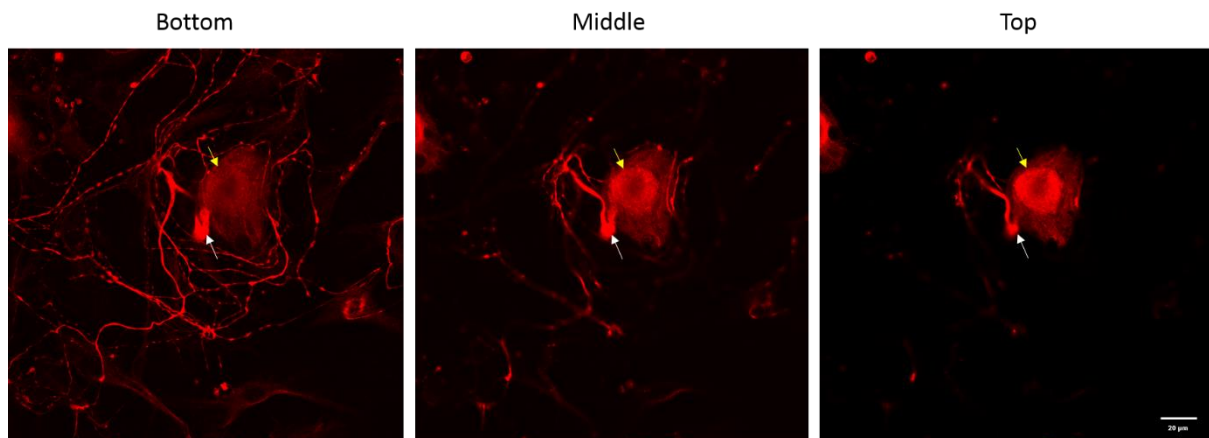


Figure 5.8: Immunostaining pattern of MAP1A-HC DRG neurons.

DRG neurons in long-term culture (>5 DIV) were fixed and immunostained with MAP1A-HC (red) polyclonal antibody. MAP1A-HC is distributed in the neurites with a distinct distribution pattern [bottom z-plane]. MAP1A-HC is highly concentrated in the axonal initial segment (white arrow) and in the perinuclear region (yellow arrow) where its intensity clearly decreases with distance – [middle and top z-planes].

Images were acquired with conventional confocal microscopy, 40 X objective. Images represent three z-planes (bottom to top of the cell).

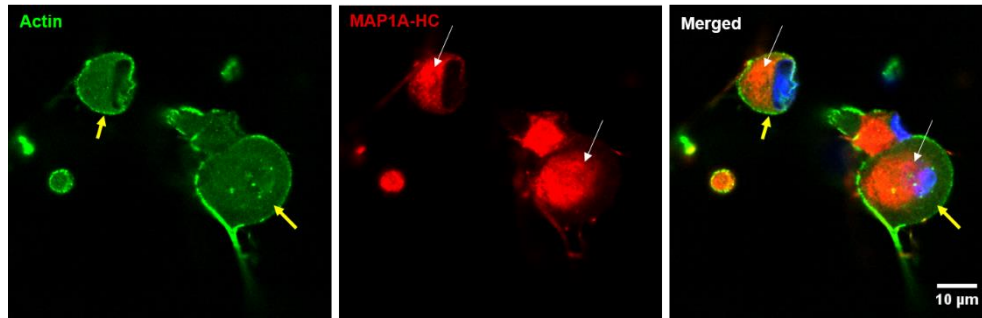


Figure 5.9: immunostaining pattern of MAP1A-HC in the soma of DRG neurons.

DRG neurons in long-term culture (>5 DIV) were fixed and co-immunostained with actin (green) monoclonal antibody and MAP1A-HC (red) polyclonal antibody. Cells nuclei were stained with DAPI (blue). MAP1A-HC is concentrated in the perinuclear region of the cytoplasm (white arrows) and radiates toward the periphery with a gradual decrease in its intensity (yellow arrows). MAP1A-HC reached the lowest intensity at the cell membrane (marked by actin).

Images were acquired with conventional confocal microscopy, 40 X objective. Images represent one z-plane (middle and toward the top of the cells).

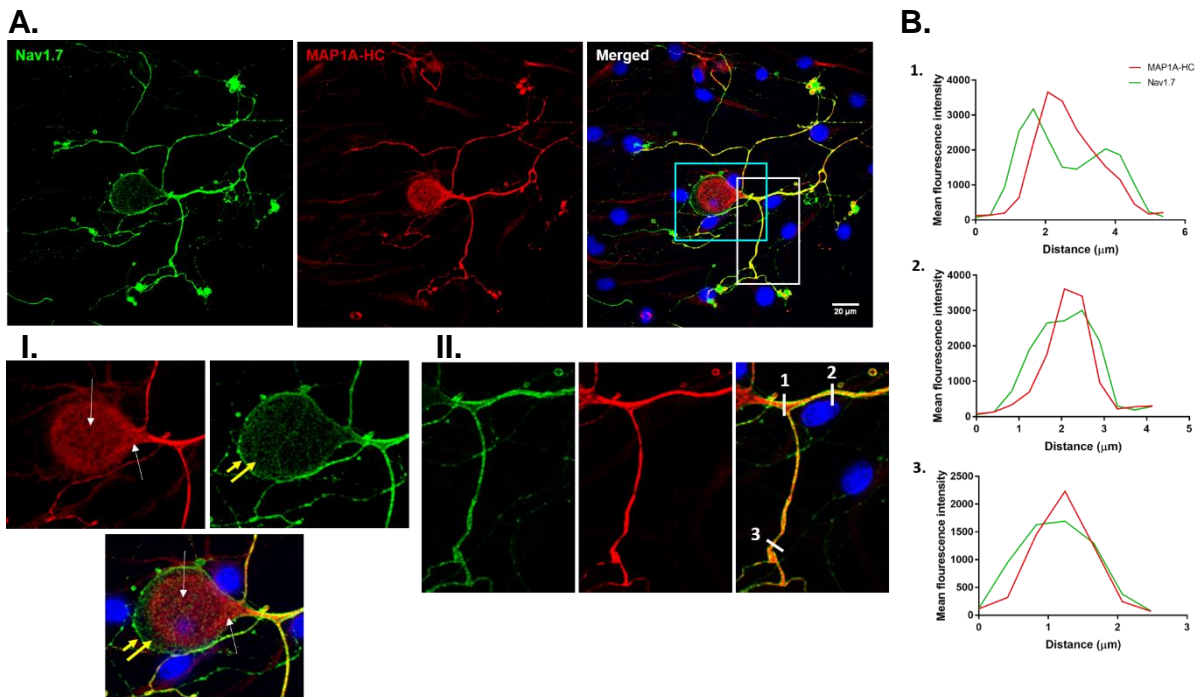


Figure 5.10: immunostaining pattern of MAP1A-HC in the soma and neurites of DRG neurons.

A. DRG neurons in long-term culture (>5 days) were fixed and co-immunostained with Nav1.7 (green) and MAP1A-HC (red) antibodies. Cells' nuclei were stained with DAPI (blue). **I.** MAP1A-HC is concentrated in the perinuclear region (white arrows) and radiates toward the periphery with a gradual decrease in its intensity (yellow arrows). MAP1A-HC is also concentrated in the axonal initial segment where it extends from this region to supply the axons and neurite (white arrows). MAP1A-HC reached the lowest intensity in the cell membrane (marked by Nav1.7). **II.** In the neurites, MAP1A-HC filled the centre of the neurites while Nav1.7 was mainly on the surface. **B.** Plot profile of different areas along the neurites (marked 1, 2, & 3 in II) showed the interior and exterior distribution of MAP1A-HC and Nav1.7, respectively.

Images were acquired with conventional confocal microscopy, 40 X objective. Images represent one z-plane (middle and toward the top of the cells).

In contrast to MAP1A-HC, LC2 was mostly concentrated towards the plasma membrane of the soma, particularly in the submembranous layer and less around the nucleus as demonstrated in Fig.5.11. LC2 was found to be homogenously distributed within the axons and neurites of the DRG neurons as shown previously in Fig. 5.5.

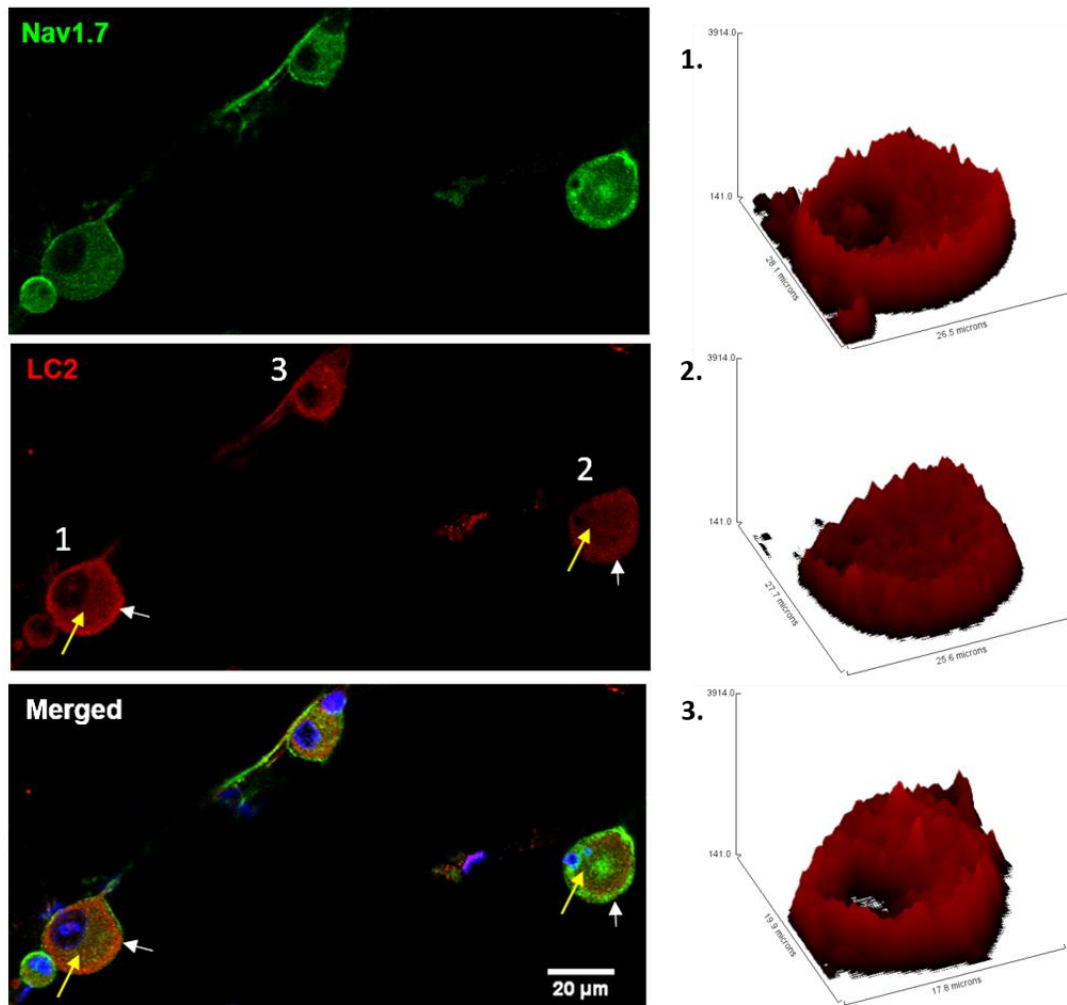


Figure 5.11: immunostaining pattern of LC2 in the soma of DRG neurons.

DRG neurons in long-term culture (>5 DIV) were fixed and co-immunostained with Nav1.7 (green) and LC2 (red) antibodies. Cells nuclei were stained with DAPI (blue). LC2 showed an opposite distribution to MAP1A-HC, where it is most concentrated in the periphery of the soma and the submembranous layer (white arrows) with a gradual decrease in its intensity toward the centre of the cell (yellow arrows). This is clearly represented by the surface plot profile of LC2 in cell 1, 2 and 3 (left panel). Nav1.7 immunostaining marks the membrane and the cytoplasm of the cells. Images were acquired with conventional confocal microscopy, 40 X objective. Images represent one z-plane (middle and toward the top of the cells). Surface plots were produced by ImageJ software.

5.4.2. LC2 interacts with Nav1.7 in Neuroblastoma-2a and mouse DRG neurons.

Y2H experiments previously done by Dr. Nassar showed an interaction between the N-terminus of the Nav1.7 channel and LC2. The Y2H library was from a rat P1 DRG cDNA library as described in Kong et al., 2001²⁵⁸. The N terminus bait is a 121 a.a. (MAMLPPPGPQSFSVHFTKQSLALIEQRISEEKAKEHKDEKDKDDEEEGPKPSSDLEA GKQLPFIYGDIPPGMVSEPLEDLDPYYADKKTFFIVLNKGKAIKFRFNATPALYMLSPFS PLRRISIK. To confirm this interaction, I carried out a co-immunoprecipitation (co-IP) experiment in mouse Neuroblastoma-2a cell line (N2a) using a monoclonal Nav1.7 antibody and non-specific monoclonal IgG antibody as a negative control, followed by immunoblotting with both Nav1.7 and LC2 antibodies. As shown in Fig.5.12, LC2 band was detected in the Nav1.7 co-IP lane (28 KD) and not in the IgG lane, which confirms the interaction between Nav1.7 and LC2. The input lane represents a positive control for the presence of Nav1.7 and LC2 proteins in the samples. Detection of Nav1.7 in the co-IP lane but not in the IgG lane was always used as a proof for successful Nav1.7-immunoprecipitation in all experiments.

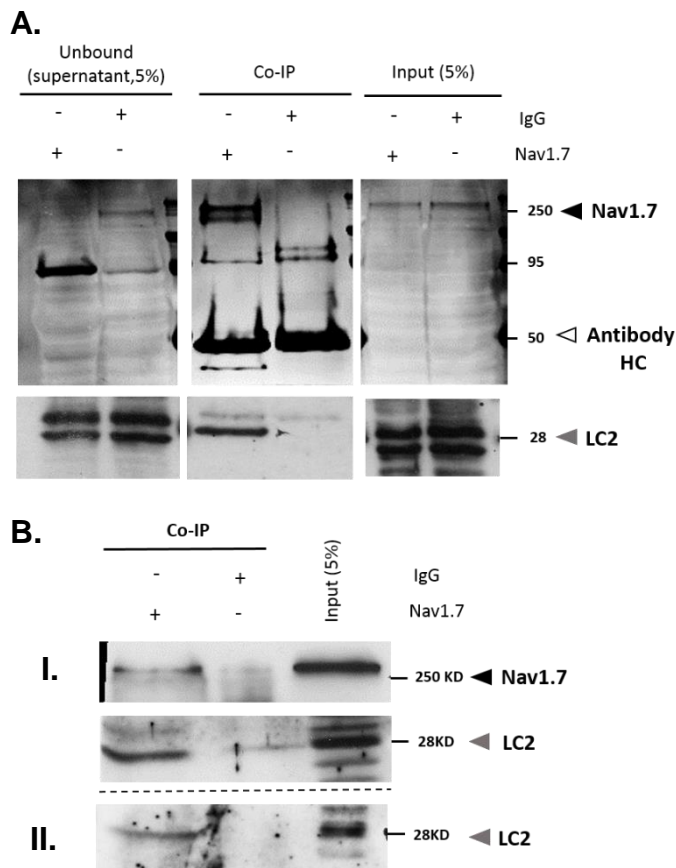


Figure 5.12: Co-immunoprecipitation of Nav1.7 and LC2 in N2a cells. Nav1.7 and LC2 interaction in N2a cells was examined by Co-Immunoprecipitation using antibody against Nav1.7 followed by immunoblotting for both Nav1.7 and LC2. 5 % of the total cell lysate was used as a positive control (input lane), while immunoprecipitation with non-specific IgG was used as a negative control (IgG IP lane). Supernatant lane represents the unbound protein to the antibody-beads complex. Nav1.7 band (250 KD - black arrows) and LC2 band (28 KD - grey arrows) appeared in both the input and the Nav1.7 IP lane but not in the IgG IP. Equal band intensity of the antibody heavy chain appeared at 50 KD in both IgG and Nav1.7 lanes (B) demonstrate other examples of Co-immunoprecipitation of LC2 with Nav1.7 antibody from N2a cell lysates. LC2 band is visible at 28KD in the Nav1.7 IP and input lanes but not in the IgG IP lane. (N=6)

Nav1.7 interacted specifically with LC2 but not with MAP1A-HC, or with the structurally related LC1, Fig. 5.14. Since one of the proposed LC2 functions is to link the microtubules and microfilaments cytoskeleton networks, we hypothesized that β III-tubulin and / or β -actin mediate Nav1.7-LC2 interaction. Due to the lack of polyclonal antibody against β III-tubulin, it was difficult to detect β III-tubulin band at 50 KD as it overlapped with the heavy chain of the antibody band (IgG, Nav1.7 and β III-tubulin are all monoclonal antibodies). To overcome this problem, I used clean-blot® secondary antibody to minimize the interference of the denatured heavy and light IgG bands in WB detection because it predominantly recognises native primary antibody (75 KD) with minimum interaction with the denatured antibody (50 KD and 25 KD). However, an overlap from the heavy-chain antibody band in the IgG IP lane was still observed which precluded the interpretation of the β III-tubulin-Nav1.7 interaction results (data not shown). A polyclonal antibody against acetylated β -tubulin was also tested in WB immunoblotting to get around the detection problem, Fig. 5.14. No band of acetylated β -tubulin was detected in the Nav1.7 IP lane which indicates a negative interaction between the Nav1.7 and the acetylated β -tubulin. Acetylated β -tubulin is known to be predominantly associated with stable MT, therefore, the lack of interaction indicates that stable MT are not involved in the Nav1.7-LC2 complex, however, it does not exclude the possibility of Nav1.7-LC2 interaction with other modified β -tubulin isoforms that are linked to other functions.

β -actin was another protein candidate that might be associated with the LC2-Nav1.7 complex. Immunoblotting against β -actin showed a strong band in Nav1.7 IP lane but not in the IgG IP lane, which indicates a specific interaction between Nav1.7 and the microfilament cytoskeleton, Fig. 5.14. However, due to some technical difficulties with the co-IP protocol at the time and due to the unavailability of the same polyclonal antibody afterwards, I was only able to perform this experiment three times, two of which showed a positive interaction. Although these results are promising, more repeats are needed to reach a stronger conclusion. Importantly, whether this interaction represents a direct association between Nav1.7 and β -actin or an indirect association that is mediated by LC2 is not known.

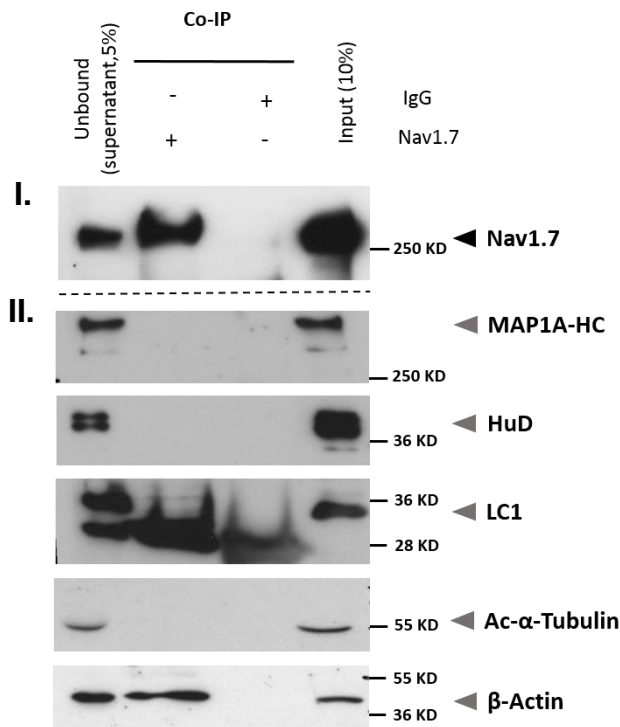


Figure 5.14: Co-immunoprecipitation of Nav1.7 in N2a cells. Antibody against Nav1.7 protein was used for co-IP, followed by immunoblotting using different polyclonal antibodies: MAP1A-HC, HuD, LC1, α -Tubulin and β -Actin. 10 % of whole cell lysate was loaded as positive control (input), IP with non-specific IgG used as a negative control, Supernatant lane represents the portion of the protein that remained unbound to the antibody-bead complex. Nav1.7 IP band was detected every time a co-IP experiment was performed (positive control of co-IP experiment). I. Nav1.7 band appeared at 250 KD (black arrow) in the IP lane as an example for positive IP. II. All of the tested polyclonal antibodies except for β -actin showed no bands in the IP lane indicating lack of interaction between Nav1.7 and the tested proteins in N2a cell line (N=3). β -Actin band is visible in the IP lane indicating an interaction of actin with Nav1.7 in N2a cells, (N=2).

Another potential protein interactor was HuD protein, an RNA-binding protein found in mammalian neurons that is shown to interact with the structurally related LC1²⁵⁹. Nav1.7 co-IP experiment in N2a cells showed no interaction between Nav1.7 and HuD, Fig. 5.14. indicating that HuD is not involved in the LC2-Nav1.7 complex, but it does not exclude the possible interaction between HuD and LC2.

In summary, endogenous Nav1.7 in both mouse N2a cells and DRG cell lysates interacts robustly with endogenous LC2. It is most likely that the interaction also involves the microfilament cytoskeleton. No interaction was detected with the homologous protein (LC1) nor with the heavy-chain of MAP1A which indicates a specific role for LC2 in regulating Nav1.7 function.

5.4.3. Knock-down of MAP1A protein in N2a and DRG neurons.

To investigate the functional role of LC2-Nav1.7 interaction, it was essential to establish an efficient KD of MAP1A gene since LC2 is produced by the enzymatic cleavage of the MAP1A protein during post-translational modifications¹⁸⁶. DRG neurons are notoriously resistant to transfection methods. Several transfection reagents (e.g. Lipofectamine, Lipofectamine 2000, Lipofectamine 3000, Lipofectamine LTX, PEI, Viromer green and Viromer blue) were initially tested to establish a transfection strategy that can be used as a standard protocol, however most of the tested reagents failed to produce a transfection efficiency higher than 15 %, data not shown.

Other methods like electroporation and virus transduction are known to be better options for DRG transfection. Electroporation, however, suffers from a very low transfection efficiency which is a limitation when dealing with a highly heterogeneous population like DRG sensory neurons. Therefore, lentivirus transduction method was a more preferable option for many reasons. First, LV transduction was shown to target all subpopulations of DRG neurons with relatively good transduction efficiency (~ 40 %) ^{260,261}. Second, LV production is simple, relatively fast and cheap (i.e. no kits or special reagents are required). Third, the availability of local support and expertise, dedicated rooms and equipment that were provided by Prof. Mimoun research group made the process feasible. Finally, the simplicity of the DRG transduction protocol compared to the other electroporation and nucleoporation methods. In Amaxa nucleoporation protocol, the harvested DRGs need to be transfected prior to seeding, which might add extra stress on the neurons and consequently result in excessive loss of DRG neurons. Whereas, lentivirus transduction protocol is more flexible as it can be applied to seeded DRG neurons at any time point and at any seeding density. For all the aforementioned reasons, we decided to use lentivirus as the standard method for *in vitro* gene manipulation in DRG neurons.

Several steps were involved in the preparation for MAP1A KD in DRG neurons. The work was divided into two main stages, stage (I) was in N2a cell line to test and optimize MAP1A miRNA sequences. Once optimised, stage (II) was started in primary

culture of DRG neurons. the work flow was performed as demonstrated in the flow chart, Fig. 5.15.

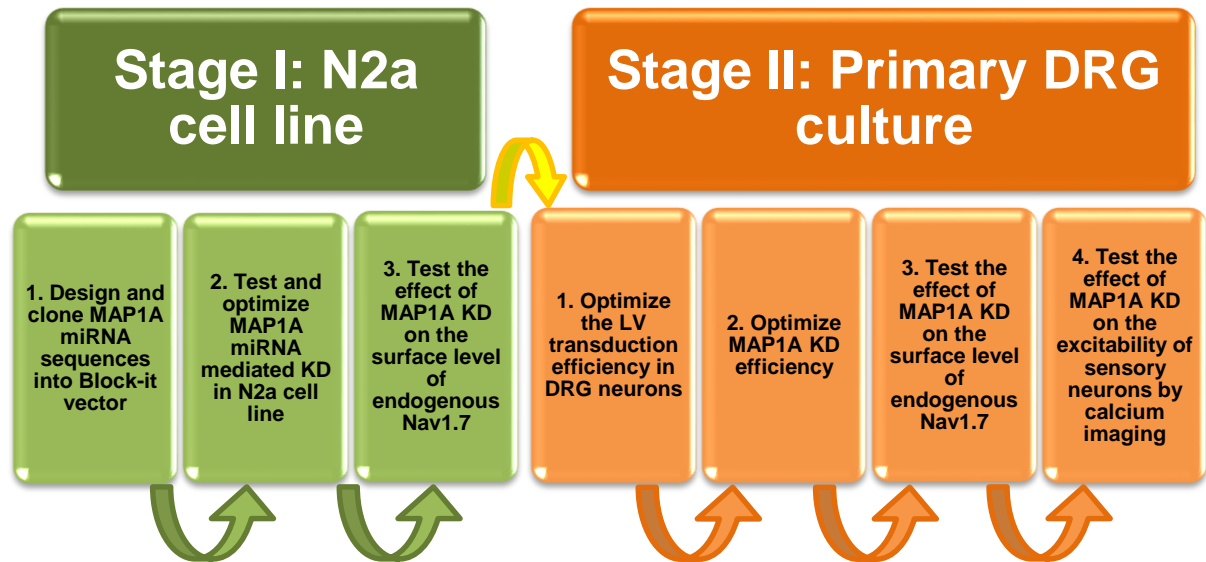


Figure 5.15: Flow chart demonstration of the work flow followed in this chapter to test the functional effect of MAP1A KD in adult mouse DRG neurons. First stage (green) demonstrate all the initial work that was performed in N2a cell line followed by stage II (orange) which represent the optimization steps as well as the functional testing of MAP1A KD in DRG neurons.

5.4.3.1. MAP1A miRNA cloning, testing and optimisation of MAP1A knock-down in N2a cells:

Four different miRNA sequences targeting different regions of MAP1A gene (heavy and light chain) that are listed in section 2.1.14 were cloned into the Block-it Pol II miR RNAi vector (Invitrogen) as described under section 2.2.11, Fig. 2.3.

The efficiency of the four MAP1A miRNA sequences to knock-down MAP1A protein in N2a cells was tested by WB. Although a high transfection efficiency was obtained (> 80 %), MAP1A KD efficiency was inconsistent. Different strategies were tested to optimise the KD efficiency (e.g. increasing DNA concentration, various DNA: PEI ratios, various time points, two sequential transfection of the same miRNA and two miRNA co-transfection), data not shown. Among the tested conditions a better KD efficiency was achieved when two miRNA plasmids were co-transfected. miRNA combinations including sequence 2 produced the highest KD efficiency. New plasmids

were made where sequence 2 was chained to miR1, miR3 or miR4 sequences. KD efficiency of the three new constructs were validated by WB. Since the heavy chain (HC) and the light chain (LC2) of MAP1A are derived from the same mRNA and due to the limited amount of LC2 antibody, MAP1A-HC antibody was routinely used to detect MAP1A KD efficiency. As shown in Fig. 5.16, the transfection of N2a cells with MAP1A miRNA sequences for 96 h resulted in 80 - 90 % KD efficiency by miRNA (2+3) and more than 50 % KD efficiency by the other two miRNAs.

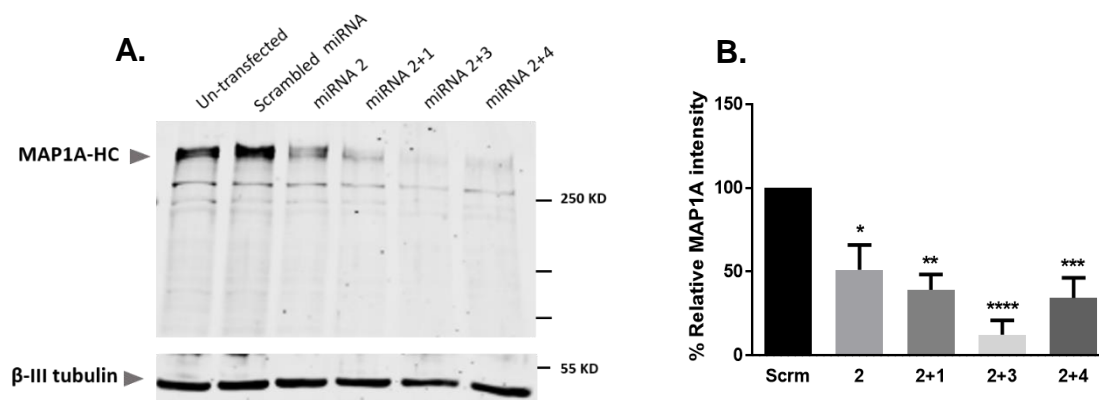


Figure 5.16: Quantification of MAP1A KD in N2a cells by miRNA chaining approach.

A. Knock-down of MAP1A protein in N2a cells. N2a cells were treated with four miRNA against MAP1A plus a non-specific miRNA (scrambled) used as a negative control. Cells were lysed after 96h of transfection and analysed by western blot to quantify the KD efficiency using polyclonal MAP1A antibody that recognizes the heavy chain of the protein (grey arrow, 350 KD) and a lower band of unknown identity. Monoclonal β -III Tubulin antibody was used as a loading control. Image Studio Lite software was used for the quantification and image processing.

B. Quantification of the percentage of MAP1A KD efficiency. Samples were compared to Scrambled miRNA with One-Way ANOVA, Multiple comparison with Dunnett post hoc test, * $P < 0.05$, ** $P < 0.01$, *** $P < 0.001$ and **** $P < 0.0001$. $N = 5$, Error bars represent SEM.

To check the specificity of MAP1A KD, I checked the level of other proteins in MAP1A KD samples, like LC1 (the light chain of MAP1B protein, encoded by MAP1B gene and share more than 50% homology to LC2) and LC3 (encoded by MAP1LC3 gene, can bind to the MAP1A-HC but mostly involved in autophagy). WB analysis showed no significant change in the level of LC1 and LC3 with miR2+1 and miR2+4, while miR2+3 caused a significant reduction in the level of these two proteins, Fig.5.17. These results suggested that miR2+3 has some off-target effect on LC1 and LC3, or that microtubule related proteins are disrupted and negatively regulated as a consequence of strong MAP1A KD that was produced by miR2+3. To avoid this effect of MAP1A miR2+3, only miR2+4 and miR2+1 were selected for LV production and for further functional experiments.

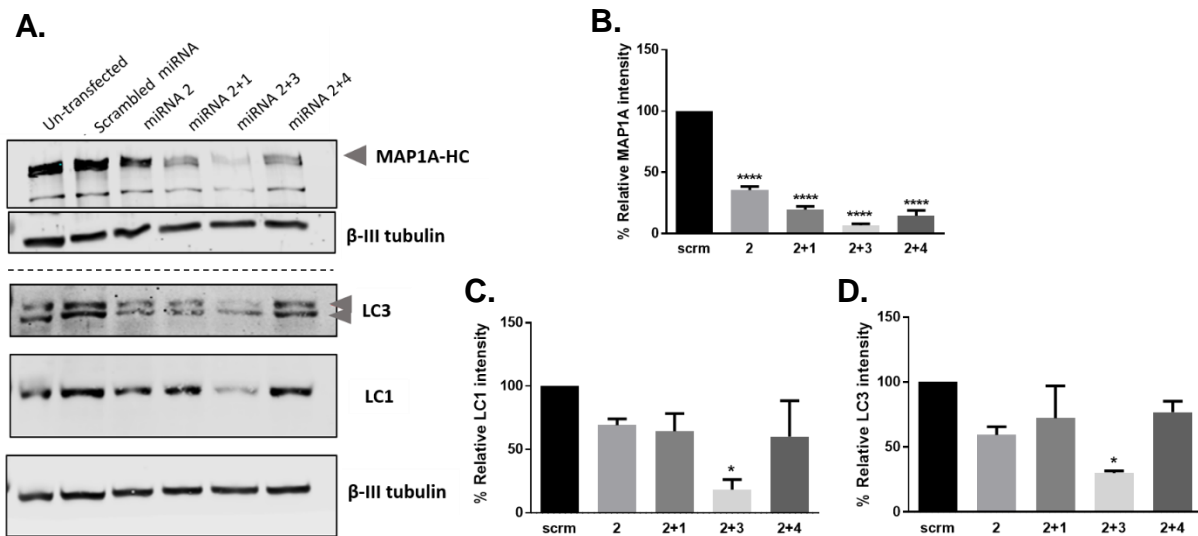


Figure 5.17: Specificity of MAP1A miRNA in N2a cells.

A. Knock-down of MAP1A protein in N2a cells. N2a cells were treated with four miRNA against MAP1A plus a non-specific miRNA (scrambled) used as a negative control. Cells were lysed after 96h of transfection and analysed by western blot to quantify the KD efficiency using polyclonal MAP1A antibody that recognizes the heavy chain of the protein (grey arrow, 350 KD) and a lower band of unknown identity. Monoclonal β -III Tubulin antibody was used as a loading control. Image Studio Lite software was used for the quantification and image processing.

B. Quantification of the percentage of MAP1A KD efficiency. Significant reduction in MAP1A protein level was observed in all MAP1A miRNA sequences. miR2+3 produced the highest KD efficiency.

C. and D. Analysis of the effect of MAP1A KD on other related proteins, LC1 in C and LC3 in D. The level of the proteins was only reduced with miR2+3 but not with the other miRNA sequences.

Samples were compared to Scrambled miRNA with One-Way ANOVA, Dunnett test, * $P < 0.05$, and **** $P < 0.0001$. $N = 2$, Error bars represent SEM.

5.4.3.2. MAP1A KD functional effect on the surface expression level of endogenous Nav1.7 in N2a cells:

Based on the evidence from the literature, it was hypothesised that the light chain of MAP1A protein (LC2) is involved in the regulation of Nav1.7 surface level. To test this hypothesis, N2a cells were treated with scrambled miRNA and MAP1A miRNAs for 96h. Surface proteins were then labelled with biotin, pulled down with Streptavidine beads and analysed for surface Nav1.7 signal by western blotting. GAPDH was used as a marker for the cytosolic fraction, while Na^+/K^+ ATPase was used as a positive control for cell membrane fraction (surface), as demonstrated in Fig. 5.18. Analysis of surface Nav1.7 in the different miRNA treated samples showed a trend of reduced surface Nav1.7 upon MAP1A KD, but neither of them were significantly different, Fig. 5.18. It is noteworthy to mention that although the starting seeding density of N2a cells

were kept constant, MAP1A miRNAs, particularly miR2+3, produced variable levels of cytotoxicity and cell death which made the samples varied in protein concentration. Therefore, the relative intensity of surface Nav1.7 to Na⁺/K⁺ ATPase intensity (surface/input) was measured to account for any loading variabilities between the samples. In conclusion, surface biotinylation experiments showed that upon MAP1A KD in N2a, Nav1.7 surface expression seems to be negatively affected. However, the effect is very modest and more data are required to obtain a stronger conclusion.

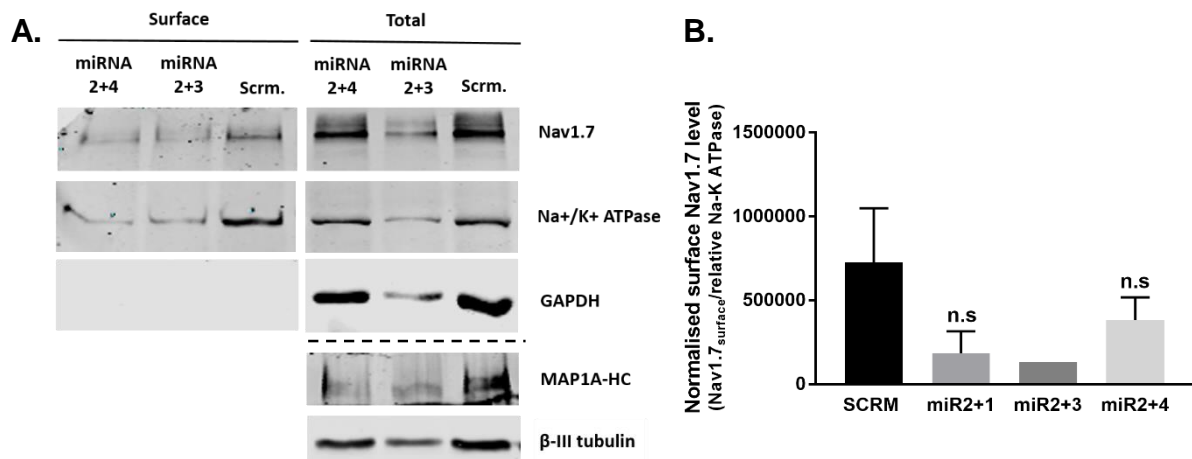


Figure 5.18: The effect on MAP1A KD on surface Nav1.7 expression level in N2a cells. **A.** N2a cells were treated with two different MAP1A miRNA and with a nonspecific scrambled miRNA (scrm) for 96hr, followed by labelling surface protein with biotin. Total lysate (10%) was used as a positive control and a loading control as well (Right-side panel). Note that miR2+3 sample were less than the other two that was mainly because of cytotoxicity and loss of cells after 96h of transfection with miR2+3. Na⁺/K⁺ ATPase was used as a surface protein marker. GAPDH used as a control for cytoplasmic fraction, no GAPDH signal in the surface fraction. Another 10% of the total lysate were resolved on a different SDS-PAGE gel to check the knock-down efficiency using MAP1A-HC antibody and βIII-tubulin as a loading control. **B.** Quantification of Nav1.7 surface protein compared to Scrambled miRNA using relative Na/K ATPase (surface / input) for normalization to account for loading variations. Only the experiments that showed > 20% reduction in MAP1A-HC signal were included in the analysis. No significant difference was detected between Scrambled miRNA and the other miRNA sequences.

Samples were compared to Scrambled miRNA with One-Way ANOVA, Dunnett test, **P* < 0.05. *N* = 4 (Scrambled miRNA & miR2+4), *N* = 2 (miR2+1), *N* = 1 (miR2+3). Error bars represent SEM.

5.4.3.3. Optimization of lentivirus multiplicity of infection (MOI) for DRG neuron transduction.

A pilot experiment with a lentivirus encoding GFP (produced by Prof. Mimoun research group at Sitran facility) was used to test the LV transduction efficiency in mouse DRG culture. Cells were transduced at various multiplicities of infection (MOIs); MOI 30 and MOI 100 and live imaged at different time points (day 3, 5 and 7 post transduction). GFP signal was used as a positive control for transduced cells. In average, 35 % of the neurons were transduced at MOI 30 with no significant difference between the different time points, Fig. 5.19 and Fig. 5.21. MOI 100 showed a better neuronal transduction efficiency (45 – 50 % in average) at day 7 post transduction, Fig. 5.20 & 5.21. These results demonstrated that LV transduction is dose and time dependent. Higher MOIs with longer incubation period increases the LV transduction. MOIs within the range of a 100 produces ~ 50 % transduction efficiency with minimum cytotoxicity.

Because DRG culture is a heterogeneous population of neurons and non-neuronal cells, I tried to minimise the growth of non-neuronal cells by incubating the culture in a serum-free medium. However, a significant number of non-neuronal cells were still available and were competing with the neurons for the uptake of the GFP virus. An alternative option to reduce the non-neuronal cells was to use anti-mitotic drugs to inhibit cell replication. However anti-mitotic drugs that interfere with microtubules polymerization were not a good choice for this particular project, so other anti-mitotic drugs like (5-fluorodeoxyuridine + uridine) that inhibit DNA replication were a more preferable strategy. However, the treatment interfered with the production of GFP and did not significantly help in reducing the non-neuronal cells in my hands, therefore I omitted the use of any antimitotic drugs in further experiment. Furthermore, although serum free condition helped in reducing the number of non-neuronal cells, it negatively affected neuronal health and survival in long incubation periods. Therefore, it was crucial to maintain the balance between the non-neuronal cells outgrowth and the health of the neurons. Series of experiments were performed to identify the best condition for DRG transduction, finally it was concluded that incubation of the DRG culture with 2.5 % serum supplemented with B27 and 0.5 ng/mL NGF are the best conditions to be used for LV-based functional experiments (described later in this chapter).

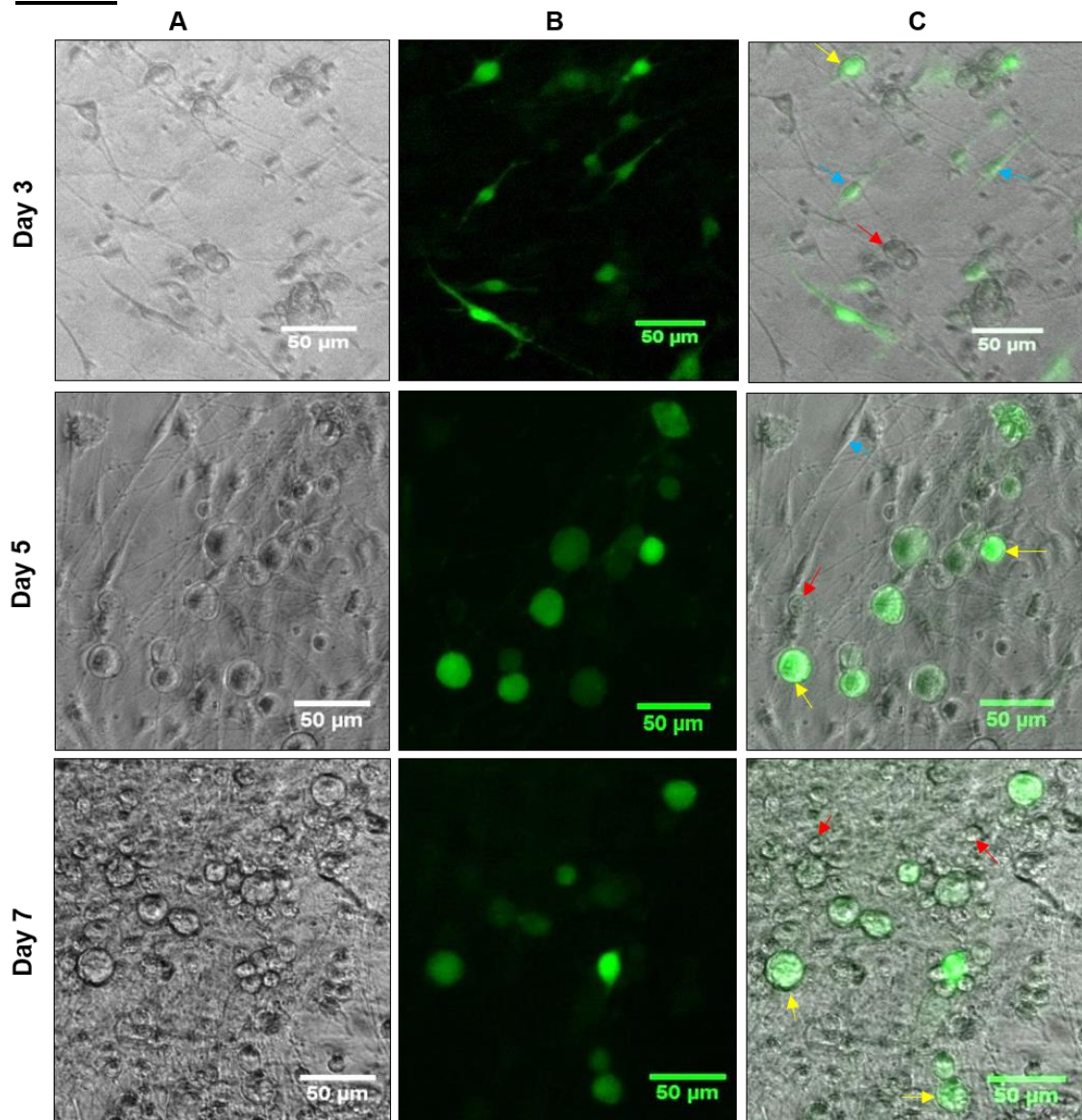
MOI 30

Figure 5.19: GFP expression in dissociated adult DRG culture transduced with GFP-lentivirus.

DRG cells were transduced at *I*. MOI = 30 using lentivirus encoding GFP. Cultures were maintained in serum free conditions and imaged at day 3, 5 and 7 DIV (days in vitro). Representative images of the GFP expressing culture (A) phase-contrast images, (B) GFP positive cells and (C) merged A & B. Cells that have a round-shape, smooth surface with defined edges were identified as neurons while long, spindle-shape, flat cells were identified as non-neuronal cells. Yellow arrows point to transduced neurons, red arrows to non-transduced neurons, and blue arrows point to non-neuronal cells. Scale bars = 50 µm

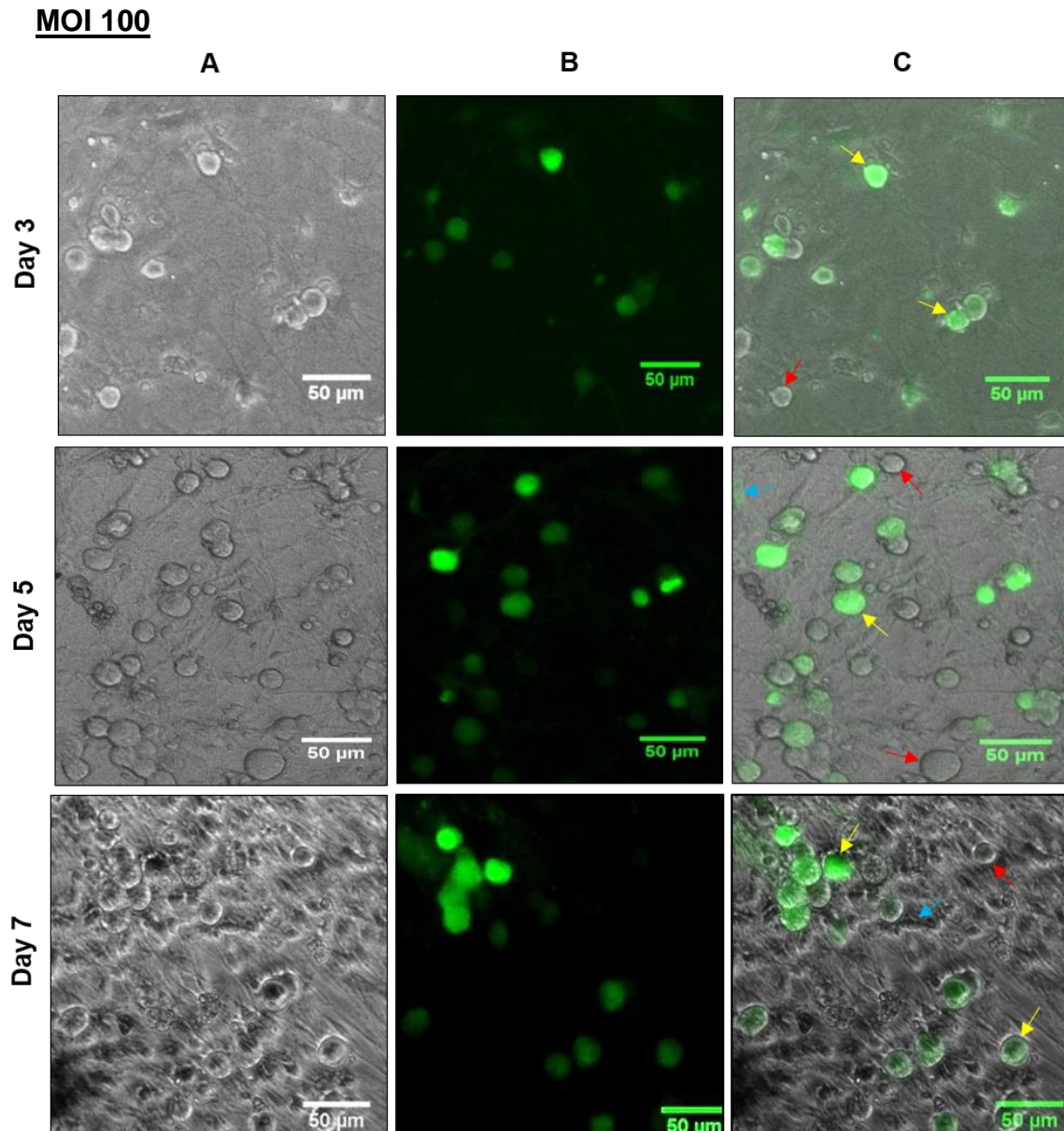
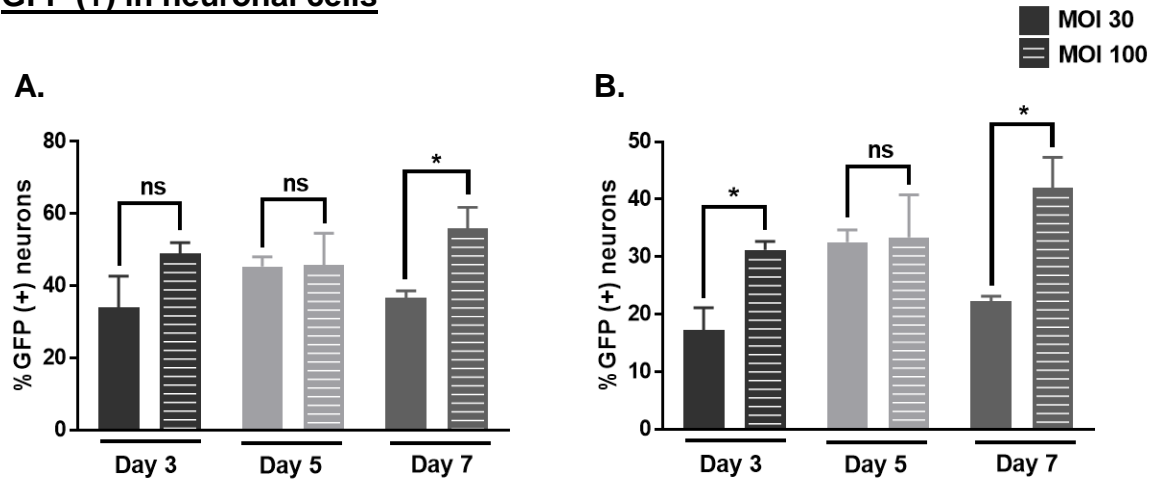
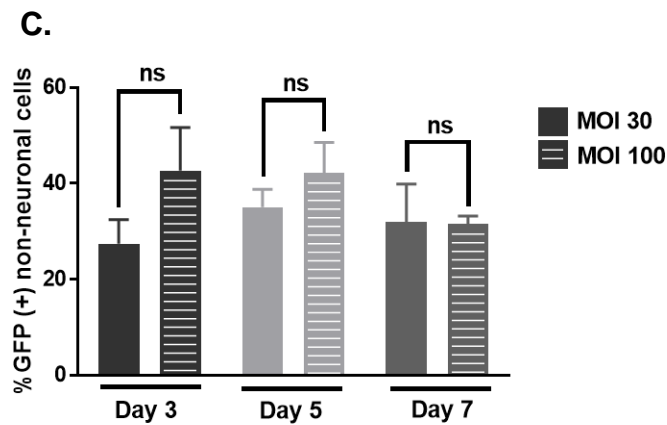


Figure 5.20: GFP expression in dissociated adult DRG culture transduced with GFP-lentivirus.

DRG cells were transduced at MOI = 100 using lentivirus encoding GFP. Cultures were maintained in serum free conditions and imaged at day 3, 5 and 7 DIV (days in vitro). Representative images of the GFP expressing culture (A) phase-contrast images, (B) GFP positive cells and (C) merged A & B. Cells that have a round-shape, smooth surface with defined edges were identified as neurons while long, spindle-shape, flat cells were identified as non-neuronal cells. Yellow arrows point to transduced neurons, red arrows to non-transduced neurons, and blue arrows point to non-neuronal cells. Scale bars = 50 μ m

GFP (+) in neuronal cells**GFP (+) in non-neuronal cells****Figure 5.21: Lentivirus transduction efficiency in adult mouse DRG culture.**

A. Percentage of GFP positive neurons using two MOI (30 and 100) at 3, 5 and 7 DIV. Day 3: MOI 30 = $34 \pm 8.7\%$, MOI 100 = $49 \pm 3\%$; Day 5: MOI 30 = $45.3 \pm 2.7\%$, MOI 100 = $45.7 \pm 9\%$; Day 7: MOI 30 = $36.7 \pm 2\%$, MOI 100 = $56 \pm 5.8\%$.

B. Percentage of only the strongly GFP positive neurons using two MOI (30 and 100) at 3, 5 and 7 DIV. Day 3: MOI 30 = $17.3 \pm 3.9\%$, MOI 100 = $31.2 \pm 1.5\%$; Day 5: MOI 30 = $32.6 \pm 2.1\%$, MOI 100 = $33.4 \pm 7.4\%$; Day 7: MOI 30 = $22.3 \pm 0.9\%$, MOI 100 = $42 \pm 5.3\%$.

C. Percentage of GFP positive non-neuronal cells using two MOI (30 and 100) at three time points 3, 5 and 7 DIV. Day 3: MOI 30 = $27.5 \pm 5\%$, MOI 100 = $42.7 \pm 9\%$; Day 5: MOI 30 = $35.1 \pm 3.7\%$, MOI 100 = $42.1 \pm 6.4\%$; Day 7: MOI 30 = $32 \pm 8\%$, MOI 100 = $31.6 \pm 1.7\%$.

Cells that have a round-shape, smooth surface with defined edges were identified as neurons while long, spindle-shape, flat cells were identified as non-neuronal cells. Cells that have GFP signal above 30 % of background were considered as strongly positive.

Two-tailed unpaired Student's *t*-test, **P* < 0.05. *N* = 3 DRG cultures.

5.4.3.4. Production of LV-MAP1A miRNA and in vitro determination of MAP1A KD efficiency in DRG sensory neurons.

For the virus production, miRNA sequences were subcloned into SIN-PGK-cPPT-GDNF-WHV vector provided by Prof. Mimoun research group as described in section 2.2.12. MAP1A KD efficiency of the newly produced LV-miRNA vector was assessed in N2a cell using WB, Fig.5.22. All single miRNA showed very low KD efficiency (in accordance with previous results), while 2+1 and 2+4 miRNA sequences consistently produced the highest KD efficiency, 54 and 48 %, respectively. Therefore, these two miRNAs were selected to proceed with the LV production.

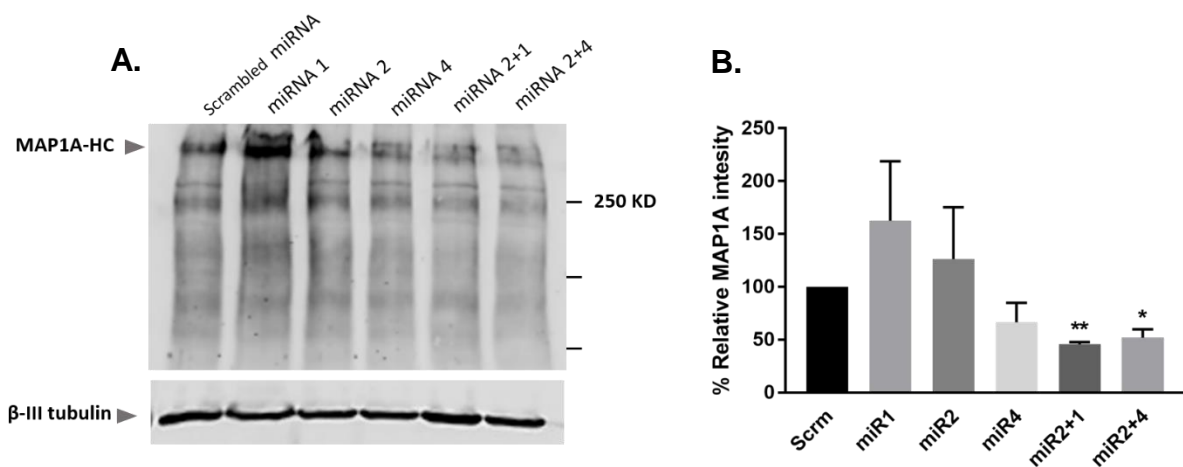


Figure 5.22: Quantification of MAP1A KD in N2a cells using LV vector.

A. Knock-down of MAP1A protein in N2a cells. N2a cells were treated with five miRNA against MAP1A plus a non-specific miRNA (scrambled) used as a negative control. Cells were lysed after 96h of transfection and analysed by western blot to quantify the KD efficiency using polyclonal MAP1A-HC antibody, MAP1A-HC band was indicated by an arrow at 350 KD. Monoclonal β III-tubulin antibody was used as a loading control. Image Studio Lite software was used for quantification and image processing. **B.** Quantification of the percentage of MAP1A KD efficiency. Samples were compared to Scrambled miRNA with Two-tailed unpaired Student's *t*-test, **P* < 0.05 and ***P* < 0.01. *N* = 2, Error bars represent SEM.

In collaboration with Prof. Mimoun group, I produced LV-MAP1A miRNA at Sitran facility as described in section 2.2.12. GFP signal in Hela cells was used to measure the titre of every new LV batch by flow cytometry to be able to accurately calculate the MOI. The transduction efficiency of the scrambled, 2+1 and 2+4 miRNAs were tested in DRG culture in a similar fashion to the LV-GFP used in the pilot experiment described in the previous section. Two extra MOIs were also tested (MOI 500 and MOI 1000), which showed a slight enhancement in the transduction efficiency, however the

cytotoxic effect on the neuronal cells was more evident therefore they were not used in further experiments, data not shown.

After assessing the transduction efficiency of the different MOIs, the next aim was to determine MAP1A KD efficiency in DRG neurons. In this case, WB was not the method of choice for the detection of MAP1A protein level in neuronal cells due to the heterogeneity of DRG culture. Also because KD efficiency would have been underestimated by the untransduced cells (~ 50 %). Other approaches were tested in order to quantify MAP1A KD in DRG neurons. One option was to isolate the transduced neurons by flow cytometry (using GFP signal and cell size) and then analyse MAP1A level in the GFP-positive fraction by WB. The isolation of DRG neurons by flow cytometry was technically challenging and required several optimization steps; starting from maintaining the health of the neurons during the detachment process, efficient, yet gentle, trituration to obtain a single cell suspension without compromising the cells health, and finally obtain a sufficient yield of the transduced neurons at the end of the flow cytometry run to be used in WB for KD analysis. However, DRG neurons in long term culture tend to always make a very strong basement layer that was hard to detach into a single cell suspension, also cells tend to clump together and block the flow cytometry machine which resulted in cell loss and inappropriate separation of pure GFP positive neuronal fraction.

As an alternative approach, I used immunofluorescence to quantify MAP1A-HC level in neuronal cells using both GFP and β -tubulin III as positive controls for transduced neuronal cells. GFP signal was very weak after fixing (at a same level to background) which made it very difficult to accurately use GFP as marker for LV transduced neurons. To overcome this problem, MAP1A-HC integrated density (I.D) of all neurons (identified by β III-tubulin immunelabelling) were included in the quantification. Analysis of MAP1A expression level in the two controls (untransduced cells and LV scrambled miRNA) showed that MAP1A expression level naturally varied between DRG neurons (low, medium, and high), Fig. 5.23. This factor added an additional complexity in quantifying MAP1A KD efficiency in such heterogeneous expression level.

To be able to detect MAP1A KD, we assumed that a shift in MAP1A distribution toward the “low MAP1A” was an evidence for protein knock-down in neurons. The

interquartile range of the integrated density of “the scrambled” MAP1A-HC fluorescence was used to set the threshold for low (< 25 %), medium (~ 50 %) and high MAP1A (> 75 %) categories in each of the experiment repeats. Percentage of cells within these bins in the scrambled miRNA was compared to that in MAP1A miR 2+1 and MAP1A miR 2+4 LV transduced neurons for each MOI (20, 50, 100 and 300), Fig. 5.24. Within all of the tested MOIs, except for MOI 100, there was a consistent trend of an increased number of “low MAP1A, < 25%” neurons accompanied by a decreased number of “high MAP1A, > 75%”. However, only at MOI 300 this trend was statistically significant, Fig. 5.24. To validate this analysis approach, the same quantification method was applied to β III-tubulin I.D signal, Fig. 5.25. Quantification of β III-tubulin I.D showed no consistent trend as that obtained with MAP1A-HC immunolabelling, which confirmed the specificity of MAP1A KD, as well as the reliability of the KD quantification method. In summary, the use of LV-MAP1A miRNA at MOI300 showed approximately 50 % transduction efficiency with significant MAP1A KD efficiency in DRG neurons and minimum cytotoxicity. Therefore, MOI 300 was used in further experiments to analyse the functional effect of MAP1A KD on DRG neurons.

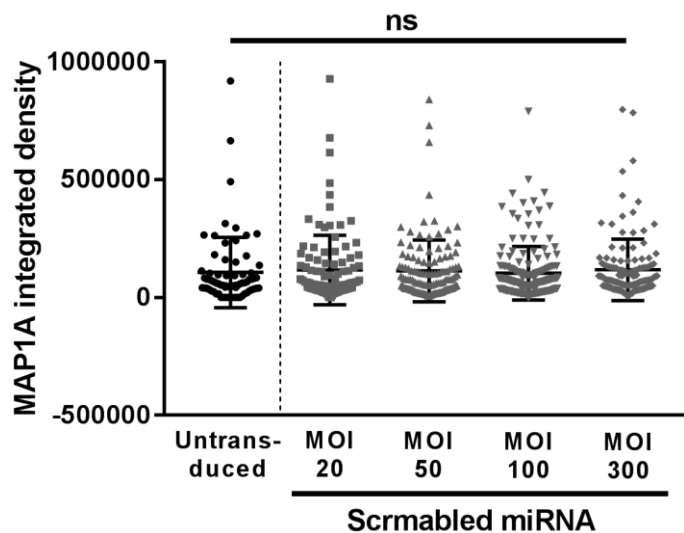


Figure 5.23: Distribution of MAP1A-HC integrated density in DRG culture. DRG cultures were transduced with scrambled miRNA LV at MOI 20, 50, 100 and 300. Cells were fixed 5 days post transduction and immunostained with MAP1A-HC antibody. The integrated density (mean grey value * area) of MAP1A-HC in DRG culture showed a wide and similar range of expression level in both control (untransduced DRG culture) and scrambled miRNA LV. The mean value in the control group was not significantly different to the mean values obtained with scrambled miRNA LV within all the tested MOIs.

Data was compared to Control group by Two-tailed unpaired Student's *t*-test, **P* < 0.05 and ***P* < 0.01. *N* = 4 DRG cultures, number of cells (*n*) for untransduced = 72 cells, SCRM_{MOI20} = 103 cells, SCRM_{MOI50} = 125 cells, SCRM_{MOI100} = 166 cells, SCRM_{MOI300} = 133 cells. Error bars represent SD.

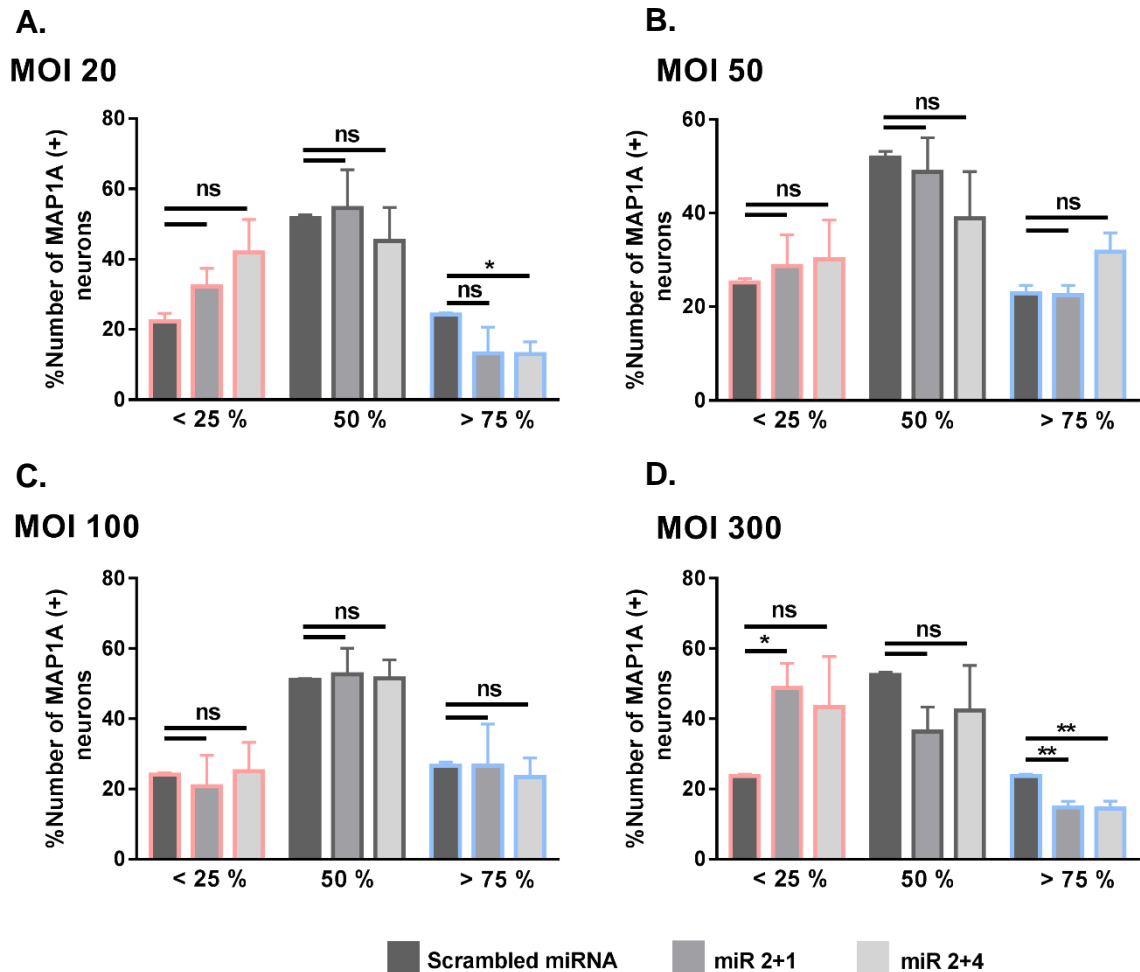


Figure 5.24: Lentivirus mediated MAP1A knock-down in adult mouse DRG culture.

Percentages of MAP1A expressing cells in different LV MOIs. MAP1A I.D was divided into 3 groups according to the interquartile range of the scrambled miRNA in each experiment (pink borders: less than 25 %, grey borders: 50 %, and blue borders: higher than 75 %). MOI 300 was the only MOI that showed signs of MAP1A KD, indicated by significantly higher percentages of (< 25 %) bin and lower percentages of (>75 %) bin in MAP1A miRNA.

A. DRG culture transduced with MOI 20 of MAP1A LV miRNA. Scrm_{< 25 %} = 22.3 ± 2.3, miR2+1_{< 25 %} = 32.27 ± 5.1, miR2+4_{< 25 %} = 41.9 ± 9.4; Scrm_{50 %} = 51.6 ± 0.97, miR2+1_{50 %} = 54.6 ± 11, miR2+4_{50 %} = 45.2 ± 9.5; Scrm_{> 75 %} = 24.2 ± 0.5, miR2+1_{> 75 %} = 13.15 ± 7.5, miR2+4_{> 75 %} = 13 ± 3.4.

B. DRG culture transduced with MOI 50 of MAP1A LV miRNA. Scrm_{< 25 %} = 25.2 ± 0.84, miR2+1_{< 25 %} = 28.7 ± 6.7, miR2+4_{< 25 %} = 30.1 ± 8.4; Scrm_{50 %} = 51.9 ± 1.3, miR2+1_{50 %} = 48.8 ± 7.3, miR2+4_{50 %} = 38.8 ± 10; Scrm_{> 75 %} = 23 ± 1.6, miR2+1_{> 75 %} = 22.5 ± 2.1, miR2+4_{> 75 %} = 31.8 ± 4.

C. DRG culture transduced with MOI 100 of MAP1A LV miRNA. Scrm_{< 25 %} = 24.1 ± 0.5, miR2+1_{< 25 %} = 20.7 ± 9, miR2+4_{< 25 %} = 25.1 ± 8.3; Scrm_{50 %} = 51 ± 0.4, miR2+1_{50 %} = 52.6 ± 7.5, miR2+4_{50 %} = 51.5 ± 5.2; Scrm_{> 75 %} = 26.5 ± 1.2, miR2+1_{> 75 %} = 26.7 ± 11.8, miR2+4_{> 75 %} = 23.4 ± 5.4.

D. DRG culture transduced with MOI 300 of MAP1A LV miRNA. Scrm_{< 25 %} = 23.8 ± 0.4, miR2+1_{< 25 %} = 48.7 ± 7.1, miR2+4_{< 25 %} = 43.2 ± 14.5; Scrm_{50 %} = 52.4 ± 0.8, miR2+1_{50 %} = 36.5 ± 7, miR2+4_{50 %} = 42.3 ± 12.8; Scrm_{> 75 %} = 23.8 ± 0.4, miR2+1_{> 75 %} = 14.8 ± 1.6, miR2+4_{> 75 %} = 14.4 ± 2.1.

Two-tailed unpaired Student's *t*-test, **P* < 0.05 and ***P* < 0.01. *N* = 4 DRG cultures. number of cells (*n*) for SCRM_{MOI20} = 103, SCRM_{MOI50} = 125, SCRM_{MOI100} = 166, SCRM_{MOI300} = 133, miR2+1_{MOI20} = 98, miR2+1_{MOI50} = 114, miR2+1_{MOI100} = 92, miR2+1_{MOI300} = 157, miR2+4_{MOI20} = 95, miR2+4_{MOI50} = 123, miR2+4_{MOI100} = 98, miR2+4_{MOI300} = 185 cells. Error bars represent SEM.

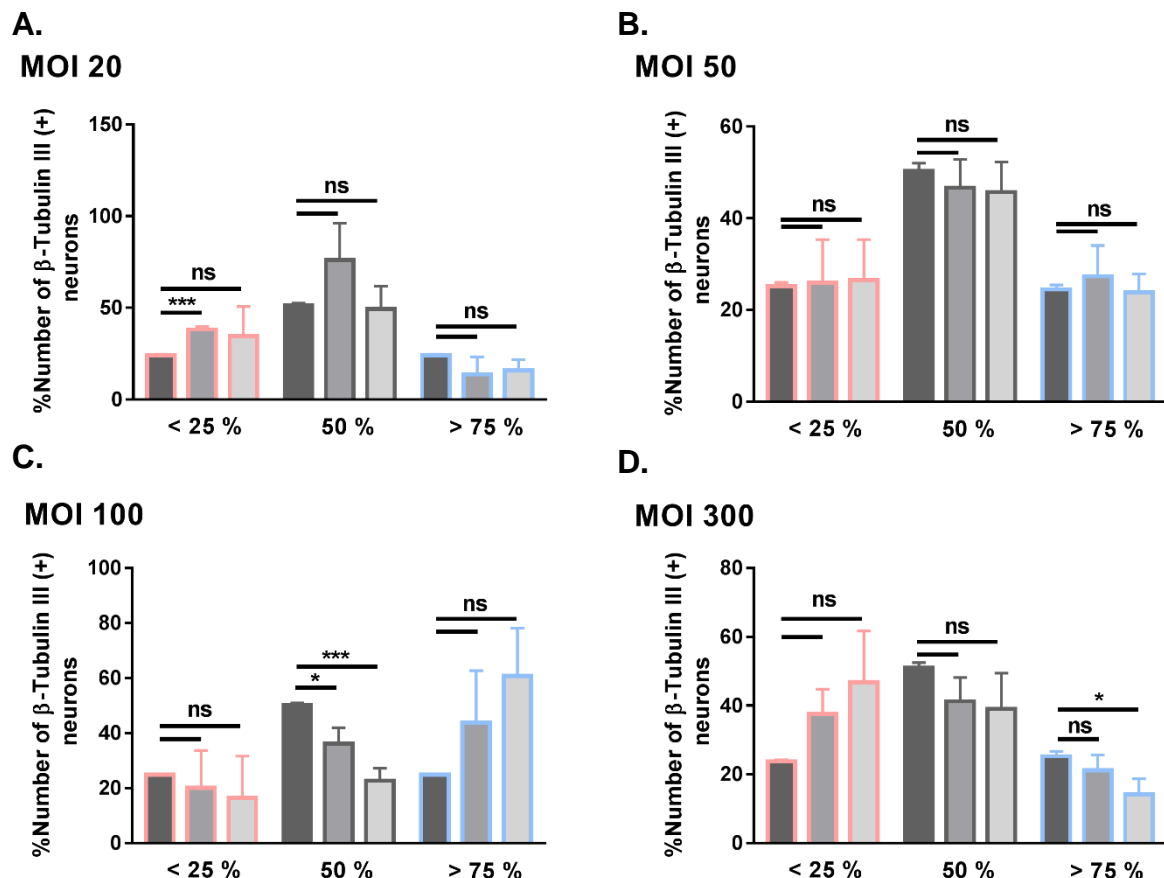


Figure 5.25: β III-tubulin expression level in adult mouse DRG culture transduced with lentivirus expressing MAP1A miRNA.

Percentages of β -Tubulin III expressing cells in different LV MOI. β -Tubulin III I.D was divided into three groups according to the interquartile range of the scrambled miRNA in each experiment (pink borders: less than 25 %, gray borders: 50 %, and blue borders: higher than 75 %).

A. DRG culture transduced with MOI 20 of MAP1A LV miRNA. Scrm_{<25%} = 24.2 ± 0.5 , miR2+1_{<25%} = 38.2 ± 1.7 , miR2+4_{<25%} = 34.7 ± 16 ; Scrm_{50%} = 51.6 ± 0.97 , miR2+1_{50%} = 76.1 ± 20.1 , miR2+4_{50%} = 49.5 ± 12.3 ; Scrm_{>75%} = 24.2 ± 0.5 , miR2+1_{>75%} = 13.6 ± 9.7 , miR2+4_{>75%} = 15.8 ± 6 .

B. DRG culture transduced with MOI 50 of MAP1A LV miRNA. Scrm_{<25%} = 25.2 ± 0.84 , miR2+1_{<25%} = 26 ± 9.4 , miR2+4_{<25%} = 26.5 ± 8.9 ; Scrm_{50%} = 50.3 ± 1.7 , miR2+1_{50%} = 46.7 ± 6.2 , miR2+4_{50%} = 45.7 ± 6.6 ; Scrm_{>75%} = 24.5 ± 1 , miR2+1_{>75%} = 27.4 ± 6.7 , miR2+4_{>75%} = 23.8 ± 4 .

C. DRG culture transduced with MOI 100 of MAP1A LV miRNA. Scrm_{<25%} = 24.9 ± 0.4 , miR2+1_{<25%} = 20.1 ± 13.5 , miR2+4_{<25%} = 16.5 ± 15.1 ; Scrm_{50%} = 50.2 ± 0.7 , miR2+1_{50%} = 36.1 ± 5.8 , miR2+4_{50%} = 22.7 ± 4.4 ; Scrm_{>75%} = 24.9 ± 0.3 , miR2+1_{>75%} = 43.7 ± 18.9 , miR2+4_{>75%} = 60.8 ± 17.4 .

D. DRG culture transduced with MOI 300 of MAP1A LV miRNA. Scrm_{<25%} = 23.8 ± 0.4 , miR2+1_{<25%} = 37.6 ± 7.2 , miR2+4_{<25%} = 46.8 ± 14.9 ; Scrm_{50%} = 51 ± 1.5 , miR2+1_{50%} = 41.2 ± 7 , miR2+4_{50%} = 39 ± 10.5 ; Scrm_{>75%} = 25.3 ± 1.4 , miR2+1_{>75%} = 21.2 ± 4.5 , miR2+4_{>75%} = 14.2 ± 4.5 .

Two-tailed unpaired Student's t-test, * $P < 0.05$ and *** $P < 0.001$. $N = 4$ DRG cultures. number of cells (n) for SCRM_{MOI20} = 103, SCRM_{MOI50} = 125, SCRM_{MOI100} = 166, SCRM_{MOI300} = 133, miR2+1_{MOI20} = 98, miR2+1_{MOI50} = 114, miR2+1_{MOI100} = 92, miR2+1_{MOI300} = 157, miR2+4_{MOI20} = 95, miR2+4_{MOI50} = 123, miR2+4_{MOI100} = 98, miR2+4_{MOI300} = 185 cells. Error bars represent SEM.

5.4.4. The effect of MAP1A KD on Nav1.7 surface expression in mouse DRG neurons:

Several lines of evidence suggest a role for MAP1 light chains in regulating the surface expression of various ion channels. The surface biotinylation data of MAP1A KD in N2a cells presented earlier in Fig. 5.18, showed a small but statistically non-significant decrease in Nav1.7 surface level in MAP1A KD compared to control. To test whether MAP1A KD in DRG neurons has a similar effect to that observed in N2a cells, I investigated the role of MAP1A on Nav1.7 surface expression in DRG neurons by immunofluorescence.

DRG neurons transduced with LV scrambled miRNA, LV-MAP1A miR 2+1 or LV-MAP1A miR 2+4 at MOI 300 were fixed at day 5 post-transduction and immunolabelled with DAPI, GFP booster, polyclonal MAP1A-HC and monoclonal Nav1.7 antibodies. Despite the use of GFP booster, this experiment suffered from the same GFP detection technical problem. Therefore, all neurons were included in the analysis regardless of the presence or absence of GFP. In control neurons (untransduced cells as well as in scrambled miRNA) there was a strong negative correlation between MAP1A-HC expression and Nav1.7 (membrane / cytoplasm) ratio, (Pearson $r = -0.59$ & -0.48 , respectively), (P-value < 0.0001), which indicated that cells that express high levels of MAP1A-HC have low Nav1.7 membrane level, and vice versa. Whereas in case of MAP1A KD, the correlation was less prominent in miR 2+1 (Pearson $r = -0.42$, P-value < 0.0001) and almost completely lost in miR 2+4 (Pearson $r = -0.3$, P-value = 0.0086), Fig. 5.26 and Fig. 5.27. [i.e. loss of MAP1A resulted in increased surface Nav1.7 levels, in contrast to the results obtained by N2a cells, Fig. 5.18]. When Nav1.7 (membrane / cytoplasm) ratio within each MAP1A expression bin (low, medium and high) was compared to scrambled miRNA, it was clear that there was a tendency for an increased Nav1.7 membrane expression in MAP1A KD groups compared to scrambled miRNA, however this increase was most clearly evident and statistically significant within the high MAP1A category only (Scrm = 0.24 vs. miR 2+1 = 0.31 and miR 2+4 = 0.38), Fig.5.28.

In summary, the relative surface expression level of Nav1.7 was shown to be increased upon MAP1A KD. This was most evident in the “high MAP1A” population,

which suggests that Nav1.7 surface expression is highly dependent on MAP1A level in this particular population of neurons. Moreover, it is unlikely that these results are due to non-specific effect of the LV transduction, since Nav1.7 surface level in scrambled miRNA was almost identical to that of the untransduced neurons.

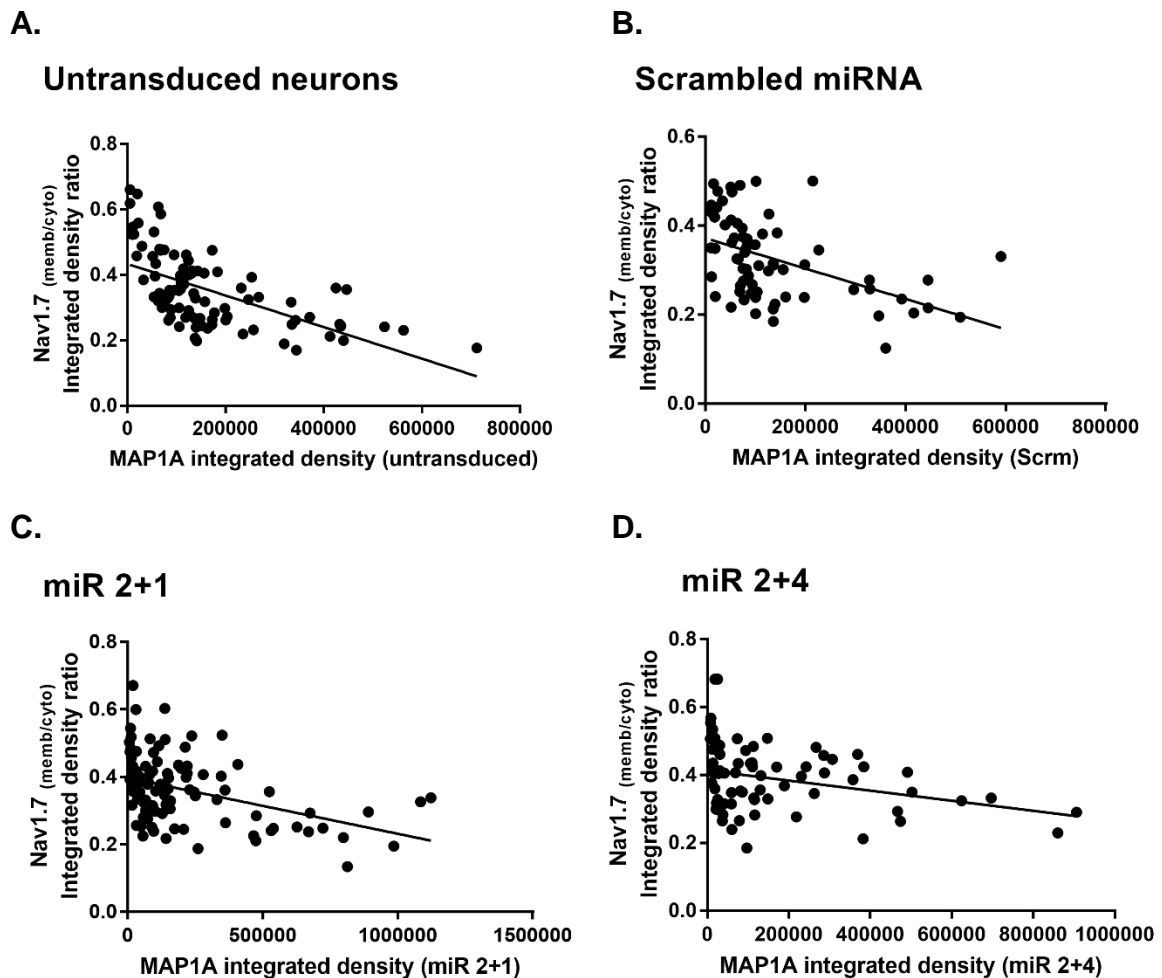


Figure 5.26: Correlation between Nav1.7 (membrane / cytoplasm) ratio and MAP1A in adult mouse DRG culture.

A. Correlation between Nav1.7_(membrane / cytoplasm) I.D ratio and MAP1A integrated density in untransduced adult mouse DRG culture. The higher the MAP1A I.D, the lower the Nav1.7_(membrane / cytoplasm) I.D ratio. Pearson $r = -0.59$, R squared = 0.35, P-value = < 0.0001.

B. Correlation between Nav1.7_(membrane / cytoplasm) I.D ratio and MAP1A integrated density in adult mouse DRG culture transduced with Scrambled miRNA at MOI 300. The higher the MAP1A I.D, the lower the Nav1.7_(membrane / cytoplasm) I.D ratio similar to (A). Pearson $r = -0.48$, R squared = 0.23, P-value = < 0.0001.

C. Correlation between Nav1.7_(membrane / cytoplasm) I.D ratio and MAP1A integrated density in adult mouse DRG culture transduced with MAP1A 2+1 miRNA at MOI 300. MAP1A KD reduces the negative correlation observed in (A & B). Pearson $r = -0.42$, R squared = 0.17, P-value = < 0.0001.

D. Correlation between Nav1.7_(membrane / cytoplasm) I.D ratio and MAP1A integrated density in adult mouse DRG culture transduced with MAP1A 2+4 miRNA at MOI 300. MAP1A KD reduces the negative correlation observed in (A & B). Pearson $r = -0.3$, R squared = 0.09, P-value = 0.0086. **P < 0.01 and ****P < 0.0001, N = 2 DRG cultures. number of cells (n) for Untransduced = 93, SCRM = 74, miR2+1 = 100, miR2+4 = 74 cells.

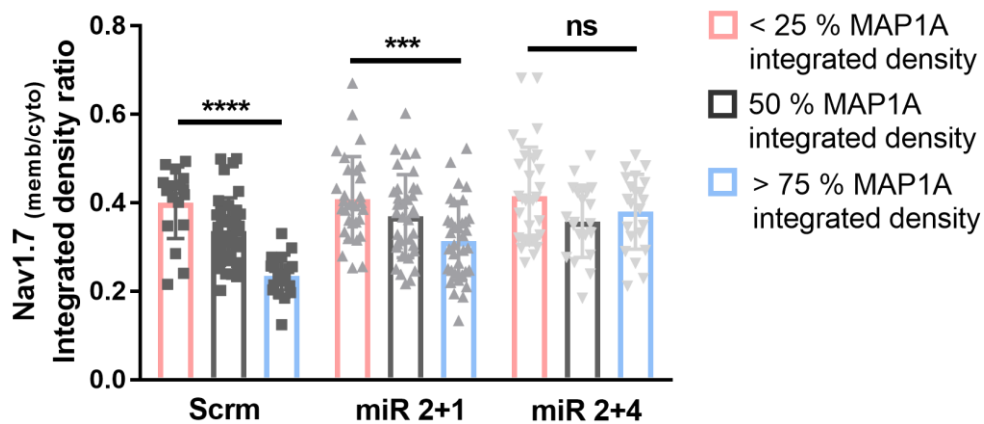


Figure 5.27: Nav1.7 (membrane / cytoplasm) ratio in LV mediated MAP1A KD in adult mouse DRG culture. The negative correlation in Nav1.7 is lost in LV-MAP1A miR2+4 group. MAP1A I.D was divided into three groups according to the interquartile range of the scrambled miRNA (MOI 300) in each experiment (pink borders: less than 25 %, grey borders: 50 %, and blue borders: higher than 75 %), Nav1.7_(membrane / cytoplasm) integrated density ratio in:

Scrambled miRNA (scrm): < 25 % = 0.4 ± 0.02 , 50 % = 0.34 ± 0.01 , > 75 % = 0.24 ± 0.01 .

MAP1A miR 2+1: < 25 % = 0.41 ± 0.02 , 50 % = 0.37 ± 0.02 , > 75 % = 0.31 ± 0.02 .

MAP1A miR 2+4: < 25 % = 0.42 ± 0.02 , 50 % = 0.36 ± 0.02 , > 75 % = 0.38 ± 0.02 .

One-way ANOVA, *** $P < 0.001$ and **** $P < 0.0001$, $N = 2$ DRG cultures, number of cells (n) for Untransduced = 93, SCRM = 74, miR2+1 = 100, miR2+4 = 74 cells. Error bars represent SD.

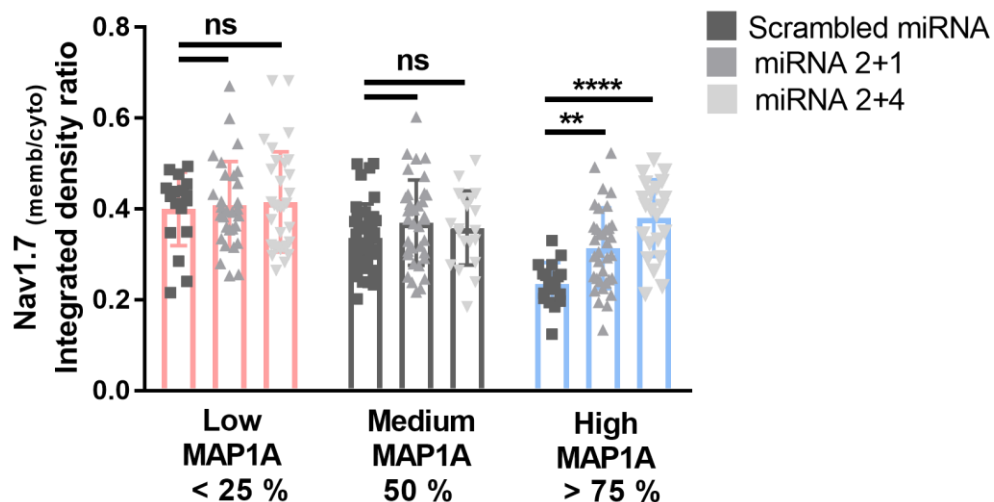


Figure 5.28: Comparison of Nav1.7 (membrane / cytoplasm) ratio in LV mediated MAP1A KD in adult mouse DRG culture within the various MAP1A expression levels. This data is the same as Fig.5.27, it shows that Nav1.7 ratio was most affected in "high MAP1A" group.

MAP1A I.D was divided into three groups according to the interquartile range of the scrambled miRNA (MOI 300) in each experiment (pink borders: less than 25 %, gray borders: 50 %, and blue borders: higher than 75 %). Nav1.7_(membrane / cytoplasm) integrated density ratio in:

Low MAP1A level (< 25%): Scrm (■) = 0.4 ± 0.02 , miR 2+1 (▲) = 0.41 ± 0.02 , miR 2+4 (▼) = 0.42 ± 0.02 .

Medium MAP1A level (50 %): Scrm (■) = 0.34 ± 0.01 , miR 2+1 (▲) = 0.37 ± 0.02 , miR 2+4 (▼) = 0.36 ± 0.02 .

High MAP1A level (> 75 %): Scrm (■) = 0.24 ± 0.01 , miR 2+1 (▲) = 0.31 ± 0.01 , miR 2+4 (▼) = 0.38 ± 0.02 . Two-tailed unpaired Student's t -test, * $P < 0.05$, ** $P < 0.01$ and **** $P < 0.0001$, $N = 2$ DRG cultures, number of cells (n) for Untransduced = 93, SCRM = 74, miR2+1 = 100, miR2+4 = 74 cells. Error bars represent SD.

5.4.5. The effect of MAP1A KD on neuronal excitability:

5.4.5.1. LV transduction increases neuronal excitability

The previous results suggested an increase in the Nav1.7 surface expression level upon MAP1A KD. Assuming that MAP1A plays a negative role in Nav1.7 membrane level, how would the MAP1A effect on Nav1.7 be translated in regards to neuronal excitability and to VTD calcium responses? To address this question, I used the calcium imaging protocol established in previous chapters to assess changes in neuronal excitability. LV transduced cells were incubated with fura-2 am and imaged at day 5 post-transduction. The calcium imaging protocol (section 2.2.13) was slightly modified to be able to identify LV transduced neurons in live imaging (section 5.3). The advantage of using live functional imaging is that the GFP signal can be used as a marker for LV transduction, and at the same time GFP negative (-) cells can be used as “internal” control. GFP positive (+) neurons transduced with MAP1A miRNA were analysed and compared to GFP (+) scrambled miRNA, Fig. 5.29. The percentage of VTD responding neurons were significantly higher in GFP (+) than GFP (-) neurons, this included scrambled miRNA as well as the other two MAP1A miRNA, (Scrm: (+) = 74 vs. 48 %, miR 2+4: (+) = 83 vs. 54 %, miR 2+1: (+) = 80 vs. (-) = 60 %), Fig. 5.29. The increase in the percentage of VTD responding neurons in the GFP (+) group indicated in Fig. 5.29 mainly came from an increase in the ID profile, Fig. 5.30,C (notice the significant increase in the ID responses between GFP (+) and GFP (-) groups). These data suggest that LV transduction of sensory neurons could increase neuronal excitability regardless of the expressed transgene.

5.4.5.2. LV-MAP1A miRNA does not affect the distribution of VTD response profiles

Next, I examined the GFP (+) group to assess MAP1A KD effect. A slight but statically non-significant increase in the percentage of VTD responses were obtained from GFP(+) MAP1A miR 2+4 and miR 2+1 compared to GFP(+) scrambled miRNA transduced neurons, Fig. 5.31 – top panel (VTD (-) %). This data indicates that MAP1A KD might produce an additional increase in neuronal excitability on top of that caused by LV transduction. However, analysis of the VTD response profiles within the two

MAP1A miRNA did not show any difference to the scrambled miRNA, Fig. 5.31, which indicates that MAP1A KD does not affect the distribution of VTD response profiles.

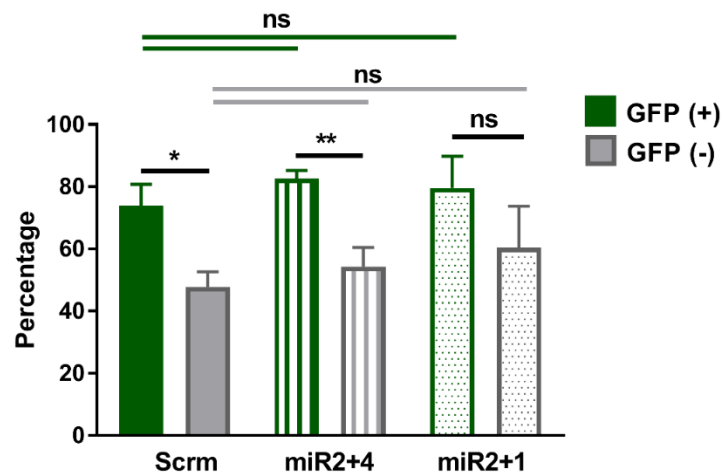


Figure 5.29: The percentage of VTD responding DRG neurons transduced with lentivirus.

Adult mouse DRG neurons transduced with MOI300 of MAP1A miRNA or Scrambled miRNA for 5 days and processed to calcium imaging at day 6 post transduction where cells were stimulated with 30 μ M VTD and 40 mM KCl. Cells with a GFP signal higher than 15 % of the background and distributed homogenously in the whole cytoplasm were considered GFP positive neurons (i.e. LV transduced neurons). Green bars represents GFP(+) neurons, grey bars represents GFP(-) neurons. Only cells that responded to KCl were considered viable neurons and were included in the analysis.

Scrm_(GFP+) = 73.9 \pm 6.9 %, Scrm_(GFP-) = 47.8 \pm 4.9 %; miR 2+4_(GFP+) = 82.7 \pm 2.6 %, miR 2+4_(GFP-) = 54.3 \pm 6.2 %; miR 2+1_(GFP+) = 79.6 \pm 10.2 %, miR 2+1_(GFP-) = 60.4 \pm 13.3 %, Data was compared with two-tailed unpaired Student's t-test, *P < 0.05, **P < 0.01, N = 4 DRG cultures for Scrm and miR2+4, and N= 2 DRG cultures for miR2+1.

number of cells (n) for Scrm_(GFP+) = 230, Scrm_(GFP-) = 133, miR2+4_(GFP+) = 289, miR2+4_(GFP-) = 140, miR2+1_(GFP+) = 85, miR2+1_(GFP-) = 36 cells. Error bars represent SEM.

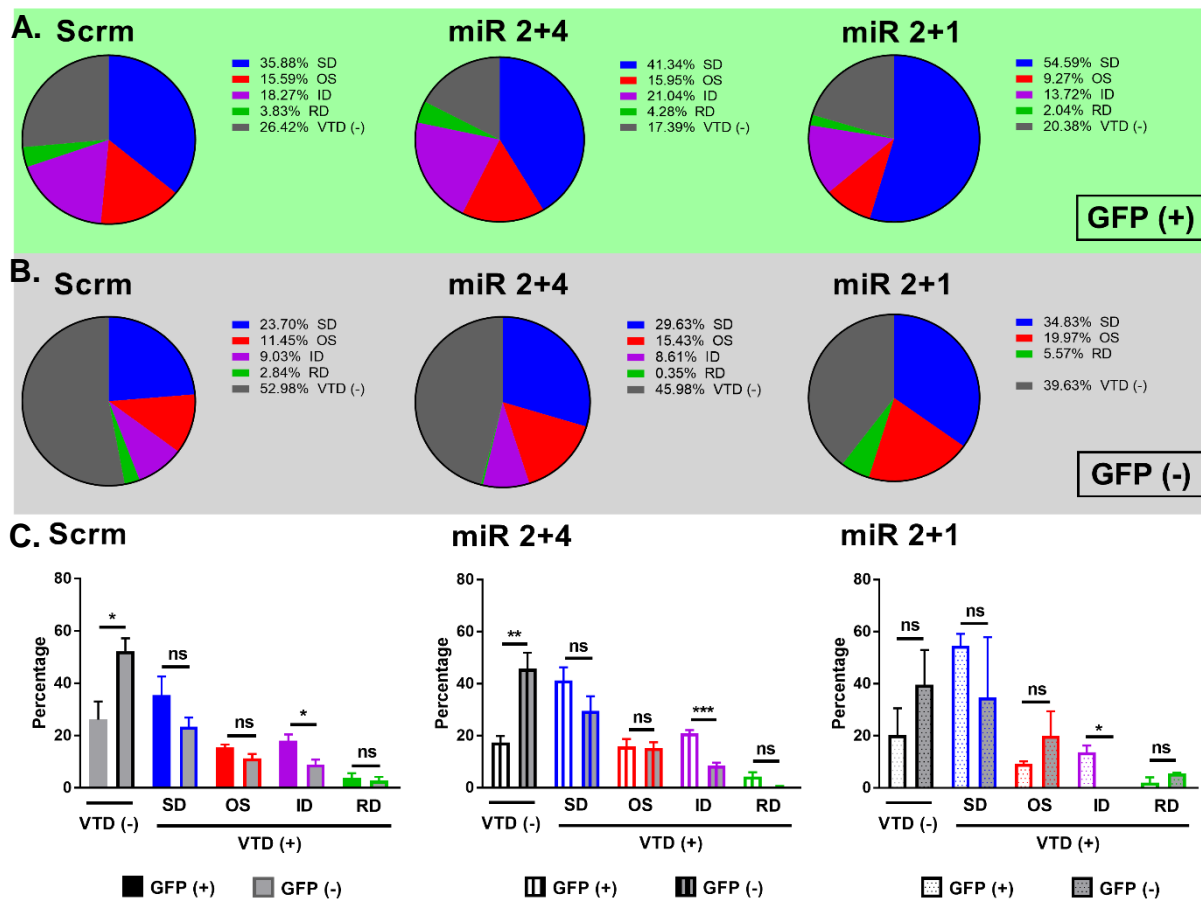


Figure 5.30: The distribution of VTD response profiles within GFP (+ & -) DRG neurons.

This figure represents similar data that were presented in figures 5.30 & 5.31, however the comparison made here is between GFP (+) and GFP (-) groups.

A. Pie chart of the distribution of VTD non-responding neurons (grey) and VTD responding neurons (coloured) in GFP(+) neurons within Scrambled miRNA, MAP1A miR2+4 and MAP1A miR2+1 groups.

B. Pie chart of the distribution of VTD non-responding neurons (grey) and VTD responding neurons (coloured) in GFP(-) neurons (i.e. non-transduced) within Scrambled miRNA, MAP1A miR2+4 and MAP1A miR2+1 groups.

C. Comparison of the percentages of VTD non-responding neurons (VTD -) and VTD response profiles between GFP (+) and GFP (-) neurons.

Scrm: VTD (-)_(GFP+) = 26.1 ± 6.9 %, VTD (-)_(GFP-) = 52.3 ± 4.9 %; SD_(GFP+) = 35.5 ± 7.1 %, SD_(GFP-) = 23.4 ± 3.6 %; OS_(GFP+) = 15.4 ± 1.1 %, OS_(GFP-) = 11.3 ± 1.7 %; ID_(GFP+) = 18.1 ± 2.3 %, ID_(GFP-) = 8.9 ± 2 %; RD_(GFP+) = 3.8 ± 1.8 %, RD_(GFP-) = 2.8 ± 1.4 %.

miR 2+4: VTD (-)_(GFP+) = 17.3 ± 2.6 %, VTD (-)_(GFP-) = 45.7 ± 6.2 %; SD_(GFP+) = 41.1 ± 5.1 %, SD_(GFP-) = 29.5 ± 5.7 %; OS_(GFP+) = 15.9 ± 2.8 %, OS_(GFP-) = 15.4 ± 2.2 %; ID_(GFP+) = 21 ± 1.2 %, ID_(GFP-) = 8.6 ± 1.1 %; RD_(GFP+) = 4.3 ± 1.7 %, RD_(GFP-) = 0.4 ± 0.4 %.

miR 2+1: VTD (-)_(GFP+) = 20.4 ± 10.2 %, VTD (-)_(GFP-) = 39.6 ± 13.3 %; SD_(GFP+) = 54.6 ± 4.6 %, SD_(GFP-) = 34.9 ± 23.1 %; OS_(GFP+) = 9.3 ± 0.9 %, OS_(GFP-) = 20 ± 9.4 %; ID_(GFP+) = 17.7 ± 2.6 %, ID_(GFP-) = 0 ± 0 %; RD_(GFP+) = 2 ± 2 %, RD_(GFP-) = 5.6 ± 0.3 %.

Cells with a GFP signal higher than 15 % of the background and distributed homogeneously in the whole cytoplasm were considered GFP positive neurons (i.e. LV transduced neurons). Only cells that responded to KCl were considered viable neurons and were included in the analysis. Percentages were calculated from total number of KCl responding neurons within each group.

Two-tailed unpaired Student's t-test, **P* < 0.05, *N* = 4 DRG cultures for Scrm and miR2+4, and *N* = 2 DRG cultures for miR2+1. number of cells (*n*) for Scrm_(GFP+) = 230, Scrm_(GFP-) = 133, miR2+4_(GFP+) = 289, miR2+4_(GFP-) = 140, miR2+1_(GFP+) = 85, miR2+1_(GFP-) = 36 cells. Error bars represent SEM.

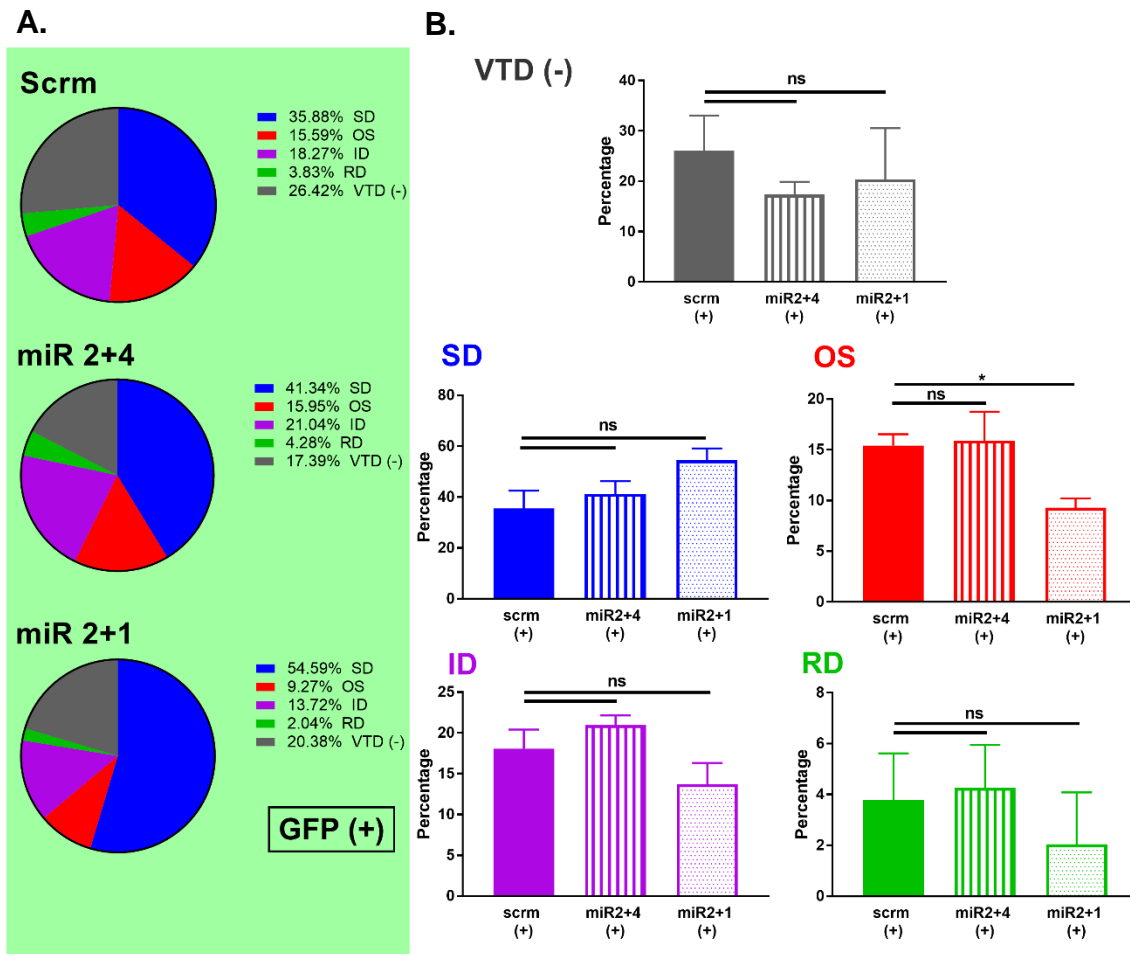


Figure 5.31: The distribution of VTD response profiles within GFP(+) DRG neurons.

Adult mouse DRG neurons transduced with MOI300 of MAP1A miRNA or Scrambled miRNA for 5 days and processed to calcium imaging at day 6 post transduction where cells were stimulated with 30 μ M VTD and 40 mM KCl.

A. Pie chart of the distribution of VTD non-responding neurons (grey) and VTD responding neurons (coloured) in GFP(+) neurons within Scrambled miRNA, MAP1A miR2+4 and MAP1A miR2+1 groups.

B. Comparison of the percentages of VTD non-responding neurons (VTD -) and VTD response profiles between neurons transduced with LV expressing MAP1A miRNA and scrambled miRNA.

VTD (-), grey: Scrm = 26.1 ± 6.9 %; miR 2+4 = 17.36 ± 2.6 %; miR 2+1 = 20.4 ± 10.2 %.

SD, blue: Scrm = 35.5 ± 7.1 %; miR 2+4 = 41.2 ± 5.1 %; miR 2+1 = 45.6 ± 4.6 %.

OS, red: Scrm = 15.4 ± 1.1 %; miR 2+4 = 15.9 ± 2.9 %; miR 2+1 = 9.2 ± 0.9 %.

ID, purple: Scrm = 18.1 ± 2.3 %; miR 2+4 = 21 ± 1.2 %; miR 2+1 = 13.7 ± 2.6 %.

RD, green: Scrm = 3.8 ± 1.8 %; miR 2+4 = 4.3 ± 1.7 %; miR 2+1 = 3.8 ± 1.8 %.

Cells with a GFP signal higher than 15 % of the background and distributed homogenously in the whole cytoplasm were considered GFP positive neurons (i.e. LV transduced neurons). Only cells that responded to KCl were considered viable neurons and were included in the analysis. Percentages were calculated from total number of KCl responding neurons within each group.

Two-tailed unpaired Student's *t*-test, **P* < 0.05, *N* = 4 DRG cultures for Scrm and miR2+4, and *N* = 2 DRG cultures for miR2+1. number of cells (*n*) for Scrm (GFP+) = 230, miR2+4 (GFP+) = 289, miR2+1 (GFP+) = 85 cells. Error bars represent SEM.

5.4.5.3. Long-term DRG culture resulted in a different distribution of VTD response profiles

Interestingly, the frequency of occurrence of the VTD response profiles in LV-MAP1A KD set of experiments showed a very different picture than what I had obtained from DRG cultures incubated for shorter periods (< 3 days), as demonstrated in chapter 3 & 4. In long term culture, there was a reduction in the number of VTD responding neurons compared to short term cultures (50 % vs. 70 %), respectively, Fig. 5.32 & Fig. 1D (chapter 3). Also, there was a clear reduction in the OS responses, with an increase in the SD profile (OS = 11 % and SD = 24 %), Fig. 5.32, A (scrm), compared to the percentages obtained with acute cultures (OS = 27 %, and SD = 14 %), Fig. 4.4 and Fig. 4.10 (A and D - control), chapter 4. The RD profile remained to be the least frequent with a clear reduction in its frequency of occurrence compared to the short-term DRG culture (3 % vs. 7 %). This distribution of VTD response profiles was observed in long-term cultures regardless of whether the DRG cultures were transduced or not, which suggests that the changes in the percentages of the VTD response profiles are LV and MAP1A KD independent, Fig. 5.30,(A &B) – [notice: both GFP(+) and GFP(-) neurons produced a higher SD and a lower OS percentages compared to acute cultures, Fig. 4.4 and Fig. 4.10 (A & D – control)]. Altogether, the reduction in the number of VTD responding neurons as well as the reduction in the percentage of OS response profile reflect a decrease in neuronal excitability of DRG culture in longer incubation periods. It remains to be investigated the molecular changes that take place in longer incubation periods of DRG cultures.

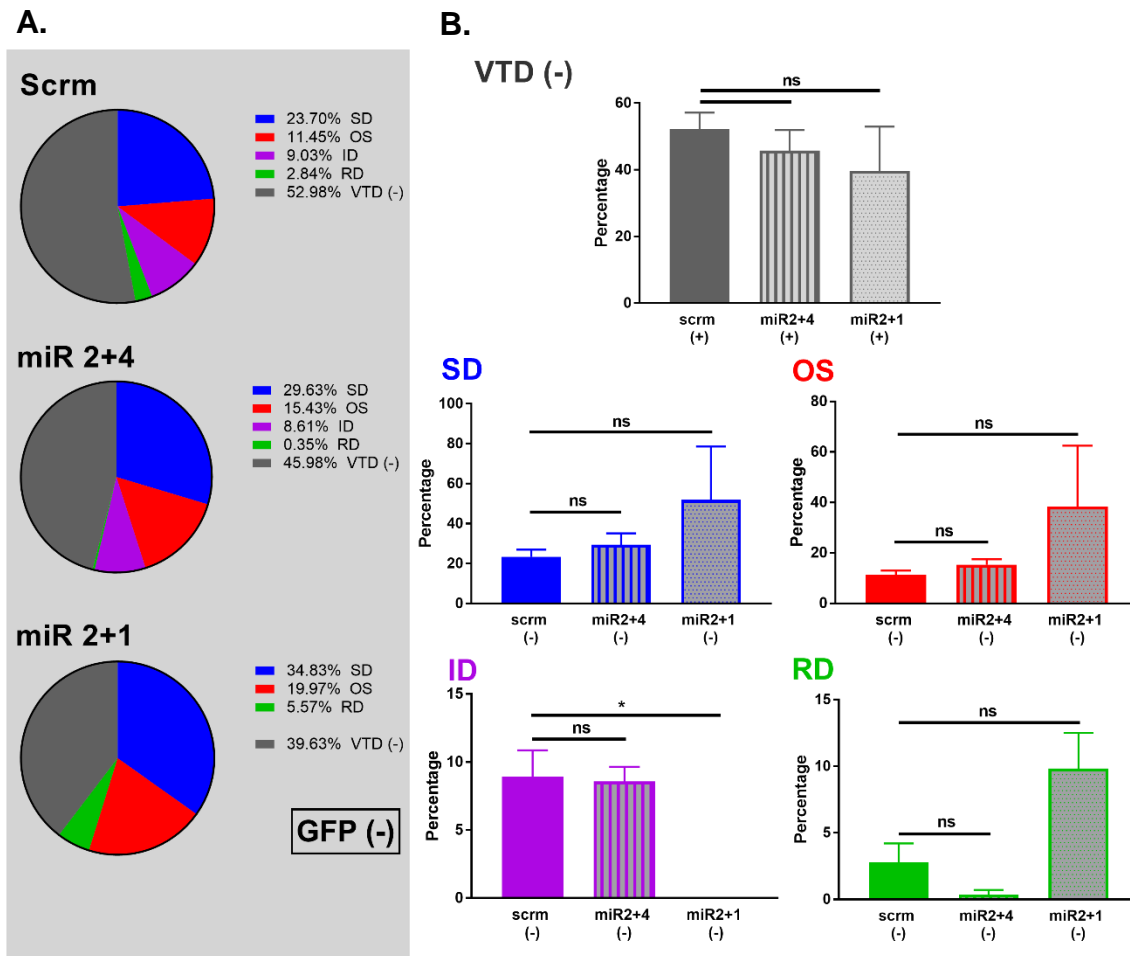


Figure 5.32: The distribution of VTD response profiles within GFP (-) DRG neurons.

Adult mouse DRG neurons transduced with MOI300 of MAP1A miRNA or Scrambled miRNA for 5 days and processed to calcium imaging at day 6 post transduction where cells were stimulated with 30 μ M VTD and 40 mM KCl.

A. Pie chart of the distribution of VTD non-responding neurons (grey) and VTD responding neurons (coloured) in GFP(-) neurons (i.e. non-transduced) within Scrambled miRNA, MAP1A miR2+4 and MAP1A miR2+1 groups.

B. Comparison of the percentages of VTD non-responding neurons (VTD -) and VTD response profiles between neurons in MAP1A miRNA and scrambled miRNA groups.

VTD (-), grey: Scrm = 52.3 ± 4.9 %; miR 2+4 = 45.7 ± 6.2 %; miR 2+1 = 39.6 ± 13.3 %.

SD, blue: Scrm = 23.4 ± 3.6 %; miR 2+4 = 29.5 ± 5.7 %; miR 2+1 = 51.8 ± 26.8 %.

OS, red: Scrm = 11.3 ± 1.7 %; miR 2+4 = 15.4 ± 2.2 %; miR 2+1 = 38.4 ± 24.1 %.

ID, purple: Scrm = 8.9 ± 1.9 %; miR 2+4 = 8.7 ± 1.1 %; miR 2+1 = 0 ± 0 %.

RD, green: Scrm = 2.8 ± 1.4 %; miR 2+4 = 0.4 ± 0.4 %; miR 2+1 = 2.8 ± 1.4 %.

Cells with a GFP signal below 15 % of the background and not-distributed homogenously in the whole cytoplasm were considered GFP negative neurons (i.e. LV non-transduced neurons). Only cells that responded to KCl were considered viable neurons and were included in the analysis.

Percentages were calculated from total number of KCl responding neurons within each group.

Two-tailed unpaired Student's *t*-test, **P* < 0.05, *N* = 4 DRG cultures for Scrm and miR2+4, and *N* = 2 DRG cultures for miR2+1. number of cells (*n*) for Scrm (GFP-) = 133, miR2+4 (GFP-) = 140, miR2+1 (GFP-) = 36 cells Error bars represent SEM.

5.4.5.4. Cell size distribution of LV-transduced DRG neurons

To ensure that LV had targeted all neuronal subtypes in my experiments, GFP (+) neuron from all the three LVs used in this set of experiments were pooled for soma size analysis. The results showed that GFP(+) neurons were normally distributed within all cell sizes. GFP(-) neurons were also normally distributed, although the whole distribution was shifted to the left, (mean diameter of GFP(-) = 18 μ m and GFP (+) = 21 μ m), Fig. 5.33, which indicates that LV transduction may have a slight preference toward medium diameter neurons. Noteworthy, the cell size range in the long-term DRG culture was narrower than the that obtained from short-term DRG culture due to significant loss of the large-diameter neurons on long-term incubation. Because of this narrow cell size range, there was no difference in the mean soma diameter between SD and the other profiles (mean diameter SD = 21, OS = 20, ID = 20.4, and RD = 22 μ m) as was shown previously in short-term DRG culture, Fig. 3, chapter 3.

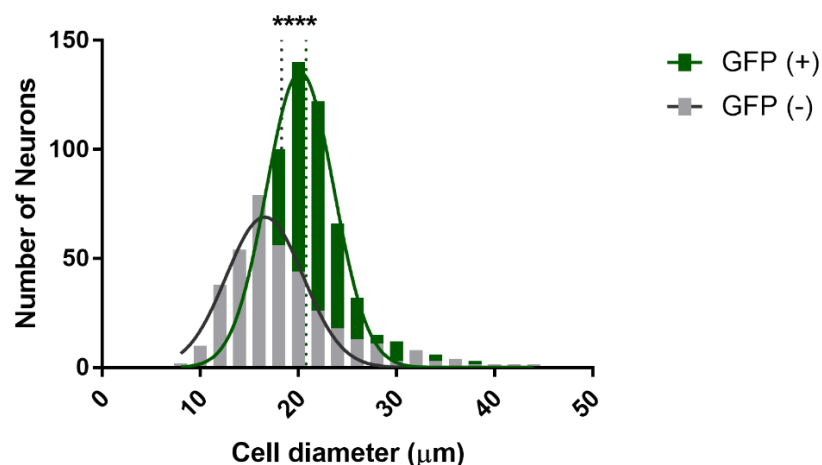


Figure 5.33: Cell size distribution of adult mouse DRG culture transduced with lentivirus expressing MAP1A miRNA.

Histogram of soma diameter of GFP(-) (grey) and GFP (+) (green) pooled from DRG neurons transduced with LV expressing scrambled miRNA and MAP1A miRNA at MOI 300.

GFP (+) : mean = $20.8 \pm 0.2 \mu\text{m}$, median = $20.4 \mu\text{m}$;

GFP (-) : mean = $18.3 \pm 0.3 \mu\text{m}$, median = $17 \mu\text{m}$.

Vertical dotted lines represent the mean of each distribution. Cells with a GFP signal higher than 15 % of the background and distributed homogenously in the whole cytoplasm were considered GFP positive neurons (i.e. LV transduced neurons).

Two-tailed unpaired Student's *t*-test, **** $P < 0.0001$. $N = 4$ DRG cultures, number of cells (n) for Scrm_(GFP+) = 519, Scrm_(GFP-) = 273 cells.

5.4.5.5. Analysis of the various VTD response parameters in LV-transduced and untransduced DRG neurons

To obtain a comprehensive picture regarding the effect of MAP1A KD on DRG neurons, several additional parameters were examined including VTD peak amplitude, Fig. 5.34, VTD AUC, Fig. 5.35, and VTD onset to response, Fig. 5.36. None of these parameters showed any difference between MAP1A miRNA and scrambled miRNA. Also, there was no difference in any of these tested parameters between LV-transduced and non-transduced neurons.

In conclusion, the number of VTD responding neurons were higher in LV-transduced than untransduced neurons. The general enhancement in DRG excitability was a consequence of LV transduction in the DRG neurons which indicates that LV transduction might have some sensitization effect on sensory neuron. Unfortunately, it seems that the sensitisation effect of LV had masked any potential specific functional role of MAP1A protein on DRG excitability in general and on Nav1.7 surface expression in particular. Other transfection methods may provide better ways for assessing the role of MAP1A on DRG excitability by calcium imaging.

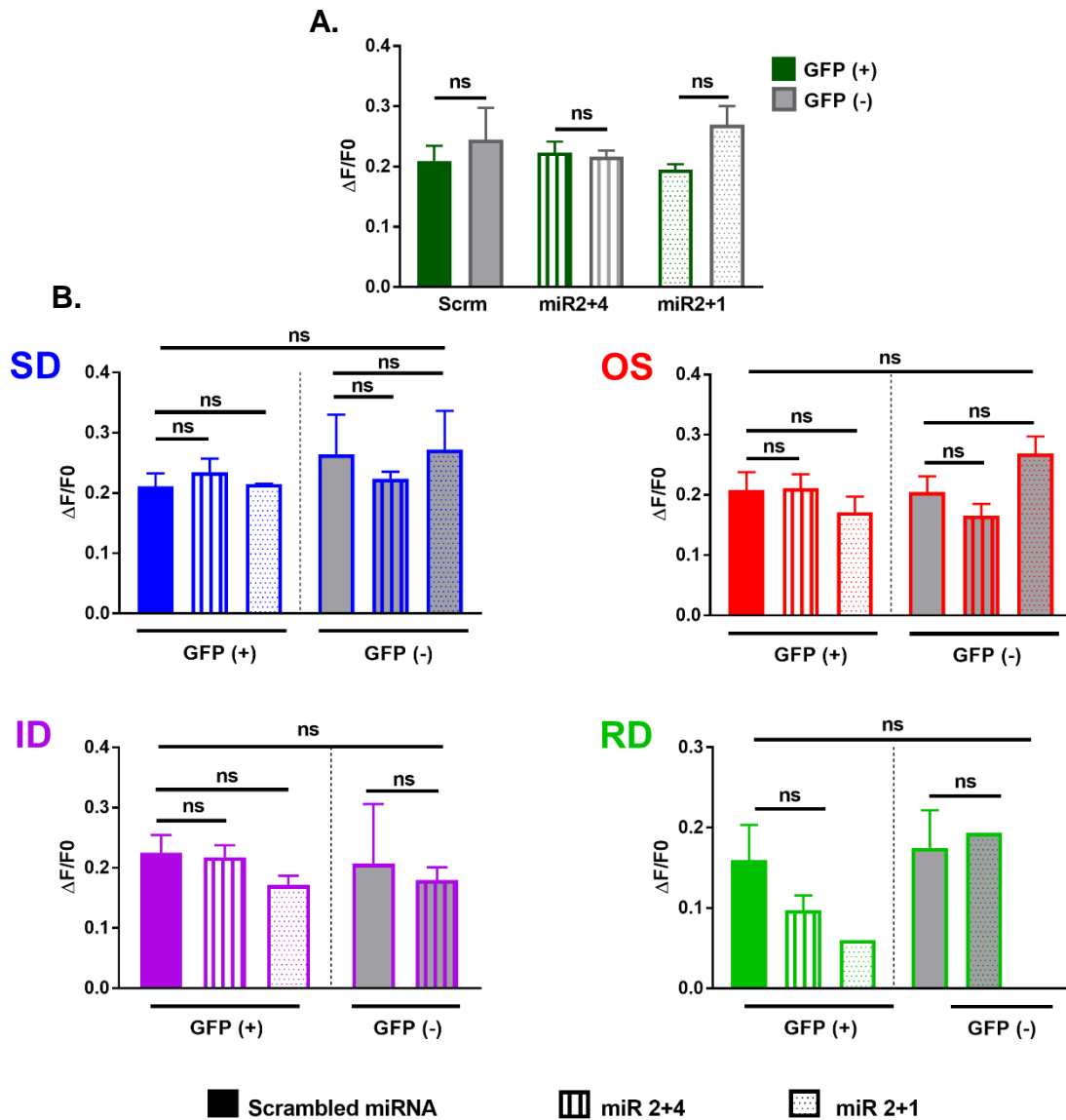


Figure 5.34: Analysis of the effect of MAP1A KD on the maximum VTD peak responses.

A. Comparison of the VTD peak amplitude in DRG neurons transduced with LV expressing MAP1A miRNA or scrambled miRNA. Green bars are GFP (+) and grey bars are GFP (-) neurons. Scrm_(GFP+) = 0.21 ± 0.02, Scrm_(GFP-) = 0.24 ± 0.05; miR2+4_(GFP+) = 0.22 ± 0.02, miR2+4_(GFP-) = 0.22 ± 0.01; miR2+1_(GFP+) = 0.12 ± 0.01, miR2+1_(GFP-) = 0.27 ± 0.03.

B. Comparison of the VTD peak amplitude within each VTD response profile in DRG neurons transduced with LV expressing MAP1A or scrambled miRNA.

SD, blue: Scrm_(GFP+) = 0.21 ± 0.02; miR2+4_(GFP+) = 0.23 ± 0.02; miR2+1_(GFP+) = 0.21 ± 0.02, Scrm_(GFP-) = 0.26 ± 0.07; miR2+4_(GFP-) = 0.22 ± 0.01; miR2+1_(GFP-) = 0.27 ± 0.06.

OS, red: Scrm_(GFP+) = 0.21 ± 0.03; miR2+4_(GFP+) = 0.21 ± 0.02; miR2+1_(GFP+) = 0.17 ± 0.03, Scrm_(GFP-) = 0.2 ± 0.03; miR2+4_(GFP-) = 0.16 ± 0.02; miR2+1_(GFP-) = 0.2 ± 0.03.

ID, purple: Scrm_(GFP+) = 0.22 ± 0.03; miR2+4_(GFP+) = 0.22 ± 0.02; miR2+1_(GFP+) = 0.17 ± 0.02, Scrm_(GFP-) = 0.21 ± 0.1; miR2+4_(GFP-) = 0.18 ± 0.02; miR2+1_(GFP-) = 0.2.

RD, green: Scrm_(GFP+) = 0.16 ± 0.04; miR2+4_(GFP+) = 0.1 ± 0.02; miR2+1_(GFP+) = 0.19; Scrm_(GFP-) = 0.18 ± 0.05; miR2+1_(GFP-) = 0.2 ± 0.06.

Data was compared with two-tailed unpaired Student's t-test, *P < 0.05, and with One-way ANOVA to compare between GFP (+) and GFP (-) groups. N = 4 DRG cultures for Scrm and miR2+4, and N = 2 DRG cultures for miR2+1. number of cells (n) for Scrm_(GFP+) = 230, Scrm_(GFP-) = 133, miR2+4_(GFP+) = 289, miR2+4_(GFP-) = 140, miR2+1_(GFP+) = 85, miR2+1_(GFP-) = 36 cells Error bars represent SEM.

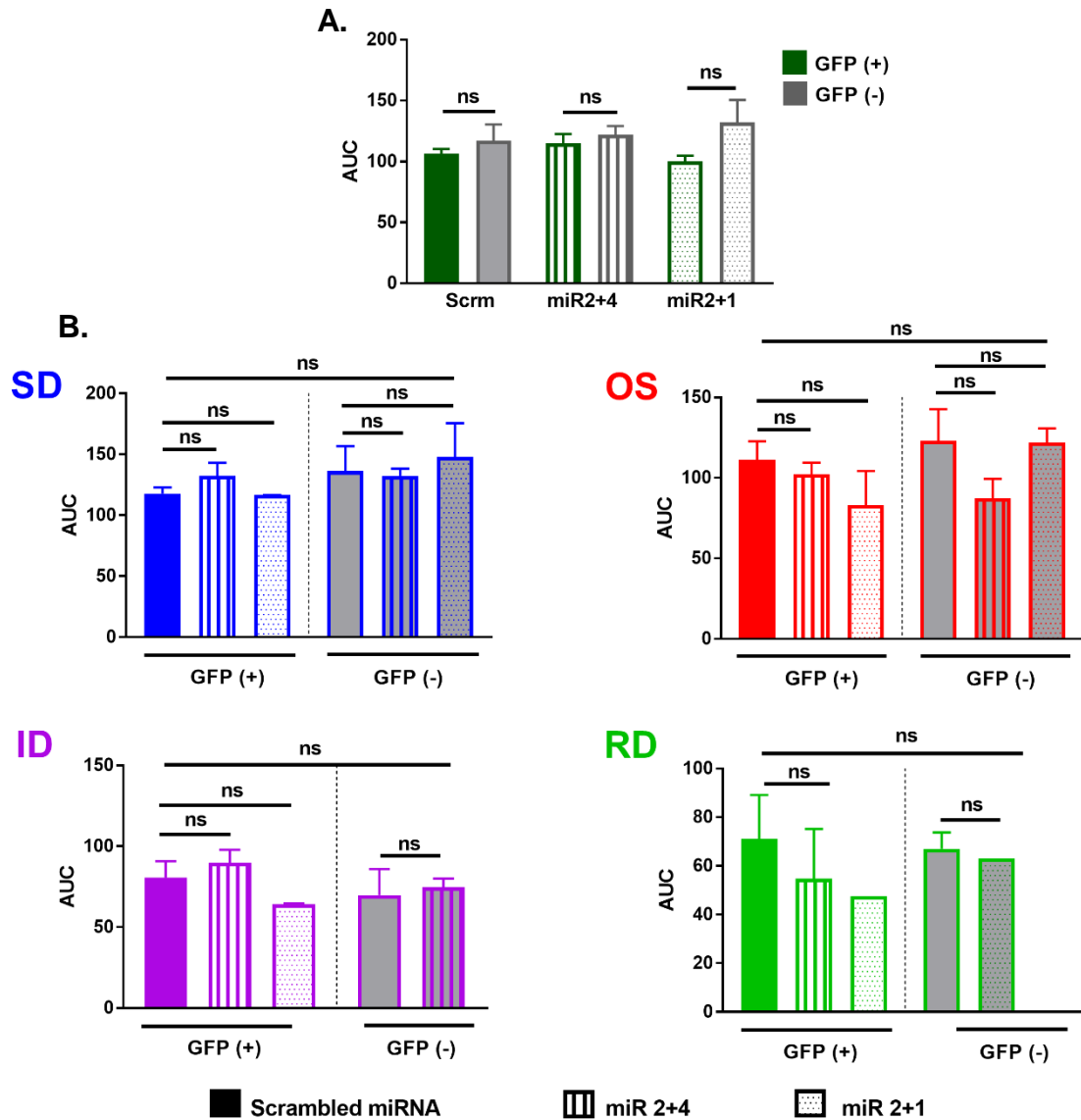


Figure 5.35: Analysis of the effect of MAP1A KD on the area under the peak (AUC) of VTD responses.

A. Comparison of the area under the curve of the VTD responses in DRG neurons transduced with LV expressing MAP1A miRNA or scrambled miRNA. Green bars are GFP (+) and grey bars are GFP (-) neurons. Scrm_(GFP+) = 106.4 ± 3.9, Scrm_(GFP-) = 117 ± 13.4; miR2+4_(GFP+) = 114.7 ± 7.8, miR2+4_(GFP-) = 121.8 ± 7.3; miR2+1_(GFP+) = 100.2 ± 4.5, miR2+1_(GFP-) = 132.3 ± 18.2.

B. Comparison of the area under the curve of the VTD responses within each VTD response profile in DRG neurons transduced with LV expressing MAP1A or scrambled.

SD, blue: Scrm_(GFP+) = 118 ± 4.8; miR2+4_(GFP+) = 132.6 ± 10.6; miR2+1_(GFP+) = 116.5 ± 0.14, Scrm_(GFP-) = 136.4 ± 20.4; miR2+4_(GFP-) = 132.3 ± 6; miR2+1_(GFP-) = 148.1 ± 27.4.

OS, red: Scrm_(GFP+) = 111 ± 11.6; miR2+4_(GFP+) = 102.2 ± 7.3; miR2+1_(GFP+) = 83.2 ± 21.2, Scrm_(GFP-) = 123 ± 19.7; miR2+4_(GFP-) = 87.3 ± 12.1; miR2+1_(GFP-) = 122 ± 8.6.

ID, purple: Scrm_(GFP+) = 80.7 ± 10.1; miR2+4_(GFP+) = 89.7 ± 8.1; miR2+1_(GFP+) = 64 ± 0.7, Scrm_(GFP-) = 69.8 ± 16; miR2+4_(GFP-) = 74.7 ± 5.3.

RD, green: Scrm_(GFP+) = 71.1 ± 18.1; miR2+4_(GFP+) = 54.8 ± 20.4; miR2+1_(GFP+) = 63.1; Scrm_(GFP-) = 67 ± 6.7; miR2+1_(GFP-) = 70.7 ± 8.1.

Data was compared with two-tailed unpaired Student's *t*-test, **P* < 0.05, and with One-way ANOVA to compare between GFP (+) and GFP (-) groups. *N* = 4 DRG cultures for Scrm and miR2+4, and *N* = 2 DRG cultures for miR2+1. number of cells (*n*) for Scrm_(GFP+) = 230, Scrm_(GFP-) = 133, miR2+4_(GFP+) = 289, miR2+4_(GFP-) = 140, miR2+1_(GFP+) = 85, miR2+1_(GFP-) = 36 cells Error bars represent SEM.

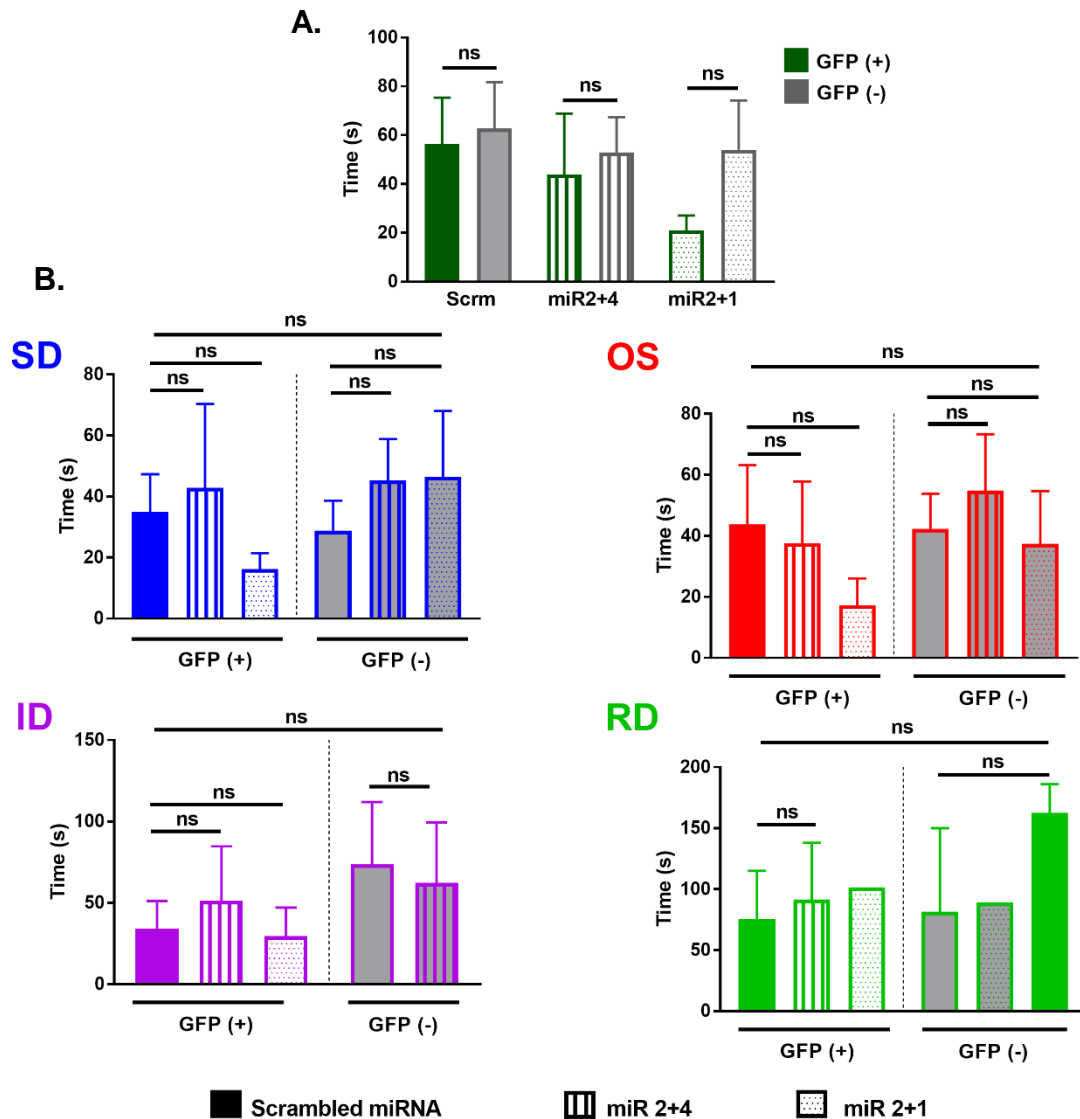


Figure 5.36: Analysis of the effect of MAP1A KD on the VTD responses onset.

A. Comparison of the onset to VTD responses in DRG neurons transduced with LV expressing MAP1A miRNA or scrambled miRNA. Only neurons that showed immediate response to KCl were included in the analysis. Green bars are GFP (+) and grey bars are GFP (-) neurons. Scrm_(GFP+) = 56.4 ± 19, Scrm_(GFP-) = 62.7 ± 19 s; miR2+4_(GFP+) = 43.9 ± 25 s, miR2+4_(GFP-) = 52.9 ± 14.4 s; miR2+1_(GFP+) = 21 ± 6.2 s, miR2+1_(GFP-) = 54 ± 20.2 s.

B. Comparison of the onset to VTD responses within each VTD response profile in DRG neurons transduced with LV expressing MAP1A or scrambled.

SD, blue: Scrm_(GFP+) = 35 ± 12.4 s; miR2+4_(GFP+) = 42.8 ± 27.6 s; miR2+1_(GFP+) = 16.2 ± 5.2 s, Scrm_(GFP-) = 28.9 ± 9.8 s; miR2+4_(GFP-) = 45.2 ± 13.6 s; miR2+1_(GFP-) = 46.5 ± 21.6 s.

OS, red: Scrm_(GFP+) = 43.7 ± 19.5 s; miR2+4_(GFP+) = 37.5 ± 20.3 s; miR2+1_(GFP+) = 17.3 ± 8.7 s, Scrm_(GFP-) = 42.3 ± 11.6 s; miR2+4_(GFP-) = 54.8 ± 18.5 s; miR2+1_(GFP-) = 37.3 ± 17.3 s.

ID, purple: Scrm_(GFP+) = 33.9 ± 17.3 s; miR2+4_(GFP+) = 51.3 ± 33.4 s; miR2+1_(GFP+) = 29.4 ± 17.6 s, Scrm_(GFP-) = 62.2 ± 37.3 s; miR2+4_(GFP-) = 74.7 ± 5.3.

RD, green: Scrm_(GFP+) = 75.5 ± 39.5 s; miR2+4_(GFP+) = 91.6 ± 46.5 s; miR2+1_(GFP+) = 89 s; Scrm_(GFP-) = 81.5 ± 68.5 s; miR2+1_(GFP-) = 162.5 ± 23.5 s.

Data was compared with two-tailed unpaired Student's *t*-test, **P* < 0.05, and with One-way ANOVA to compare between GFP (+) and GFP (-) groups. *N* = 4 DRG cultures for Scrm and miR2+4, and *N* = 2 DRG cultures for miR2+1. number of cells (*n*) for Scrm_(GFP+) = 230, Scrm_(GFP-) = 133, miR2+4_(GFP+) = 289, miR2+4_(GFP-) = 140, miR2+1_(GFP+) = 85, miR2+1_(GFP-) = 36 cells Error bars represent SEM.

5.4.6. Localisation of Nav1.7 binding site in LC2.

For full characterisation of Nav1.7-LC2 interaction, knock-down and overexpression of the protein of interest are both equally important. Therefore, I started the first step of the overexpression experiments which included designing tagged LC2 full length and deletion constructs, cloning and validation of protein expression. However, due to limited time and resources, I was not able to continue testing the LC2 deletion constructs in pull-down experiments in order to map the interaction site, nor performing rescue experiment to complement the knock-down results. Therefore, in this section I will only describe the initial steps that I performed for the overexpression experiments.

Full length and truncated versions of LC2 cDNA were cloned into myc-tagged mammalian expression vector PcDNA3-myc (*Invitrogen*), according to the protocol described in section 2.2.8. All cDNA constructs were checked and validated by DNA sequencing. N2a cells were transfected with LC2 constructs and analysed by western blotting 48 h post-transfection. Cell lysates were divided into two SDS-PAGE gel and analysed by either LC2 polyclonal antibody or myc- polyclonal antibody. Identical bands were identified by both antibodies, except that LC2 antibody recognised an additional band at 28 KD which belongs to the endogenous LC2, Fig. 5.37,B. Also, the construct coding for the actin-binding domain (20/12) gave one band with myc-antibody but not with LC2-antibody, this is mainly due to the fact that this domain lacks the epitope required for LC2 antibody binding. LC2 deletion constructs were tested in both N2a (Fig.5.37) and HEK-293 cells (data not shown), both cells showed similar results. The results of this experiment not only validate the use of the LC2 cDNA constructs for further overexpression experiments, but also indirectly validate the specificity of the LC2 polyclonal antibody that was used in Nav1.7 co-IP experiments.

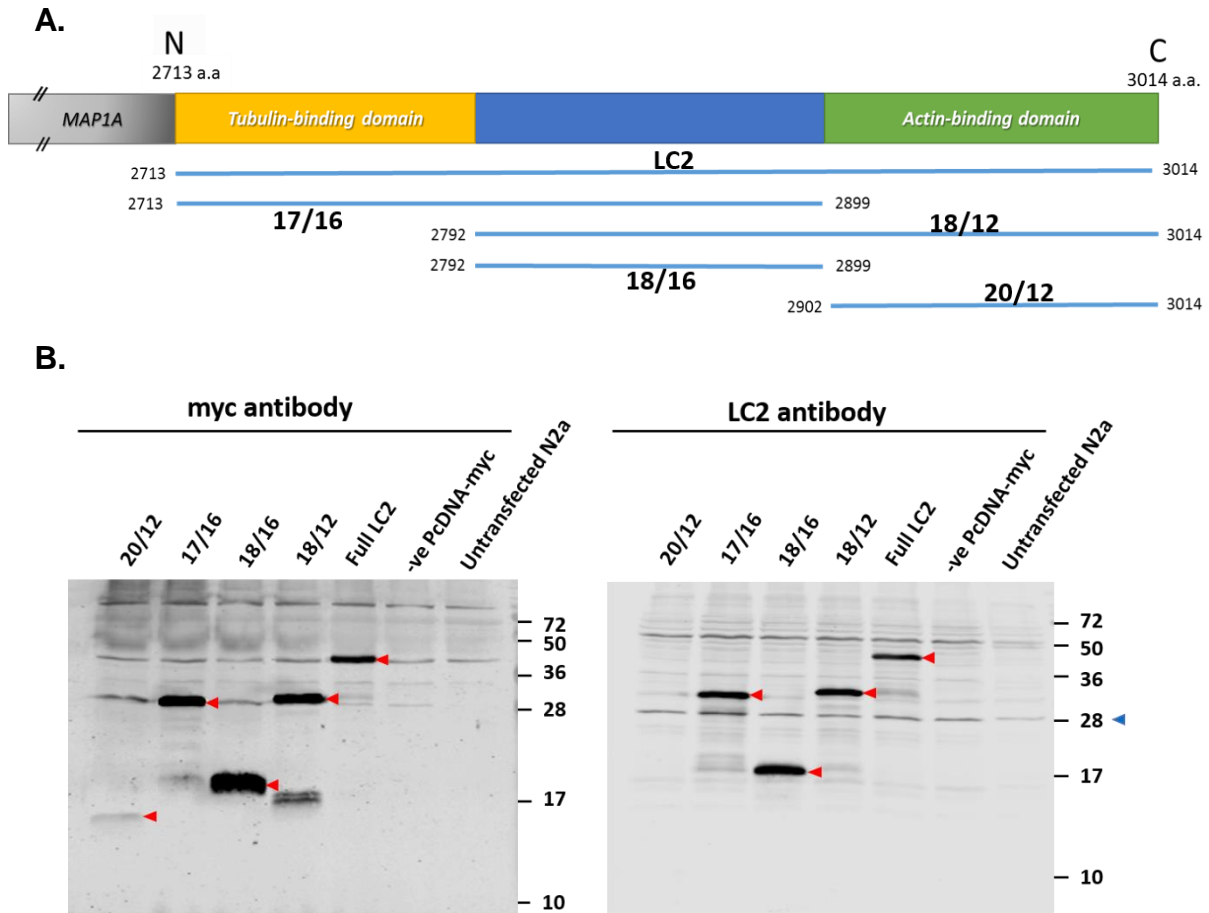


Figure 5.37: Validation of the expression of LC2 deletion mutants by western blotting.
A. Schematic representation of MAP1A-light chain (LC2) domains and cDNA constructs. LC2 (300 amino acids) consists mainly of three major areas: Tubulin-binding domain on the N-terminus, Actin-binding domain on the C-terminus and a middle area with unknown functional features. Each DNA construct was given two numbers for identification which are demonstrated on the scheme.
B. Western blot analysis of N2a cells transfected with different LC2 deletion constructs. Cells were lysed 48 h post-transfection. WB membranes were probed with polyclonal myc antibody (left) and with polyclonal LC2 antibody (right). Both antibodies identified overexpressed bands (red arrows), LC2 antibody also identified endogenous LC2 (28 KD, blue arrow). 20/12 deletion construct (Actin-binding domain) was only identified by myc-antibody and not LC2-antibody because it lacks the epitope required for LC2 antibody binding.

After confirming that LC2 constructs are expressed and produce proteins of the correct molecular weight. I wanted to check their subcellular distribution. Endogenous LC2 showed a homogenous distribution in the DRG neurons soma that extended all the way to the neurites. Immunostaining of LC2-myc in N2a cells, showed homogenous distribution of the protein however it was hard to clearly identify the distribution pattern due to the morphology, cell size and nature of the N2a cells, i.e. rounded shape, small cytoplasm to nucleus ratio with high tendency for the cells to cluster together, (data not shown). Therefore, another attempt was done with Caco-2 cell line, human epithelial colorectal adenocarcinoma cells that are characterised by having a large cytoplasm to nucleus ratio and tend to form a flat sheet which make them ideal for studying cytoskeletal proteins. localization of overexpressed LC2-myc in Caco-2 cells (Fig.5.38) showed a similar distribution pattern to endogenous LC2 in the submembranous layer, Fig. (5.11). LC2-myc was concentrated mostly at the peripheral protrusions of the cell. LC2 also showed a clear filamentous distribution in the cytoplasm which suggests that LC2-myc may decorate MT in the epithelial cells. In conclusion, overexpression of LC2-myc in Caco-2 cells showed similar distribution pattern to endogenous LC2 in DRG neurons and can be used for further colocalization and rescue experiments.

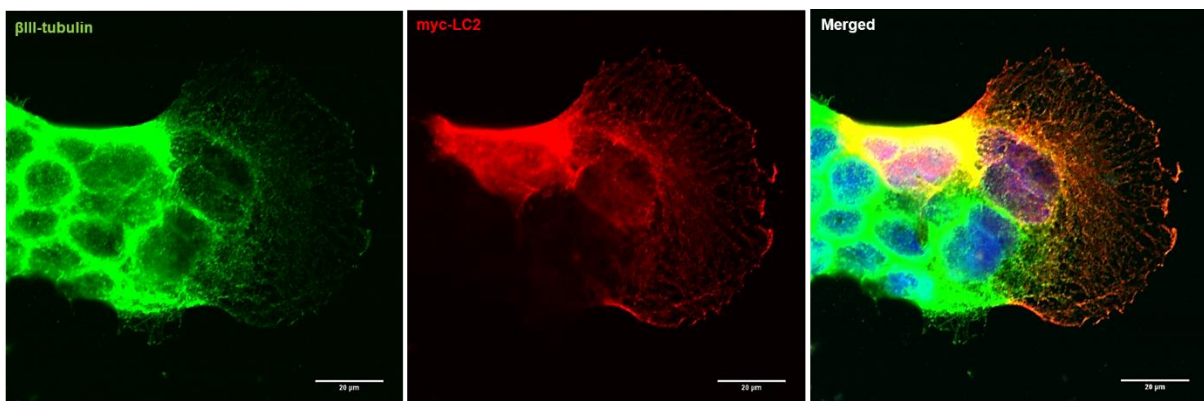


Figure 5.38: Validation of the expression of LC2-myc by immunostaining. A. Caco-2 cells were transfected with LC2-myc, fixed 48 h post-transfection and immune-labelled with β III-tubulin (green), myc-antibody (red) and DAPI (blue). LC2-myc showed homogenous distribution in the cytoplasm and spread evenly throughout the cell extensions where it concentrated the most at the peripheral protrusions of the cell. Images were acquired with conventional confocal microscopy, 40 X objective. Images represent one z-plane (middle of the cells).

5.5. Discussion:

The data presented in this chapter aimed to validate and characterise the interaction between Nav1.7 and LC2 that was identified by a Y2H screen. I confirmed the novel interaction between LC2 and Nav1.7 channel by co-IP experiments in both N2a cells and mouse DRG neurons. I also characterised the distribution pattern of MAP1A heavy and light chains in mouse sensory neurons by immunofluorescence where both LC2 and MAP1A-HC showed a distinct distribution pattern in the soma and neurites of cultured mouse DRG neurons. In addition, I investigated the functional consequences of MAP1A-KD on Nav1.7 membrane expression and neuronal excitability by surface biotinylation, immunostaining and calcium imaging. Nav1.7 surface expression was shown to be increased upon MAP1A KD in DRG neurons. Therefore, these results could suggest that Nav1.7 surface pool is regulated by MAP1A / LC2. However, it remains to be investigated the mechanisms by which MAP1A / LC2 regulates Nav1.7 surface expression level in DRG neurons.

5.5.1. MAP1A (HC and LC2) showed distinct distribution patterns in mouse DRG neurons.

Characterisation of the expression and distribution pattern of the two components of MAP1A protein was performed on both mouse DRG sections and *in vitro* cultures (short- and long- term cultures). LC2 was co-expressed with various neuronal markers in DRG sections. No preferential expression was observed among DRG subpopulations. In retrospect, a more detailed quantification of the expression level of LC2 and MAP1A-HC as well as a better optimisation of some of the antibodies tested at the time could have provided a stronger support to my observations, yet these experiments were among some of the very first experiments in this project, they were carried out mainly to confirm the expression of LC2 in mouse DRGs before moving to the next steps. LC2 immunostaining was clearly and consistently expressed in all types of cells. Therefore, at that time, there was no rationale to thoroughly characterise LC2 expression in every neuronal subpopulation. In addition, LC2 was occasionally exhibited nuclear immunostaining. Others have also reported similar observation in heterologous expression system when only LC2 was expressed (without the HC). The physiological significance of nuclear localization of LC2 in DRG neurons remain to be investigated.

In vitro DRG cultures provided insights on the distribution of MAP1A-HC and LC2 in the axons and neurites of the DRG neurons. LC2 was present in the soma, axons and neurites. While MAP1A-HC showed a distinct beaded organisation in the axons and neurites that co-localised with Nav1.7 clusters. MAP1A-HC beaded organisation was only detectable at ~ 5 DIV, a similar observation was made in hippocampal neurons²⁶² as well as in DRG neurons²⁶³, where the unique actin rings arrangement was only detectable at a similar time point and was maintained in mature neurons in long term cultures. The localisation of MAP1A-HC with Nav1.7 clusters indicates a physiological importance for such cytoskeletal organisation that could be involved in Nav1.7 trafficking or anchoring. It was clear from the current results that not all axons and neurites demonstrated similar MAP1A-HC beaded pattern, therefore, it is important to investigate later time points for better characterisation of MAP1A-HC distribution pattern. Also, to use a more advanced microscopy (e.g. STORM microscopy) combined with various markers (e.g. ankyrin G, MAP2, KIF5 and dynein) to identify different neuronal regions (AIS, axon, and secondary neurites), neuronal subpopulations, as well as other cytoskeletal components that could colocalize or overlap with the gaps produced by MAP1A-HC distribution, for example MAP2 protein.

The regular distribution of MAP1A-HC significantly correlated with Nav1.7 clusters while none of the other cytoskeletal proteins (β III-tubulin, actin and LC2) showed such organisation and colocalization. This could suggest a unique role for MAP1A-HC in regulating Nav1.7 distributions along the axons and neurites. Unfortunately, I was not able to measure the extent of disruption in Nav1.7 clusters in MAP1A KD neurons, due to the inability to identify transduced neurons due to the loss of GFP signal in immunostaining and the weak MAP1A-KD efficiency. It will be very interesting in the future to investigate the physiological importance of MAP1A-HC on the localisation of Nav1.7 and other potential ion channels by using MAP1A KO animals.

MAP1A (HC & LC2) soma distribution in DRG neurons were evident in two complementary regions in the cytoplasm; HC was mainly in the perinuclear region and filling the centre of the cytoplasm, while LC2 was mainly found in the peripheral cytoplasmic region close to the plasma membrane. In agreement with this observation, cellular fractionation and subsequent WB analysis of hippocampal neurons showed

an enrichment of MAP1A-HC in the cytoplasm fraction while LC2 was mainly enriched in the plasma membrane fraction²¹⁵. In addition, it was reported that LC1 can be found in a MAP1B-HC independent pool (unbound LC1)^{189,256}, similar observation was suggested for LC2. Altogether, the consistent distribution patterns of MAP1 heavy and light chains in DRG neurons as well as in other cell types agrees with the proposed role of LC2 as a linker of the two major cytoskeleton networks. The intracellular localisation of the “free” light chains pool infers a role in regulating the movement of the membrane proteins from and to the plasma membrane.

5.5.2. Nav1.7 interacts with the Light chain (LC2) of microtubule-associated protein 1 A (MAP1A) in N2a cells and DRG neurons.

Y2H interaction between the N-terminus bait of Nav1.7 channel and LC2 was confirmed by co-IP experiments with endogenous full length proteins in both mouse DRG neurons and N2a cell lines. Nav1.7 co-IP demonstrated a specific interaction with LC2 but not with MAP1A-HC or LC1. Nav1.7 also interacted with β -actin, however it is not known whether this was a result of the LC2 interactome or due to direct interaction with Nav1.7 itself. Analysis of Nav1.7 protein sequence using ELM database (The Eukaryotic Linear Motif resource for functional sites in proteins) predicted an actin-binding domain in the N-terminus site of the Nav1.7 channel. Nav1.7 co-IP experiments in MAP1A KO animals could better address the nature of Nav1.7 and actin interaction.

Both LC1 and LC2 share a highly-homologous actin-binding domain that allows binding to the microfilament cytoskeleton. In addition, both LC1 and LC2 have a structurally unrelated (non-homologous) microtubule-binding domain in their N-terminus domain that are equally efficient in stabilizing microtubules. The fact that Nav1.7 co-IP results showed an interaction with LC2 but not with LC1, suggest that the interaction was most likely with the N-terminus domain of the LC2. In agreement, most of the light chains specific interactions (e.g. interaction of LC2 with Cav2.2 ion channel²¹⁵ and of LC1 with Nav1.6 ion channel²⁰²) were mediated by the N-terminus of LC2. Further pull-down experiments with LC2 deletion constructs can better address this point.

Admittedly, although the interaction was detected by Nav1.7 immunoprecipitation in two cell models; N2a cells and DRG sensory neurons, several additional experiments are required. First, confirmation of the interaction by a reciprocal co-IP experiment where LC2 being precipitated instead of Nav1.7. Unfortunately, the LC2 antibody was not suitable for IP experiments in my hands. Additional attempt was done by using LC2-myc transfected in N2a cells (Myc-pull down experiment – data not shown) which also failed to detect the interaction between Nav1.7 and LC2-myc, probably because of endogenous Nav1.7 is already bound to LC2. Therefore, this experiment is better addressed in the future by heterologously co-expressing Nav1.7 and LC2 in HEK293 cells. Second, investigation of the specificity of LC2-Nav1.7 interaction. To better understand the physiological function of LC2 in sensory neurons, it would be important to address whether LC2 interacts specifically to Nav1.7 or it also interacts with other VGSC. Due to the lack of time and resources, I was not able to investigate this aspect in the current study.

5.5.3. Nav1.7 surface expression level and activity increased upon LC2 KD.

The identification of the novel Nav1.7-LC2 interaction led us to further investigate its physiological significance in DRG neurons. The effect of MAP1A KD on Nav1.7 was studied in both N2a cells and DRG neurons using surface biotinylation and immunostaining, respectively.

MAP1A was endogenously expressed in N2a cells. Knock-down of MAP1A resulted in almost 80 % reduction in the protein level, yet Nav1.7 surface expression level was not significantly affected. Notably, there was a small but consistent reduction in the endogenous Nav1.7 surface level in all tested miRNA sequences in N2a cells. This data could hint to a potential role of LC2 in promoting Nav1.7 trafficking to the membrane, in a similar fashion to what have been described for Nav1.6/LC1²⁰², and 5HT3/LC1²⁰¹ interactions in HEK-293 cells. However, the increasing cell death upon MAP1A KD in N2a cells might compromised the data. Therefore, the N2a surface biotinylation results demonstrated in Fig. 5.18 should be interpreted with caution.

Lentivirus encoding MAP1A-miRNA was used to study the effect of MAP1A KD in DRG neurons *in vitro*. Quantitative analysis of Nav1.7 surface intensity in DRG neurons by immunofluorescence showed a negative correlation to MAP1A-HC in LV untransduced, and LV-scrambled miRNA transduced neurons. This negative correlation was lost in cells that were transduced with LV encoding MAP1A miRNA sequences. These results suggested an increase in Nav1.7 surface expression level upon MAP1A KD in some mouse DRG neurons, in contrast to the N2a results, Fig. 5.18. The effect of MAP1A KD on Nav1.7 surface intensity level was most prominent in the “high MAP1A” group compared to the low and medium MAP1A groups. This could suggest that MAP1A is the predominant MAP in the high MAP1A population of neurons, Fig. 5.28. While in the other two groups, where MAP1A is not highly expressed, other structurally and functionally redundant MAPs (e.g. MAP1B and MAP2) could play a more dominant role in regulating Nav1.7 surface expression - particularly since the interaction of these MAPs with Nav1.7 in DRG has not been ruled out in this study.

To complement the ICC results, calcium imaging was performed to further investigate the potential effects of MAP1A KD on neuronal excitability. The percentage of VTD responding neurons and the frequency of occurrence of VTD subtypes along with other parameters including peak amplitude, AUC and VTD response latency were measured in LV-transduced neurons using GFP signal as a marker for LV transduction. Unfortunately, this experiment was confounded by the fact that LV transduction by itself increased neuronal excitability, Fig. 5.29. Therefore, the MAP1A-KD specific action should be interpreted with caution. Analysis of the GFP(+) results, however, showed a small increase in the percentage of VTD responding neurons in MAP1A KD neurons than in control. The increase was equally distributed between all VTD subtypes, Fig. 5.31, except for a decrease in the OS profile in miR2+1, with no obvious effect on any of the other parameters (peak amplitude, AUC and latencies). Based on the previous characterisation of VTD responses by pharmacological blockers, the MAP1A KD phenotype was opposite to the results obtained with Nav1.7 blocker (PF-04856264), Fig. 4.3 & 4.4, chapter 4. Therefore, these data could reflect a potential small increase in Nav1.7 surface level, in consistence with the immunofluorescence results, Fig. 5.28. The observed decrease in the percentage of occurrence of the OS profile in Fig. 5.31, could suggest that miR2+1 sequence has

some non-specific effects on some targets that might contribute to calcium oscillations in DRG neurons (e.g. Cav2.2). Further experiments may better address this point.

The increased Nav1.7 surface level in MAP1A KD neurons (indicated by ICC and potentially calcium imaging results), suggests that MAP1A-LC2 could play a role in either promoting Nav1.7 internalisation or in inhibiting Nav1.7 membrane insertion. As described earlier, LC1 was proposed to serve as an adaptor that links Cav2.2 channel to the ubiquitin conjugase UBE2L3 to promote Cav2.2 ubiquitination and degradation *in vitro*^{204,205}. Interestingly, prediction of the ubiquitination sites of Nav1.7 by Ubsite web server (UbPred) predicted three ubiquitination sites in the N-terminus (ubiquitination score: high (0.9) and medium (0.74 and 0.78)). Therefore, and based on the evidence from the literature and from the current results, it is plausible to propose a model where LC2 binds to the microfilaments and acts as an adaptor that facilitate the ubiquitination of the Nav1.7 channel and internalization, Fig. 5.39. Further experiments using microfilament disrupting agents could reveal the role of actin in regulating the proposed interaction model. Also, this model does not exclude other potential PTM changes that lead to Nav1.7 internalization or reduced anchoring.

LC2 was found to interact with Cav2.2 and links the channel to the actin cytoskeleton at the presynaptic terminals of the hippocampal neurons. These findings indicate that the final fate of the channel (ubiquitination and internalisation or membrane targeting and retention) via LC1 and LC2 depends largely on the site of interaction and on the presence or absence of other proteins within the interacting complex. Therefore, differences in the composition of the interactome could also explain the discrepancies in the results obtained from N2a cells and DRG neurons. Again this could reflect the need of other protein components that can determine the final role of the interacting complex. One potential candidate that might influence the nature of the interaction is the β -subunits as they have been shown to be differentially expressed in various populations of DRG neurons and promote channel anchoring at the plasma membrane via the interaction with ankyrin-G and cytoskeletal proteins^{264,265}.

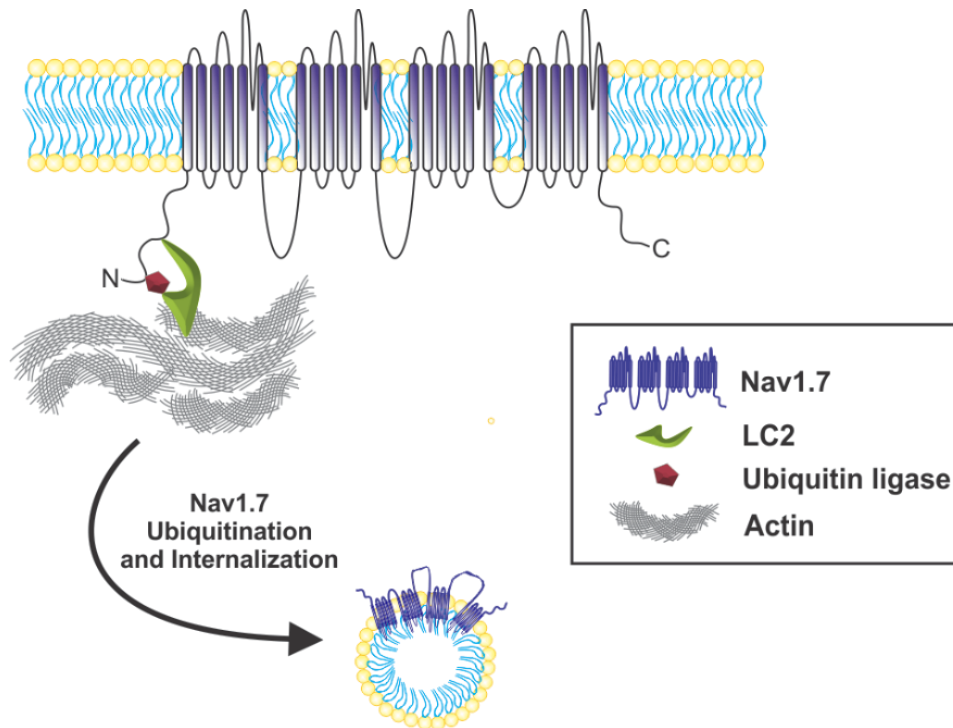


Figure 5.39: Schematic diagram that illustrates the role of LC2 in regulating Nav1.7 membrane expression in DRG sensory neurons. LC2 interacts with the N-terminus of Nav1.7 at the cell membrane and to actin cytoskeleton. LC2 acts as an adaptor protein for binding of other proteins and enzymes that promote channel internalization (e.g. ubiquitin ligase enzyme). Enhancement and stabilization of the LC2-Nav1.7-Actin protein complex may provide a strategy for reducing surface Nav1.7 levels and pain relief.

Also, the phosphorylation / dephosphorylation state of the light chain has a crucial role in determining the binding affinity to a particular cytoskeleton and in determining the ultimate function of the interacting LC-protein complex¹⁸⁹. It is not known how the various β -subunits, or PTM of both Nav1.7 and MAP1A proteins could influence Nav1.7-LC2 interaction in N2a cells and DRG neurons, and what are the other components that are involved regulating the function of Nav1.7-LC2 interaction.

One of the main difficulties in this study was the efficiency of the MAP1A KD. Despite an almost 80 % KD efficiency in N2a and despite the relatively high LV transduction efficiency in DRG, MAP1A KD was rather weak and suboptimal. It is therefore important to investigate the interaction in MAP1A KO animals. In addition, given the fact that the light chains of MAP1A and MAP1B are interchangeable with some degree of structural and functional redundancy, it might be even better to study the interaction in a MAP1A and MAP1B double KO to clearly understand the contribution of the light

chains in regulating surface Nav1.7 level – although, currently, there is no evidence for the availability of MAP1A & MAP1B DKO in the literature.

In conclusion, the results presented in this chapter showed some role of the cytoskeleton in regulating Nav1.7 surface expression levels. Further experiments are needed to reveal how this interaction changes neuronal excitability in pathological conditions, if any. LC2 mediated-Nav1.7 internalization process may be exploited to design new Nav1.7 targeting strategies for pain relief.

CHAPTER 6
DISCUSSION

Chapter 6: Discussion

Chronic pain is a serious global issue that affects approximately 20 % of the people worldwide. It accounts for 15 – 20 % of hospital visits. 10 % of the people worldwide are estimated to be newly diagnosed with pain per year^{266,267}. Over the past decades, human and animal studies suggested the inhibition of the peripheral drive as an effective strategy for chronic pain relief. Several peripherally expressed ion channels have shown to be critical for the development of chronic pain. Today, the research focus is to understand the properties and the molecular mechanisms that regulate these ion channels, investigate new targeting strategies and screen for potentially effective and safe analgesics. Nav1.7 ion channel is a crucial player in eliciting pain signaling. Therefore, the current study aimed to investigate the functional significance of a novel interaction of Nav1.7 with the light chain of microtubule-associated protein 1A (LC2) in DRG sensory neurons. We suspected that the interaction might have different degree of contribution to Nav1.7 membrane density in the various cell types of DRG neurons. Therefore, we wanted to use a functional screen that is more suitable for heterogeneous population as in DRG. This would allow us to go through a large number of DRG neurons that represent different functional subtypes. Therefore, I first used calcium imaging in a novel approach to assess neuronal excitability. Data for developing and characterizing the VTD based calcium imaging assay are presented in chapter 3 and 4. Finally, I applied my screening assay to investigate the functional relevance of the Nav1.7-LC2 interaction as presented in chapter 5. In this chapter I will discuss the main findings and observations, the questions that this study has raised, the current major limitations and future perspectives.

6.1. The use of Veratridine in assessing neuronal excitability of DRG neurons - An old drug, a new tale.

The first aim of the current study was to establish a high-throughput assay to study neuronal excitability and Nav1.7 function in DRG sensory neurons, *in vitro*. The results provided a detailed characterization of the calcium responses elicited by the application of veratridine to cultured DRG neurons. It included characterization of the VTD responses, neuronal subtypes and Nav1.7 and Nav1.8 ion channels contributions to the VTD calcium responses. The results demonstrated in here provide the basis for

a high-throughput screen for novel analgesics in DRG neurons and in functional studies.

VTD based calcium imaging assay can be used in functional studies, as demonstrated in this study. VTD calcium responses can reflect the effect of a specific protein interaction or treatment on neuronal excitability with the advantage of detecting specific effects that occur in distinct neuronal subtypes (e.g. nociceptors). This is particularly important because the investigated effect could be masked by the presence of other “unaffected” neuronal subpopulation as in WB, or it might not be detected due to the low-throughput screening efficiency as in patch-clamp electrophysiology. In addition, VTD calcium responses reflect the sum changes in the actions of several classes of ion channels, ion exchanges and receptors. The advantage is that it can predict potential off-targets effects.

For example, by using calcium imaging I demonstrated an unexpected sensitizing effect of LV transduction on DRG neurons, chapter 5. The exact mechanism of the sensory neurons sensitization is not clear. In the current study, LV transduction did not seem to affect Nav1.7 surface expression (as evident from Nav1.7 immunofluorescence experiments, Fig. 5.26, where scrambled miRNA showed a similar Nav1.7 membrane expression level as the untransduced neurons). Nav1.8 is also shown to not be affected by LV transduction in DRG neurons²⁶⁸. This indicates that the DRG sensitization is probably mediated by other ion channels and receptor. This sensitization effect detected by calcium imaging would have taken much efforts and “chance” to be detected by assays that examine specific target at a time.

LV vector is derived from human immunodeficiency virus (HIV). It has been shown that LV envelope contains the glycoprotein gp120 that is associated with neurotoxicity in primary cortical neurons²⁶⁹. In addition, LV infection of primary feline DRG culture produced an upregulation of inducible nitric oxide synthase and neuroinflammation mediated by LV- activated macrophages in culture²⁷⁰. The molecular mechanism of the LV neurovirulence is not completely understood. Therefore, the VTD based calcium imaging assay can be used as a model for investigating different aspects of viral induced sensitization in DRG subpopulation and screen for potential neuroprotective compounds against HIV-related sensory neuropathy.

Another application of the proposed calcium assay is in drug screen for novel analgesics. Changes in ion channel expression and distribution pattern are associated with enhanced excitability and hypersensitivity of nociceptors in chronic pain. Drug screen for novel analgesics is mainly based on the ability of the tested drug to specifically bind and effectively alter the activity of the target protein to restore neuronal excitability to basal levels. Characterization of novel drugs usually takes place in heterologous system where the protein target is being transiently or stably expressed. However, the results obtained by various assays (e.g. patch clamps and FLIPR) from the heterologous expression system do not necessarily always agree with that obtained from native tissues. For example, A-803467 was shown to bind heterologously expressed hNav1.8 three times higher than other VGSCs. However, in rat DRG, A-803467 efficacy was significantly reduced to almost the half²⁴⁷. In addition, in human DRG, a similar concentration of A-803467 that blocked the hNav1.8 in HEK293 cells (<100nM) completely failed to produce any TTX-R blockade and was only effective at much higher concentrations (1 μ M)²⁷¹. Failure of a “specific” drug to produce the desired outcomes in native tissues has a direct consequence on the drug development process and may explain the reason for failure of many clinical trials. Therefore, the investment in developing a high-throughput assay in primary sensory neurons will help to thoroughly interrogate and characterize the tested drugs in pre-clinical studies. This will rectify the number of drugs sent to the clinical studies pipeline but with higher chances of success. The emergence of human DRGs studies in recent years have highlighted some important similarities between rodents and humans and have argued with the continued use of rodent DRG (as well as human) as a model system to investigate potential pain targets^{245,271,272}. Given the extremely limited number of primary neurons (particularly from human), the high heterogeneity and the high costs associated with both animal or human studies compared to cell lines, it is essential to have direct, efficient and comprehensive method for assessing neuronal excitability, in vitro. In the current study, we proposed the use of VTD based calcium imaging as a new assay to assess the excitability of DRG neurons.

The difference in the percentage of occurrence of VTD response profiles between the long-term (Fig. 5.30) and short-term cultures (Fig. 4.4 & 4.10 (A & D) in chapter 4) highlights significant changes in the molecular constellation of sensory neurons that need to be further investigated. It is not known whether the reduction in the OS profile

(27 % in short became 11 % in long term cultures) and the increase in the SD profile (14 % in short became 24 % in long term cultures) is due to altered expression of certain ion channels (e.g. reduced Nav1.8 or increased VGKC) or due to altered biophysical activity or trafficking of the ion channels at the cell membrane. It has been shown previously that activated (phosphorylated) p38 is required for enhanced Nav1.8 activity ²⁷³. However, p38 activity is reduced with time in culture with a subsequent reduction in neuronal excitability, which could explain the reduced OS response profile (reduced neuronal excitability). Further investigation is required to identify the main changes between the two culture conditions and their consequences on the interpretation of experiment findings, particularly from those performed on culture (> 3 DIV) as in knock-down studies.

Finally, due to the wide gaps in translational pain research, many are interested in studying pain signalling in hDRG “human pain in a dish” ²⁷⁴. This new approach requires development of better research strategies to maximise the use of the hDRG neurons and improved preclinical studies outcomes. VTD based calcium assay is a new assay that holds promise to thoroughly interrogate and screen large number of neurons in an easy, direct, affordable and minimally invasive way. This study provides the first evidence for the usefulness of VTD response profiles in functional assays and drug screen. However, many more efforts should be invested for further development of this assay. For example, the VTD response profiles described in this study were obtained from mouse DRG neurons and by using VGSC pharmacological blockers. Further characterization in other species (rat and human) and in genetically ablated VGSC animals, as well as testing other ion channel classes are essential complementary studies that need to be addressed in the future. In addition, VTD response profiles in this study represent the “baseline” responses in normal conditions. It will be interesting in the future to test in vitro sensitization models like PGE2- or inflammatory soup- induced inflammation ²²⁶ and sensitization, streptozotocin-induced diabetic neuropathy ²⁷⁵ and paclitaxel-induced peripheral neuropathy ²⁷⁴ to validate the suitability of VTD based calcium imaging assay in determining neuronal excitability in various contexts. Further experiments may highlight the molecular nature of the VTD non-responding neurons “silent nociceptors”. We hypothesized that these neurons have little or no TTX-S and high TTX-R channels. However, it remains to be seen

whether the in vitro sensitization models can activate these “silent” neurons and what type of VTD-response profile they may produce upon activation.

6.2. LC2 specifically interacts with Nav1.7 and negatively regulates Nav1.7 membrane expression in DRG neurons.

Most of the currently available research data largely cover the molecular interaction and biological functions of MAP2, MAP1B and tau proteins in the CNS with relatively limited data for MAP1A in the CNS in general and in the PNS in particular. In addition, most of the MAPs functional studies were investigated either in brain tissue sections, brain extracts or hippocampal neurons in vitro, or in heterologous expression systems for simplicity, leaving a wide gap in the literature regarding the functional properties of MAPs in the PNS. Therefore, this study provides an insight into our current understanding of MAP1A distribution in the DRG sensory neurons and may indicate a very interesting and distinct function for MAP1A in regulating Nav1.7 VGSC surface expression in the PNS.

The co-localization of MAP1A with Nav1.7 at the neurites, Fig. 5.7 suggests a role for MAP1A in regulating Nav1.7 trafficking. Since I could not detect a direct interaction of MAP1A-HC with Nav1.7 but only with LC2, Fig. 5.14, and Fig. 5.13, respectively, it is possible that MAP1A-Nav1.7 co-localization in the neurites is mediated by the “MT-bound” fraction of LC2, Fig. 5.5. In contrast, regulation of Nav1.7 at the cell membrane is most likely mediated by the “MT-free” fraction of LC2 via the actin cytoskeleton. In support of this, immunostaining data of DRG neurons in culture showed an enrichment of LC2 but not MAP1A-HC in the submembranous compartment, Fig. 5.9 – 5.11.

This study has raised several questions. First, what is the role of MAP1A/LC2 function in DRG neurons? It has been demonstrated previously that the binding affinity of MAP1 proteins is highly dependent on the post-translational modifications. Phosphorylation of MAP1 proteins has higher MT-binding affinity ¹⁷⁸, while dephosphorylation of MAP1 proteins promotes microfilament binding ¹⁷⁹. Casein kinase II enzyme is shown to be the primary kinase that phosphorylate both MAP1A and MAP1B in N2a cells ¹⁷⁸. Casein kinase II is ubiquitously expressed in DRG neurons ³⁹ and therefore it could be also involved in MAP1A / MAP1B post-translational phosphorylation and function regulation in sensory neurons.

Second, what are the molecular components that associate with the MAP1A-Nav1.7 clusters at the neurites? There is no data available in the literature to compare MAP1A distribution observed here to other studies nor the distribution relationship between MAPs and other ion channels. However, it has been shown that Ankyrin G and KIF5B promote the microtubule-mediated forward transport of VGSC in DRG neurons^{276,277}, therefore, it is possible that MAP1A interacts with these two proteins at the axons and neurites. Advanced microscopy techniques, like STORM microscopy could be useful to reveal the molecular components of the clusters and their nanoscale structural arrangement which could provide an insight into the role of MAP1A in Nav1.7 axonal trafficking²⁷⁸.

Third, what are the other potential components in the LC2-Nav1.7 complex? The mode of the interaction was not investigated in the current study, however evidence for some key proteins can provide initial guidance in the search for the molecular mechanism. I have proposed that the interaction might involve a ubiquitin-ligase enzyme which could promote N-terminus ubiquitination of Nav1.7 and internalization via the actin microfilament. In support of this hypothesis, RhoB has been shown to specifically interact with LC2²⁷⁹. RhoB is a small GTP-binding protein that is involved in several fundamental cellular functions some of which are regulation of endocytic trafficking, signaling pathways and actin cytoskeleton²⁸⁰. These functions in addition to the strategic location of RhoB at the plasma membrane and the early endosomal compartment indicates a potential role for RhoB in regulating Nav1.7 endocytosis that is mediated by LC2 and actin cytoskeleton.

And finally, what are the functional implications of Nav1.7/LC2 interaction? As demonstrated previously, Nav1.7 channel is widely accepted as a key channel in setting pain baseline threshold in nociceptors and contributes to inflammation and nerve-injury induced pain. Therefore, targeting Nav1.7 to relieve pain is the prime focus of many pharmaceutical industries. This study offers an insight into the role of the cytoskeleton in regulating Nav1.7 intracellular trafficking. Cytoskeleton networks have been shown to regulate signaling pathways. ERK1/2 pathway is of a particular interest. ERK1/2 MAPK has been implicated in inflammation and mediates Nav1.7 enhanced activity in inflammation¹²². Activation of ERK pathway is dependent on the cytoskeleton integrity²⁵⁵. The results demonstrated in here might highlight a potential role for LC2 as an adaptor that mediates ERK pathway activation and Nav1.7 function.

A better understanding of the nature and function of LC2/Nav1.7 interaction in normal and pathological conditions, could lead to a therapeutic strategy based on indirect targeting of Nav1.7-interacting proteins and/or any of the downstream effectors.

Another probable implication of LC2-Nav1.7 interaction is in the rodent brain. Tubby mice arise from a spontaneous mutation in the *tub* gene (an obesity gene that is mainly expressed in the hypothalamus) in the C57BL/6J mouse colony. Homozygous tubby mice are characterized by late-onset obesity associated with hyperinsulinemia and neurosensory deficits (e.g. hearing loss and retinal degeneration) ^{281,282}. Later investigations have showed that MAP1A sequence polymorphism is crucial for the tubby mice associated hearing loss phenotype ²⁸². Although the exact mechanism is not clear, but it was suggested that impaired interaction between MAP1A and PSD-95 (a major protein component in the postsynaptic density that is essential for maintaining the proper synaptic architecture and function) could play a role in the phenotype. Recently, Nav1.7 functional role in the mouse brain has been investigated. Interestingly, Nav1.7 was found to be highly expressed in the hypothalamus and is specifically involved in regulating body weight. Tissue-specific KD of Nav1.7 gene prevented the development of obesity. It is suggested that the specific synaptic localization of Nav1.7 at distinct subcellular compartments (e.g. dendritic branches) is critical for Nav1.7 proper synaptic integration of the excitatory postsynaptic potentials (EPSP) and body weight regulation ²⁸³. Since LC2 has been shown to interact with postsynaptic density proteins (PSD-93 and PSD-95) ^{214,284}, it is not unlikely that LC2 might be involved in regulating Nav1.7 synaptic functions through PSD proteins in the hypothalamus. If this hypothesis is true, then, MAP1A^{-/-} KO animals should develop late-onset obesity phenotype consistent with the earlier two mouse models. However, no data is currently available to prove this point, since the cerebellar Purkinje cells were the only region that was analyzed in the MAP1A^{-/-} KO animals and no other phenotypes were reported ¹⁹⁹. Future studies could better address this point.

6.3. Limitations of MAP1A – Nav1.7 work:

The discrepancy in the results between MAP1A potential function in regulating Nav1.7 membrane expression in N2a (Fig. 5.18) and DRG neurons (Fig. 5.26) emphasizes the importance to validate any cell line observation into native tissues. One important factor that might contributed to such opposing results could be related to the KD

methods used for each cell type. MAP1A KD in DRG neurons was achieved by LV transduction, while in N2a cells the DNA transfection was mediated via PEI-vehicle which is known to have some cytotoxic effect that confounded the N2a phenotype. In addition, N2a cells are a neuron-like cell line that originates from the spontaneous tumor in albino mouse. Therefore, the discrepancies in results could suggest a differential regulation of Nav1.7 by MAP1A protein in various cell types. Moreover, differences in the differential expression of β -subunits, splice variant, post-translational enzymes and other interacting components are also additional factors that could account for the observed discrepancies. At the same time, the use of DRG, although essential, was very challenging and slowly progressing compared to cell lines. The limited number of cells, the high level of heterogeneity and the low transfection efficiency are some of the main limitations associated with the use of DRG neurons. Another limitation is the MAP1A KD suboptimal efficiency in DRG neurons. Therefore, studies that investigate highly expressed proteins, like the cytoskeletal and the cytoskeleton-related proteins, are best done by KO than KD approach to obtain a clearer picture of the phenotype. In addition, calcium imaging results demonstrated an increased neuronal excitability in GFP(+) neurons [i.e. LV-transduced neurons]. Other transfection methods have to be tested.

Quantification of Nav1.7 surface expression was done by measuring the surface Nav1.7 integrated density in the soma. The effect of MAP1A KD on Nav1.7 in the neurites terminals was not assessed due to technical challenges. The extensive neurite outgrowth and the cross-crossing between neuronal and non-neuronal cells in long-term DRG culture made it difficult to accurately quantify Nav1.7 at the terminals. It is therefore important to emphasize that the results demonstrated in this study mainly reflects altered Nav1.7 surface expression levels in the DRG soma only, while the effect of LC2 on Nav1.7 at the terminals remains to be addressed in the future.

BIBLIOGRAPHY

Bibliography

- 1 Ahuja, S. *et al.* Structural basis of Nav1.7 inhibition by an isoform-selective small-molecule antagonist. *Science (New York, N.Y.)* **350**, aac5464, doi:10.1126/science.aac5464 (2015).
- 2 Vetter, I. *et al.* Nav1.7 as a pain target - From gene to pharmacology. *Pharmacology & therapeutics* **172**, 73-100, doi:10.1016/j.pharmthera.2016.11.015 (2017).
- 3 Shiomura, Y. & Hirokawa, N. The molecular structure of microtubule-associated protein 1A (MAP1A) in vivo and in vitro. An immunoelectron microscopy and quick-freeze, deep-etch study. *The Journal of neuroscience : the official journal of the Society for Neuroscience* **7**, 1461-1469 (1987).
- 4 Sato-Yoshitake, R., Shiomura, Y., Miyasaka, H. & Hirokawa, N. Microtubule-associated protein 1B: molecular structure, localization, and phosphorylation-dependent expression in developing neurons. *Neuron* **3**, 229-238 (1989).
- 5 Momin, A. & Wood, J. N. Sensory neuron voltage-gated sodium channels as analgesic drug targets. *Current opinion in neurobiology* **18**, 383-388, doi:10.1016/j.conb.2008.08.017 (2008).
- 6 Halpain, S. & Dehmelt, L. The MAP1 family of microtubule-associated proteins. *Genome biology* **7**, 224, doi:10.1186/gb-2006-7-6-224 (2006).
- 7 Matus, A. Microtubule-associated proteins: their potential role in determining neuronal morphology. *Annual review of neuroscience* **11**, 29-44, doi:10.1146/annurev.ne.11.030188.000333 (1988).
- 8 Bahring, R. & Covarrubias, M. Mechanisms of closed-state inactivation in voltage-gated ion channels. *J Physiol* **589**, 461-479, doi:10.1113/jphysiol.2010.191965 (2011).
- 9 Cravchik, A., Reddy, D. & Matus, A. Identification of a novel microtubule-binding domain in microtubule-associated protein 1A (MAP1A). *Journal of cell science* **107 (Pt 3)**, 661-672 (1994).
- 10 Waxman, S. G. & Zamponi, G. W. Regulating excitability of peripheral afferents: emerging ion channel targets. *Nature neuroscience* **17**, 153-163, doi:10.1038/nn.3602 (2014).
- 11 Kapitein, L. C. & Hoogenraad, C. C. Which way to go? Cytoskeletal organization and polarized transport in neurons. *Molecular and cellular neurosciences* **46**, 9-20, doi:10.1016/j.mcn.2010.08.015 (2011).
- 12 Conde, C. & Caceres, A. Microtubule assembly, organization and dynamics in axons and dendrites. *Nat Rev Neurosci* **10**, 319-332, doi:10.1038/nrn2631 (2009).
- 13 Basbaum, A. I., Bautista, D. M., Scherrer, G. & Julius, D. Cellular and molecular mechanisms of pain. *Cell* **139**, 267-284, doi:10.1016/j.cell.2009.09.028 (2009).
- 14 Herzog, W. & Weber, K. Fractionation of brain microtubule-associated proteins. Isolation of two different proteins which stimulate tubulin polymerization in vitro. *European journal of biochemistry* **92**, 1-8 (1978).
- 15 Howard, J. & Hyman, A. A. Dynamics and mechanics of the microtubule plus end. *Nature* **422**, 753-758, doi:10.1038/nature01600 (2003).
- 16 Dubin, A. E. & Patapoutian, A. Nociceptors: the sensors of the pain pathway. *The Journal of clinical investigation* **120**, 3760-3772, doi:10.1172/JCI42843 (2010).

- 17 Prescott, S. A., Ma, Q. & De Koninck, Y. Normal and abnormal coding of painful sensations. *Nature neuroscience* **17**, 183-191, doi:10.1038/nn.3629 (2014).
- 18 Gasser, H. S. & Erlanger, J. The Action Potential in Fibers of Slow Conduction in Spinal Roots and Somatic Nerves. *Proceedings of the Society for Experimental Biology and Medicine* **26**, 647-649, doi:10.3181/00379727-26-4441 (1929).
- 19 Gasser, H. S. The classification of nerve fibers. (1941).
- 20 Maxwell, D. J. & Réthelyi, M. Ultrastructure and synaptic connections of cutaneous afferent fibres in the spinal cord. *Trends in Neurosciences* **10**, 117-123, doi:[http://dx.doi.org/10.1016/0166-2236\(87\)90056-7](http://dx.doi.org/10.1016/0166-2236(87)90056-7) (1987).
- 21 Lawson, S. N. Phenotype and function of somatic primary afferent nociceptive neurones with C-, Delta- or Aalpha/beta-fibres. *Experimental physiology* **87**, 239-244 (2002).
- 22 Liu, Y. & Ma, Q. Generation of somatic sensory neuron diversity and implications on sensory coding. *Current opinion in neurobiology* **21**, 52-60, doi:10.1016/j.conb.2010.09.003 (2011).
- 23 Lawson, S. N., Perry, M. J., Prabhakar, E. & McCarthy, P. W. Primary sensory neurones: neurofilament, neuropeptides, and conduction velocity. *Brain research bulletin* **30**, 239-243 (1993).
- 24 Patapoutian, A. & Reichardt, L. F. Trk receptors: mediators of neurotrophin action. *Current opinion in neurobiology* **11**, 272-280 (2001).
- 25 Li, L. *et al.* The functional organization of cutaneous low-threshold mechanosensory neurons. *Cell* **147**, 1615-1627, doi:10.1016/j.cell.2011.11.027 (2011).
- 26 Wang, H., Rivero-Melian, C., Robertson, B. & Grant, G. Transganglionic transport and binding of the isolectin B4 from *Griffonia simplicifolia* I in rat primary sensory neurons. *Neuroscience* **62**, 539-551 (1994).
- 27 Silverman, J. D. & Kruger, L. Selective neuronal glycoconjugate expression in sensory and autonomic ganglia: relation of lectin reactivity to peptide and enzyme markers. *Journal of neurocytology* **19**, 789-801 (1990).
- 28 Bennett, D. L. *et al.* A distinct subgroup of small DRG cells express GDNF receptor components and GDNF is protective for these neurons after nerve injury. *The Journal of neuroscience : the official journal of the Society for Neuroscience* **18**, 3059-3072 (1998).
- 29 Teichert, R. W. *et al.* Functional profiling of neurons through cellular neuropharmacology. *Proceedings of the National Academy of Sciences of the United States of America* **109**, 1388-1395, doi:10.1073/pnas.1118833109 (2012).
- 30 Teichert, R. W. *et al.* Characterization of two neuronal subclasses through constellation pharmacology. *Proc Natl Acad Sci U S A* **109**, 12758-12763, doi:10.1073/pnas.1209759109 (2012).
- 31 Teichert, R. W., Memon, T., Aman, J. W. & Olivera, B. M. Using constellation pharmacology to define comprehensively a somatosensory neuronal subclass. *Proceedings of the National Academy of Sciences of the United States of America* **111**, 2319-2324, doi:10.1073/pnas.1324019111 (2014).
- 32 Smith, N. J. *et al.* Comparative functional expression of nAChR subtypes in rodent DRG neurons. *Frontiers in cellular neuroscience* **7**, 225, doi:10.3389/fncel.2013.00225 (2013).

- 33 Mohammed, Z. A., Doran, C., Grundy, D. & Nassar, M. A. Veratridine produces distinct calcium response profiles in mouse Dorsal Root Ganglia neurons. *Scientific Reports* **7**, 45221, doi:10.1038/srep45221 (2017).
- 34 Chiu, I. M. *et al.* Transcriptional profiling at whole population and single cell levels reveals somatosensory neuron molecular diversity. *eLife* **3**, doi:10.7554/eLife.04660 (2014).
- 35 Xiao, H. S. *et al.* Identification of gene expression profile of dorsal root ganglion in the rat peripheral axotomy model of neuropathic pain. *Proceedings of the National Academy of Sciences of the United States of America* **99**, 8360-8365, doi:10.1073/pnas.122231899 (2002).
- 36 Manteniotis, S. *et al.* Comprehensive RNA-Seq expression analysis of sensory ganglia with a focus on ion channels and GPCRs in Trigeminal ganglia. *PLoS one* **8**, e79523, doi:10.1371/journal.pone.0079523 (2013).
- 37 Goswami, S. C. *et al.* Molecular signatures of mouse TRPV1-lineage neurons revealed by RNA-Seq transcriptome analysis. *The journal of pain : official journal of the American Pain Society* **15**, 1338-1359, doi:10.1016/j.jpain.2014.09.010 (2014).
- 38 Thakur, M. *et al.* Defining the nociceptor transcriptome. *Frontiers in molecular neuroscience* **7**, 87, doi:10.3389/fnmol.2014.00087 (2014).
- 39 Usoskin, D. *et al.* Unbiased classification of sensory neuron types by large-scale single-cell RNA sequencing. **18**, 145-153, doi:10.1038/nn.3881 (2015).
- 40 Li, C. L. *et al.* Somatosensory neuron types identified by high-coverage single-cell RNA-sequencing and functional heterogeneity. *Cell research* **26**, 83-102, doi:10.1038/cr.2015.149 (2016).
- 41 Stahl, W. L. & Harris, W. E. Na⁺,K⁺-ATPase: structure, function, and interactions with drugs. *Advances in neurology* **44**, 681-693 (1986).
- 42 Dib-Hajj, S. D., Cummins, T. R., Black, J. A. & Waxman, S. G. Sodium channels in normal and pathological pain. *Annual review of neuroscience* **33**, 325-347, doi:10.1146/annurev-neuro-060909-153234 (2010).
- 43 Black, J. A., Frezel, N., Dib-Hajj, S. D. & Waxman, S. G. Expression of Nav1.7 in DRG neurons extends from peripheral terminals in the skin to central preterminal branches and terminals in the dorsal horn. *Molecular pain* **8**, 82, doi:10.1186/1744-8069-8-82 (2012).
- 44 Weiss, J. *et al.* Loss-of-function mutations in sodium channel Nav1.7 cause anosmia. *Nature* **472**, 186-190, doi:10.1038/nature09975 (2011).
- 45 Goldin, A. L. *et al.* Messenger RNA coding for only the alpha subunit of the rat brain Na channel is sufficient for expression of functional channels in *Xenopus* oocytes. *Proceedings of the National Academy of Sciences of the United States of America* **83**, 7503-7507 (1986).
- 46 Brackenbury, W. J. & Isom, L. L. Na⁽⁺⁾ Channel β Subunits: Overachievers of the Ion Channel Family. *Frontiers in pharmacology* **2**, 53, doi:10.3389/fphar.2011.00053 (2011).
- 47 Catterall, W. A. From ionic currents to molecular mechanisms: the structure and function of voltage-gated sodium channels. *Neuron* **26**, 13-25 (2000).
- 48 Noda, M. *et al.* Primary structure of *Electrophorus electricus* sodium channel deduced from cDNA sequence. *Nature* **312**, 121-127 (1984).
- 49 Hartshorne, R. P., Messner, D. J., Coppersmith, J. C. & Catterall, W. A. The saxitoxin receptor of the sodium channel from rat brain. Evidence for two nonidentical beta subunits. *The Journal of biological chemistry* **257**, 13888-13891 (1982).

- 50 McCormick, K. A. *et al.* Molecular determinants of Na⁺ channel function in the extracellular domain of the beta1 subunit. *The Journal of biological chemistry* **273**, 3954-3962 (1998).
- 51 Yu, F. H. *et al.* Sodium Channel β 4, a New Disulfide-Linked Auxiliary Subunit with Similarity to β 2. *The Journal of Neuroscience* **23**, 7577-7585 (2003).
- 52 Messner, D. J. & Catterall, W. A. The sodium channel from rat brain. Separation and characterization of subunits. *The Journal of biological chemistry* **260**, 10597-10604 (1985).
- 53 Shah, B. S. *et al.* beta3, a novel auxiliary subunit for the voltage-gated sodium channel, is expressed preferentially in sensory neurons and is upregulated in the chronic constriction injury model of neuropathic pain. *The European journal of neuroscience* **12**, 3985-3990 (2000).
- 54 Coward, K. *et al.* Sodium channel beta1 and beta2 subunits parallel SNS/PN3 alpha-subunit changes in injured human sensory neurons. *Neuroreport* **12**, 483-488 (2001).
- 55 Lopez-Santiago, L. F. *et al.* Sodium Channel β 2 Subunits Regulate Tetrodotoxin-Sensitive Sodium Channels in Small Dorsal Root Ganglion Neurons and Modulate the Response to Pain. *The Journal of Neuroscience* **26**, 7984-7994, doi:10.1523/jneurosci.2211-06.2006 (2006).
- 56 Lopez-Santiago, L. F., Brackenbury, W. J., Chen, C. & Isom, L. L. Na⁺ channel Scn1b gene regulates dorsal root ganglion nociceptor excitability in vivo. *The Journal of biological chemistry* **286**, 22913-22923, doi:10.1074/jbc.M111.242370 (2011).
- 57 Pertin, M. *et al.* Upregulation of the Voltage-Gated Sodium Channel β 2 Subunit in Neuropathic Pain Models: Characterization of Expression in Injured and Non-Injured Primary Sensory Neurons. *The Journal of Neuroscience* **25**, 10970-10980, doi:10.1523/jneurosci.3066-05.2005 (2005).
- 58 Catterall, W. A. Voltage-dependent gating of sodium channels: correlating structure and function. *Trends in Neurosciences* **9**, 7-10 (1986).
- 59 Guy, H. R. & Seetharamulu, P. Molecular model of the action potential sodium channel. *Proceedings of the National Academy of Sciences of the United States of America* **83**, 508-512 (1986).
- 60 Goldin, A. L. Resurgence of sodium channel research. *Annual review of physiology* **63**, 871-894, doi:10.1146/annurev.physiol.63.1.871 (2001).
- 61 Akopian, A. N., Sivilotti, L. & Wood, J. N. A tetrodotoxin-resistant voltage-gated sodium channel expressed by sensory neurons. *Nature* **379**, 257-262, doi:10.1038/379257a0 (1996).
- 62 Souslova, V. A., Fox, M., Wood, J. N. & Akopian, A. N. Cloning and characterization of a mouse sensory neuron tetrodotoxin-resistant voltage-gated sodium channel gene, Scn10a. *Genomics* **41**, 201-209, doi:10.1006/geno.1997.4669 (1997).
- 63 Dib-Hajj, S. D., Tyrrell, L., Black, J. A. & Waxman, S. G. NaN, a novel voltage-gated Na channel, is expressed preferentially in peripheral sensory neurons and down-regulated after axotomy. *Proceedings of the National Academy of Sciences of the United States of America* **95**, 8963-8968 (1998).
- 64 Dib-Hajj, S., Black, J. A., Cummins, T. R. & Waxman, S. G. NaN/Nav1.9: a sodium channel with unique properties. *Trends Neurosci* **25**, 253-259 (2002).
- 65 Fang, X. *et al.* The presence and role of the tetrodotoxin-resistant sodium channel Na(v)1.9 (NaN) in nociceptive primary afferent neurons. *The Journal*

- of neuroscience : the official journal of the Society for Neuroscience* **22**, 7425-7433 (2002).
- 66 Fang, X. *et al.* Intense isolectin-B4 binding in rat dorsal root ganglion neurons distinguishes C-fiber nociceptors with broad action potentials and high Nav1.9 expression. *The Journal of neuroscience : the official journal of the Society for Neuroscience* **26**, 7281-7292, doi:10.1523/jneurosci.1072-06.2006 (2006).
- 67 Waxman, S. G., Kocsis, J. D. & Black, J. A. Type III sodium channel mRNA is expressed in embryonic but not adult spinal sensory neurons, and is reexpressed following axotomy. *J Neurophysiol* **72**, 466-470 (1994).
- 68 Beckh, S., Noda, M., Lübbert, H. & Numa, S. Differential regulation of three sodium channel messenger RNAs in the rat central nervous system during development. *The EMBO journal* **8**, 3611-3616 (1989).
- 69 Schaller, K. L., Krzemien, D. M., Yarowsky, P. J., Krueger, B. K. & Caldwell, J. H. A novel, abundant sodium channel expressed in neurons and glia. *The Journal of neuroscience : the official journal of the Society for Neuroscience* **15**, 3231-3242 (1995).
- 70 Beckh, S. Differential expression of sodium channel mRNAs in rat peripheral nervous system and innervated tissues. *FEBS Lett* **262**, 317-322 (1990).
- 71 Crill, W. E. Persistent sodium current in mammalian central neurons. *Annual review of physiology* **58**, 349-362, doi:10.1146/annurev.ph.58.030196.002025 (1996).
- 72 Kostyuk, P. G., Veselovsky, N. S. & Tsyndrenko, A. Y. Ionic currents in the somatic membrane of rat dorsal root ganglion neurons-I. Sodium currents. *Neuroscience* **6**, 2423-2430 (1981).
- 73 Dib-Hajj, S. D. *et al.* Two tetrodotoxin-resistant sodium channels in human dorsal root ganglion neurons. *FEBS Lett* **462**, 117-120 (1999).
- 74 Sangameswaran, L. *et al.* A novel tetrodotoxin-sensitive, voltage-gated sodium channel expressed in rat and human dorsal root ganglia. *The Journal of biological chemistry* **272**, 14805-14809 (1997).
- 75 Zhang, X., Priest, B. T., Belfer, I. & Gold, M. S. Voltage-gated Na⁺ currents in human dorsal root ganglion neurons. *eLife* **6**, doi:10.7554/eLife.23235 (2017).
- 76 Cummins, T. R., Howe, J. R. & Waxman, S. G. Slow Closed-State Inactivation: A Novel Mechanism Underlying Ramp Currents in Cells Expressing the hNE/PN1 Sodium Channel. *The Journal of Neuroscience* **18**, 9607-9619 (1998).
- 77 Herzog, R. I., Cummins, T. R., Ghassemi, F., Dib-Hajj, S. D. & Waxman, S. G. Distinct repriming and closed-state inactivation kinetics of Nav1.6 and Nav1.7 sodium channels in mouse spinal sensory neurons. *J Physiol* **551**, 741-750, doi:10.1113/jphysiol.2003.047357 (2003).
- 78 Cummins, T. R., Sheets, P. L. & Waxman, S. G. The roles of sodium channels in nociception: Implications for mechanisms of pain. *PAIN* **131**, 243-257, doi:<http://dx.doi.org/10.1016/j.pain.2007.07.026> (2007).
- 79 Cummins, T. R. *et al.* A novel persistent tetrodotoxin-resistant sodium current in SNS-null and wild-type small primary sensory neurons. *The Journal of neuroscience : the official journal of the Society for Neuroscience* **19**, Rc43 (1999).
- 80 Sangameswaran, L. *et al.* Structure and function of a novel voltage-gated, tetrodotoxin-resistant sodium channel specific to sensory neurons. *The Journal of biological chemistry* **271**, 5953-5956 (1996).

- 81 Han, C. *et al.* Sporadic onset of erythralgia: a gain-of-function mutation in Nav1.7. *Annals of neurology* **59**, 553-558, doi:10.1002/ana.20776 (2006).
- 82 Renganathan, M., Cummins, T. R. & Waxman, S. G. Contribution of Na(v)1.8 sodium channels to action potential electrogenesis in DRG neurons. *J Neurophysiol* **86**, 629-640 (2001).
- 83 Toledo-Aral, J. J. *et al.* Identification of PN1, a predominant voltage-dependent sodium channel expressed principally in peripheral neurons. *Proceedings of the National Academy of Sciences of the United States of America* **94**, 1527-1532 (1997).
- 84 Djouhri, L. *et al.* Sensory and electrophysiological properties of guinea-pig sensory neurones expressing Na(v) 1.7 (PN1) Na(+) channel α subunit protein. *The Journal of Physiology* **546**, 565-576, doi:10.1113/jphysiol.2002.026559 (2003).
- 85 Ahmad, S. *et al.* A stop codon mutation in SCN9A causes lack of pain sensation. *Human molecular genetics* **16**, 2114-2121, doi:10.1093/hmg/ddm160 (2007).
- 86 Morinville, A. *et al.* Distribution of the voltage-gated sodium channel Na(v)1.7 in the rat: expression in the autonomic and endocrine systems. *J Comp Neurol* **504**, 680-689, doi:10.1002/cne.21484 (2007).
- 87 Pinto, F. M. *et al.* Molecular and functional characterization of voltage-gated sodium channels in human sperm. *Reproductive biology and endocrinology : RB&E* **7**, 71, doi:10.1186/1477-7827-7-71 (2009).
- 88 Rice, F. L. *et al.* Sodium channel Nav1.7 in vascular myocytes, endothelium, and innervating axons in human skin. *Molecular pain* **11**, 26, doi:10.1186/s12990-015-0024-3 (2015).
- 89 Zhang, Q. *et al.* Na⁺ current properties in islet alpha- and beta-cells reflect cell-specific Scn3a and Scn9a expression. *J Physiol* **592**, 4677-4696, doi:10.1113/jphysiol.2014.274209 (2014).
- 90 Cox, J. J. *et al.* An SCN9A channelopathy causes congenital inability to experience pain. *Nature* **444**, 894-898, doi:10.1038/nature05413 (2006).
- 91 Goldberg, Y. P. *et al.* Loss-of-function mutations in the Nav1.7 gene underlie congenital indifference to pain in multiple human populations. *Clinical genetics* **71**, 311-319, doi:10.1111/j.1399-0004.2007.00790.x (2007).
- 92 Nilsen, K. B. *et al.* Two novel SCN9A mutations causing insensitivity to pain. *Pain* **143**, 155-158, doi:10.1016/j.pain.2009.02.016 (2009).
- 93 Cox, J. J. *et al.* Congenital insensitivity to pain: novel SCN9A missense and in-frame deletion mutations. *Human mutation* **31**, E1670-1686, doi:10.1002/humu.21325 (2010).
- 94 Emery, E. C. *et al.* Novel SCN9A Mutations Underlying Extreme Pain Phenotypes: Unexpected Electrophysiological and Clinical Phenotype Correlations. *The Journal of Neuroscience* **35**, 7674-7681, doi:10.1523/JNEUROSCI.3935-14.2015 (2015).
- 95 Minett, M. S. *et al.* Endogenous opioids contribute to insensitivity to pain in humans and mice lacking sodium channel Nav1.7. *Nature communications* **6**, 8967, doi:10.1038/ncomms9967 (2015).
- 96 Yang, Y. *et al.* Mutations in SCN9A, encoding a sodium channel alpha subunit, in patients with primary erythralgia. *Journal of medical genetics* **41**, 171-174 (2004).

- 97 McDonnell, A. *et al.* Inherited erythromelalgia due to mutations in SCN9A: natural history, clinical phenotype and somatosensory profile. *Brain* **139**, 1052-1065, doi:10.1093/brain/aww007 (2016).
- 98 Cummins, T. R., Dib-Hajj, S. D. & Waxman, S. G. Electrophysiological properties of mutant Nav1.7 sodium channels in a painful inherited neuropathy. *The Journal of neuroscience : the official journal of the Society for Neuroscience* **24**, 8232-8236, doi:10.1523/jneurosci.2695-04.2004 (2004).
- 99 Dib-Hajj, S. D. *et al.* Gain-of-function mutation in Nav1.7 in familial erythromelalgia induces bursting of sensory neurons. *Brain* **128**, 1847-1854, doi:10.1093/brain/awh514 (2005).
- 100 Fertleman, C. R. *et al.* SCN9A mutations in paroxysmal extreme pain disorder: allelic variants underlie distinct channel defects and phenotypes. *Neuron* **52**, 767-774, doi:10.1016/j.neuron.2006.10.006 (2006).
- 101 Dib-Hajj, S. D., Yang, Y. & Waxman, S. G. Genetics and molecular pathophysiology of Na(v)1.7-related pain syndromes. *Advances in genetics* **63**, 85-110, doi:10.1016/s0065-2660(08)01004-3 (2008).
- 102 Hoeijmakers, J. G., Faber, C. G., Lauria, G., Merkies, I. S. & Waxman, S. G. Small-fibre neuropathies--advances in diagnosis, pathophysiology and management. *Nature reviews. Neurology* **8**, 369-379, doi:10.1038/nrneurol.2012.97 (2012).
- 103 Holland, N. R. *et al.* Small-fiber sensory neuropathies: clinical course and neuropathology of idiopathic cases. *Annals of neurology* **44**, 47-59, doi:10.1002/ana.410440111 (1998).
- 104 McManis, P. G., Windebank, A. J. & Kiziltan, M. Neuropathy associated with hyperlipidemia. *Neurology* **44**, 2185-2186 (1994).
- 105 Magri, F. *et al.* Intraepidermal nerve fiber density reduction as a marker of preclinical asymptomatic small-fiber sensory neuropathy in hypothyroid patients. *European journal of endocrinology* **163**, 279-284, doi:10.1530/eje-10-0285 (2010).
- 106 Hoitsma, E. *et al.* Small fibre neuropathy in sarcoidosis. *Lancet (London, England)* **359**, 2085-2086 (2002).
- 107 Gondim, F. A., Brannagan, T. H., 3rd, Sander, H. W., Chin, R. L. & Latov, N. Peripheral neuropathy in patients with inflammatory bowel disease. *Brain* **128**, 867-879, doi:10.1093/brain/awh429 (2005).
- 108 Polydefkis, M. *et al.* Reduced intraepidermal nerve fiber density in HIV-associated sensory neuropathy. *Neurology* **58**, 115-119 (2002).
- 109 Tembl, J. I. *et al.* Neurologic complications associated with hepatitis C virus infection. *Neurology* **53**, 861-864 (1999).
- 110 Faber, C. G. *et al.* Gain of function Nav1.7 mutations in idiopathic small fiber neuropathy. *Annals of neurology* **71**, 26-39, doi:10.1002/ana.22485 (2012).
- 111 Attal, N. *et al.* EFNS guidelines on the pharmacological treatment of neuropathic pain: 2010 revision. *European journal of neurology* **17**, 1113-e1188, doi:10.1111/j.1468-1331.2010.02999.x (2010).
- 112 Nassar, M. A. *et al.* Nociceptor-specific gene deletion reveals a major role for Nav1.7 (PN1) in acute and inflammatory pain. *Proceedings of the National Academy of Sciences of the United States of America* **101**, 12706-12711, doi:10.1073/pnas.0404915101 (2004).
- 113 Minett, M. S. *et al.* Distinct Nav1.7-dependent pain sensations require different sets of sensory and sympathetic neurons. *Nature communications* **3**, 791, doi:10.1038/ncomms1795 (2012).

- 114 Ahn, H. S. *et al.* Nav1.7 is the predominant sodium channel in rodent olfactory sensory neurons. *Molecular pain* **7**, 32, doi:10.1186/1744-8069-7-32 (2011).
- 115 Gingras, J. *et al.* Global Nav1.7 knockout mice recapitulate the phenotype of human congenital indifference to pain. *PloS one* **9**, e105895, doi:10.1371/journal.pone.0105895 (2014).
- 116 Akopian, A. N. *et al.* The tetrodotoxin-resistant sodium channel SNS has a specialized function in pain pathways. *Nature neuroscience* **2**, 541-548, doi:10.1038/9195 (1999).
- 117 Nassar, M. A. *et al.* Nerve injury induces robust allodynia and ectopic discharges in Nav1.3 null mutant mice. *Molecular pain* **2**, 33, doi:10.1186/1744-8069-2-33 (2006).
- 118 Amaya, F. *et al.* The voltage-gated sodium channel Na(v)1.9 is an effector of peripheral inflammatory pain hypersensitivity. *The Journal of neuroscience : the official journal of the Society for Neuroscience* **26**, 12852-12860, doi:10.1523/jneurosci.4015-06.2006 (2006).
- 119 Ji, R. R., Baba, H., Brenner, G. J. & Woolf, C. J. Nociceptive-specific activation of ERK in spinal neurons contributes to pain hypersensitivity. *Nature neuroscience* **2**, 1114-1119, doi:10.1038/16040 (1999).
- 120 Dai, Y. *et al.* Phosphorylation of extracellular signal-regulated kinase in primary afferent neurons by noxious stimuli and its involvement in peripheral sensitization. *The Journal of neuroscience : the official journal of the Society for Neuroscience* **22**, 7737-7745 (2002).
- 121 Obata, K. & Noguchi, K. MAPK activation in nociceptive neurons and pain hypersensitivity. *Life sciences* **74**, 2643-2653, doi:10.1016/j.lfs.2004.01.007 (2004).
- 122 Stamboulian, S. *et al.* ERK1/2 mitogen-activated protein kinase phosphorylates sodium channel Na(v)1.7 and alters its gating properties. *The Journal of neuroscience : the official journal of the Society for Neuroscience* **30**, 1637-1647, doi:10.1523/jneurosci.4872-09.2010 (2010).
- 123 Li, G. D. *et al.* Expression of fibroblast growth factors in rat dorsal root ganglion neurons and regulation after peripheral nerve injury. *Neuroreport* **13**, 1903-1907 (2002).
- 124 Yang, L. *et al.* FGF13 Selectively Regulates Heat Nociception by Interacting with Nav1.7. *Neuron* **93**, 806-821.e809, doi:10.1016/j.neuron.2017.01.009 (2017).
- 125 Fotia, A. B. *et al.* Regulation of neuronal voltage-gated sodium channels by the ubiquitin-protein ligases Nedd4 and Nedd4-2. *The Journal of biological chemistry* **279**, 28930-28935, doi:10.1074/jbc.M402820200 (2004).
- 126 Laedermann, C. J. *et al.* Dysregulation of voltage-gated sodium channels by ubiquitin ligase NEDD4-2 in neuropathic pain. *The Journal of clinical investigation*, doi:10.1172/JCI68996 (2013).
- 127 Schmidt, J., Rossie, S. & Catterall, W. A. A large intracellular pool of inactive Na channel alpha subunits in developing rat brain. *Proceedings of the National Academy of Sciences of the United States of America* **82**, 4847-4851 (1985).
- 128 Laedermann, C. J., Syam, N., Pertin, M., Decosterd, I. & Abriel, H. beta1- and beta3- voltage-gated sodium channel subunits modulate cell surface expression and glycosylation of Nav1.7 in HEK293 cells. *Front Cell Neurosci* **7**, 137, doi:10.3389/fncel.2013.00137 (2013).

- 129 Bennett, E., Urcan, M. S., Tinkle, S. S., Koszowski, A. G. & Levinson, S. R. Contribution of sialic acid to the voltage dependence of sodium channel gating. A possible electrostatic mechanism. *The Journal of general physiology* **109**, 327-343 (1997).
- 130 Zhang, Y., Hartmann, H. A. & Satin, J. Glycosylation influences voltage-dependent gating of cardiac and skeletal muscle sodium channels. *The Journal of membrane biology* **171**, 195-207 (1999).
- 131 Tyrrell, L., Renganathan, M., Dib-Hajj, S. D. & Waxman, S. G. Glycosylation alters steady-state inactivation of sodium channel Nav1.9/NaN in dorsal root ganglion neurons and is developmentally regulated. *The Journal of neuroscience : the official journal of the Society for Neuroscience* **21**, 9629-9637 (2001).
- 132 Nogales, E., Wolf, S. G. & Downing, K. H. Structure of the alpha beta tubulin dimer by electron crystallography. *Nature* **391**, 199-203, doi:10.1038/34465 (1998).
- 133 Lowe, J., Li, H., Downing, K. H. & Nogales, E. Refined structure of alpha beta-tubulin at 3.5 Å resolution. *Journal of molecular biology* **313**, 1045-1057, doi:10.1006/jmbi.2001.5077 (2001).
- 134 Akhmanova, A. & Steinmetz, M. O. Tracking the ends: a dynamic protein network controls the fate of microtubule tips. *Nature reviews. Molecular cell biology* **9**, 309-322, doi:10.1038/nrm2369 (2008).
- 135 Akhmanova, A. & Hoogenraad, C. C. Microtubule minus-end-targeting proteins. *Current biology : CB* **25**, R162-171, doi:10.1016/j.cub.2014.12.027 (2015).
- 136 Howard, J. & Hyman, A. A. Growth, fluctuation and switching at microtubule plus ends. *Nature reviews. Molecular cell biology* **10**, 569-574, doi:10.1038/nrm2713 (2009).
- 137 Kapitein, L. C. & Hoogenraad, C. C. Building the Neuronal Microtubule Cytoskeleton. *Neuron* **87**, 492-506, doi:10.1016/j.neuron.2015.05.046 (2015).
- 138 Kollman, J. M., Merdes, A., Mourey, L. & Agard, D. A. Microtubule nucleation by gamma-tubulin complexes. *Nature reviews. Molecular cell biology* **12**, 709-721, doi:10.1038/nrm3209 (2011).
- 139 Erickson, H. P. Gamma-tubulin nucleation: template or protofilament? *Nature cell biology* **2**, E93-96, doi:10.1038/35014084 (2000).
- 140 Burton, P. R. & Paige, J. L. Polarity of axoplasmic microtubules in the olfactory nerve of the frog. *Proceedings of the National Academy of Sciences of the United States of America* **78**, 3269-3273 (1981).
- 141 Stepanova, T. *et al.* Visualization of microtubule growth in cultured neurons via the use of EB3-GFP (end-binding protein 3-green fluorescent protein). *The Journal of neuroscience : the official journal of the Society for Neuroscience* **23**, 2655-2664 (2003).
- 142 Binder, L. I., Frankfurter, A. & Rebhun, L. I. The distribution of tau in the mammalian central nervous system. *The Journal of cell biology* **101**, 1371-1378 (1985).
- 143 Schoenfeld, T. A., McKerracher, L., Obar, R. & Vallee, R. B. MAP 1A and MAP 1B are structurally related microtubule associated proteins with distinct developmental patterns in the CNS. *The Journal of neuroscience : the official journal of the Society for Neuroscience* **9**, 1712-1730 (1989).
- 144 Ludueña, R. F. Are tubulin isotypes functionally significant. *Molecular Biology of the Cell* **4**, 445-457 (1993).

- 145 Sullivan, K. F. Structure and utilization of tubulin isotypes. *Annual review of cell biology* **4**, 687-716, doi:10.1146/annurev.cb.04.110188.003351 (1988).
- 146 Denoulet, P., Edde, B. & Gros, F. Differential expression of several neurospecific beta-tubulin mRNAs in the mouse brain during development. *Gene* **50**, 289-297 (1986).
- 147 Joshi, H. C. & Cleveland, D. W. Differential utilization of beta-tubulin isotypes in differentiating neurites. *The Journal of cell biology* **109**, 663-673 (1989).
- 148 Renthall, R., Schneider, B. G., Miller, M. M. & Luduena, R. F. Beta IV is the major beta-tubulin isotype in bovine cilia. *Cell Motil Cytoskeleton* **25**, 19-29, doi:10.1002/cm.970250104 (1993).
- 149 Raff, E. C., Hoyle, H. D., Popodi, E. M. & Turner, F. R. Axoneme beta-tubulin sequence determines attachment of outer dynein arms. *Current biology : CB* **18**, 911-914, doi:10.1016/j.cub.2008.05.031 (2008).
- 150 Keays, D. A. *et al.* Mutations in alpha-tubulin cause abnormal neuronal migration in mice and lissencephaly in humans. *Cell* **128**, 45-57, doi:10.1016/j.cell.2006.12.017 (2007).
- 151 Fallet-Bianco, C. *et al.* Neuropathological phenotype of a distinct form of lissencephaly associated with mutations in TUBA1A. *Brain* **131**, 2304-2320, doi:10.1093/brain/awn155 (2008).
- 152 Tischfield, M. A. *et al.* Human TUBB3 mutations perturb microtubule dynamics, kinesin interactions, and axon guidance. *Cell* **140**, 74-87, doi:10.1016/j.cell.2009.12.011 (2010).
- 153 Cederquist, G. Y. *et al.* An inherited TUBB2B mutation alters a kinesin-binding site and causes polymicrogyria, CFEOM and axon dysinnervation. *Human molecular genetics* **21**, 5484-5499, doi:10.1093/hmg/ddc393 (2012).
- 154 Niwa, S., Takahashi, H. & Hirokawa, N. beta-Tubulin mutations that cause severe neuropathies disrupt axonal transport. *The EMBO journal* **32**, 1352-1364, doi:10.1038/emboj.2013.59 (2013).
- 155 Janmey, P. A. The cytoskeleton and cell signaling: component localization and mechanical coupling. *Physiological reviews* **78**, 763-781 (1998).
- 156 Lange, K. & Brandt, U. Calcium storage and release properties of F-actin: evidence for the involvement of F-actin in cellular calcium signaling. *FEBS Lett* **395**, 137-142 (1996).
- 157 Kolodney, M. S. & Elson, E. L. Contraction due to microtubule disruption is associated with increased phosphorylation of myosin regulatory light chain. *Proceedings of the National Academy of Sciences of the United States of America* **92**, 10252-10256 (1995).
- 158 Lai, H. C. & Jan, L. Y. The distribution and targeting of neuronal voltage-gated ion channels. *Nat Rev Neurosci* **7**, 548-562, doi:10.1038/nrn1938 (2006).
- 159 Sampson, L. J., Leyland, M. L. & Dart, C. Direct interaction between the actin-binding protein filamin-A and the inwardly rectifying potassium channel, Kir2.1. *The Journal of biological chemistry* **278**, 41988-41997, doi:10.1074/jbc.M307479200 (2003).
- 160 Petrecca, K., Miller, D. M. & Shrier, A. Localization and enhanced current density of the Kv4.2 potassium channel by interaction with the actin-binding protein filamin. *The Journal of neuroscience : the official journal of the Society for Neuroscience* **20**, 8736-8744 (2000).
- 161 Galli, A. & DeFelice, L. J. Inactivation of L-type Ca channels in embryonic chick ventricle cells: dependence on the cytoskeletal agents colchicine and

- taxol. *Biophysical journal* **67**, 2296-2304, doi:10.1016/s0006-3495(94)80715-5 (1994).
- 162 Dehmelt, L. & Halpain, S. Actin and microtubules in neurite initiation: are MAPs the missing link? *Journal of neurobiology* **58**, 18-33, doi:10.1002/neu.10284 (2004).
- 163 Roll-Mecak, A. & McNally, F. J. Microtubule-severing enzymes. *Curr Opin Cell Biol* **22**, 96-103, doi:10.1016/j.ceb.2009.11.001 (2010).
- 164 Mao, C. X. *et al.* Microtubule-severing protein Katanin regulates neuromuscular junction development and dendritic elaboration in *Drosophila*. *Development (Cambridge, England)* **141**, 1064-1074, doi:10.1242/dev.097774 (2014).
- 165 Stone, M. C. *et al.* Normal spastin gene dosage is specifically required for axon regeneration. *Cell reports* **2**, 1340-1350, doi:10.1016/j.celrep.2012.09.032 (2012).
- 166 Hirokawa, N., Niwa, S. & Tanaka, Y. Molecular motors in neurons: transport mechanisms and roles in brain function, development, and disease. *Neuron* **68**, 610-638, doi:10.1016/j.neuron.2010.09.039 (2010).
- 167 Janke, C. The tubulin code: molecular components, readout mechanisms, and functions. *The Journal of cell biology* **206**, 461-472, doi:10.1083/jcb.201406055 (2014).
- 168 Hammond, J. W., Cai, D. & Verhey, K. J. Tubulin modifications and their cellular functions. *Curr Opin Cell Biol* **20**, 71-76, doi:10.1016/j.ceb.2007.11.010 (2008).
- 169 Dehmelt, L. & Halpain, S. The MAP2/Tau family of microtubule-associated proteins. *Genome biology* **6**, 204, doi:10.1186/gb-2004-6-1-204 (2005).
- 170 Chien, C. L., Lu, K. S., Lin, Y. S., Hsieh, C. J. & Hirokawa, N. The functional cooperation of MAP1A heavy chain and light chain 2 in the binding of microtubules. *Experimental cell research* **308**, 446-458, doi:10.1016/j.yexcr.2005.05.007 (2005).
- 171 Bloom, G. S., Schoenfeld, T. A. & Vallee, R. B. Widespread distribution of the major polypeptide component of MAP 1 (microtubule-associated protein 1) in the nervous system. *The Journal of cell biology* **98**, 320-330 (1984).
- 172 Bernhardt, R. & Matus, A. Light and electron microscopic studies of the distribution of microtubule-associated protein 2 in rat brain: a difference between dendritic and axonal cytoskeletons. *J Comp Neurol* **226**, 203-221, doi:10.1002/cne.902260205 (1984).
- 173 Huber, G., Alaimo-Beuret, D. & Matus, A. MAP3: characterization of a novel microtubule-associated protein. *The Journal of cell biology* **100**, 496-507 (1985).
- 174 Parysek, L. M., Wolosewick, J. J. & Olmsted, J. B. MAP 4: a microtubule-associated protein specific for a subset of tissue microtubules. *The Journal of cell biology* **99**, 2287-2296 (1984).
- 175 Vallee, R. B. & Davis, S. E. Low molecular weight microtubule-associated proteins are light chains of microtubule-associated protein 1 (MAP 1). *Proceedings of the National Academy of Sciences of the United States of America* **80**, 1342-1346 (1983).
- 176 Papasozomenos, S. C. & Binder, L. I. Phosphorylation determines two distinct species of Tau in the central nervous system. *Cell Motil Cytoskeleton* **8**, 210-226, doi:10.1002/cm.970080303 (1987).

- 177 Hampel, H. *et al.* Total and phosphorylated tau protein as biological markers of Alzheimer's disease. *Experimental Gerontology* **45**, 30-40, doi:<http://dx.doi.org/10.1016/j.exger.2009.10.010> (2010).
- 178 Diaz-Nido, J., Serrano, L., Mendez, E. & Avila, J. A casein kinase II-related activity is involved in phosphorylation of microtubule-associated protein MAP-1B during neuroblastoma cell differentiation. *The Journal of cell biology* **106**, 2057-2065 (1988).
- 179 Pedrotti, B. & Islam, K. Dephosphorylated but not phosphorylated microtubule associated protein MAP1B binds to microfilaments. *FEBS Lett* **388**, 131-133 (1996).
- 180 Sattilaro, R. F. Interaction of microtubule-associated protein 2 with actin filaments. *Biochemistry* **25**, 2003-2009 (1986).
- 181 Riederer, B. & Matus, A. Differential expression of distinct microtubule-associated proteins during brain development. *Proceedings of the National Academy of Sciences of the United States of America* **82**, 6006-6009 (1985).
- 182 Bloom, G. S., Luca, F. C. & Vallee, R. B. Microtubule-associated protein 1B: identification of a major component of the neuronal cytoskeleton. *Proceedings of the National Academy of Sciences of the United States of America* **82**, 5404-5408 (1985).
- 183 Ma, D., Nothias, F., Boyne, L. J. & Fischer, I. Differential regulation of microtubule-associated protein 1B (MAP1B) in rat CNS and PNS during development. *Journal of neuroscience research* **49**, 319-332 (1997).
- 184 Bouquet, C. *et al.* Microtubule-Associated Protein 1B Controls Directionality of Growth Cone Migration and Axonal Branching in Regeneration of Adult Dorsal Root Ganglia Neurons. *The Journal of Neuroscience* **24**, 7204-7213, doi:10.1523/jneurosci.2254-04.2004 (2004).
- 185 Meixner, A. *et al.* MAP1B is required for axon guidance and is involved in the development of the central and peripheral nervous system. *The Journal of cell biology* **151**, 1169-1178 (2000).
- 186 Langkopf, A., Hammarback, J. A., Muller, R., Vallee, R. B. & Garner, C. C. Microtubule-associated proteins 1A and LC2. Two proteins encoded in one messenger RNA. *J Biol Chem* **267**, 16561-16566 (1992).
- 187 Mei, X., Sweatt, A. J. & Hammarback, J. A. Regulation of microtubule-associated protein 1B (MAP1B) subunit composition. *Journal of neuroscience research* **62**, 56-64, doi:10.1002/1097-4547(20001001)62:1<56::AID-JNR6>3.0.CO;2-# (2000).
- 188 Hammarback, J. A., Obar, R. A., Hughes, S. M. & Vallee, R. B. MAP1B is encoded as a polyprotein that is processed to form a complex N-terminal microtubule-binding domain. *Neuron* **7**, 129-139 (1991).
- 189 Noiges, R. *et al.* Microtubule-associated protein 1A (MAP1A) and MAP1B: light chains determine distinct functional properties. *J Neurosci* **22**, 2106-2114 (2002).
- 190 Mann, S. S. & Hammarback, J. A. Molecular characterization of light chain 3. A microtubule binding subunit of MAP1A and MAP1B. *Journal of Biological Chemistry* **269**, 11492-11497 (1994).
- 191 Noble, M., Lewis, S. A. & Cowan, N. J. The microtubule binding domain of microtubule-associated protein MAP1B contains a repeated sequence motif unrelated to that of MAP2 and tau. *The Journal of cell biology* **109**, 3367-3376 (1989).

- 192 Chien, C.-L., Lu, K.-S., Lin, Y.-S., Hsieh, C.-J. & Hirokawa, N. The functional cooperation of MAP1A heavy chain and light chain 2 in the binding of microtubules. *Experimental cell research* **308**, 446-458, doi:<http://dx.doi.org/10.1016/j.yexcr.2005.05.007> (2005).
- 193 Vaillant, A. R., Muller, R., Langkopf, A. & Brown, D. L. Characterization of the microtubule-binding domain of microtubule-associated protein 1A and its effects on microtubule dynamics. *The Journal of biological chemistry* **273**, 13973-13981 (1998).
- 194 Takei, Y., Teng, J., Harada, A. & Hirokawa, N. Defects in axonal elongation and neuronal migration in mice with disrupted tau and map1b genes. *The Journal of cell biology* **150**, 989-1000 (2000).
- 195 DiTella, M. C., Feiguin, F., Carri, N., Kosik, K. S. & Caceres, A. MAP-1B/TAU functional redundancy during laminin-enhanced axonal growth. *Journal of cell science* **109 (Pt 2)**, 467-477 (1996).
- 196 Teng, J. *et al.* Synergistic effects of MAP2 and MAP1B knockout in neuronal migration, dendritic outgrowth, and microtubule organization. *The Journal of cell biology* **155**, 65-76, doi:10.1083/jcb.200106025 (2001).
- 197 Edelman, W. *et al.* Neuronal abnormalities in microtubule-associated protein 1B mutant mice. *Proceedings of the National Academy of Sciences of the United States of America* **93**, 1270-1275 (1996).
- 198 Takei, Y. *et al.* Delayed development of nervous system in mice homozygous for disrupted microtubule-associated protein 1B (MAP1B) gene. *The Journal of cell biology* **137**, 1615-1626 (1997).
- 199 Liu, Y., Lee, J. W. & Ackerman, S. L. Mutations in the microtubule-associated protein 1A (Map1a) gene cause Purkinje cell degeneration. *The Journal of neuroscience : the official journal of the Society for Neuroscience* **35**, 4587-4598, doi:10.1523/jneurosci.2757-14.2015 (2015).
- 200 Gamblin, T. C., Nachmanoff, K., Halpain, S. & Williams, R. C., Jr. Recombinant microtubule-associated protein 2c reduces the dynamic instability of individual microtubules. *Biochemistry* **35**, 12576-12586, doi:10.1021/bi961135d (1996).
- 201 Sun, H. *et al.* Modulation of 5-HT₃ receptor desensitization by the light chain of microtubule-associated protein 1B expressed in HEK 293 cells. *J Physiol* **586**, 751-762, doi:10.1113/jphysiol.2007.136440 (2008).
- 202 O'Brien, J. E. *et al.* Interaction of Voltage-gated Sodium Channel Nav1.6 (SCN8A) with Microtubule-associated Protein Map1b. *Journal of Biological Chemistry* **287**, 18459-18466, doi:10.1074/jbc.M111.336024 (2012).
- 203 Eriksson, M. *et al.* MAP1B binds to the NMDA receptor subunit NR3A and affects NR3A protein concentrations. *Neuroscience letters* **475**, 33-37, doi:10.1016/j.neulet.2010.03.039 (2010).
- 204 Gandini, M. A. *et al.* CaV2.2 channel cell surface expression is regulated by the light chain 1 (LC1) of the microtubule-associated protein B (MAP1B) via UBE2L3-mediated ubiquitination and degradation. *Pflugers Archiv : European journal of physiology* **466**, 2113-2126, doi:10.1007/s00424-014-1476-4 (2014).
- 205 Gandini, M. A., Sandoval, A., Zamponi, G. W. & Felix, R. The MAP1B-LC1/UBE2L3 complex catalyzes degradation of cell surface CaV2.2 channels. *Channels (Austin, Tex.)* **8**, 452-457, doi:10.4161/19336950.2014.949162 (2014).

- 206 Maurer, M. H. *et al.* Cloning of a novel neuronally expressed orphan G-protein-coupled receptor which is up-regulated by erythropoietin, interacts with microtubule-associated protein 1b and colocalizes with the 5-hydroxytryptamine 2a receptor. *Journal of neurochemistry* **91**, 1007-1017, doi:10.1111/j.1471-4159.2004.02799.x (2004).
- 207 Piao, L., Ho, W. K. & Earm, Y. E. Actin filaments regulate the stretch sensitivity of large-conductance, Ca²⁺-activated K⁺ channels in coronary artery smooth muscle cells. *Pflugers Archiv : European journal of physiology* **446**, 523-528, doi:10.1007/s00424-003-1079-y (2003).
- 208 Park, S. M. *et al.* Direct interaction between BKCa potassium channel and microtubule-associated protein 1A. *FEBS Letters* **570**, 143-148, doi:<http://dx.doi.org/10.1016/j.febslet.2004.06.037> (2004).
- 209 Chen, L. *et al.* Stargazin regulates synaptic targeting of AMPA receptors by two distinct mechanisms. *Nature* **408**, 936-943, doi:10.1038/35050030 (2000).
- 210 Dakoji, S., Tomita, S., Karimzadegan, S., Nicoll, R. A. & Bredt, D. S. Interaction of transmembrane AMPA receptor regulatory proteins with multiple membrane associated guanylate kinases. *Neuropharmacology* **45**, 849-856 (2003).
- 211 Schnell, E. *et al.* Direct interactions between PSD-95 and stargazin control synaptic AMPA receptor number. *Proceedings of the National Academy of Sciences of the United States of America* **99**, 13902-13907, doi:10.1073/pnas.172511199 (2002).
- 212 Tomita, S. *et al.* Functional studies and distribution define a family of transmembrane AMPA receptor regulatory proteins. *The Journal of cell biology* **161**, 805-816, doi:10.1083/jcb.200212116 (2003).
- 213 Ives, J. H., Fung, S., Tiwari, P., Payne, H. L. & Thompson, C. L. Microtubule-associated protein light chain 2 is a stargazin-AMPA receptor complex-interacting protein in vivo. *The Journal of biological chemistry* **279**, 31002-31009, doi:10.1074/jbc.M402214200 (2004).
- 214 Brenman, J. E. *et al.* Localization of postsynaptic density-93 to dendritic microtubules and interaction with microtubule-associated protein 1A. *J Neurosci* **18**, 8805-8813 (1998).
- 215 Leenders, A. G. M. *et al.* The Role of MAP1A Light Chain 2 in Synaptic Surface Retention of CaV2.2 Channels in Hippocampal Neurons. *The Journal of Neuroscience* **28**, 11333-11346, doi:10.1523/jneurosci.3078-08.2008 (2008).
- 216 Tomblor, E. *et al.* G protein-induced trafficking of voltage-dependent calcium channels. *The Journal of biological chemistry* **286**, 21952-21952, doi:10.1074/jbc.A111.508829 (2011).
- 217 Tsien, R. Y. New calcium indicators and buffers with high selectivity against magnesium and protons: design, synthesis, and properties of prototype structures. *Biochemistry* **19**, 2396-2404 (1980).
- 218 Grynkiewicz, G., Poenie, M. & Tsien, R. Y. A new generation of Ca²⁺ indicators with greatly improved fluorescence properties. *The Journal of biological chemistry* **260**, 3440-3450 (1985).
- 219 Miyawaki, A. *et al.* Fluorescent indicators for Ca²⁺ based on green fluorescent proteins and calmodulin. *Nature* **388**, 882-887, doi:10.1038/42264 (1997).

- 220 Paredes, R. M., Etzler, J. C., Watts, L. T. & Lechleiter, J. D. Chemical Calcium Indicators. *Methods (San Diego, Calif.)* **46**, 143-151, doi:10.1016/j.ymeth.2008.09.025 (2008).
- 221 Akerboom, J. *et al.* Crystal structures of the GCaMP calcium sensor reveal the mechanism of fluorescence signal change and aid rational design. *The Journal of biological chemistry* **284**, 6455-6464, doi:10.1074/jbc.M807657200 (2009).
- 222 Yamada, Y. *et al.* Quantitative comparison of genetically encoded Ca indicators in cortical pyramidal cells and cerebellar Purkinje cells. *Frontiers in cellular neuroscience* **5**, 18, doi:10.3389/fncel.2011.00018 (2011).
- 223 Teichert, R. W., Schmidt, E. W. & Olivera, B. M. Constellation pharmacology: a new paradigm for drug discovery. *Annual review of pharmacology and toxicology* **55**, 573-589, doi:10.1146/annurev-pharmtox-010814-124551 (2015).
- 224 Imperial, J. S. *et al.* A family of excitatory peptide toxins from venomous crassispirine snails: using Constellation Pharmacology to assess bioactivity. *Toxicon : official journal of the International Society on Toxinology* **89**, 45-54, doi:10.1016/j.toxicon.2014.06.014 (2014).
- 225 Kim, A. Y. *et al.* Pirt, a Phosphoinositide-Binding Protein, Functions as a Regulatory Subunit of TRPV1. *Cell* **133**, 475-485, doi:10.1016/j.cell.2008.02.053 (2008).
- 226 Emery, E. C. *et al.* In vivo characterization of distinct modality-specific subsets of somatosensory neurons using GCaMP. *Science advances* **2**, e1600990, doi:10.1126/sciadv.1600990 (2016).
- 227 Kim, Y. S. *et al.* Coupled Activation of Primary Sensory Neurons Contributes to Chronic Pain. *Neuron*, doi:10.1016/j.neuron.2016.07.044 (2016).
- 228 Smith-Edwards, K. M., DeBerry, J. J., Saloman, J. L., Davis, B. M. & Woodbury, C. J. Profound alteration in cutaneous primary afferent activity produced by inflammatory mediators. *eLife* **5**, doi:10.7554/eLife.20527 (2016).
- 229 Chisholm, K. I., Khovanov, N., Lopes, D. M., La Russa, F. & McMahon, S. B. Large scale in vivo recording of sensory neuron activity with GCaMP6. *bioRxiv* (2017).
- 230 Cui, Z. J. Types of voltage-dependent calcium channels involved in high potassium depolarization-induced amylase secretion in the exocrine pancreatic tumour cell line AR4-2J. *Cell research* **8**, 23-31, doi:10.1038/cr.1998.3 (1998).
- 231 Pall, M. L. Electromagnetic fields act via activation of voltage-gated calcium channels to produce beneficial or adverse effects. *Journal of Cellular and Molecular Medicine* **17**, 958-965, doi:10.1111/jcmm.12088 (2013).
- 232 Uebele, V. N., Nuss, C. E., Renger, J. J. & Connolly, T. M. Role of voltage-gated calcium channels in potassium-stimulated aldosterone secretion from rat adrenal zona glomerulosa cells. *The Journal of steroid biochemistry and molecular biology* **92**, 209-218, doi:10.1016/j.jsbmb.2004.04.012 (2004).
- 233 Brosenitsch, T. A. & Katz, D. M. Physiological patterns of electrical stimulation can induce neuronal gene expression by activating N-type calcium channels. *The Journal of neuroscience : the official journal of the Society for Neuroscience* **21**, 2571-2579 (2001).
- 234 DG, C. *Minor insecticides of plant origin in Naturally occurring insecticides.* (Dekker, 1971).

- 235 Ulbricht, W. Effects of veratridine on sodium currents and fluxes. *Reviews of physiology, biochemistry and pharmacology* **133**, 1-54 (1998).
- 236 Ulbricht, W. The effect of veratridine on excitable membranes of nerve and muscle. *Ergebnisse der Physiologie, biologischen Chemie und experimentellen Pharmakologie* **61**, 18-71 (1969).
- 237 Ulbricht, W. voltage clamp studies of veratrinized frog nodes. *J Cell Comp Physiol* **66**, 91-98, doi:10.1002/jcp.1030660516 (1965).
- 238 Barnes, S. & Hille, B. Veratridine modifies open sodium channels. *J Gen Physiol* **91**, 421-443 (1988).
- 239 Sigel, E. Effects of veratridine on single neuronal sodium channels expressed in *Xenopus* oocytes. *Pflügers Archiv : European journal of physiology* **410**, 112-120 (1987).
- 240 Stevens, M., Peigneur, S. & Tytgat, J. Neurotoxins and their binding areas on voltage-gated sodium channels. *Frontiers in pharmacology* **2**, 71, doi:10.3389/fphar.2011.00071 (2011).
- 241 Felix, J. P. *et al.* Functional assay of voltage-gated sodium channels using membrane potential-sensitive dyes. *Assay and drug development technologies* **2**, 260-268, doi:10.1089/1540658041410696 (2004).
- 242 Lee, Y. *et al.* MicroRNA genes are transcribed by RNA polymerase II. *The EMBO journal* **23**, 4051-4060, doi:10.1038/sj.emboj.7600385 (2004).
- 243 Hulsen, T., de Vlieg, J. & Alkema, W. BioVenn – a web application for the comparison and visualization of biological lists using area-proportional Venn diagrams. *BMC Genomics* **9**, 1-6, doi:10.1186/1471-2164-9-488 (2008).
- 244 McCormack, K. *et al.* Voltage sensor interaction site for selective small molecule inhibitors of voltage-gated sodium channels. *Proceedings of the National Academy of Sciences of the United States of America* **110**, E2724-2732, doi:10.1073/pnas.1220844110 (2013).
- 245 Alexandrou, A. J. *et al.* Subtype-Selective Small Molecule Inhibitors Reveal a Fundamental Role for Nav1.7 in Nociceptor Electrogenesis, Axonal Conduction and Presynaptic Release. *PloS one* **11**, e0152405, doi:10.1371/journal.pone.0152405 (2016).
- 246 Theile, J. W., Fuller, M. D. & Chapman, M. L. The Selective Nav1.7 Inhibitor, PF-05089771, Interacts Equivalently with Fast and Slow Inactivated Nav1.7 Channels. *Molecular pharmacology* **90**, 540-548, doi:10.1124/mol.116.105437 (2016).
- 247 Jarvis, M. F. *et al.* A-803467, a potent and selective Nav1.8 sodium channel blocker, attenuates neuropathic and inflammatory pain in the rat. *Proceedings of the National Academy of Sciences of the United States of America* **104**, 8520-8525, doi:10.1073/pnas.0611364104 (2007).
- 248 Deuis, J. R. *et al.* Analgesic Effects of GpTx-1, PF-04856264 and CNV1014802 in a Mouse Model of Nav1.7-Mediated Pain. *Toxins* **8**, doi:10.3390/toxins8030078 (2016).
- 249 Vasylyev, D. V., Han, C., Zhao, P., Dib-Hajj, S. & Waxman, S. G. Dynamic-clamp analysis of wild-type human Nav1.7 and erythromelalgia mutant channel L858H. *J Neurophysiol* **111**, 1429-1443, doi:10.1152/jn.00763.2013 (2014).
- 250 Zainab Mohammed, C. D., David Grundy, Mohammed A. Nassar. Veratridine produces distinct calcium response profiles in mouse Dorsal Root Ganglia neurons. *Scientific Reports* **In press** (2017).

- 251 Browne, L. E., Blaney, F. E., Yusaf, S. P., Clare, J. J. & Wray, D. Structural determinants of drugs acting on the Nav1.8 channel. *The Journal of biological chemistry* **284**, 10523-10536, doi:10.1074/jbc.M807569200 (2009).
- 252 Lopez, M. G., Artalejo, A. R., Garcia, A. G., Neher, E. & Garcia-Sancho, J. Veratridine-induced oscillations of cytosolic calcium and membrane potential in bovine chromaffin cells. *J Physiol* **482 (Pt 1)**, 15-27 (1995).
- 253 Sharif Naeini, R., Witty, M. F., Seguela, P. & Bourque, C. W. An N-terminal variant of Trpv1 channel is required for osmosensory transduction. *Nature neuroscience* **9**, 93-98, doi:10.1038/nn1614 (2006).
- 254 Prager-Khoutorsky, M., Khoutorsky, A. & Bourque, C. W. Unique interweaved microtubule scaffold mediates osmosensory transduction via physical interaction with TRPV1. *Neuron* **83**, 866-878, doi:10.1016/j.neuron.2014.07.023 (2014).
- 255 Dina, O. A., McCarter, G. C., de Coupade, C. & Levine, J. D. Role of the Sensory Neuron Cytoskeleton in Second Messenger Signaling for Inflammatory Pain. *Neuron* **39**, 613-624, doi:[http://dx.doi.org/10.1016/S0896-6273\(03\)00473-2](http://dx.doi.org/10.1016/S0896-6273(03)00473-2) (2003).
- 256 Mei, X., Sweatt, A. J. & Hammarback, J. A. Regulation of microtubule-associated protein 1B (MAP1B) subunit composition. *Journal of neuroscience research* **62**, 56-64, doi:10.1002/1097-4547(20001001)62:1<56::aid-jnr6>3.0.co;2-# (2000).
- 257 Gupta, M. & Yarwood, S. J. MAP1A light chain 2 interacts with exchange protein activated by cyclic AMP 1 (EPAC1) to enhance Rap1 GTPase activity and cell adhesion. *The Journal of biological chemistry* **280**, 8109-8116, doi:10.1074/jbc.M413697200 (2005).
- 258 Kong, H., Boulter, J., Weber, J. L., Lai, C. & Chao, M. V. An evolutionarily conserved transmembrane protein that is a novel downstream target of neurotrophin and ephrin receptors. *The Journal of neuroscience : the official journal of the Society for Neuroscience* **21**, 176-185 (2001).
- 259 Fujiwara, Y. *et al.* Microtubule association of a neuronal RNA-binding protein HuD through its binding to the light chain of MAP1B. *Biochimie* **93**, 817-822, doi:10.1016/j.biochi.2011.01.008 (2011).
- 260 Yu, H. *et al.* Lentiviral gene transfer into the dorsal root ganglion of adult rats. *Molecular pain* **7**, 63, doi:10.1186/1744-8069-7-63 (2011).
- 261 Fleming, J. *et al.* Adeno-associated virus and lentivirus vectors mediate efficient and sustained transduction of cultured mouse and human dorsal root ganglia sensory neurons. *Human gene therapy* **12**, 77-86, doi:10.1089/104303401450997 (2001).
- 262 Xu, K., Zhong, G. & Zhuang, X. Actin, spectrin, and associated proteins form a periodic cytoskeletal structure in axons. *Science (New York, N.Y.)* **339**, 452-456, doi:10.1126/science.1232251 (2013).
- 263 He, J. *et al.* Prevalent presence of periodic actin-spectrin-based membrane skeleton in a broad range of neuronal cell types and animal species. *Proceedings of the National Academy of Sciences of the United States of America* **113**, 6029-6034, doi:10.1073/pnas.1605707113 (2016).
- 264 Ho, C., Zhao, J., Malinowski, S., Chahine, M. & O'Leary, M. E. Differential expression of sodium channel beta subunits in dorsal root ganglion sensory neurons. *The Journal of biological chemistry* **287**, 15044-15053, doi:10.1074/jbc.M111.333740 (2012).

- 265 Wood, J. N., Boorman, J. P., Okuse, K. & Baker, M. D. Voltage-gated sodium channels and pain pathways. *Journal of neurobiology* **61**, 55-71, doi:10.1002/neu.20094 (2004).
- 266 Treede, R.-D. *et al.* A classification of chronic pain for ICD-11. *Pain* **156**, 1003-1007, doi:10.1097/j.pain.000000000000160 (2015).
- 267 Goldberg, D. S. & McGee, S. J. Pain as a global public health priority. *BMC public health* **11**, 770, doi:10.1186/1471-2458-11-770 (2011).
- 268 Mikami, M. & Yang, J. Short hairpin RNA-mediated selective knockdown of Nav1.8 tetrodotoxin-resistant voltage-gated sodium channel in dorsal root ganglion neurons. *Anesthesiology* **103**, 828-836 (2005).
- 269 Bagetta, G. *et al.* Inducible nitric oxide synthase is involved in the mechanisms of cocaine enhanced neuronal apoptosis induced by HIV-1 gp120 in the neocortex of rat. *Neuroscience letters* **356**, 183-186, doi:10.1016/j.neulet.2003.11.065 (2004).
- 270 Zhu, Y. *et al.* Lentivirus infection causes neuroinflammation and neuronal injury in dorsal root ganglia: pathogenic effects of STAT-1 and inducible nitric oxide synthase. *Journal of immunology (Baltimore, Md. : 1950)* **175**, 1118-1126 (2005).
- 271 Zhang, X., Priest, B. T., Belfer, I. & Gold, M. S. Voltage-gated Na(+) currents in human dorsal root ganglion neurons. *eLife* **6**, e23235, doi:10.7554/eLife.23235 (2017).
- 272 Davidson, S. *et al.* Human sensory neurons: Membrane properties and sensitization by inflammatory mediators. *Pain* **155**, 1861-1870, doi:10.1016/j.pain.2014.06.017 (2014).
- 273 Hudmon, A. *et al.* Phosphorylation of sodium channel Na(v)1.8 by p38 mitogen-activated protein kinase increases current density in dorsal root ganglion neurons. *The Journal of neuroscience : the official journal of the Society for Neuroscience* **28**, 3190-3201, doi:10.1523/jneurosci.4403-07.2008 (2008).
- 274 Xiao, Y., Xia, Z., Wu, Y. & Zhao, B. Sodium channel Nav1.7 expression is upregulated in the dorsal root ganglia in a rat model of paclitaxel-induced peripheral neuropathy. *SpringerPlus* **5**, 1738, doi:10.1186/s40064-016-3351-6 (2016).
- 275 Peeraer, E. *et al.* Pharmacological evaluation of rat dorsal root ganglion neurons as an in vitro model for diabetic neuropathy. *Journal of Pain Research* **4**, 55-65, doi:10.2147/JPR.S15452 (2011).
- 276 Barry, J. *et al.* Ankyrin-G directly binds to kinesin-1 to transport voltage-gated Na⁺ channels into axons. *Dev Cell* **28**, 117-131, doi:10.1016/j.devcel.2013.11.023 (2014).
- 277 Su, Y. Y. *et al.* KIF5B promotes the forward transport and axonal function of the voltage-gated sodium channel Nav1.8. *The Journal of neuroscience : the official journal of the Society for Neuroscience* **33**, 17884-17896, doi:10.1523/jneurosci.0539-13.2013 (2013).
- 278 Leterrier, C. *et al.* Nanoscale Architecture of the Axon Initial Segment Reveals an Organized and Robust Scaffold. *Cell reports* **13**, 2781-2793, doi:10.1016/j.celrep.2015.11.051 (2015).
- 279 Lajoie-Mazenc, I. *et al.* MAP1A light chain-2 interacts with GTP-RhoB to control epidermal growth factor (EGF)-dependent EGF receptor signaling. *The Journal of biological chemistry* **283**, 4155-4164, doi:10.1074/jbc.M709639200 (2008).

- 280 Jaffe, A. B. & Hall, A. Rho GTPases: biochemistry and biology. *Annual review of cell and developmental biology* **21**, 247-269, doi:10.1146/annurev.cellbio.21.020604.150721 (2005).
- 281 Noben-Trauth, K., Naggert, J. K., North, M. A. & Nishina, P. M. A candidate gene for the mouse mutation tubby. *Nature* **380**, 534-538, doi:10.1038/380534a0 (1996).
- 282 Kleyn, P. W. *et al.* Identification and characterization of the mouse obesity gene tubby: a member of a novel gene family. *Cell* **85**, 281-290 (1996).
- 283 Branco, T. *et al.* Near-Perfect Synaptic Integration by Na(v)1.7 in Hypothalamic Neurons Regulates Body Weight. *Cell* **165**, 1749-1761, doi:10.1016/j.cell.2016.05.019 (2016).
- 284 Ikeda, A. *et al.* Microtubule-associated protein 1A is a modifier of tubby hearing (moth1). *Nature genetics* **30**, 401-405, doi:10.1038/ng838 (2002).